# Chemical Investigations of Inorganic Nanostructures

A Thesis submitted in partial fulfillment
of the requirements of the degree of

## Doctor of Philosophy

By

### K. P. Kalyanikutty

Chemistry and Physics of Materials Unit

Jawaharlal Nehru Centre for Advanced Scientific Research

(A Deemed University)

Bangalore – 560064 (INDIA)

August 2008

*Dedicated to my dear parents*

# Declaration

I hereby declare that this thesis entitled "**Chemical Investigations of Inorganic Nanostructures**" is an authentic record of research work carried out by me under the supervision of Prof. C. N. R. Rao, FRS at the Chemistry and Physics of Materials Unit, Jawaharlal Nehru Centre for Advanced Scientific Research, Bangalore, India.

In keeping with the general practice of reporting scientific observations, due acknowledgement has been made whenever work described here has been based on the findings of other investigators. Any oversight due to error of judgement is regretted.

K. P. Kalyanikutty

# Certificate

Certified that the work described in this thesis entitled "**Chemical Investigations of Inorganic Nanostructures**" has been carried out by Ms. K. P. Kalyanikutty under my supervision at the Chemistry and Physics of Materials Unit, Jawaharlal Nehru Centre for Advanced Scientific Research, Bangalore, India.

Prof. C. N. R. Rao

# *Acknowledgements*

# Preface

This thesis deals with the synthesis, characterization, growth and properties of inorganic nanomaterials such as the 1D nanostructures of metal oxides and chalcogenides, and the 2D nanostructures of metal chalcogenides in the form of ultrathin films.

After a brief overview of inorganic nanomaterials (Chapter 1), the results obtained on nanowires by the carbon-assisted method are described in Chapter 2. Nanowires of the oxides MgO, $GeO_2$, and doped and undoped ITO have been prepared by the simple and versatile method. In the case of MgO, apart from nanowires the carbothermal method has been successful in yielding a variety of nanostructures which include nanotubes as well as branched and patterned nanowires.

Chapter 3 describes the synthesis of nanotubes and nanowires of metal chalcogenides by a hydrogel-assisted template route. The nanostructures of the semiconducting materials- CdS, ZnS and CuS obtained by the method have been characterized by electron microscopy and optical spectroscopy. Evidence for oriented attachment of nanocrystals leading to the growth of the one-dimensional nanostructures has been observed in TEM images.

The use of liquid-liquid interface for the preparation of thin films of metal sulfides and selenides has been illustrated in Chapter 4. Thus, thin films of ZnS, PbS, CdSe and CuSe have been prepared at the organic-water interface under ambient conditions. The ZnS, PbS and CuSe films have been found to be single-crystalline by TEM analysis. In addition to the single-crystalline thin films of metal sulfides, the method has also been used for the preparation of the bilayered film of metal sulfides-CdS-CuS. A time evolution study of the polycrystalline film of Au, CdS as well as

single-crystalline CuS has been carried out by employing atomic force microscope. High resolution atomic force microscopy study on the effect of mechanical vibrations on the formation of Au nanoparticulate films has been presented. Besides describing features of such nanocrystalline films and their mode of formation, the interfacial rheological properties of the polycrystalline CdS film as well as single-crystalline CuS film have been examined. An important advantage of the study of materials formed at the liquid-liquid interface is that it provides a means to investigate the interface itself. In addition, it enables one to obtain substrate-free single-crystalline films of materials.

In Chapter 5, the results of high-temperature synthesis of mesoporous Fm3m aluminosilicates are presented. It has been found that the synthesis temperature plays a significant role in controlling the Al content, pore volume, pore diameter, and acidity of the materials. These aluminosilicate materials have been demonstrated to show high catalytic activity in the acetylation of veratrole by acetic anhydride even at a temperature as low as 35 $^{o}$C.

# Contents

3. **Hydrogel-assisted synthesis of nanotubes and nanorods of CdS,**

   **ZnS and CuS, showing some evidence for oriented attachment** **87**

Summary 87

# CHAPTER 1

# A Brief Overview of Nanomaterials

## 1.1 Introduction

'Nanoscience' and 'nanotechnology' have become the current buzzwords due to the immense opportunities they have created in various fields including physics, chemistry and biology. Nanoscience is the science of objects having at least one dimension less than 100 nm. Such nanometer scale structures (or nanomaterials), whose properties are considerably different from those of atoms as well as those of bulk materials, represent a rapidly expanding and challenging area of research that crosses the borders between many areas of physical sciences and engineering [1,2]. Nanotechnology, which deals with the fabrication of devices within the nanosize (1-100 nm) regime, can be seen as an extension of existing sciences into the nanoscale.

The first use of the concepts in 'nanotechnology' was in "There's Plenty of Room at the Bottom", a talk given by physicist Richard Feynman in 1959. Feynman described a process by which the ability to manipulate individual atoms and molecules might be developed, using one set of precise tools to build and operate another proportionally smaller set, so on down to the needed scale [3]. The decades since then have witnessed the invention of techniques for imaging and manipulating individual atoms and molecules, for example, the scanning tunneling microscopy (STM). Thus, were opened new doors to the nanoworld. The real breakthrough in nanoscience happened in 1983 with the experimental observation of the then most intriguing phenomenon: atom-by-atom reconstruction in Si(111) using STM [4].

_____

Numerous methods for the synthesis of nanoparticles, nanowires and nanotubes, and their assemblies have been devised. This, in turn, has led to the discovery of novel nanostructures of many inorganic nanomaterials. Apart from the established techniques of electron microscopy, diffraction methods and spectroscopic tools, scanning probe microscopies have proved to be a powerful means for studying nanomaterials.
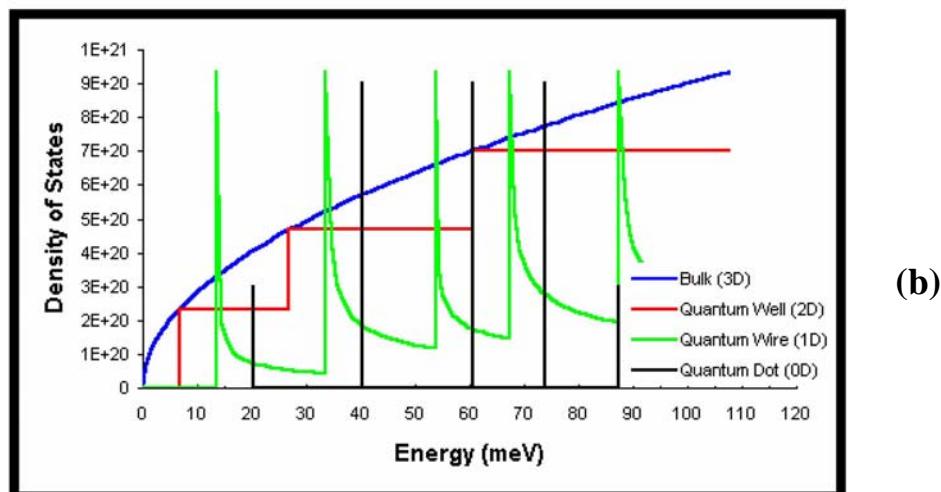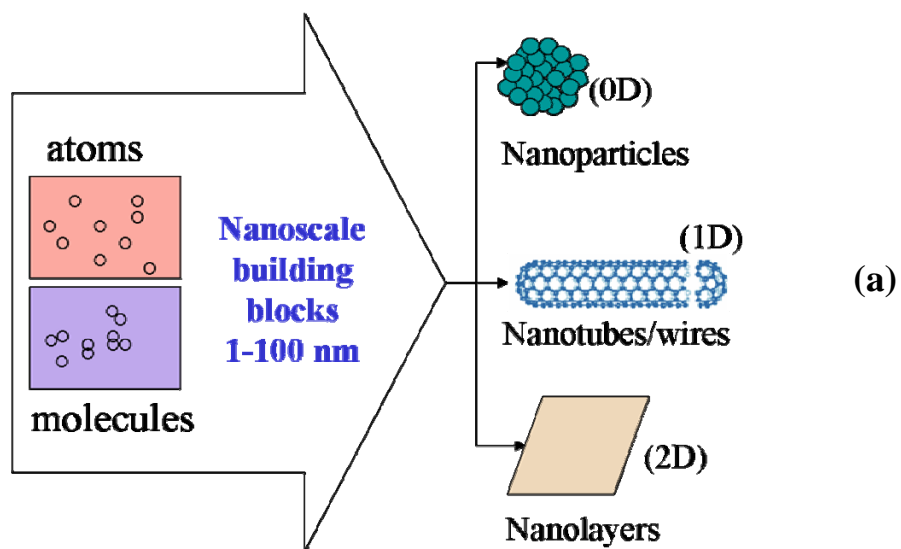
**Figure 1.1.** Schematic showing (a) formation of 0D, 1D and 2D nanomaterials from molecular components and (b) density of states for bulk (blue), quantum well (red), quantum wire (green) and quantum dot (black).

_____

The two main approaches followed in nanotechnology are: (i) bottom-up approach in which the nanomaterials or devices are built starting from molecular components [see Figure 1.1a] and (ii) top-down approach wherein the nanoobjects are constructed from bulk materials or large entities. Reducing 1, 2 or 3 dimensions (D) of a bulk material to the nanometer scale produces, for e.g. nanometer thick 2D layers, 1D nanotubes or nanowires or 0D nanoclusters, respectively [5]. A schematic illustration, showing the density of states versus energy for nanostructures of various dimensions, is given in Figure 1.1b. The density of states changes remarkably with dimension. For 2D nanostructures it is a step function with steps occurring at the energy of each quantized level. In the case of 1D nanostructures, van Hove singularities are observed. For 0D nanostructures, the density of states shows quantization at particular energy levels. The quantum confinement of electrons by the potential walls of nanomaterials can provide one of the most powerful means to control the electrical, optical, magnetic, and thermoelectric properties of a solid-state functional material. Suitable control of these properties of nanomaterials, which depend on their size, can lead to new stream of science as well as new devices and technologies, the underlying theme of nanotechnology.

Much of the fascination with nanotechnology stems from the unique quantum and surface phenomena that matter exhibits at the nanoscale [6]. A number of physical properties change when compared to macroscopic systems. One example is the increase in surface area to volume of materials. Materials reduced to the nanoscale show significantly different properties compared to those exhibited on a macroscale, enabling unique applications. Size affects the structure of nanocrystals of semiconductor materials such as CdS and CdSe, and also their properties such as the melting point and the electronic absorption. Even metals show nonmetallic band gaps

when the diameter of the nanocrystals is in the 1-2 nm range. For instance, in Hg clusters, $\sim$ 300 atoms are required to close the gap. Also, reactivity increases drastically at the nanoscale. Noble metal such as gold which is chemically inert in its bulk state shows excellent catalytic powers at the nanoscale.

## 1.2    Nanocrystals

Nanocrystals are aggregates of a few hundred or even tens of thousands of atoms that combine into a crystalline form of matter known as a "cluster". Typically a few nanometers in diameter, nanocrystals are larger than molecules but smaller than bulk solids and therefore frequently exhibit physical and chemical properties somewhere in between. Metal clusters have been known to man from ancient times, though the foundation of modern colloid science was laid by Michael Faraday in 1857 [7]. The secret behind the color of the Lycurgus cup (a Roman dichroic glass beaker in the British Museum dated to 4 A.D.) which appears red in transmitted light and green in reflected light was found to be due to Au and Ag nanocrystals impregnated in glass. Due to the confinement of electron wave function to the physical dimensions of the particles in small nanocrystals (or the quantum confinement), electron energy levels are discrete, unlike in the bulk where the levels are continuous [8,9]. Nanocrystals possess high surface area, with a large fraction of its atoms on the surface. These materials are commonly referred to as 'quantum dots,' indicating that they are quantum confined in three dimensions. Their properties can vary considerably with size. By precisely controlling a nanocrystal's size and surface, its electronic, magnetic, and optical properties can be changed. The electronic absorption spectrum of metal nanocrystals in the visible region is dominated by the plasmon band and the surface plasmon excitations impart characteristic colors to metal sols.

_____

This absorption is due to the itinerant electron gas on the particle surface and is characteristic of a nanocrystal of a given size. In semiconductor nanocrystals, exciton peaks dominate the absorption. As the particle size decreases below the Bohr radius of the semiconductor material, the electron becomes more confined in the particle. This confinement leads to an increase in the band gap energy. Furthermore, the valence and the conduction bands break into quantized energy levels. A series of nanocrystalline-semiconductor suspensions under ultraviolet illumination with the only variation between samples being the size of the particles is shown in Figure 1.2. The band gap emission is observed to shift through the entire visible region, from red to blue, as the size of the nanocrystal is decreased.



**Figure 1.2.** Suspensions of CdSe quantum dots under ultraviolet excitation.

### 1.2.1   Synthetic strategies

Chemical synthesis of sols of metals and semiconductors results in nanoparticles embedded in a layer of organic ligands or stabilizing agents, which prevent the aggregation and precipitation of nanoparticles out of the solution [8,9]. The stabilizing agents employed include surfactants such as long chain thiols or amines or polymeric ligands such as polyvinylpyrrolidone (PVP). Choice of the reduction technique, time, and capping material determines the size and shape of the

_____

nanocrystals generated. Sphere, cube, rod, and triangular prism- shaped nanoparticles in Au, Pt and Ag with various reduction techniques and capping agents have been generated [8c]. Reduction of metal salts dissolved in appropriate solvents like alcohols, glycols, metal borohydrides, etc produces small metal particles of varying distributions [9b]. The popular citrate route to spherical Au nanoparticles involves the addition of chloroauric acid to a boiling solution of sodium citrate [10,11]. The size distribution of gold nanospheres generated is controlled by the reaction temperature, the ratio of gold to citrate, and the order of addition of the reagents. Reduction of $HAuCl_4$ with tetrakis(hydroxymethyl)phosphonium chloride (THPC), which also acts as a capping agent, results in Au nanocrystals with diameters between 1 and 2 nm [12]. The Brust method [13] which has been widely employed for the preparation of organic-capped Au nanocrystals, by the reduction of $AuCl_4^-$ by $NaBH_4$ in the presence of an alkanethiol, is carried out in a water-toluene mixture in the presence of a phase-transfer reagent such as tetraoctylammonium bromide (TOAB). Nanocrystals of Au, Ag, Pt and Cu have been obtained by dispersing the respective metal salts in toluene followed by their reduction using TOAB [14]. Using a mixture of borohydride and hydrogen peroxide as the reducing agent, Ag nanoprisms as well as branched Au nanocrystals have been synthesized [15]. The polyol process has been employed to obtain cubic, cubohedral and octahedral- shaped Pt nanocrystals [16].

Synthesis of II–IV semiconductor nanocrystals has attracted great attention in the past few years [8b,10]. The methods commonly employed for the synthesis include solution-based methods, solvothermal, thermolysis and precursor decomposition. In the case of semiconductor nanocrystals such as CdS, CdSe, ZnS, PbS, etc, arrested precipitation is generally followed [9b]. The nanoparticles so obtained possess a broad distribution in diameter. Thermolysis methods involving the

_____

decomposition of organometallic precursors are also used to prepare semiconductor nanocrystals [9b]. Clusters of controlled sizes have been generated traditionally by ablation of a metal target in vacuum followed by mass selection of plume to yield cluster beams. CdSe nanocrystals have been prepared by Bawendi and co-workers by the controlled reaction of dimethyl cadmium and trioctylphosphine selenide in a high-boiling solvent [17]. Reacting cadmium stearate with S and Se under solvothermal conditions in the presence of tetralin yields size-tunable CdS and CdSe nanocrystals [18]. By the reaction of cadmium acetate dihydrate with thioacetamide in imidazolium [BMIM]-based ionic liquids hexagonal CdS nanocrystals have been obtained [19]. Nanocrystals of several metal sulfides such as CdS, ZnS, PbS and MnS with different shapes and sizes have been prepared by Hyeon and co-workers by the thermolysis of metal–oleylamine complexes in the presence of S and oleylamine [20]. Alivisatos and co-workers have reported the formation of hollow CoS nanocrystals (Figure 1.3), obtained by reacting Co nanocrystals with molecular sulfur dissolved in dichlorobenzene [21].
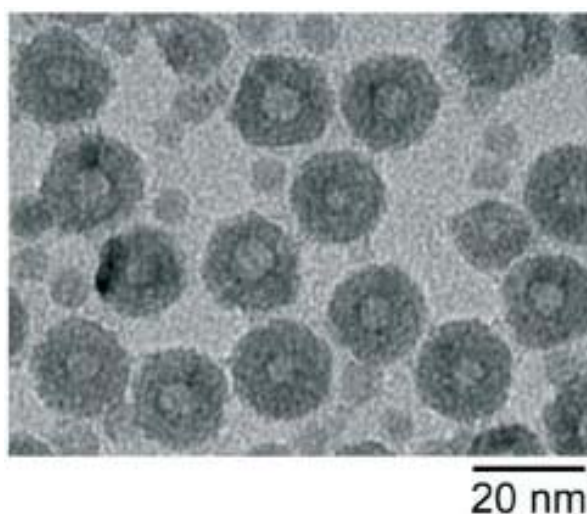


**Figure 1.3.** TEM image of hollow CoS nanocrystals

_____

**1.2.2   Nanocrystalline 2D films at liquid-liquid interfaces**

2D arrays or films of nanocrystals, a combination of notional two and zero dimensionalities, have attracted much attention because of their potential applications in nanodevices. In this context, the interfaces, formed between two different phases with common boundaries, are considered to be an important means to generate two-dimensional self-assemblies of nanocrystals [10,22]. They provide a constrained environment for organized assembly. Due to interfacial interactions, atoms at the interfaces are more prone to react with the surrounding species, thus bringing about many useful properties. The air-water interface has been exploited for the preparation of films of metals and semiconductors. For example, nanocrystal assemblies of gold have been prepared at the air-water interface by employing Langmuir-Blodgett (LB) technique [23]. Using a chloroform solution of $Au_{55}(PPh_3)_{12}Cl_6$, Schmid *et al.* [24] have self-assembled $Au_{55}$ nanocrystals into monolayers in an LB trough. The electrochemical deposition of Pt and Pd particles at the organic–water interface has been reported by Dryfe *et al.* [25]. Bawendi and co-workers [26] have prepared monolayers of monodisperse trioctylphosphine oxide capped CdSe quantum dots by the LB method. By exposing an LB film of lead stearate to $H_2S$, nanoparticles of PbS have been generated in the form of films [27]. Properties of thin films obtained by the LB technique are determined by the nature of the substrate as well as the reaction conditions, and the films are generally polycrystalline.

Unlike the air-water interface, the liquid-liquid (organic-aqueous) interface has not been investigated sufficiently, and it is only a decade since some concerted efforts have been carried out for understanding the interface in detail [28]. The liquid-liquid surface possesses unique thermodynamic properties such as viscosity and density. A liquid-liquid interface is a non-homogeneous region having a thickness in

_____

the order of a few nanometers. The interface is not sharp, since there is always a little solubility of one phase in the other. One of the problems that has been studied in depth at the liquid-liquid interface relates to interfacial charge transfer reactions and dynamics. Using X-ray reflectivity and molecular dynamics simulations, Schlossman and co-workers have found that ion sizes and ion-solvent interactions affect the ion distributions near the interface [29]. The thickness of the interface being of the order of several atoms, a dimension comparable to that of the nanostructures, the control over the dynamic process across the interfaces is usually the determining factor for the growth of nanostructures while they might be negligible for bulk materials. Thus, the interface between two immiscible liquids offers an important alternative path for the self-assembly and chemical manipulation of nanocrystals. Nanoparticles are highly mobile at the interface and rapidly achieve an equilibrium assembly by the reduction in interfacial energy. The three parameters which have been found to influence the energy of assembly process at the liquid-liquid interface are: (i) the nature of the interface, (ii) surface modification of the nanoparticles at the interface and (iii) the effective radius of the nanoparticles, smaller nanoparticles adsorbing weakly to the interface than larger ones [30]. Binks and Clint [31a] have theoretically treated the wetting of silica particles in terms of the surface energies at the oil-water interface to interpret the interactions between the solid and the liquid phases, and to predict the oil-water contact angles for a solid of given hydrophobicity. Their treatment rationalizes the experimental finding that nonpolar oils favor the formation of oil/water emulsions and polar ones favor water/oil emulsions. Only if the contact angle is exactly $90^o$ will the particle be located at the middle of the oil-water interface. Recently, they have developed a new method of measuring the contact angle of solid particles at liquid interfaces called the film-calliper method [31b].

_____

The assembly of phosphine oxide functionalized CdSe nanoparticles at the toluene-water interface has been studied by employing fluorescence spectroscopy [32]. By investigating the interactions of a variety of particles such as uncharged, charged, functionalized and non-functionalized, deposited at dodecanediol dimethacrylate/water interface, Benkoski *et al.* [33] have shown that nanoparticles aggregate into a wide variety of complex morphologies. There are a few assorted reports in the literature where the liquid-liquid interface or a mixture of immiscible liquids has been used for the synthesis or crystallization of nanostructures and other materials. Langmuir films of silver nanoparticles have been prepared at the water-dichloromethane interface [34]. Dodecanethiol capped Ag nanoparticles have been self-assembled at the trichloroethylene-water interface [35]. Sathaye *et al.* [36] have prepared CdS nanoparticles in the form of LB films by reacting aqueous $CdCO_3$ solution with $CS_2$ in $CCl_4$. Monodisperse, luminescent nanocrystals of CdS have been prepared by mixing a solution of Cd-myristic acid and *n*-triphenylphosphine oxide in toluene with an aqueous solution of thiourea, followed by heating under stirring [37]. Stucky and co-workers [38] have prepared mesoporous fibers of silica by treating the silica precursor dissolved in an organic phase such as hexane, toluene or $CCl_4$ with surfactant molecules dissolved in the aqueous phase. Although the assembly of pre-generated nanoparticles at the liquid-liquid interfaces has been examined to some extent, this interface has not been exploited for the synthesis of nanoparticles and their assemblies.

Recently, the liquid–liquid interface has been employed for obtaining ultra-thin nanocrystalline films of a variety of materials [10,22]. The method involves dissolving an organic precursor of the relevant metal in the organic layer and the appropriate reagent in the aqueous layer. The product formed by the reaction at the

_____
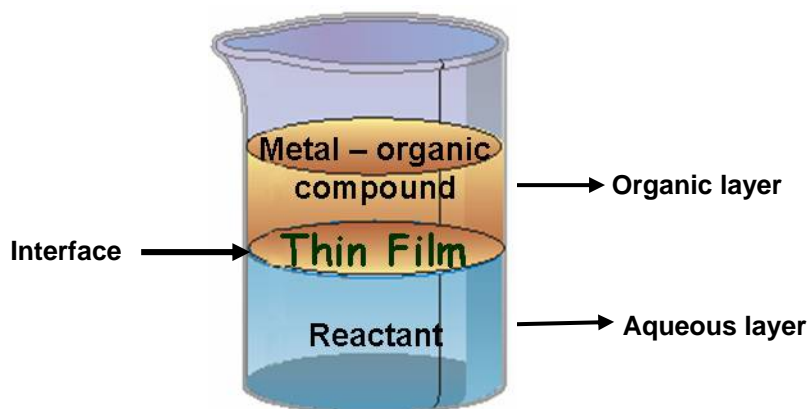


**Figure 1.4.** Schematic showing the formation of a thin film of the inorganic material at the liquid-liquid interface.

interface contains ultra-thin nanocrystalline films of the relevant material formed by closely packed nanocrystals (see the schematic given in Figure 1.4). Unlike chemical methods such as the LB technique where non-single-crystalline films are obtained by assembling nanocrystals or CVD and related techniques where stringent conditions as well as substrates are required, this simple one-step synthetic technique has been shown to yield nanocrystals of metals such as Au, Ag, and Pd, chalcogenides such as CdS and NiS as well as extended single-crystalline films of CuO, ZnO, CuS at room temperature.

### 1.2.3   Properties of nanocrystals

The intense colors exhibited by metal colloids are due to their surface plasmon absorption. The surface plasmon resonance is caused by the coherent motion of the conduction band electrons which interact with an electromagnetic field [39]. As the wave front of light passes, the electric field of the incident light induces a polarization of free electrons of the nanoparticle. As a result, the electron density in the particle gets polarized to one surface and oscillates in resonance with the light's frequency

causing a standing oscillation (see Figure 1.5) [8c]. This surface plasmon resonance is found to be dependent on the shape, size and dielectric constants of both the metal and the surrounding medium. The surface plasmon resonance was theoretically explained by Mie [40] in 1908, including linear optical properties such as extinction and scattering of small spherical metal particles.
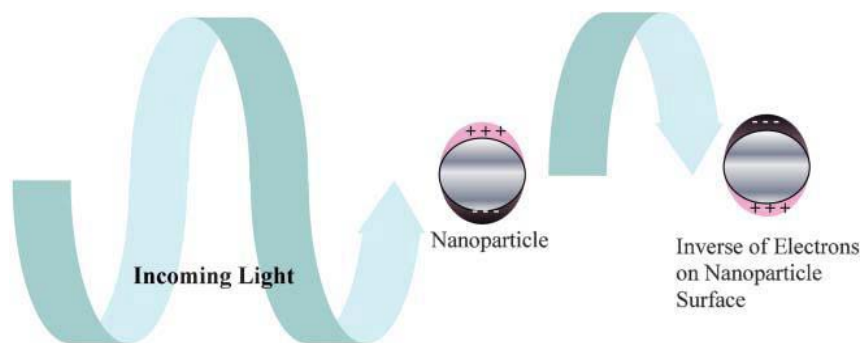


**Figure 1.5.** Origin of the surface plasmon resonance in metal nanoparticles.

Colloidal semiconductor nanocrystals combine the physical and chemical properties of molecules with the optoelectronic properties of semiconductors. Their color is highly controllable, a direct consequence of quantum confinement on the electronic states. The quantum confinement effect is divided into three regimes, depending on the relationship of the radius of the nanocrystal (r) with the Bohr radius (r$_B$) of the bulk exciton (or the electron-hole pair). r$_B$ = $\varepsilon\hbar^2$ / $\mu e^2$, where $\mu$ is the exciton-reduced mass and $\varepsilon$ is the dielectric constant of the semiconductor [8b]. Weak, intermediate and strong confinement correspond to r $>>$ r$_B$, r $\sim$ r$_B$, and r $<<$ r$_B$, respectively. With decreasing size of the nanocrystal, the energy of the lowest electron and hole quantum-size levels as well the total energy of the optical transitions between these levels decreases. Also, the Coulomb interaction existing between the

_____

optically created electron and hole significantly affects the optical properties of the nanocrystal.

The two important factors which control the properties of nanoparticles are their size and surface characteristics [8]. As the radius of the nanocrystals decreases the surface to volume ratio increases. The surface atoms in nanoparticles are chemically more active compared to their bulk counterparts because they have fewer adjacent coordinate atoms or more dangling bonds. Thus, there is a large energy associated with the surface of nanocrystals. Smaller the nanocrystal, larger is the contribution made by the surface energy to the overall energy of the system. But, at the same time, the imperfection of the particle surface induces additional electronic states in the band gap, which act as electron or hole trap centers. At high densities of surface defects, the emission band gets red-shifted due to the defect band formation.

A direct consequence of the size effect in nanocrystals is the observed decrease in their melting point, as the surface energy is always lower in the liquid phase compared to the solid phase [8b]. The surface atoms move to minimize the surface area and the unfavorable surface interactions in the dynamic fluid phase. In the solid phase, rigid bonding geometries cause stepped surfaces with high-energy edge and corner atoms. Melting, thus helps to reduce the total surface energy of the system, and stabilizes the liquid phase over the solid phase.

### 1.2.4   Applications of nanocrystals

Catalysis is one of the areas, which has witnessed explosive growth by the use of nanoparticles as catalysts. The electrocatalytic activities of Pt nanoparticles for methanol, formic acid, and formaldehyde electrooxidation have been investigated [41]. The use of Ag nanoparticles to enhance the redox activity of organosulfur

13

_____

compounds [42] and that of Pt nanoparticles on the electrochemical oxidation of oxalic acid have been reported [43]. Faceted thiol-capped Au-Pt alloy nanoparticles which possess dual advantage of CO oxidation at the Au sites and methanol oxidation at the Pt sites have been prepared by Zhong and co-workers [44]. Nanosized alloys of Sn-Sb dispersed on carbon have been found to be good anodes for lithium batteries [45]. A device consisting of 2-naphthalenethiol-capped Au nanocrystals/polystyrene composite sandwiched in between two Al electrodes has been shown to act as a potential memory device [46]. A nanoswitch has been devised by attaching Au nanoparticles to a bipyridinium moiety anchored to a gold substrate. By controlling the substrate-to-solution potential, they could switch the bipyridinium ion between its oxidized and reduced states [47].

Electrode surfaces modified with metal nanoparticles have found immense applications as biosensors. Gold nanoparticles have been found to retain activity of bimolecules, with electrochemical activity intact [48]. These nanoparticles, in addition to providing large catalytic surface areas, have been observed to act as conduction centers facilitating the transfer of electrons. The optical response of metal nanocrystals to changes in dielectric constant of the surrounding medium has been used to design probes which respond to for example, protein-protein interactions [9c]. Ag nanotriangles have been used to detect biotin-streptavidin binding by immobilizing biotin on the particles [49]. Kotov and co-workers have shown that molecular springs, fabricated by linking CdTe and Au nanocrystals via polymers, can act as nanothermometers [50].

Semiconductor nanocrystals find many applications in optoelectronic systems such as light emitting diodes (LEDs) and photovoltaic cells, or as components of future nanoelectronic devices [8a,9c]. Bilayer LEDs with a PPV layer at the anode

___

and a plain TOPO-coated CdSe nanocrystal layer at the cathode have been reported [51]. Poly(2-hexylthiophene)-CdSe nanorod multilayers have been used for fabricating solar cells [52]. Photocurrent generation and electroluminescence (EL) have been observed from devices built using CdS nanocrystals and polymers [53]. Reducing the electronic interaction between nanocrystals and their surroundings removes non-radiative decay pathways and reduces the rate of change of charge separation at the nanocrystal-polymer interface [8a]. Thus, higher photoluminescence and EL efficiencies have been reported in devices consisting of CdSe cores capped with CdS layers [54]. Efficient photodetectors based on PbSe nanocrystal-polymer composites have been fabricated; the observed photocurrent gain having been attributed to carrier multiplication in PbSe nanocrystals and efficient charge transport through the polymer matrix [55]. Klein *et al.* [56] have reported the fabrication of a single-electron transistor from a colloidal nanocrystal of CdSe. In Figure 1.6 is given a diagram of their device. This device structure enables the number of charge carriers on the nanocrystal to be tuned directly, and so permits the measurement of energy required for the addition of successive charge carriers. Such
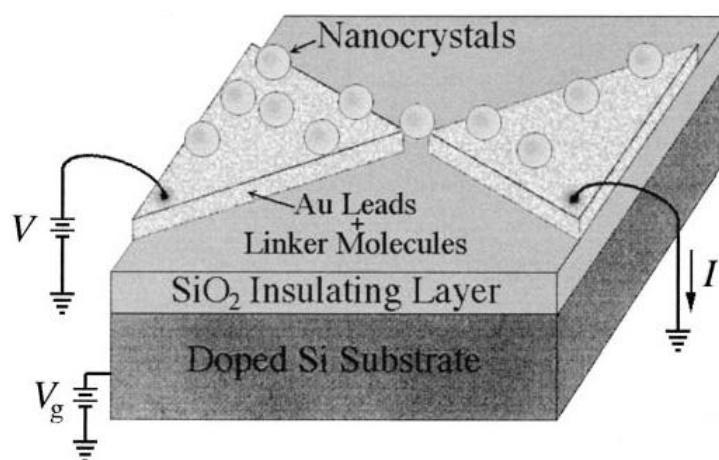


**Figure 1.6.** Diagram of the single-electron transistor.

measurements are invaluable in understanding the energy-level spectra of small electronic systems.

## 1.3 Nanowires

One-dimensional nanostructures such as nanowires (NWs), nanorods and nanobelts have attracted much attention due to their importance in basic scientific research and technological applications [57-59]. Their interesting properties such as greater mechanical toughness, higher luminescence efficiency etc, when compared to their bulk counterparts, make them superior. In comparison to the zero-dimensional nanostructures (0D), the one-dimensional nanostructures pose as better model systems for investigating the dependence of electronic transport, optical and mechanical properties on the size confinement and dimensionality. They also represent critical components in various nanoscale devices. The area of inorganic nanowires especially, is one of intense activity. An important aspect of nanowires relates to the assembly of individual atoms into such unique 1D nanostructures in a controlled fashion. The synthesis of nanowires with controlled composition, size, purity and crystallinity is no easy task and requires a proper understanding of the nucleation and growth process at the nanometer regime. Many nanolithographic techniques, such as proximal-probe patterning, electron-beam or focused ion-beam writing, etc, have been employed for the synthesis of nanowires and other 1D nanostructures [60]. Since these physical methods are generally slow and costly, researchers have been investigating chemical routes towards the synthesis of 1D nanostructures. The common chemical methods include solution and vapor based methods, as well as solvothermal, hydrothermal and carbothermal methods [58].

_____

**1.3.1   Synthetic Strategies**

Crystallization is the essence of one-dimensional nanostructure formation [60]. When the concentration of the building blocks (atoms, ions or molecules) of a solid becomes sufficiently high, homogenous nucleation takes place, leading to the formation of small nuclei or clusters. Subsequently, larger clusters are formed from these small clusters, which serve as seeds. The formation of a perfect crystal requires a reversible pathway between the building blocks on the solid surface and those in a fluid phase (vapor, solution or melt). These conditions allow the building blocks to easily adopt correct positions in developing the long-range ordered, crystalline lattice. Also, to attain homogeneous composition and uniform morphology, the building blocks have to be supplied at a well-controlled rate. Many synthetic strategies have been developed as the "bottom-up" approach for generating 1D nanostructures [57]. Figure 1.7 shows some of these strategies that include: (a) use of intrinsically anisotropic crystallographic structure of a solid to accomplish 1D growth; (b) introduction of a liquid-solid interface to reduce the symmetry of a seed; (c) use of templates to direct the formation of nanowires; (d) the use of capping agents to kinetically control the growth rates of a seed; (e) self assembly of 0D nanostructures, and (f) size-reduction of 1D nanostructures. Broadly these strategies can be classified into (1) nanowire growth in the gas phase and (2) solution-based growth.

***Vapor-phase growth of nanowires***

Vapor-phase approach has been extensively investigated in the formation of 1D nanostructures such as whiskers, nanowires and nanorods, due to its simplicity and accessibility. This vapor-phase growth was first observed in the formation of Hg nanofibers by Volmer and Estermann in 1921, when Hg vapor was condensed on a

_____
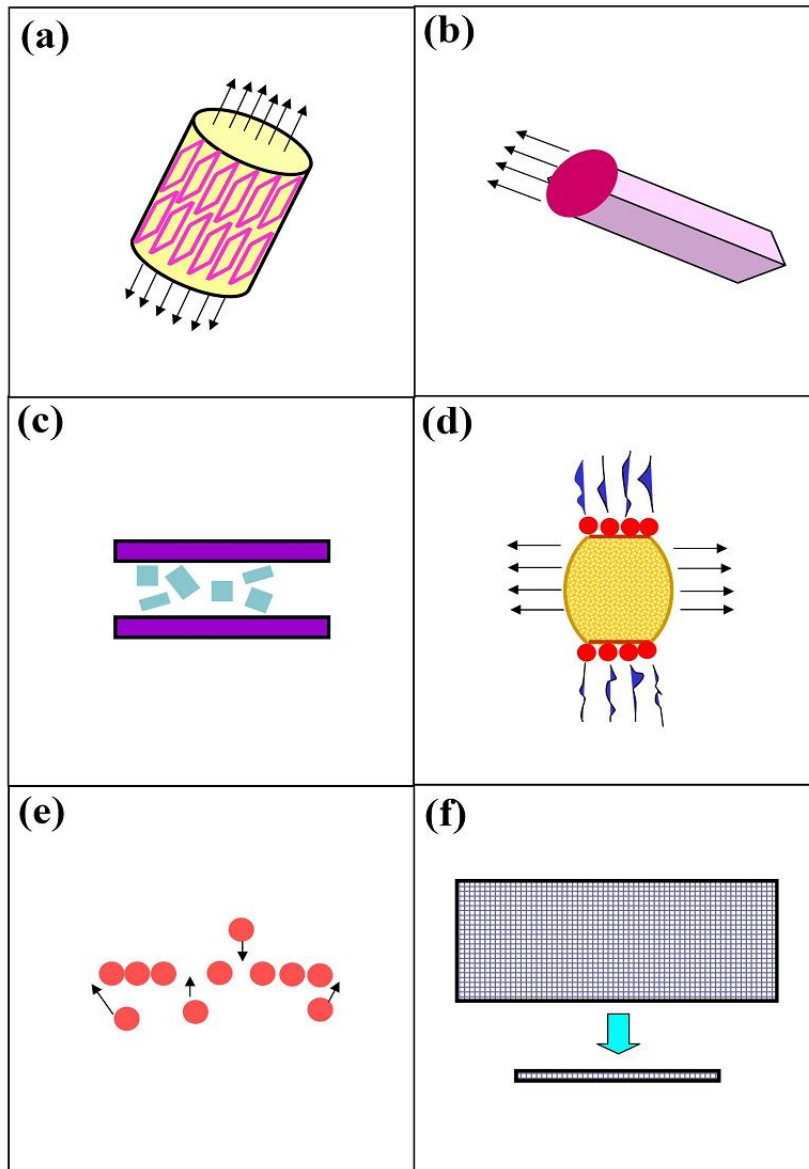


**Figure 1.7.** Schematic illustration of different strategies for achieving 1D growth (see text for details).

glass surface cooled below the melting point of mercury [61]. An important factor which determines the morphology of the product here is the level of supersaturation. A low supersaturation is required for whisker growth whereas a medium supersaturation leads to bulk growth. At high supersaturation, powders are formed by homogeneous nucleation in the vapor-phase. The two main mechanisms involved in

_____

the growth of nanowires in the vapor-phase are (i) vapor-solid and (ii) vapor-liquid-solid mechanism.

### *Vapor-liquid-solid growth*

The most extensively studied among the vapor-phase methods is the vapor-liquid-solid (VLS) method. This mechanism was proposed by Wagner in 1960s during his studies on the growth of single-crystalline whiskers of Si [62]. This process has since then been employed for the synthesis of nanowires of many materials such as Si [63], Ge [64], ZnO [65] and ZnS [66]. According to this mechanism, a liquid alloy acts as the nucleation site for the formation of the nanowires. First, the gaseous reactant undergoes dissolution into the nanosized liquid droplets of an impurity metal catalyst, and forms a liquid alloy at a temperature higher than the eutectic point. Since the liquid surface has a large accommodation coefficient, it becomes the preferred deposition site for the incoming vapors of the reactant material. After the liquid becomes supersaturated with vapor, the nanowire growth occurs by precipitation at the liquid-solid interface. The 1D growth is mainly induced and dictated by the liquid droplets, with the size of the droplets remaining constant through out the process. Thus, the diameter of the nanowires formed by the VLS method is determined by the size of the catalyst particles, which act as soft templates to limit the lateral growth of an individual nanowire [57]. The major steps involved in a VLS process are schematically illustrated in Figure 1.8. The selection of a proper impurity for the VLS growth is an important criterion. The equilibrium phase diagram helps in the prediction of the catalyst materials to be used, as well as the reaction conditions for the growth of the nanowires. This method helps in the synthesis of uniform-sized nanowires; and also patterned nanowires through the patterned deposition of catalyst
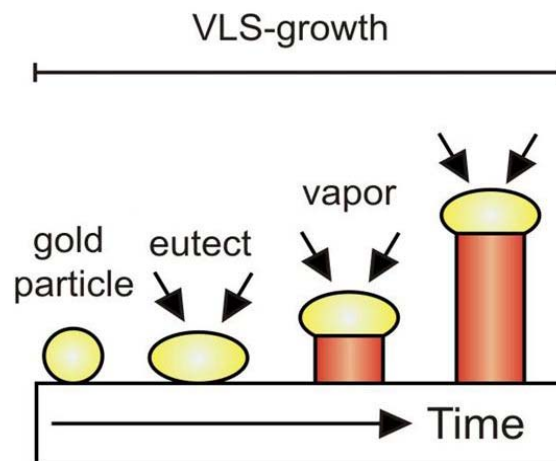
**Figure 1.8.** Schematic showing the growth of a nanowire via the VLS mechanism.

particles. Nanowires of GaP of different diameters have been grown by Lieber and co-workers by changing the size of the gold particles serving as the catalyst [67].

### *Vapor-solid growth*

Apart from the VLS mechanism, 1D nanostructures have also been grown via the classical vapor-solid (VS) mechanism [68]. In a typical VS process, vapor-species are first generated by physical evaporation, chemical reduction, and other kinds of gaseous reactions. These species are subsequently transported and condensed onto the surface of a solid substrate placed in a cooler zone. A large number of single-crystalline metal oxide nanowires have been grown via this mechanism. Due to the presence of trace amounts of oxygen in reaction systems, majority of the products reported are oxides. Thus, nanowires of oxides of Zn [69], Mg [70] and In [71] have been synthesized by this method. By properly controlling the supersaturation factor it has been possible to obtain large quantities of 1D nanostructures by this method. Thus, Zhu and co-workers have obtained nanowires of $Si_3N_4$, SiC, as well as of some oxides starting from the commercially available powders of these materials [73].

_____

*Carbothermal method*

Another very useful and versatile chemical method employed for the synthesis of nanowires is the carbothermal method [73]. Nanowires of a number of oxides such as $Ga_2O_3$, $Al_2O_3$, ZnO, $SiO_2$ and $In_2O_3$, nitrides such as $Si_3N_4$ and carbides such as SiC, as well as of elemental Si, have been prepared by this method [74]. In a typical carbothermal method a carbon source is heated with a metal oxide in a flowing gas. The carbon sources generally used are activated carbon or charcoal (which are easily oxidized on heating in air) and carbon nanotubes or graphite (which are more stable to oxidation on heating). First, carbon reduces the metal oxide to give a suboxide. The suboxide when heated in the presence of either $O_2$, $N_2$/$NH_3$ or C, gives rise to oxide, nitride or carbide nanowires respectively. In this method, the flow rate of the gas is an important factor, which determines the morphology of the final products.

$$\text{Metal oxide} + \text{C} \longrightarrow \text{Metal suboxide} + \text{CO}$$

$$\text{Metal suboxide} + \text{O}_2 \longrightarrow \text{Metal oxide nanowires}$$

$$\text{Metal suboxide} + \text{NH}_3 \longrightarrow \text{Metal nitride nanowires}$$

$$\text{Metal suboxide} + \text{N}_2 \longrightarrow \text{Metal nitride nanowires}$$

$$\text{Metal suboxide} + \text{C} \longrightarrow \text{Metal carbide nanowires}$$
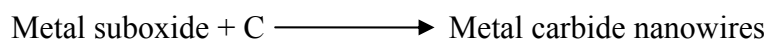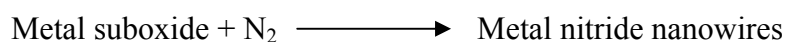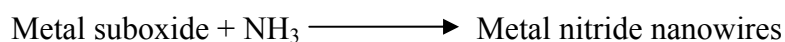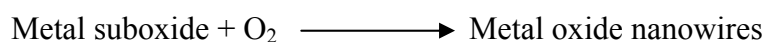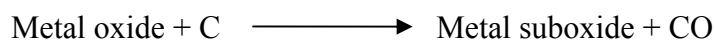
*Solution-based growth and other methods*

The majority of chemical methods adopted for the synthesis of inorganic nanowires are solution-based. This synthetic strategy involves mainly reactions that are confined and directed by templates or by the use of appropriate capping agents. One of the extensively used solution routes to 1D nanostructures is the solvothermal method which uses a solvent under pressures and temperatures above its critical point to increase the solubility of the solid precursor and to speed up the reaction leading to

_____

crystal growth and assembly process. In this method the precursor and a capping agent such as amine are taken in a suitable solvent (water or an organic solvent), and heated in an autoclave at high temperature. This method has been exploited for the synthesis of 1D nanostructures of a variety of materials including Ge [75], $\alpha$- and $\beta$-$MnO_2$ [76], CuS [77] and $Sb_2Se_3$ [78]. CdS nanowires of diameter 25 nm and length 20-40 microns have been synthesized using a solvent mixture of ethylene diamine and dodecanethiol [79]. The synthesis of a variety of nanostructures including nanowires of ZnO, by carrying out solvothermal reaction over a ZnO coated substrate, has been reported [80]. Another efficient solution-based method to grow nanowires is the oriented attachment, where nanoparticles undergo fusion along a given crystallographic direction. Thus via this mechanism 1D nanostructures of a variety of materials such as Au, CdTe, PbSe, ZnS, ZnO, and $SnO_2$ have been prepared [58].

In the template-based technique, the template serves as a scaffold against which other kinds of materials, with morphologies complimentary to that of the template, are generated. The channels are filled using a solution route, sol-gel technique or an electrochemical route to produce nanowires. After the reaction, the nanowires could be released from the templates by selectively removing the template from the host matrix. Nanowires of various inorganic materials such as $SnO_2$, ZnO, Ag, and Pt have been prepared using anodic alumina membranes (AAMs) [81]. Apart from AAMs and polymer membranes, mesoporous silica has also been used as templates for the synthesis of inorganic nanowires [82]. Mesophase structures self-assembled from surfactants provide another class of versatile templates for the synthesis of nanowires in large amounts. CNTs have been used as templates for the synthesis of inorganic nanowires. By coating CNTs with oxide gels and then burning off the carbon, single-crystalline nanorods of a variety of metal oxides including

_____

$V_2O_5$, $WO_3$, $MoO_3$ and $Sb_2O_5$ as well as metallic $MoO_2$, $RuO_2$ and $IrO_2$ have been prepared [83].

### 1.3.2   Properties of nanowires and their applications

Nanowires show very distinct electric, optical, and thermal properties due to their large surface area and possible quantum confinement, when compared with their bulk counterparts. The thermal stability of nanowires is of critical importance for their implementation as building blocks in nanoscale electronic and photonic devices. It is well documented that the melting point of a solid material will be greatly reduced when it is processed as nanostructures [84]. In their investigations on the melting and recrystallization of Ge nanowires encapsulated by carbon-sheaths, Yang and co-workers [85] observed the melting point to be inversely proportional to the diameter of the nanowire. The other distinct feature that they observed in the melting-recrystallization cycle was a large hysterisis loop. As a result of the drastic reduction in melting point associated with nanowires, it becomes easier to cut, interconnect and weld nanowires, thus enabling one to fabricate functional devices with them.

Mechanical properties of nanowires of a variety of inorganic materials have been investigated using atomic force microscope (AFM) and scanning tunneling microscope (STM). Studies carried out on Au nanowires using STM supplemented with a force sensor, have shown that the bond strength of the nanowire is about twice that of the bulk metal [86]. An AFM-based study reported by Boland and co-workers find that the Young's modulus of gold nanowires is independent of diameter, but the yield strength is largest for the nanowires with smallest diameter, up to 100 times that of bulk metal [87]. The elastic modulus of ZnO nanowires has been measured to be

_____

20-30 GPa [88]. A large increase in elastic and tensile strength has been observed on the incorporation of nanowires of $Al_2O_3$ and SiC in poly(vinyl alchohol) [89].

As a result of quantum confinement, nanowires of some metals have been reported to undergo transition from metal to semiconductor as their diameters are reduced below certain values. Two-probe measurements on arrays of single-crystalline Bi nanowires, made by Dresselhaus *et al.* [90] showed a metal-to-semiconductor transition at a diameter of ~ 50 nm. But four-probe measurements carried out on polycrystalline Bi nanowires by Heath and co-workers did not show any clear semimetal-insulator transition or enhancement in thermoelectric power [91]. Such a behavior has been accounted to the polycrystalline nature of the nanowires. Individual single-crystalline Si nanowires have been reported to exhibit Coulomb blockade oscillations, with coherent charge transport [92]. Gate-dependent 1D transport in single-crystal $In_2O_3$ nanowire transistor has been looked into at low temperatures [93].

Optical properties of nanowires are also influenced by quantum confinement phenomena due to the radial confinement of carriers if the diameter of the NW becomes comparable to the exciton Bohr radius of the semiconductor. Optical absorption and emission from the NWs has been found to be predominantly polarized along the long axis of the wires [94]. The observed polarization anisotropy is a purely classical phenomenon arising from the anisotropic geometry of the NWs – where the diameter of the wire is much smaller than the wavelength of light but the length is much larger – and also due to the large dielectric mismatch between the free standing NW and its surrounding environment. Absorption edge of Si nanowires was found to be considerably blue-shifted when compared with the indirect band gap of bulk Si (1.1 eV), by Korgel *et al.* [95]. They also observed sharp, discrete features in the

_____

absorption spectra and relatively strong band-edge photoluminescence, arising due to quantum-confinement effects with additional contributions from the surface states. Lieber and co-workers have shown anisotropy in PL (photoluminescence) intensities in single InP nanowires in directions parallel and perpendicular to the axis of the nanowire [96]. Yang and co-workers observed lasing from single ZnO nanowires at room temperature, under an excitation with a Nd:YAG laser (266 nm) [97]. Studies on ZnO nanowires as potential room-temperature ultraviolet lasers show that control of defect density and the optimal microstructure of the nanowires to produce strong optical confinement are necessary for the room temperature lasing activity [98]. Temperature-dependent and time-resolved photoluminescence measurements have been carried out to explore the lasing properties of single CdS nanowires [99]. The studies reveal that an exciton-exciton interaction is a dominant factor for lasing at low temperatures, while an exciton-phonon process dominates at high temperatures. Optically pumped room-temperature lasing has been reported in GaN nanowires [100].

Nanowires are ideal building blocks for nanoscale electronics and optoelectronics. Nanowires of semiconducting elements such as Si and Ge, as well as those of ZnO, InP, GaN, CdS and CdSe have been studied extensively, towards their applications in nanotechnology [58,59,101]. These nanowires have been assembled into nanometric scale devices including field-effect transistors (FETs), LEDs, p-n junction diodes, logic gates and sensors. By assembling *n-* and *p-*type Si nanowires, FETs have been fabricated [102]. Using aligned ZnO nanowires grown on a Si or a polymer substrate, the conversion of nanoscale mechanical energy into electrical energy has been demonstrated with AFM [103]. The first use of NW field-effect devices to detect analytes in solution was reported by Lieber and his group [104], with

_____

the sensing of hydrogen-ion concentration or pH. They illustrated the transformation

of boron-doped (*p*-type) Si NW FETs into nanosensors, by modifying the $SiO_2$

surface with 3-aminopropyltriethoxy silane (APTES) to provide a surface that can

undergo protonation and deprotonation, where changes in the surface charge

chemically gate the Si NW (Figure 1.9).
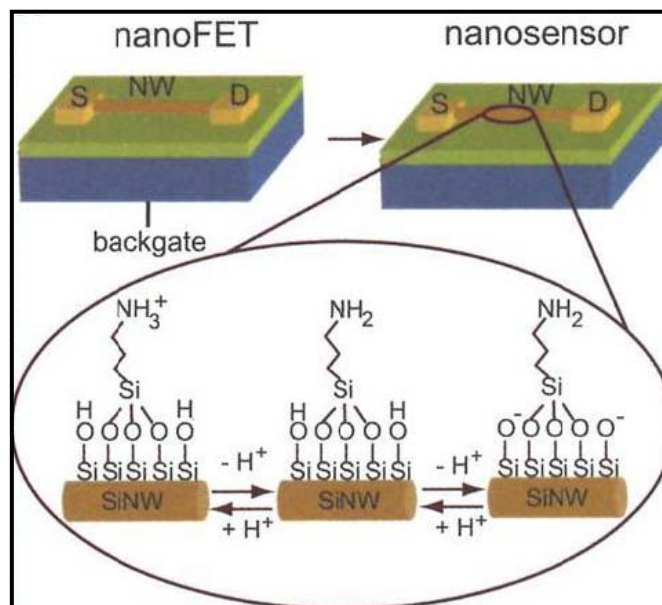


**Figure 1.9.** Schematic illustrating the conversion of a NW FET into NW nanosensors for pH sensing. Zoom of the APTES-modified Si NW surface illustrating changes in the surface charge state with pH is given.

## 1.4    Nanotubes

There has been great interest in the synthesis and characterization of one-dimensional nanotubes, since the discovery of the carbon nanotubes (CNTs) in 1991 by Iijima [5]. CNTs are either single- or multi-walled. Unlike the SWNTs which are single-layered, multi-walled carbon nanotubes (MWNTs), are made up of multiple layers of graphene sheets. A SWNT can be visualized by cutting $C_{60}$ structure across the middle and adding a cylinder of graphite of the same diameter. If $C_{60}$ is bisected normal to a five-fold axis, an armchair tube is formed, and if it is bisected normal to a

_____

three-fold axis, a zigzag tube is formed [60]. In addition to these two types of nanotubes which are non-chiral, a variety of chiral tubes can also be formed with the screw axis along the axis of the tube. In Figure 1.10a is given the models of the three types of CNTs. The structure of a SWNT is uniquely characterized by the chiral vector, $C_h = na_1 + ma_2$, where $a_1$ and $a_2$ are unit vectors in a 2D graphene lattice and n and m are integers. The vector $C_h$ connects two crystallographically equivalent sites on a 2D graphene sheet and the chiral angle ($\theta$) is the angle it makes with respect to the zigzag direction as can be seen from Figure 1.10b. A tube is formed by rolling up the graphene sheet in such a way that the two points connected by the chiral vector coincide. The translational vector, T, is directed along the axis of SWNT and perpendicular to $C_h$. The magnitude of T corresponds to the length of the (n,m) SWNT unit cell. Once these are specified, other structural properties such as the diameter and the chiral angle can be determined.

A number of strategies have been employed for the synthesis of CNTs [106]. Arc-evaporation of graphite or the pyrolysis of hydrocarbons such as acetylene or benzene over a metal catalyst, are the usually followed methods for the preparation of CNTs. Pyrolysis of organometallic precursors provides a one-step synthetic method for CNTs [107]. Electrochemical synthesis as well as growth of aligned CNT bundles inside the pores of alumina membranes has also been reported [108]. Small diameter SWNTs with controlled density and ordered locations have been obtained using polyferrocenylsilane block copolymer precursors [109]. SWNTs as well as double-walled CNTs have been obtained over Fe-Co alloy nanoparticles by the reduction of $Mg_{0.90}Fe_xCo_yO$ ($x + y = 0.1$) solid solutions in $H_2$-$CH_4$ [110]. Aligned MWNT bundles have been prepared by nebulized spray pyrolysis using solutions of organometallics such as ferrocene in hydrocarbon solvents [111].

_____
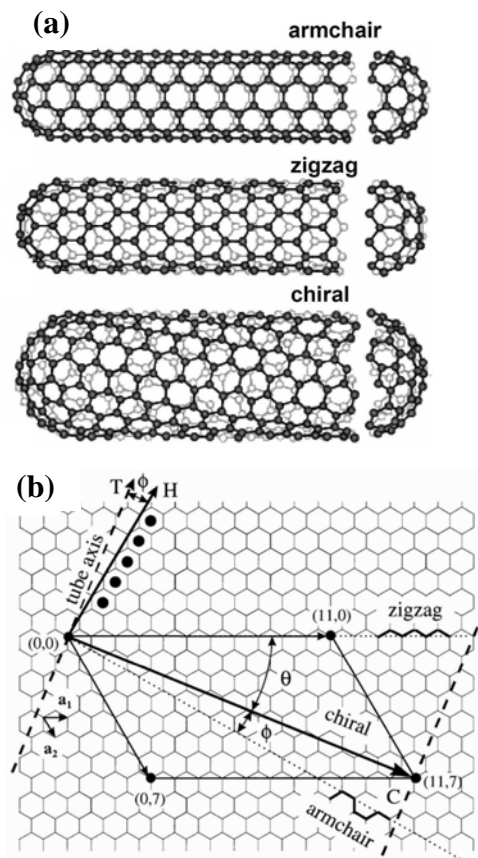


**Figure 1.10.** (a) Models of three types of SWNTs and (b) a 2D grapheme sheet showing the chiral vector, chiral angle and the translational vector.

Carbon nanotubes have been used as cathodes and their electron emission properties have been studied [112]. High performance n-type carbon nanotube FETs with chemically doped contacts have been fabricated [113]. Individual SWNTs have been reported to form ideal p-n junction diodes, which under illumination show significant power conversion efficiencies [114]. Novel electrical switching behavior and logic in Y-junctions CNTs has been investigated [115]. The mutual interaction of the electron currents in the three branches of the Y-junctions is shown to be the basis for a new logic device, which works without an external gate. Hydrogen storage capacities of CNTs have been explored [116]. Gundiah *et al.* have measured $H_2$ adsorption systematically on well-characterized samples of SWNTs, MWNTs, aligned

_____

MWNTs as well as carbon fibers [117]. They could achieve a maximum storage capacity of 3.7 wt%. MWNT mats constituting nanotubes oriented randomly within the plane of the film have been shown to exhibit actuation [118]. An individual CNT partially filled with liquid Ga has been found to act as a thermometer as well as an electrical switch [119].

Nanotubes of several solids having structure comparable to graphite, such as BN, and some transition metal oxides and dichalcogenides have been well reported [58,120]. Thus, $MoS_2$ and $WS_2$ nanotubes have been synthesized by Tenne and co-workers [121], starting with the metal oxides as well as by the decomposition of the metal trisulfides. BN nanotubes have been synthesized by CVD, oven heating of ball-milled B powders and plasma-jet method [122]. Nanotubes of solids lacking layered structure, such as silica, alumina, metals, and silicon have also been synthesized. Single-crystalline nanotubes of GaN [123], Si [124] and $Fe_3O_4$ [125] have been prepared by epitaxial-casting against single-crystalline nanowires. Gundiah *et al.* have prepared nanotubes of $SiO_2$, $TiO_2$, $ZrO_2$, ZnO and $WO_3$ and of $ZnSO_4$ and $BaSO_4$ by a hydrogel route [126]. Archer and co-workers have reported the synthesis of electrochemically active needle-like $Co_3O_4$ nanotubes by a self-supported topotactic approach [127].

## 1.5    Concluding remarks

Thus, as seen in the above discussions, nanoworld has been witnessing explosive growth in the last few years by the concerted efforts of scientists, the world over. With the availability of new synthetic techniques as well as new tools for the characterization and manipulation of nanomaterials, the potential applications envisaged for them are soon turning into a reality. But the scaling up process of most of the powerful nanomaterials, for their commercialization, is still a distant dream. In

_____

the coming years, it is hoped that new methods would emerge for the facile scaling up

of nanomaterials, so that they are easily available for use in our day to day life.

_____

31

## 1.6   References

[1] C. N. R. Rao, A. Müller, A. K. Cheetham, in The Chemistry of Nanomaterials (C. N. R. Rao, A. Müller, and A. K. Cheetham, eds.), Wiley-VCH, Weinheim, 2004, **1**, 1.

[2] G. M. Whitesides, *Small* 2005, **1**, 172.

[3] R. P. Feynman, *Eng. Sci.* 1960, **23**, 22.

[4] G. Binning, H. Rohrer, Ch. Gerber, E. Weibel, *Phys. Rev. Lett.* 1983, **50**, 120.

[5] Encyclopedia of Nanoscience and Nanotechnology, Ed. H. S. Nalwa, ASPBS, 2004.

[6] E. Roduner, *Chem. Soc. Rev.* 2006, **35**, 583.

[7] M. Faraday*, Philos. Trans. R. Soc. London.* 1857, **147**, 145.

[8] a) "Semiconductor and metal nanocrystals", Ed. V. L. Klimov, Marcel Dekker, Inc. New York, 2004. b) C. Burda, X. Chen, R. Narayanan, M A. El-Sayed, *Chem. Rev.* 2005, **105**, 1025. c) S. Eustis, M A. El-Sayed, *Chem. Soc. Rev.* 2006, **35**, 209.

[9] a) C. N. R. Rao, G. U. Kulkarni, P. J. Thomas, P. P. Edawrds, *Chem. Eur. J.* 2002, **8**, 29. b) G. U. Kulkarni, P. J. Thomas, C. N. R. Rao in The Chemistry of Nanomaterials (C. N. R. Rao, A. Müller, and A. K. Cheetham, eds.), Wiley-VCH, Weinheim, 2004, **1**, 51. c) P. J. Thomas, P. O'Brien in The Nanomaterials Chemistry (C. N. R. Rao, A. Müller, and A. K. Cheetham, eds.), Wiley-VCH, Weinheim, 2007, 1.

[10] C. N. R. Rao, S. R. C. Vivekchand, K. Biswas, A. Govindaraj, *Dalton Trans.* 2007, 3728.

[11] M-C. Daniel, D. Astruc, *Chem. Rev.* 2004, **104**, 293.

[12] D. G. Duff, A. Baiker, P. P. Edwards, *Langmuir*, 1993, **9**, 2301.

[13] M. Brust, M. Walker, D. Bethell, D. J. Schiffrin, R. Whyman, *J. Chem. Soc., Chem. Commun.*, 1994, 801.

[14] N. R. Jana, X. Peng, *J. Am. Chem. Soc.*, 2003, **125**, 14280.

[15] G. S. Metraux, C. A. Mirkin, *Adv. Mater.* 2005, **17**, 412.

[16] H. Song, F. Kim, S. Connor, G. A. Samorjai, P. Yang, *J. Phys. Chem. B*, 2005, **109**, 188.

[17] C.B. Murray, D.J. Norris, M.G. Bawendi, *J. Am. Chem. Soc.* 1993, 115, 8706.

[18] a) U. K. Gautam, M. Rajamathi, F. Meldrum, P. Morgan, R. Seshadri, *Chem. Commun.*, 2001, 629. b) U. K. Gautam, R. Seshadri, C. N. R. Rao, *Chem. Phys. Lett.*, 2003, **375**, 560.

[19] K. Biswas, C. N. R. Rao, *Chem. Eur. J.*, 2007, **13**, 6123.

[20] J. Joo, H. B. Na, T. Yu, J. H. Yu, Y. W. Kim, F. Wu, J. Z. Zhang, T. Hyeon, *J. Am. Chem. Soc.*, 2003, **125**, 11100.

[21] Y. Yin, C. K. Erdonmez, A. Cabot, S. Hughes, A. P. Alivisatos, *Adv. Funct. Mater.* 2006, **16**, 1389.

[22] C. N. R. Rao, G. U. Kulkarni, V. V. Agrawal, U. K. Gautam, M. Ghosh, U. Tumkurkar, *J. Colloid Inerface Sci.* 2005, **289**, 305.

[23] K. S. Mayya, V. Patil, M. Sastry, *Langmuir* 1997**, 13**, 2575.

[24] G. Schmid, M. Baumle, N. Beyer, *Angew. Chem. Int. Ed.* 2000, **39**, 181.

[25] M. Platt, R. A. W. Dryfe, E. P. L. Roberts, *Electrochim. Acta* 2004, **49**, 3937.

[26] B. O. Dabbousi, C. B. Murray, M. F. Rubner, M. G. Bawendi, *Chem. Mater.* 1994, **6**, 216.

[27] R. Zhu, G. Min, Y. Wei, H. J. Schmitt, *J. Phys. Chem.* 1992, **96**, 8210.

[28] a) K. B. Eisenthal, *Acc. Chem. Res.* 1993**, 26,** 636**.** b) I. Benjamin, *Chem. Rev.* 1996, **96**, 1449.

[29] G. Luo, S. Malkova, J.Yoon, D. G. Schultz, B. Lin, M. Meron, I. Benjamin, P. Vanysek, M. L. Schlossman, *Science* 2006, **311**, 216.

[30] W. H. Binder, *Angew. Chem. Int. Ed.* 2005, **44**, 2.

[31] a) B. P. Binks,; J. H. Clint, *Langmuir* 2002, **18**, 1270. b) T. S. Horozov, D. A. Braz, P. D. I. Fletcher, B.P. Binks, J. H. Clint, *Langmuir* 2008, **24**, 1678.

[32] Y. Lin, H. Skaff, T. Emrick, A. D. Dinsmore, T. P. Russel, *Science* 2003**, 299,** 226.

[33] J. Benkoski, R. L. Jones, J. F. Doughlas, A. Karim, *Langmuir* 2007, **23**, 3530.

[34] H. Schwartz, Y. Harel, S. Efrima, *Langmuir* 2001, **17**, 3884.

[35] L. L. Dai, R. Sharma, C. Wu, *Langmuir* 2007, **21**, 2641.

[36] S. D. Sathaye, K. R. Patil, D. V Paranjape, A. Mitra, S. V. Awate, A. B. Mandale, *Langmuir* 2000, **16***, 3487.

[37] D. Pan, S. Jiang, L. An, B. Jiang, *Adv. Mater.* 2004, **16**, 982.

[38] F. Kleitz, F. Marlow, G. D. Stucky, F. Schuth, *Chem. Mater.* 2001, **13**, 3587.

[39] G. Thomas, in The Nanomaterials Chemistry (C. N. R. Rao, A. Müller, and A. K. Cheetham, eds.), Wiley-VCH, Weinheim, 2007, 185.

[40] G. Mie, *Ann. Phys.* 1908, **25**, 329.

[41] S. Devarajan, S. Sampath, in The Chemistry of Nanomaterials (C. N. R. Rao, A. Müller, and A. K. Cheetham, eds.), Wiley-VCH, Weinheim, 2004, **2**, 646.

[42] J-E. Park, O. Hatozaki, N. Oyama, *Chem. Lett.* 2003, **32**, 138.

[43] S. N. Pronk'Kin, O.A. Petrii, G. A. Tsirlina *et al.*, *J. Electroanal. Chem.* 2000, **480**, 112.

[44] Y. Lou, M. M. Maye, L. Han Li Han, Jin Luo, C-J. Zhong, *Chem. Commun.* 2001, 473.

[45] H. Li, Q. Wang, L. Shi et. al. *Chem. Mater.* 2002, **14**, 103.

_____

[46] J. Ouyang, C-W. Chu, D. Sieves, Y. Yanga, *Appl. Phys. Lett.* 2005, **86**, 123507.

[47] D. I. Gittins, D. Bethell, D. J. Schiffrin, R. J. Nichols, *Nature* 2000, **408**, 67.

[48] C. J. Loweth, W. B. Caldwell, X. Peng, A. P. Alivisatos, P. G. Schultz, *Angew. Chem. Int. Ed.* 1999, **38**, 1808.

[49] A. J. Haes, R. P. V Duyne, *J. Am. Chem. Soc.* 2002, **124**, 10596.

[50] J. Lee, A. O. Govorov, N. A. Kotov, *Angew. Chem. Int. Ed.* 2005, **44**, 7439.

[51] A. P. Alivisatos, *Science* 1996, **271**, 933.

[52] W. U. Huynh, J. J. Dittmer, A. P. Alivisatos, *Science* 2002, **295**, 2425.

[53] K. S. Narayan, A. G. Manoj, J. Nanda, D. D. Sarma, *Appl. Phys. Lett.* 1999, **74,** 871.

[54] M. C. Schlamp, X. Peng,  A. P. Alivisatos, *J. Appl. Phys.* 1997, **82**, 5837.

[55] D. Qi, M. Fischbein, M. Drndic, S. Selmic: *Appl. Phys. Lett.* 2005, **86,** 93103.

[56] D. L. Klein, R. Roth, A. K. L. Lim, A. P. Alivisatos, P. L. Mc Euen *Nature* **389**, 699.

[57] Y. Xia, P. Yang, Y. Sun, Y. Wu, B. Mayers, B. Gates, Y. Yin, F. Kim, H. Yan *Adv. Mater.* 2003, **15**, 353.

[58] C. N. R. Rao, S. R. C. Vivekchand, A. Govindaraj, in The Nanomaterials Chemistry (C. N. R. Rao, A. Müller, and A. K. Cheetham, eds.), Wiley-VCH, Weinheim, 2007, 45.

[59] C. M. Lieber, Z. L. Wang, *MRS Bull.* 2007, **32**, 99.

[60] A. Govindaraj, C. N. R. Rao, in The Chemistry of Nanomaterials (C. N. R. Rao, A. Müller, and A. K. Cheetham, eds.), Wiley-VCH, Weinheim, 2004, **1**, 208.

[61] M. Volmer, I. Estermann, *Z. Phys.* 1921, **7**, 13.

[62] R. S. Wagner, W. C. Ellis, *Appl. Phys. Lett.* 1964, **4**, 89.

[63] D. C. Lee, T. Hanrath, B. A. Korgel, *Angew. Chem., Int. Ed.* 2005, **44**, 3573.

_____

[64] Y. Wu, P. Yang, *J. Am. Chem. Soc.* 2001, **123**, 3165.

[65] M. H. Huang, Y. Wu, H. Feick, N. Tran, E. Weber, P. Yang, *Adv. Mater.* 2001, **13**, 113.

[66] Y. Wang, L. Zhang, C. Liang, G. Wang, X. Peng, *Chem. Phys. Lett.* 2002, **57**, 314.

[67] M. S. Gudiksen, C. M. Lieber, *J. Am. Chem. Soc.* 2000, **122**, 8801.

[68] R. S. Wagner, in Whisker Technology, ed. A. P. Levitt, Wiley-Interscience, New York 1940, 47.

[69] S.-Te Ho, K.-C. Chen, H.-A. Chen, H.-Y. Lin, C.-Y. Cheng, H.-N. Lin, *Chem. Mater.* 2007**, 19**, 4083.

[70] Y. Yin, G. Zhang, Y. Xia, *Adv. Funct. Mater.* 2002, **12**, 293.

[71] X. S. Peng, G. W. Meng, J. Zhang, X. F. Wang, Y. W. Wang, C. Z. Wang, L. D. Zhang, *J. Mater. Chem.* 2002, **12**, 602.

[72] Y. Zhang, N. Wang, S. Gao, R. He, S. Miao, J. Liu, J. Zhu, X. Zhang, *Chem. Mater.* 2002, **14**, 3564.

[73] C. N. R. Rao, G. Gundiah, F. L. Deepak, A. Govindaraj, A. K. Cheetham, *J. Mater. Chem.* 2004, **14**, 440.

[74] a) G. Gundiah, A. Govindaraj, C. N. R. Rao, *Chem. Phys. Lett*., 2002, **351**, 189. b) G. Gundiah, F. L. Deepak , A. Govindaraj, C. N. R. Rao, *Topics Cat.*, 2003, **23**, 137. c) F. L. Deepak, G. Gundiah, M. M. Seikh, A. Govindaraj, C. N. R. Rao, *J. Mater. Res.* 2004, **19**, 2216. d) K C. Kam, F. L. Deepak, A. K. Cheetham, C. N. R. Rao, *Chem. Phys. Lett.* 2004, **397**, 329.

[75] J. R. Heath, F. K. L. Goues**,** *Chem. Phys. Lett. 1993*, **208**, 263.

[76] X. Wang, Y. Li, *J. Am. Chem. Soc.* **2002,** *124*, *2880.

[77] Q. Lu, F. Gao, D. Zhao, *Nano Lett.* 2002, **2**, 725.

[78] H-W. Chang, B. Sarkar, C. W. Liu, *Cryst. Growth Des.* 2007, **7**, 2691.

[79] Dan Xu, Z. Liu, J. Liang, Y. Qian**,** *J. Phys. Chem. B* 2005**, 109***,* 14344.

[80] B. Wen, Y. Huang, J. J. Boland, *J. Phys. Chem. C* 2008, **112**, 106.

[81] Huczko, *Appl. Phys. A* 2000, **70**, 365.

**[**82**]** K.-B. Lee, S.-M. Lee, J. Cheon, *Adv. Mater.* 2001, 13, 517.

[83] B. C. Satishkumar, A. Govindaraj, M. Nath, C. N. R. Rao, *J. Mater. Chem.* 2000, **10**, 2115.

[84] P. Buffat, J.-P. Borel, *Phys. Rev.* 1976, **13**, 2287.

[85] Y. Wu, P. Yang, *Adv. Mater.* 2001, **13**, 520.

[86] G. R. Bollinger, S. R. Bahn, N. Agraït, K. W. Jacobsen, S. Vieira, *Phys. Rev. Lett.* 2001, **87**, 26101.

[87] B. Wu, A. Heidelberg, J. J. Boland, *Nature Mater.* 2005, **4**, 525.

[88] J. Song, X. Wang, E. Riedo, Z. L. Wang, *Nano Lett.* 2005, **5**, 1954.

[89] S. R. C. Vivekchand, U. Ramamurty, C. N. R. Rao, *Nanotech.* 2006, **17**, S344.

[90] Z. Zhang, X. Sun, M. S. Dresselhaus, *Phys. Rev. B* 2001, **61**, 4850.

[91] A. Boukai, K. Xu, J. R. Heath, *Adv. Mater.* 2006, **18**, 864.

[92] S. R. C. Vivekchand, K. C. Kam, G. Gundiah, A. Govindaraj, A. K. Cheetham C. N. R. Rao,  J. Mater. Chem., 2005, **15**, 4922.

[93] F. Liu, M. Bao, K. L. Wang, C. Li, B. Lei, C. Zhou, *Appl. Phys. Lett.* 2005, 86, 213101.

[94] R. Agarwal, C. M. Lieber**,** *Appl. Phys. A* 2006, **85**, 209.

[95] X. Lu, T. Hanrath, K. P. Johnston, B. A. Korgel, *Nano Lett.* 2003, **3**, 93.

[96] J. F. Wang, M. S. Gudiksen, X. F. Duan, Y. Cui, C. M. Lieber, *Science* 2001, **293**, 1455.

[97] J. C. Johnson, H. Yan, R. D. Schaller, L. H. Haber, R. J. Saykally, P. Yang, *J. Phys. Chem. B*, 2001, **105**, 11387.

[98] S. Hirano, N. Takeuchi, S. Shimada, K. Masuya, K. Ibe, H. Tsunakawa, M. Kuwabara, *J. Appl. Phys.* 2005, **98**, 94305.

[99] S. Gradečak, F. Qian, Y. Li, H.-G. Park, C. M. Lieber, *Appl. Phys. Lett.* 2005, **87**, 173111.

[100] R. Agarwal, C. J. Barrelet, C. M. Lieber, *Nano Lett.* 2005, **5**, 917.

[101] Y. Huang, X. Duan, C. M. Lieber, *Small* 2005, **1**, 142.

[102] G. Zheng, W. Lu, S. Jin, C. M. Lieber, *Adv. Mater.* 2004, 16, 1890.

[103] Z. L. Wang, J. Song, *Science* 2006, **312**, 242.

[104] Y. Cui, Q. Wei, H. Park, C. M. Lieber, *Science* 2001, **293**, 1289.

[105] S. Iijima, *Nature* 1991, **354**, 56.

[106] C. N. R. Rao, B. C. Satishkumar, A. Govindaraj, M. Nath, *Chem. Phys. Chem.* 2001, **2**, 78.

[107] C. N. R. Rao, A. Govindaraj, *Acc. Chem. Res.* 2002, **35**, 998.

[108] G. Che, B. B. Lakshmi, C. R. Martin, E. R. Fisher, R. S. Ruoff, *Chem. Mater.* 1998, **10**, 260.

[109] J. Q. Lu, T. E. Kopley, N. Moll *et al.*, *Chem. Mater.* 2005, **17**, 2227.

[110] P. Coquay, A. Peigney, E. D. Grave, E. Flahaut, R. E. Vandenberghe, C. Laurent, *J. Phys. Chem. B* 2005, **109**, 17813.

[111] S. R. C. Vivekchand, L. M. Cele, F. L. Deepak, A. R. Raju, A. Govindaraj, *Chem. Phys. Lett.* 2004, **386,** 313-318.

[112] K. B. K. Teo, E. Minoux *et al.*, *Nature* 2005, **437**, 968.

[113] A. Javey, R. Tu, D. B. Farmer, J. Guo, R. G. Gordon, H. Dai, *Nano Lett.* 2005, **5**, 345.

_____

[114] J. U. Lee, *Appl. Phys. Lett.* 2005, **87**, 73101.

[115] P. R. Bandaru, C. Daraio, S. Jin, A. M. Rao, *Nat. Mater.* 2005, **4**, 663.

[116] A. C. Dillon, K. M. Jones, T. A. Bekkedahl, C. H. Kiang, D. S. Bethune, M. J. Heben, *Nature* 1997, **386**, 377.

[117] G. Gundiah, A. Govindaraj, N. Rajalakshmi, K. S. Dhathathreyan, C. N. R. Rao, *J. Mater. Chem.*, 2003, **13**, 209.

[118] M. Hughes, G. M. Spinks, *Adv. Mater.* 2005, **17**, 443.

[119] P. S. Dorozhkin, S. V. Tovstonog, D. Golberg, J. Zhan, Y. Ishikawa, M. Shiozawa, H. Nakanishi, K. Nakata, Y. Bando, *Small* 2005, **1**, 1088.

[120] C. N. R. Rao, M. Nath, *Dalton Trans.* 2003,1.

[121] a) L. Marguilis, G. Salitra, R. Tenne, *Nature*, 1993, **365**, 113. b) Y. Feldman, E. Wasserman, D. J. Srolovitch, R. Tenne, *Science*, 1995, **267**, 222.

[122] D. Golberg, Y. Bando,C. Tang, C. Zhi, *Adv. Mater.* 2007, **19**, 2413.

[123] J. Goldberger, R. He, Y. Zhang, S. Lee, H. Yan, H.-J. Choi, P. Yang, *Nature*, 2003, **422**, 599.

[124] J. Hu, Y. Bando, Z. Liu, J. Zhan, D. Golberg, T. Sekiguchi, *Angew. Chem. Ed.* 2003, **43**, 63.

[125] Z. Liu, D. Zhang, S. Han, C. Li, B. Lei, W. Lu, J. Fang, C. Zhou, *J. Am. Chem. Soc.* 2005, **127**, 6.

[126] G. Gundiah, S. Mukhopadhyay, U. G. Tumkurkar, A. Govindaraj, U. Maitra, C. N. R. Rao, *J. Mater. Chem.*, 2003, **13,** 2118.

[127] X. W. Lou, D. Deng, J. Y. Lee, J. Feng, L. A. Archer, *Adv. Mater.* 2008, **20**, 258.

# CHAPTER 2

# Carbon-assisted Synthesis of Metal Oxide Nanowires

**SUMMARY**[*]

This chapter deals with the synthesis of nanowires of some metal oxides by carbothermal method. MgO nanowires and related nanostructures have been prepared by carbon-assisted synthesis, starting from polycrystalline MgO or Mg without the use of metal catalysts. The study has been carried out with different sources of carbon, all of them yielding the nanostructures with some differences. It has been possible to obtain nanotrees and other interesting nanostructures by this method. A vapor-solid (VS) mechanism of one-dimensional growth seems to be operative in the reactions carried out.

GeO$_2$ nanowires have been prepared by heating a mixture of Ge powder and carbon in an Ar + O$_2$ mixture at 900 $^o$C. The nanowires have been characterized by X-ray diffraction, scanning electron microscopy, transmission electron microscopy and spectroscopic measurements. The nanowires are single-crystalline with diameters in the 15-250 nm range. They exhibit characteristic blue luminescence. In the case of GeO$_2$ also VS mechanism seems to be involved in the formation of nanowires.

Sn-doped In$_2$O$_3$ (ITO) nanowires have been prepared by carbon-assisted synthesis starting with a powdered mixture of the metal nitrates or with a citric acid

gel formed by the metal nitrates. Copious quantities of nanowires could be grown on gold-sputtered Si substrates. The ITO nanowires were single-crystalline and optically transparent. $In_2O_3$ nanowires doped with both Sn and Zn have also been prepared by the procedures described. In the case of undoped- and doped- ITO, nanowires form by the vapor-liquid-solid (VLS) mechanism.

_____

## 2.1    Introduction

Synthesis of nanowires of metals, metal oxides, nitrides, carbides etc by various routes including chemical vapor deposition, physical evaporation and laser ablation, has been reported in literature [1,2]. The mechanism of formation of many of these nanostructures involves a VS or VLS growth process. Compared to the methods mentioned above, a very simple and versatile method that is being exploited is the carbon-assisted method [3]. Thus, crystalline nanowires of metal oxides such as $Ga_2O_3$, $Al_2O_3$, ZnO, $SiO_2$ and $In_2O_3$ [4-7], nitrides such as $Si_3N_4$ and carbides such as SiC [8], as well as of elemental Si, have been prepared under carbothermal conditions. In this method carbon is made to react with a metal oxide in a flowing gas. Here carbon acts as a catalyst, reducing the metal oxide to the respective suboxide, which after further reaction, gives rise to the desired nanowires. For example, reaction in an atmosphere of ammonia gives rise to nitrides, or an inert atmosphere and a slight excess of carbon results in carbides. We have been able to prepare single-crystalline nanowires of MgO, $GeO_2$ and ITO via this method by employing different sources of carbon. It has also been possible to obtain interesting nanostructures, other than nanowires. By employing the carbothermal method we could avoid metal catalyst impurities, which is the main advantage of this method.

## 2.2    Scope of the present study

### 2.2.1    Nanowires and related nanostructures of MgO

MgO is a wide band gap insulator, showing high secondary electron emission yield [9]. One-dimensional nanostructures of MgO have attracted some attention because of their unique ability to pin the magnetic flux lines within a high temperature superconductor [10,11]. The MgO nanorods in this case were obtained starting with a

mixture of MgO powder and graphite; but their investigation was not focused on the growth of these nanorods under different experimental conditions, nor using different sources of carbon. Due to their appreciable strength, high melting point and low density, MgO whiskers find suitable applications in spaceflight and other composite materials [12,13]. Several methods of synthesis of MgO nanostructures have been reported in literature. Thus, Zhu *et al.* [14] have prepared MgO fishbone fractal nanostructures by selective Co-catalyzed growth. Starting with a halide source, MgO nanorods [15] and nanobelts have been prepared [16]. Li *et al.* [17] have reported the preparation of network-like MgO nanostructures on a Si substrate by the CVD process using IR radiation to heat a Mg/Al target under vacuum. MgO nanowires have been prepared by the direct heating of Mg in oxygen [18] as well as by oxide-assisted growth using $B_2O_3$ powder [19]. Yin *et al.* [20] have achieved this through a vapor-phase precursor method, starting with $MgB_2$ powder. Nanobelts of MgO have been prepared by thermal evaporation of Mg powder [21] as well as by starting with $Mg_3N_2$ [22]. The synthesis of two- and three-dimensional MgO nanostructures as well as networked rectangular MgO nanostructures has been reported [23,24]. Multidimensional MgO nanostructures with cone shaped branching have been reported recently [25]. The synthesis of MgO and Ga-filled MgO nanotubes has also been reported, where carbon was used to reduce $Ga_2O_3$ to obtain metallic Ga which then catalyzed the formation of MgO nanotubes [26,27]. In the above synthetic procedures, carbon has not been effectively looked into, specially in the absence of additional catalysts like B/Si powder [28], nor has carbon been employed as a reactant as in carbon-assisted syntheses of metal oxide nanowires [29]. We have, therefore, investigated the carbon-assisted synthesis of MgO nanowires and related nanostructures, by varying the source of carbon and other reaction conditions. We

_____

have employed polycrystalline MgO as well as Mg as the starting material, and not used any catalyst other than carbon in the synthesis.

### 2.2.2   Nanowires of GeO$_2$

We have been interested in the nanowires of germanium oxide since they find useful applications in optical fiber technology and other areas. Even though GeO$_2$ is similar to SiO$_2$, GeO$_2$-based glass is thought to have a refractive index greater than the corresponding silicate glass. GeO$_2$ also has a higher linear coefficient of thermal expansion than SiO$_2$ and finds applications in vacuum technology [30]. There have been a few reports on the synthesis of GeO$_2$ nanowires and nanorods. Thus, Bai *et al.* [31] prepared GeO$_2$ nanowires by a physical evaporation process starting with Ge powder mixed with 8 wt% Fe. Laser ablation of Ge targets in an Ar atmosphere at 820 $^{\circ}$C also yielded GeO$_2$ whiskers [32]. A confined reaction in carbon nanotubes was employed by Zang *et al.* [33] to prepare GeO$_2$ nanowires with diameters in the range 50-200 nm. A carbothermal reduction process, wherein a mixture of GeO$_2$ and activated carbon heated at 840 $^{\circ}$C was used to obtain nanowires with diameters in the range 50-120 nm [34]. Gu *et al.* [35] employed the VLS process to prepare GeO$_2$ nanowires by depositing Ge vapor onto gold nanoparticles, the diameter of the nanowires depending on the size of the Au particles. GeO$_2$ nanowires with diameters between 60 and 400 nm were obtained by Hu *et al.* [36] by heating a mixture of Ge and Fe(NO$_3$)$_3$ at high temperatures. In all the reports so far, none of the workers has established the single-crystalline nature of the nanowires by high-resolution electron microscopy (HREM). Furthermore, some of the methods employed to prepare the nanowires are cumbersome. We report the synthesis of germanium oxide nanowires

by a simple carbon-assisted reaction involving the use of Ge powder along with a carbon source.

### 2.2.3  Doped and undoped ITO nanowires

Though the synthesis and characterization of one-dimensional nanostructures of several binary metal oxides such as ZnO, $In_2O_3$, $SnO_2$, MgO and $GeO_2$ have been studied extensively [1,2], there are only very few investigations on the nanostructures of doped metal oxides. We have been interested in synthesizing nanowires of the well-known transparent conducting oxide, indium tin oxide (ITO), which finds applications in optoelectronic devices, flat-panel displays, organic light emitting diodes and solar cells [37–40]. There have been a few reports on the 1D nanostructures of ITO in the literature. Thus, Yu *et al.* [41] prepared ITO nanowires by employing a co-precipitation-anneal process at 500 $^{o}$C using ether as the solvent, starting with a mixture of In and Sn chlorides. ITO nanowhiskers were obtained by Wan *et al.* [42] by heating a mixture of In metal and SnO at 900 $^{o}$C in a flow of $N_2$ and $O_2$. ITO nanofibers have been prepared by heating a mixture of In and Sn metals in an Ar + $O_2$ mixture in the 900-1100 $^{o}$C range for different durations [43]. Nanowires of $SnO_2$ doped with In have been reported by the carbothermal reaction of a mixture of In and Sn oxides with graphite at 840 $^{o}$C [44]. In view of the importance of ITO nanowires, it seemed desirable to have a simple and reliable method for the synthesis. We have, therefore, carried out the carbon-assisted synthesis of ITO nanowires, since the method has been very effective for the preparation of various types of inorganic nanowires [29]. We have also extended the synthetic protocol to obtain nanowires of $In_2O_3$ doped with both Sn and Zn. This is in the context of the efforts to develop new and improved transparent conducting oxides. Poeppelmeier

_____

and co-workers [45] have indeed demonstrated that by doping Zn and Sn into $In_2O_3$, the conducting properties of ITO are retained while the cost is significantly reduced.

## 2.3    Experimental and related aspects

### 2.3.1  Synthesis

*Nanowires and related nanostructures of MgO*

The experimental setup used for the synthesis of the metal oxide nanowires is shown in Figure 2.1. It consists of stainless steel gas flow lines and a programmable furnace fitted with a quartz or alumina tube. In the reactions where an alumina tube was used, the reactants were placed in an alumina boat. When a quartz tube was used, the reactants were placed in a quartz boat or a quartz tube with diameter lesser than the outer tube. The flow rates of the gases used were controlled using mass flow controllers. Four different procedures were employed for the synthesis of MgO nanostructures. In procedure 1(a), activated carbon, prepared by the thermal decomposition of polyethylene glycol (600 units) at 800 $^{o}C$ in an Ar atmosphere, for 5 h [29], was mixed with MgO powder in a molar ratio (carbon: MgO) of 1:1 and ground well to get a fine powder. This mixture was placed in an alumina boat and heated in an alumina tube at 1300 $^{o}C$ (3 $^{o}C$/ min) for 5 h in an Ar atmosphere of 50 standard cubic centimeter per minute (sccm). A white spongy product, obtained at the end of the reaction was collected for further study. The above reaction was carried out in a quartz boat, starting with Mg powder at 850 $^{o}C$, procedure 1(b). In procedure 2(a) charcoal (Sarabhai Chemicals, India), which was activated by heating in a mixture of $H_2$ and He at 600 $^{o}C$ for 5h [29], was mixed with MgO powder in the molar ratio 1:1. The rest of the procedure was the same as in 1(a). In procedure 2(b), Mg powder was used instead of MgO. Graphite powder was used as yet another source of carbon in

procedure 3. The reaction conditions were the same as in procedures 1 and 2. In procedure 3(a), graphite was mixed with MgO powder in the molar ratio 1:0.6 and placed in an alumina boat. In procedure 3(b), Mg powder was taken instead of MgO, ground with graphite powder in the ratio 1:1 and the reaction carried out in a quartz boat. In procedure 4(a) the reaction was carried out with multi-walled carbon nanotubes (MWNTs) as the carbon source, mixing them with MgO powder in the molar ratio (MWNTs: MgO) 1:0.6. In procedure 4(b) Mg powder was taken with MWNTs in a quartz boat. The MWNTs that were used in the reaction were prepared by the arc discharge method [41]. The reaction conditions are described in table 2.1. The products obtained in all the above reactions were white in colour, which were characterized by various experimental techniques. These techniques have been described at the end of this section.
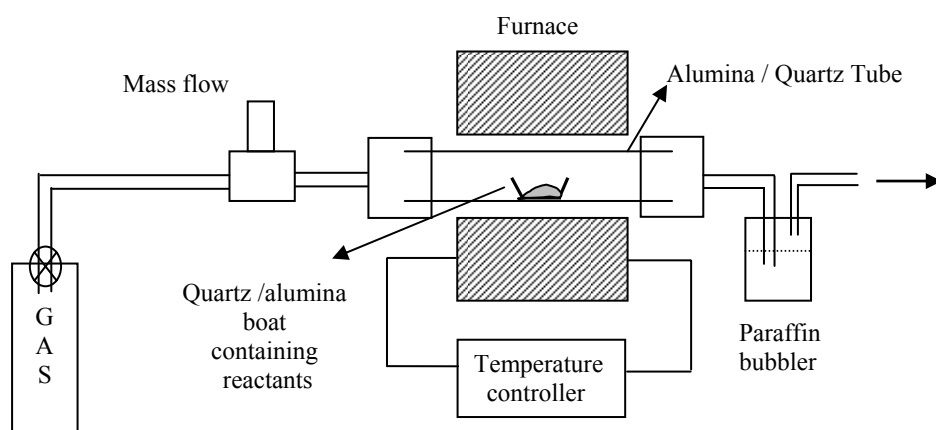


**Figure 2.1.** Experimental set up for the synthesis of nanowires by the carbon-assisted route

### *Nanowires of GeO$_2$*

GeO$_2$ nanowires were prepared using two sources of carbon: (i) commercial charcoal (Sarabhai Chemicals, India), activated by heating in a mixture of H$_2$ and He at 700 $^{\circ}$C and (ii) activated carbon. The reaction using activated charcoal is

_____

designated as procedure (i) and the one with activated carbon as procedure (ii). In procedure (i), Ge powder was mixed with the activated charcoal in a molar ratio 1:0.15 and the mixture ground to a fine powder. The powder was taken in a quartz tube of 0.8 cm diameter and 8 cm length, one end of which was sealed. This quartz tube was placed at the center of a larger quartz tube (outer diameter 1.5 cm) and heated in the horizontal tubular furnace at 900 $^{\circ}$C for 5 h in a mixture of Ar and $O_2$ flowing at 50 sccm and 75 sccm respectively. A gray/white product was collected in the inner tube. In procedure (ii), activated carbon prepared by us was employed for the reaction instead of activated charcoal. In this case too, Ge powder was mixed with activated carbon (molar ratio 1:0.15) and ground to a fine powder; and the reaction carried out in the same manner as in procedure (i). The products from both the reactions were characterized by various techniques.

### *Doped and undoped ITO nanowires*

ITO nanowires were prepared by employing two different procedures, starting with a mixture of $In_2O_3$ powder and Sn metal. In procedure 1, $In_2O_3$ powder (Aldrich, USA) and Sn metal (Qualigens, India) were taken in the molar ratio of 40:1 and dissolved in conc. $HNO_3$. The mixture of nitrates obtained from the solution was mixed with graphite powder (microcrystal grade, Alfa Aesar, USA) in a molar ratio of 1:0.5, ground to a fine powder, and placed in an alumina boat. Silicon substrates, cleaned with nitric acid and annealed at 350 $^{\circ}$C, were patterned with gold by a dc sputtering process. The Au-patterned substrates were placed over the nitrate mixture in the alumina boat. The boat was then placed at the center of an alumina tube and the temperature slowly raised to 900 $^{\circ}$C at a rate of 3 $^{\circ}$C/min in a flow of 100 sccm of Ar gas, and the reaction allowed to proceed at 900 $^{\circ}$C for 3 h. After the furnace had

cooled, the patterned regions on the substrate were found to be covered with a whitish product, which was characterized (Figure 2.2). In procedure 2, to the nitrate solution containing In and Sn ions (taken in a molar ratio of 10:1), an aqueous solution of citric acid (0.35 g in 10 mL $H_2O$) was added under stirring. The solution was neutralized by the addition of ethylenediamine. The resultant solution formed a white gel on slight warming. The gel was dried by raising the temperature to 180 $^\circ$C in steps while holding at 60 $^\circ$C, 80 $^\circ$C, 120 $^\circ$C and 160 $^\circ$C for 4 h each. The gel was kept at 180 $^\circ$C for 2 days to obtain a black product. The dried gel was ground into a powder, placed in an alumina boat and the reaction carried out over Au-patterned Si substrates as in procedure 1. The whitish product obtained was characterized.

In both procedures 1 and 2, we could add zinc acetate to the acidic solution, thereby enabling the synthesis of Zn-doped ITO. The molar percentages of Zn:Sn:In being 5:5:90.
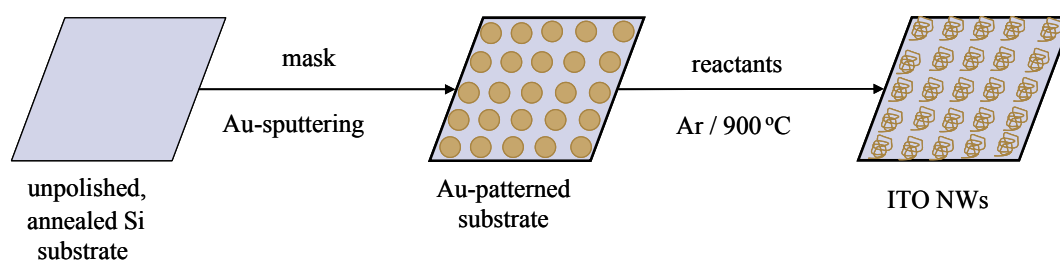


**Figure 2.2.** Schematic of the reaction for synthesizing ITO nanowires using Si substrate.

### 2.3.2    Techniques used for characterization

***X-ray diffraction:*** X-ray diffraction (XRD) patterns were recorded using Cu K$\alpha$ radiation on a Rich-Siefert, XRD-3000-TT diffractometer.

_____

***Scanning electron microscopy:*** Scanning electron microscope (SEM) images were obtained on a LEICA S440i SEM. Energy dispersive analysis of X-rays (EDAX) was performed with a Oxford microanalysis group 5526 system attached to the SEM employing Links (ISIS) software and a Si (Li) detector. For SEM and EDAX analysis the samples were spread onto a conducting carbon tape pasted on an aluminium stub, followed by sputter-coating with gold.

***Transmission electron microscopy:*** Transmission electron microscope (TEM) images were obtained with a JEOL JEM 3010, operating with an accelerating voltage of 300 kV. The samples were prepared by dispersing the product in $CCl_4$. A drop of the suspension was then put on a holey carbon coated Cu grid and allowed to evaporate slowly.

***UV-Vis absorption spectroscopy and Photoluminescence:*** UV-Vis absorption measurements were carried out at room temperature with a Perkin-Elmer model Lambda 900 UV/Vis/NIR spectrometer. Photoluminescence (PL) measurements were carried out at room temperature with a Perkin-Elmer model LS50B luminescence spectrometer. The excitation wavelengths used depended on the samples studied. The samples were prepared by ultrasonicating the product in $CCl_4$ to form a dispersion.

***Infrared spectroscopy:*** Infrared (IR) spectra were recorded with a Bruker FT-IR spectrometer. The samples were prepared by grinding with KBr and pressing into a disk.

***X-ray photoelectron spectroscopy:*** X-ray photoelectron spectroscopy (XPS) measurements were carried out using a VG scientific ESCALAB V spectrometer. The apparatus was operated at a vacuum of $10^{-8}$ Torr and the specimen was irradiated using a MgKα X-ray energy of 1254 eV.

_____

## 2.4 Results and discussion

### 2.4.1 Nanowires and related nanostructures of MgO

The various procedures mentioned in the experimental section, all gave MgO nanostructures as verified by the XRD patterns. The patterns were characteristic of the cubic structure of MgO (a = 4.211 Å; JCPDS card: No. 45-0946). A typical XRD pattern [product obtained by procedure 4(b)] is given in Figure 2.3. It must be noted that when MgO or Mg powder alone was heated in an alumina boat at 1300 $^{\circ}$C or 850 $^{\circ}$C for 5 h in an Ar atmosphere, we failed to obtain nanostructures of MgO.
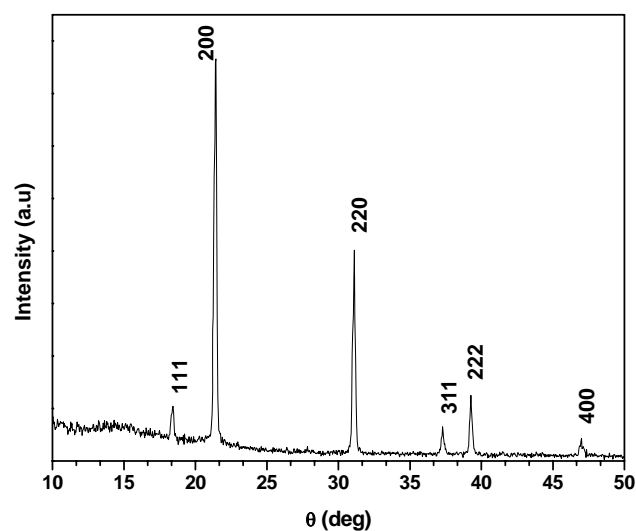


**Figure 2.3.** XRD pattern of the MgO nanostructures obtained by the reaction of MWNTs with Mg powder [procedure 4(b)].

The product obtained from the reaction of activated carbon with MgO powder by procedure 1(a) contained different types of nanostructures. The SEM image in Figure 2.4a reveals the high yield of the product obtained. The diameter of the nanostructures varies from 20-200 nm, with lengths going up to several tens of microns. The sample contained various nanostructures, including nanosheets and

_____

nanobelts, as revealed by the Figure 2.4b. The nanosheets have a width of about 8 μm

and length in the range of tens of micrometres. The nanobelts on the other hand are of

widths ranging from 50-200 nm and lengths going to several micrometres. The high-

magnification TEM image in Figure 2.4c shows an interesting feature with jagged-

edges. The inset in Figure 2.4c shows the selected area electron diffraction (SAED)

pattern of this jagged-edged nanostructure, revealing its single-crystalline nature. The

reflections correspond to the (2 2 2) and (4 2 0) planes of cubic MgO. In Figure 2.4d
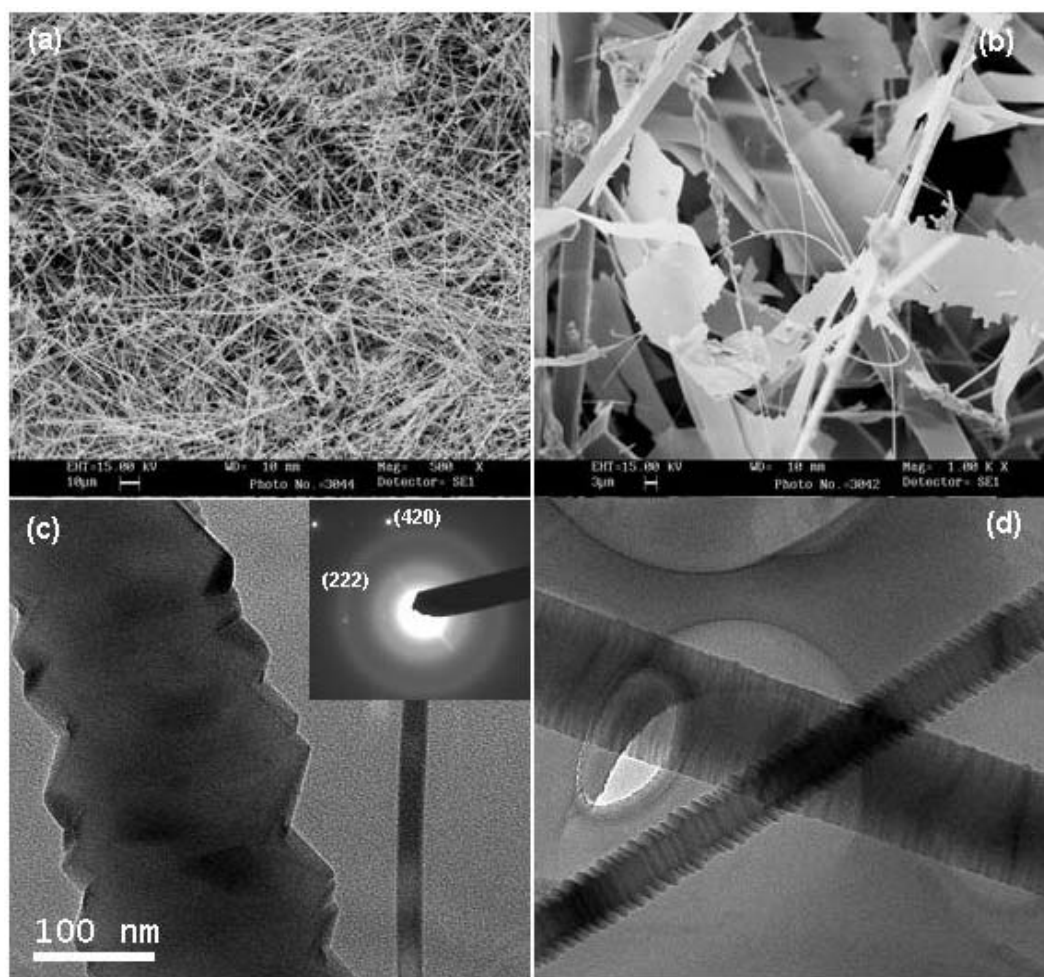


**Figure 2.4.** (a) and (b) SEM images of MgO nanostructures obtained by the reaction of activated carbon with MgO powder; (c) and (d) TEM images of jagged-edged nanostructures obtained by the reaction of activated carbon with MgO powder. Inset in (c) is the SAED pattern of the nanostructure.

is given a low-magnification TEM image of saw-like nanostructures. The jagged-edged or the saw-like structure is an interesting observation in the case of MgO and has not been reported in the literature previously.

When the reaction was carried out using commercial activated charcoal, by procedure 2(a), we obtained a good yield of different nanostructures comprising nanowires and nanobelts with high aspect ratios. The SEM image in Figure 2.5a shows the morphology of the different nanostructures formed. The transmission electron micrograph in Figure 2.5b shows the nanostructures, comprising nanobelts along with different shapes and edge structures. The diameter of the nanostructures varies from 20 to 50 nm, with length extending to several tens of micrometers.
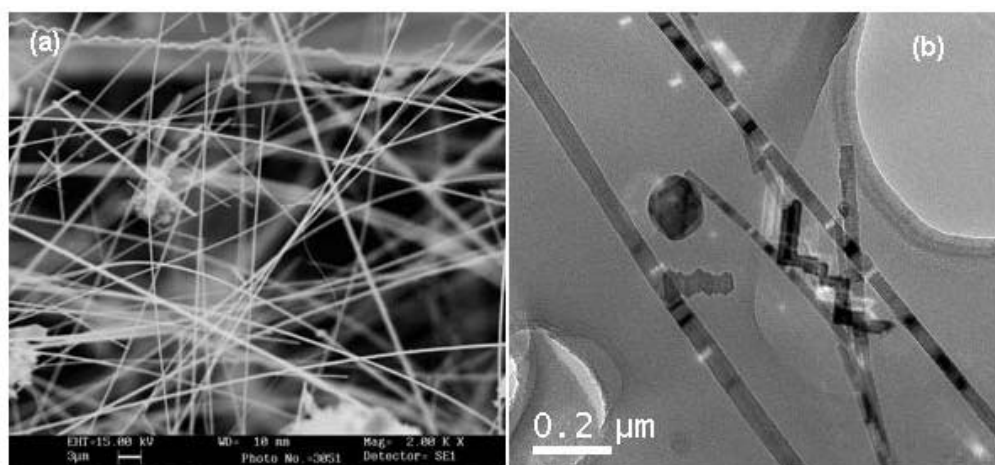


**Figure 2.5.** (a) SEM and (b) TEM images of MgO nanostructures prepared by procedure 2(a), reacting activated charcoal with MgO powder.

The reaction of MgO powder with graphite, by procedure 3(a) also yielded a mixture of different nanostructures including belts, wires etc, as can be seen in the SEM image in Figure 2.6. The diameter of the nanowires varies in the range 50-200 nm and their length extends to several tens of microns.

_____
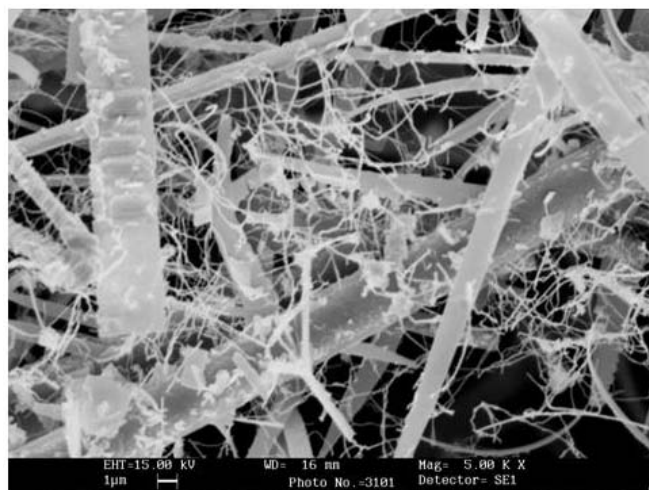


**Figure 2.6.** (a) SEM image of the MgO nanostructures prepared by procedure 3(a), reacting graphite with MgO powder.
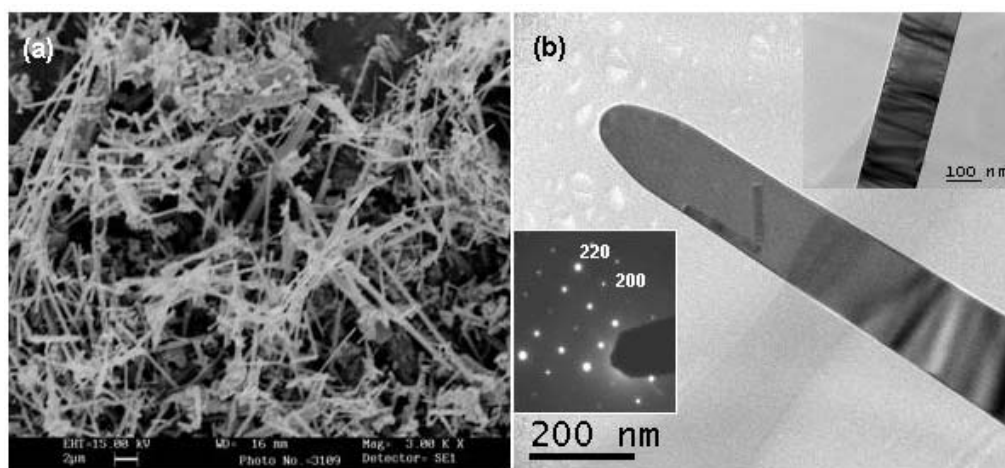


**Figure 2.7.** (a) SEM image of the MgO nanostructures prepared by procedure 4(a), reacting MWNTs with MgO powder; (b) TEM image of a finger-shaped nanowire obtained by procedure 4(a). The SAED pattern of the nanowire and the TEM image of another nanowire are shown as the insets.

The use of MWNTs as the carbon source, by procedure 4(a), gave the best yield of uniform nanowires (see the SEM image in Figure 2.7a). The diameter of the nanowires varies from 50-150 nm and their length extends to tens of microns. In Figure 2.7b is shown a finger-shaped nanowire with decreasing diameter towards the apex. The inset in Figure 2.7b is the SAED pattern of the nanowire taken from its

_____

apex. The reflections correspond to the (2 0 0) and (2 2 0) planes of cubic MgO. The TEM image of yet another nanowire is shown as an inset in Figure 2.7b.

The high-resolution transmission electron microscopy (HREM) image of a nanowire, prepared by procedure 4(a), given in Figure 2.8 shows a lattice spacing of 0.21 nm corresponding to the spacing between the (2 0 0) planes of cubic MgO. The growth direction of the nanowire (shown by an arrow in Figure 2.8) is perpendicular to the (2 0 0) planes and is along the <1 0 0> axis. The SAED pattern and HREM image confirm the single-crystalline nature of the nanowires. By employing MWNTs, we could obtain nanowires of uniform distribution.

The reaction of Mg powder with activated carbon by procedure 1(b) gave nanowire-networks in good yield. The SEM image in Figure 2.9a reveals the overall morphology of the 1D nanostructures. The image shows single nanowires as well as those that form complex junctions along with star shaped nanostructures [25].
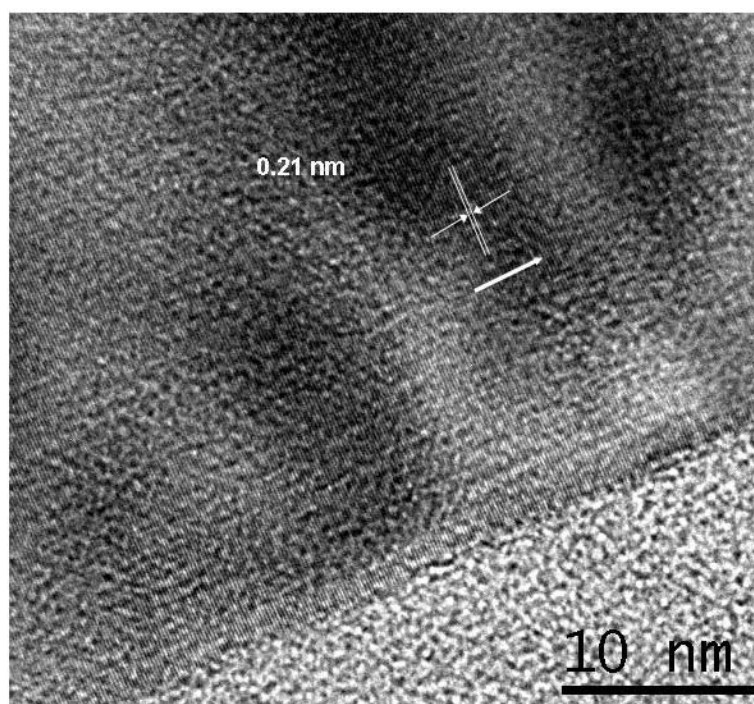


**Figure 2.8.** HREM image of a MgO nanowire obtained by the reaction of MWNTs with MgO.

_____

In Figure 2.9b is given the TEM image of one such nanostructure having a T-junction. SAED pattern of the nanostructure showing reflections from the (200) and (400) lattice planes of cubic MgO is given as an inset in Figure 2.9b. TEM images
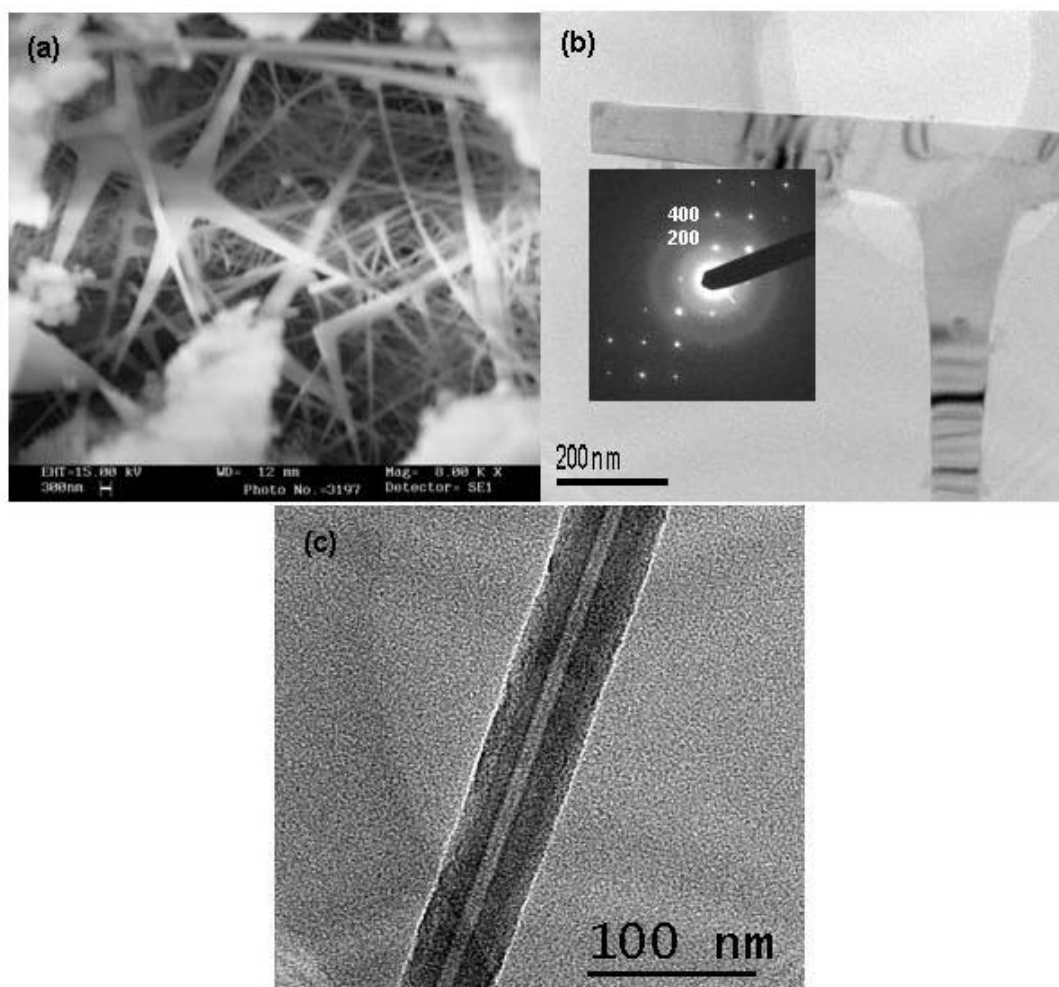


**Figure 2.9.** (a) SEM image of the MgO nanostructures including star-shaped ones prepared by procedure 1(b), employing activated carbon and Mg powder. TEM images of: (b) a nanostructure with a T-junction and (c) a MgO nanotube prepared by procedure 1(b). Inset in (b) is the SAED pattern of the nanostructure.

revealed the formation of MgO nanotubes also, as can be seen from Figure 2.9c. The diameter of the nanotube is ~ 50 nm and the length extends up to a micron.

The reaction of Mg powder with activated charcoal by procedure 2(b) also gave nanostructures with complex networks, as revealed by the SEM image in Figure 2.10a. The TEM image in Figure 2.10b shows nanostructures with T-junction. The slight shrinkage in cross-section along the direction of branch length may be due to the gradual decrease in the vapor supply during its growth. The diameter of the nanostructures varies from 100 nm to 300 nm and their length extends to tens of micrometers. A nanowire with a peculiar dot-pattern can also be seen in Figure 2.10b. The presence of dot-patterns in this case is significant and can be understood similar to that of the dot-patterned $GeO_2$ nanowires reported by Hu *et al.* [36]. According to them, Ge atoms in the Ge phase zone, formed from a disproportionation reaction, are responsible for the formation of dot-patterned $GeO_2$ nanowires.
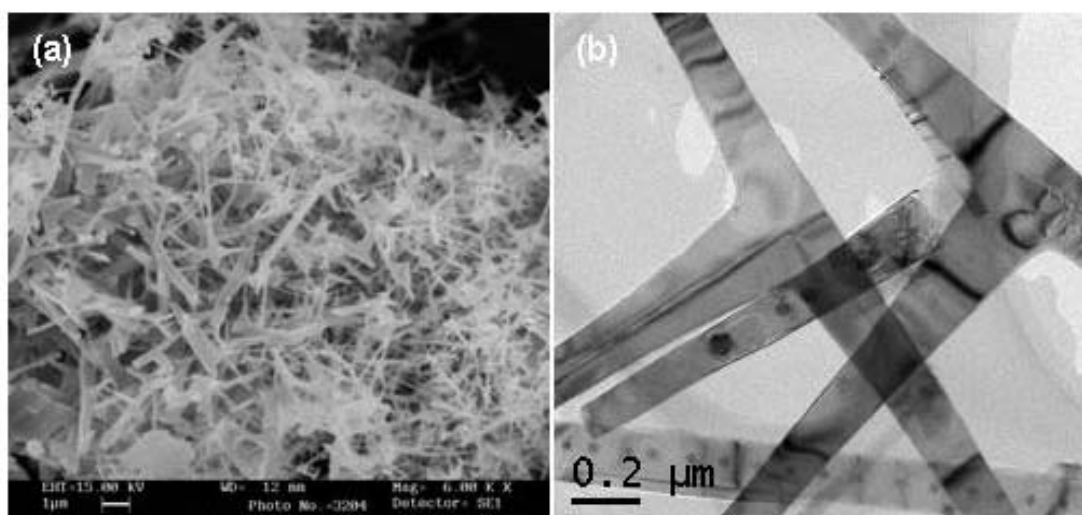


**Figure 2.10.** (a) SEM and (b) TEM images of the MgO nanostructures including star-shaped nanowires produced by procedure 2(b), employing activated charcoal and Mg powder.

_____

The reaction of Mg with graphite powder, by procedure 3(b) yielded interesting nanostructures of MgO. The SEM images in Figures 2.11a and 2.11b show the very high yields of the product obtained. In Figure 2.11c we show one such nanostructure, a nanotree-like morphology with nanotube branches. The diameter of these nanotubes is about 100 nm and their length extends to a few microns. Such nanotrees are reminiscent of those obtained with $In_2O_3$ by Kam *et al.* [7], although the mechanism of formation of these structures is likely to be different. Procedure 3(b) also gave nanostructures with complex networks and dot-patterns, as revealed by the TEM image in Figure 2.11d.
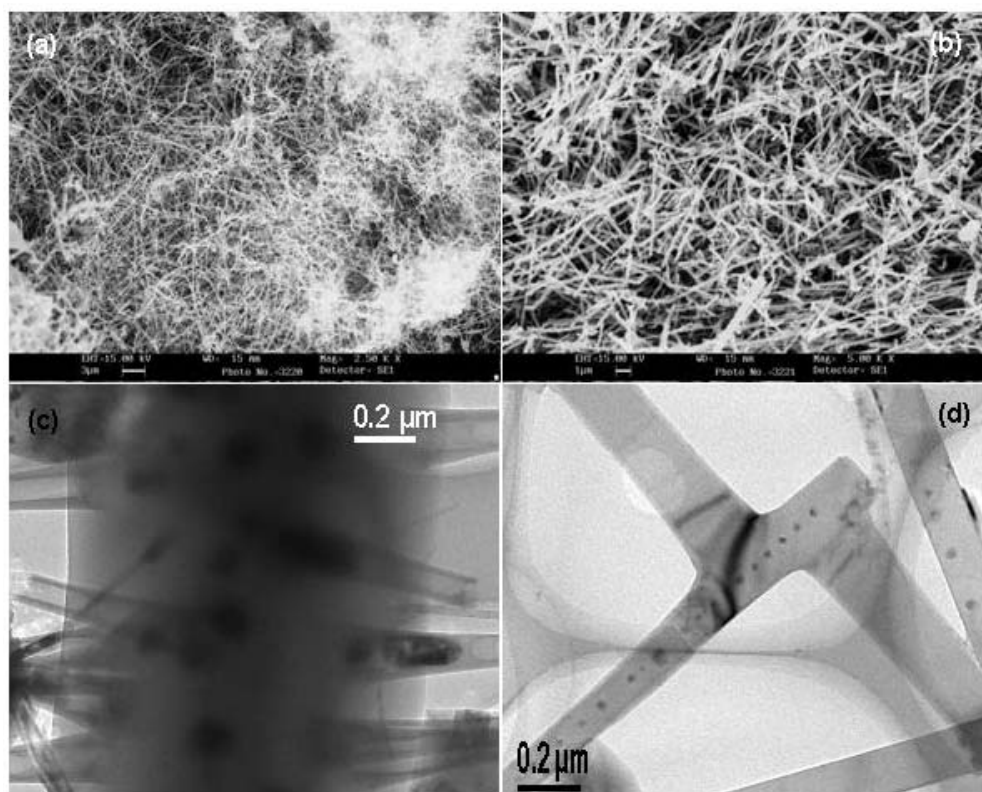


**Figure 2.11.** (a) and (b) SEM images showing high yields of the MgO nanostructures prepared by procedure 3(b), employing graphite and Mg powder. TEM images: (c) a MgO nanotree with protruding nanotube fingers and (d) MgO nanostructures with complex networks and dot-patterns obtained by procedure 3(b).

_____
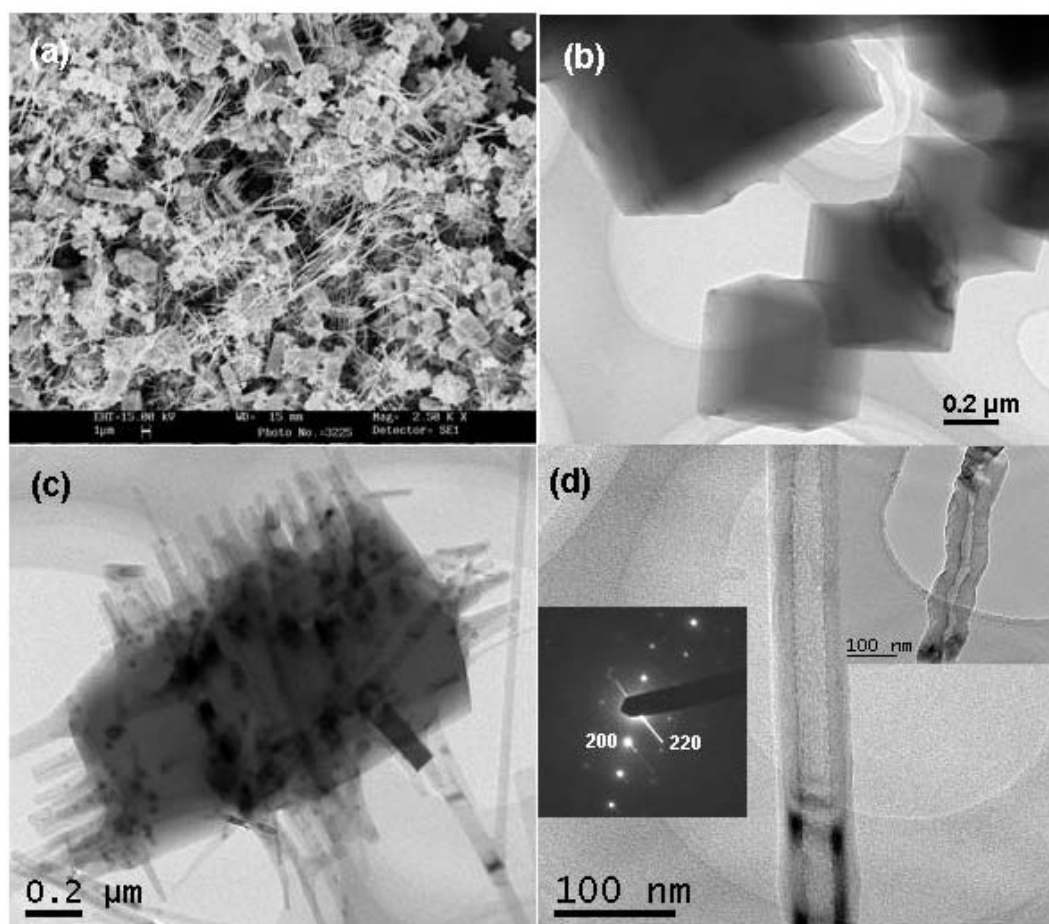


**Figure 2.12.** (a) SEM image showing high yields of MgO cubes with nanorod-fingers, prepared by procedure 4(b), employing MWNTs and Mg powder. TEM images: (b) MgO cubes merged at their vertices; (c) a cube with nanorods originating from it and (d) a well-formed, straight nanotube obtained by procedure 4(b). Insets show the SAED pattern of the nanotube and the TEM image of a helical-shaped nanotube obtained by procedure 3(b).

When the reaction was carried out with MWNTs by procedure 4(b), mainly structures such as nanocubes with nanorod-fingers originating from them were obtained (see SEM image in Figure 2.12a). Nanocubes merged at their corners can be seen in Figure 2.12b. In Figure 2.12c is shown the TEM image of a structure with nanorods originating from it. Such nanocubes with nanorods originating from them have been observed for the first time in the case of MgO. In Figure 2.12d we show the TEM image of a single nanotube, obtained by this preparation. The diameter of the

_____

nanotube is ~ 60 nm and its length goes up to a micron. The SAED pattern of the

nanotube (inset in Figure 2.21d) confirms its single-crystalline nature. The top inset in

Figure 2.12d shows a helical shaped nanotube obtained from the reaction of Mg

powder and graphite by procedure 3(b). The difference in the shape of the nanotube

obtained by changing the carbon source can be clearly seen here.

The MgO 1D nanostructures showed characteristic photoluminescence

properties. The PL spectrum of the product obtained by procedure 4(a) is given in

Figure 2.13. With an excitation wavelength of 315 nm, we obtained a peak at around

440 nm. Rosenblatt and co-workers [47] have obtained a similar band by time-

resolved spectra of bulk MgO with different defect densities. They have attributed

these bands to $F^+$ and F centers. Zhang and Zhang [21] have reported an intensive

green light emission from MgO nanobelts. The 440 nm emission peak in our case may

also be attributed to the existence of oxygen vacancies or surface states of the 1D

MgO nanostructures.
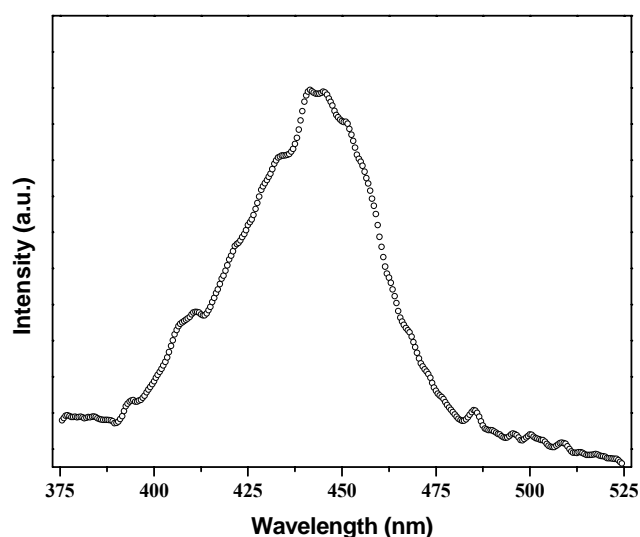


**Figure 2.13.** Room temperature PL spectrum of the MgO nanostructures obtained by procedure 4(a), employing MWNTs and MgO powder.

_____

The growth of the different 1D nanostructures of MgO can be explained in terms of vapor-solid mechanism [29]. In the absence of a clear knowledge of the occurrence of a suboxide of Mg, we suggest the following mechanism:

$$MgO + C \rightarrow \ Mg + CO \qquad\qquad (a)$$

$$2Mg + O_2 \ \rightarrow \ 2MgO \qquad\qquad (b)$$

MgO first gets reduced to the metal by the reaction with carbon as shown by the equation (a). This would be the case even if a suboxide were to be formed as an intermediate. The metal particles then combine with the oxygen present in the reaction system [5, 6] to give MgO particles as in equation (b). The oxide particles get transported by the Ar gas and are deposited in the boat. The MgO nanostructures are finally formed from the nuclei of MgO particles. The morphology of these nanostructures is determined by the level of supersaturation of the MgO vapor, resulting in the formation of MgO nanowires, nanotubes as well as the other complex networks. A schematic of the VS mechanism involved in the formation of nanowires is given in Figure 2.21. The nanowires and nanotubes may require a lower supersaturation than the complex networks or the cubes, the complex structures being favored by the presence of defects. After a nanowire grows to a certain length, the defects present in it may switch the growth direction, resulting in the formation of branches perpendicular to it.

Thus, we have synthesized nanowires and various other nanostructures of MgO (Table 2.1) in good yields via the carbon-assisted route, starting with Mg or MgO powder as the sources of Mg. The variety of nanostructures obtained includes nanosheets, nanobelts and nanotrees. The jagged-edged or saw-like 1D nanostructures

_____

have not been reported in the literature before. The nanocubes with nanorod outgrowths have also been observed for the first time. The reaction conditions and the products have been summarized in table 2.1.

| Procedure | Source | Nanostructures |
|-----------|--------|----------------|
| 1(a) | Activated carbon: MgO (1:1) | Sheets, belts, wires, jagged-edge structures. |
| 1(b) | Activated carbon: Mg (1:1) | Star shaped wires, complex networks, tubes. |
| 2(a) | Activated charcoal: MgO (1:1) | Wires, belts, zigzag shaped structures. |
| 2(b) | Activated charcoal: Mg (1:1) | Wires, T-junctions, complex networks. |
| 3(a) | Graphite: MgO (1:0.6) | Wires, belts. |
| 3(b) | Graphite: Mg (1:1) | Tree-like structures, tubes. |
| 4(a) | MWNTs: MgO (1:0.6) | Wires. |
| 4(b) | MWNTs: Mg (1:1) | Tubes, cubes with finger outgrowths. |

**Table 2.1**. MgO nanostructures obtained under different experimental conditions.

### 2.4.2 Nanowires of $GeO_2$

The reaction of Ge powder with activated charcoal by procedure (i) gave a high yield of nanowires, as seen in the SEM image in Figure 2.15a. The nanowires have diameters in the 50-250 nm range and grow in a quasi-aligned manner. The length of the nanowires goes up to several tens of micrometers. The XRD pattern of

_____

the nanowires, shown in Figure 2.14a, confirms them to be $GeO_2$ of hexagonal structure (a = 4.985 Å, c = 5.648 Å, JCPDS card no.: 43-1016).
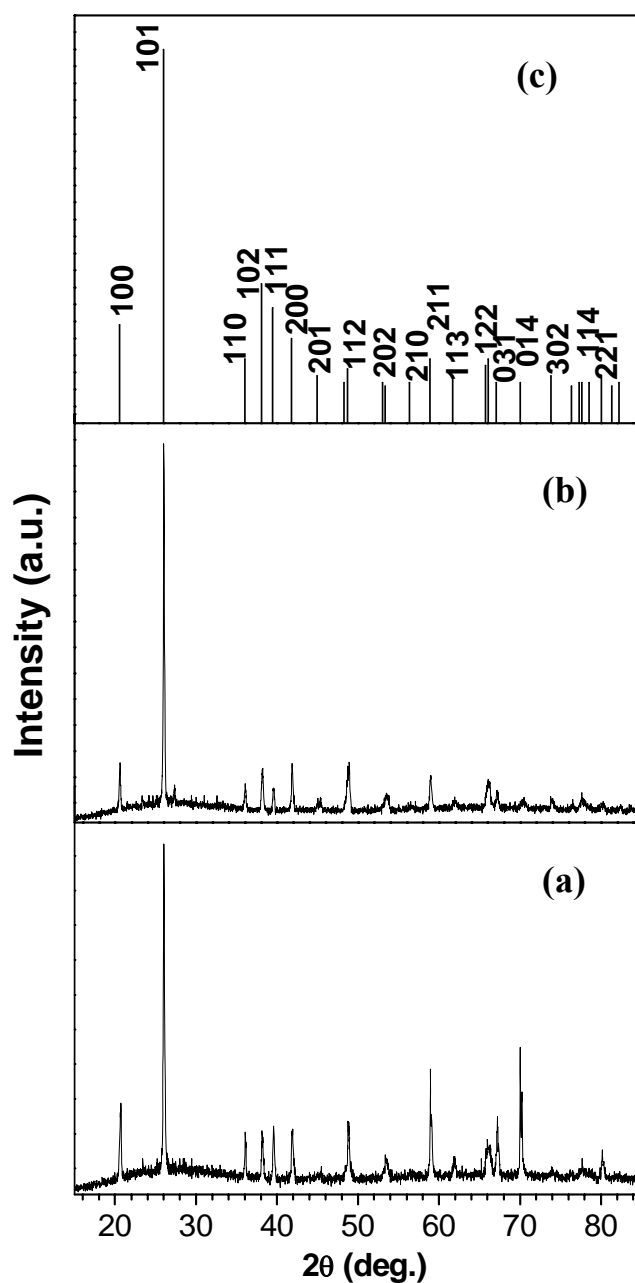


**Figure 2.14.** XRD patterns of (a) the product obtained by procedure (i); (b) procedure (ii) and (c) the XRD pattern of hexagonal $GeO_2$ from JCPDS (card no.43-1016).

_____

The low-magnification TEM image in Figure 2.15b shows nanowires with diameters of ~ 100 nm. The ends of the nanowires do not show the presence of metal droplets. The individual nanowires are single-crystalline, as evidenced from the SAED pattern given in Figure 2.15c. The reflections correspond to the (110), (111) and (100) planes of hexagonal $GeO_2$.
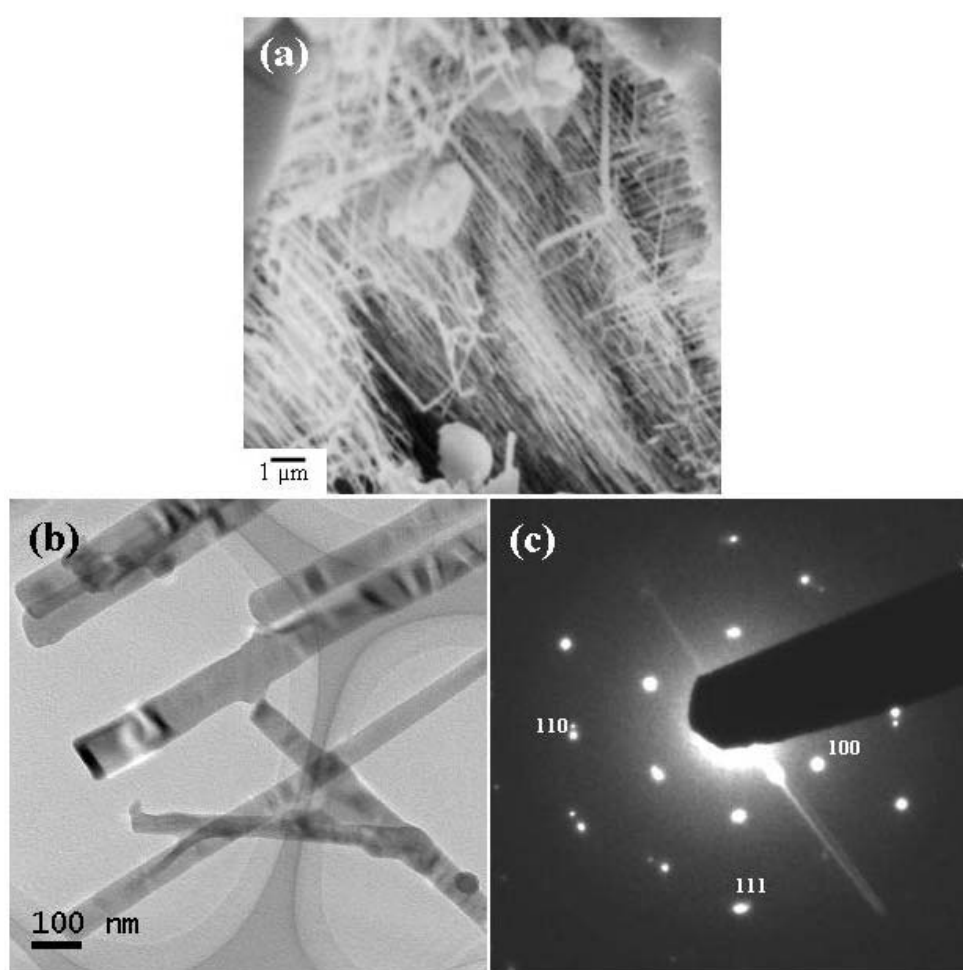


**Figure 2.15.** (a) SEM image of $GeO_2$ nanowires obtained by the reaction of Ge powder with activated charcoal at 900 °C by procedure (i); (b) TEM image of the nanowires obtained by procedure (i) along with (c) the corresponding SAED pattern.

_____
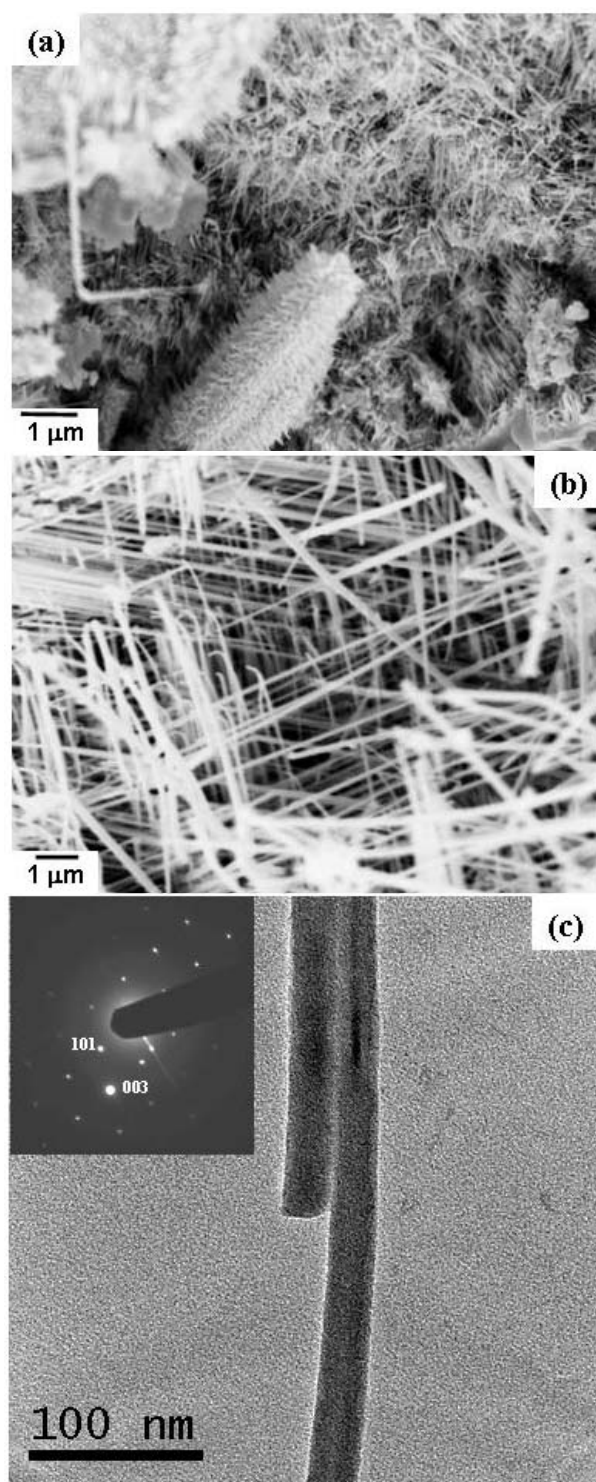


**Figure 2.16.** (a) Electron micrographs of the GeO$_2$ nanowires obtained by the reaction of Ge powder with activated carbon at 900 $^o$C by procedure (ii): (a) and (b) SEM images, and (c) low-magnification TEM image along with the corresponding SAED pattern shown as an inset.

_____

SEM images of the product obtained by procedure (ii) are shown in Figures 2.16a and 2.16b. The low-magnification SEM image in Figure 2.16a reveals that the nanowires are obtained in high yields. The image in Figure 2.16b shows that here again the nanowires grow in a quasi-aligned manner. The diameter of the nanowires varies in the 15-250 nm range and length extends to several tens of micrometers. The XRD pattern of the $GeO_2$ nanowires (Figure 2.14b) is consistent with the hexagonal structure. Figure 2.16c shows a typical TEM image of the nanowires with diameter of around 25 nm. The inset is the corresponding SAED pattern showing the Bragg reflections corresponding to the (101) and (003) planes of hexagonal $GeO_2$.

$GeO_2$ nanowires obtained by various routes have been reported to be extremely sensitive to electron radiation [31,36]. Amorphization of the nanowires was found to occur in seconds on exposure to the electron beam, with the disappearance of the electron diffraction spots. This has prevented the workers from obtaining HREM images. The nanowires synthesized by us seem to be more stable and did not get damaged by the electron beam. We show a typical HREM image of a single nanowire in Figure 2.17 grown by procedure (ii), confirming beyond doubt the single-crystalline nature of the nanowires. The spacing between the planes is 0.33 nm, corresponding to the (101) planes of hexagonal $GeO_2$. The arrow denotes the growth direction of the nanowire, which makes an angle of $\sim 30^{o}$ with the lattice planes.

The reaction of Ge powder with multi-walled carbon nanotubes (prepared in our lab by the arc-discharge method) as the carbon source also gave $GeO_2$ nanowires, though in a low yield. In Figure 2.18 is given an SEM image of the nanowires.

The formation of $GeO_2$ nanowires by the carbon-assisted route can be explained as follows. The first step is likely to involve the reduction of the surface oxide layer on the Ge powder by carbon to give Ge vapor. The vapor containing Ge

_____
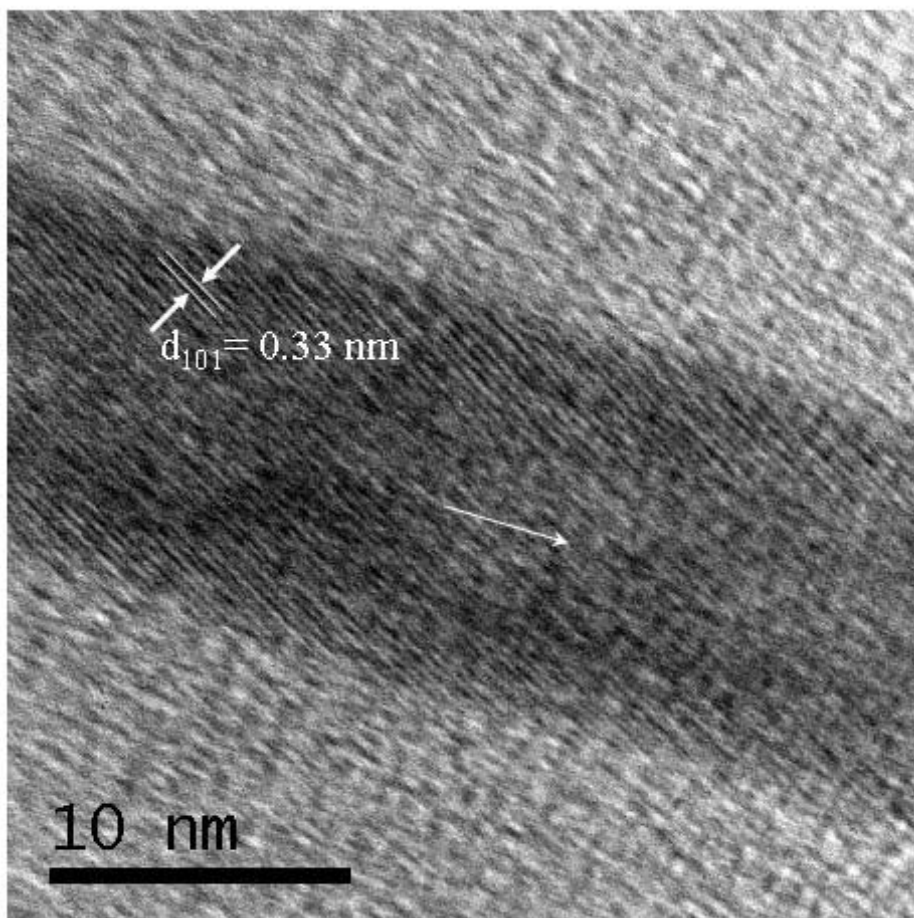


**Figure 2.17.** HREM image of a single $GeO_2$ nanowire grown by procedure (ii). The arrow denotes the direction of growth of the nanowire.
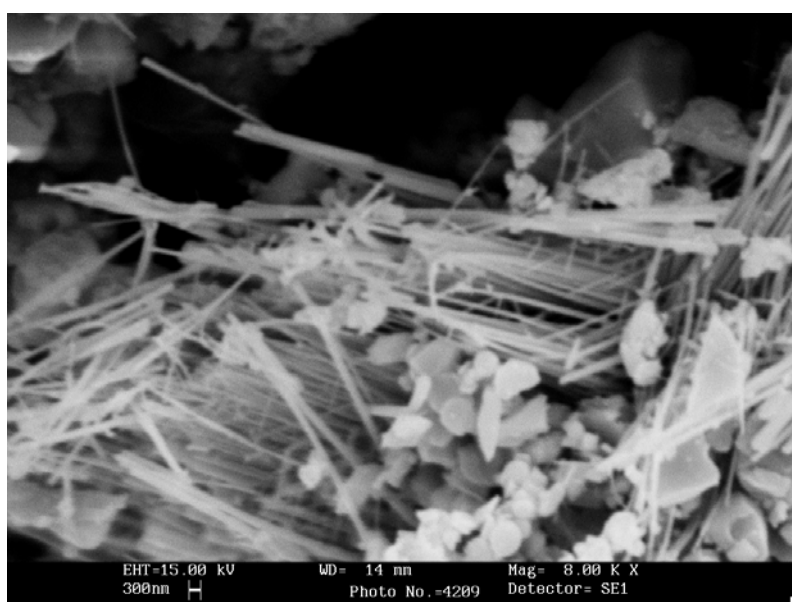


**Figure 2.18.** SEM image of $GeO_2$ nanowires obtained by reacting MWNTs with Ge powder.

particles reacts with the ambient oxygen to form oxidic nuclei from which the nanowires emanate. This process would conform to the VS growth mechanism of formation of nanowires (see Figure 2.21).

Figure 2.19 shows the IR spectrum of the $GeO_2$ nanowires obtained by procedure (i). We observe a broad band at $\sim$ 876 $cm^{-1}$, characteristic of Ge-O stretching [48].
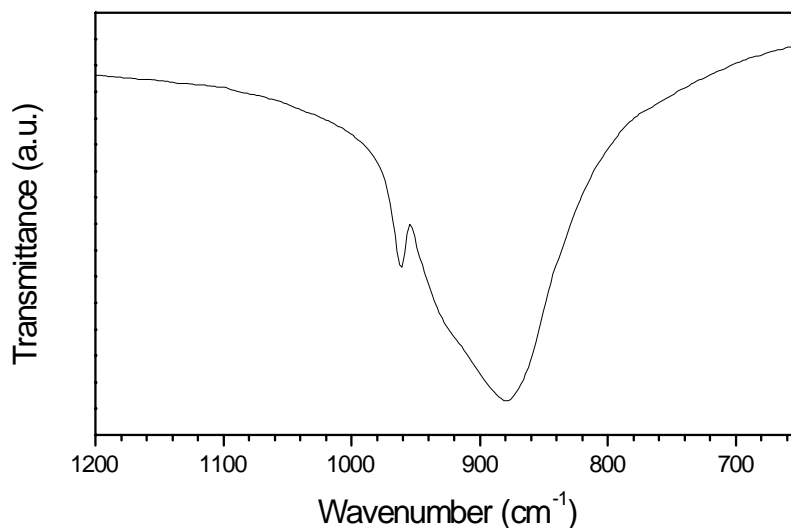


**Figure 2.19.** Infrared spectrum of the $GeO_2$ nanowires obtained by procedure (i).

The PL spectrum of the $GeO_2$ nanowires obtained by procedure (i), recorded at two different excitation wavelengths are given in Figure 2.20. Using an excitation wavelength of 250 nm, we obtained a peak at $\sim$ 380 nm (Figure 2.20a), similar to that of the $GeO_2$ nanocrystals with a PL band around $\sim$ 400 nm [48,49]. The $GeO_2$ nanocrystals were embedded in a silica matrix, which might account for the slight shift in the peak position. The origin of this band is the Ge/O related defect in the nanowires. We also show the spectrum recorded using an excitation wavelength of 450 nm (Figure 2.20b). We observe a band centered at $\sim$ 600 nm. The peak position is

_____
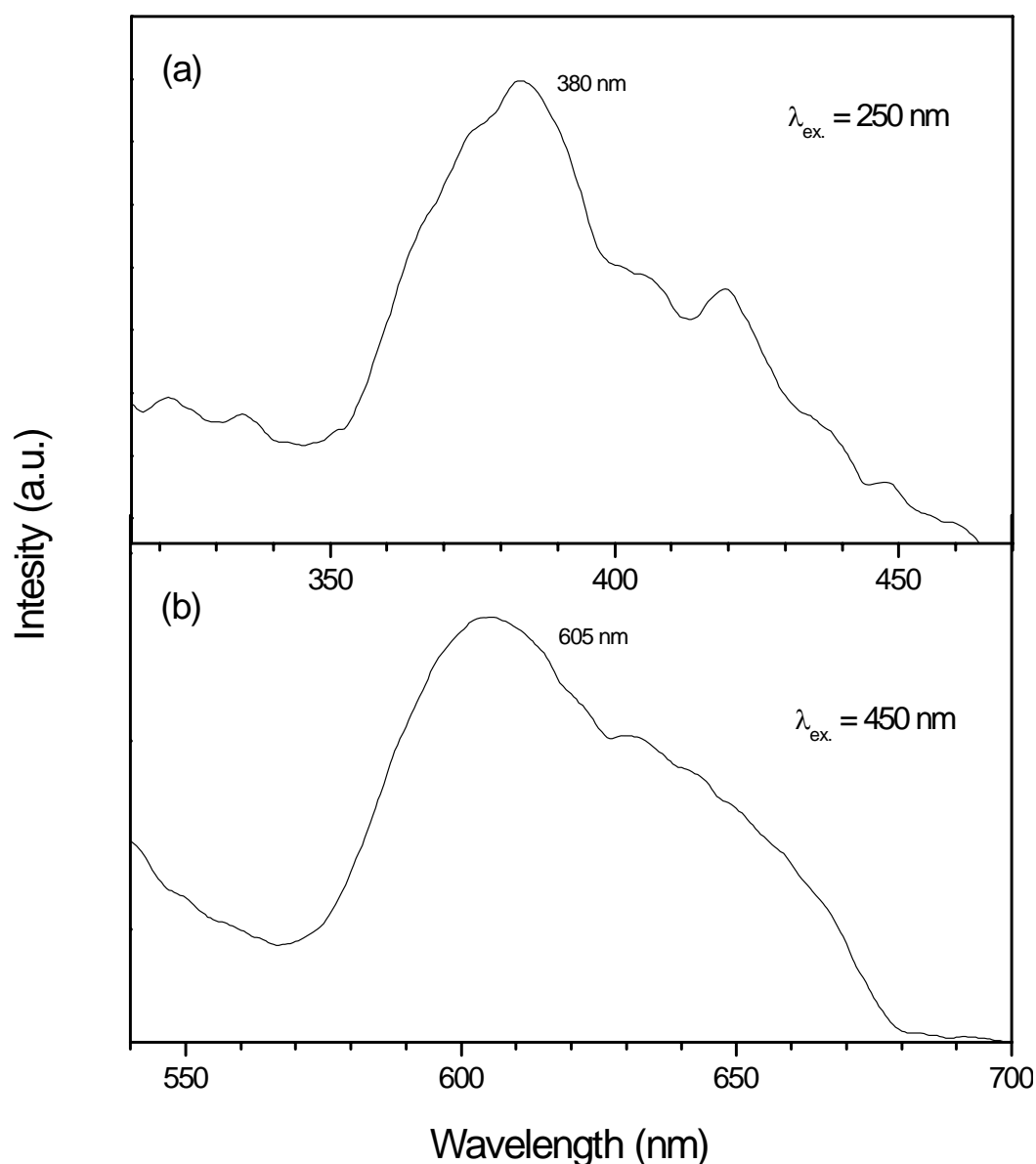


**Figure 2.20.** Room-temperature photoluminescence spectra of the $GeO_2$ nanowires prepared by procedure (i) using an excitation of (a) 250 nm and (b) 450 nm.

in agreement with the literature [49].

In conclusion, it has been possible to obtain $GeO_2$ nanowires, starting from Ge powder, by a simple carbon-assisted route. We have been successful in establishing the single-crystalline nature of the nanowires, convincingly using HREM for the first time. The nanowires also show characteristic luminescent properties.

**C, Δ**

**Ar / {Ar + O$_2$}**

**Oxide coating**

**Metal particles**

**O$_2$**

**Nucleation**

**Growth**

**NWs**

**Metal oxide particles**
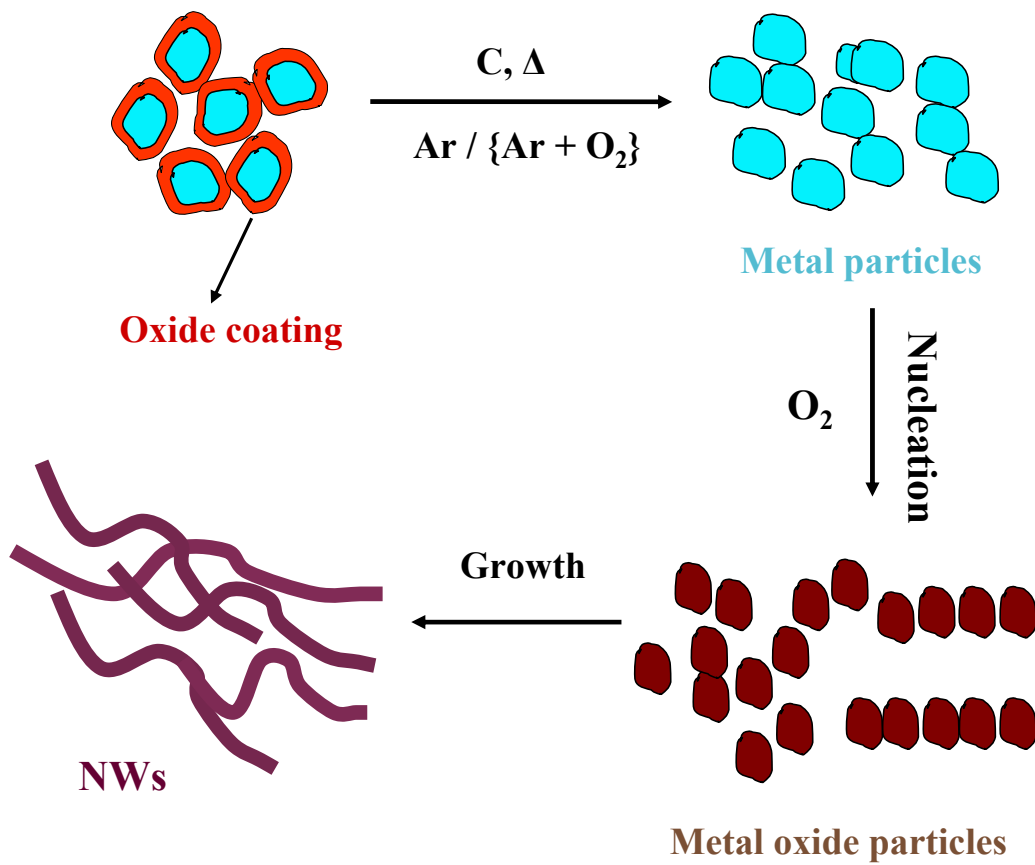
**Figure 2.21.** Schematic of VS mechanism involved in the formation of metal-oxide nanowires

_____

### 2.4.3   Doped and undoped ITO nanowires

The XRD pattern of the substrate covered with the whitish product obtained from procedure 1 is shown in Figure 2.22a. The pattern corresponds to that of cubic $In_2O_3$ (JCPDS Card No. 06-0416; a = 10.11 Å).
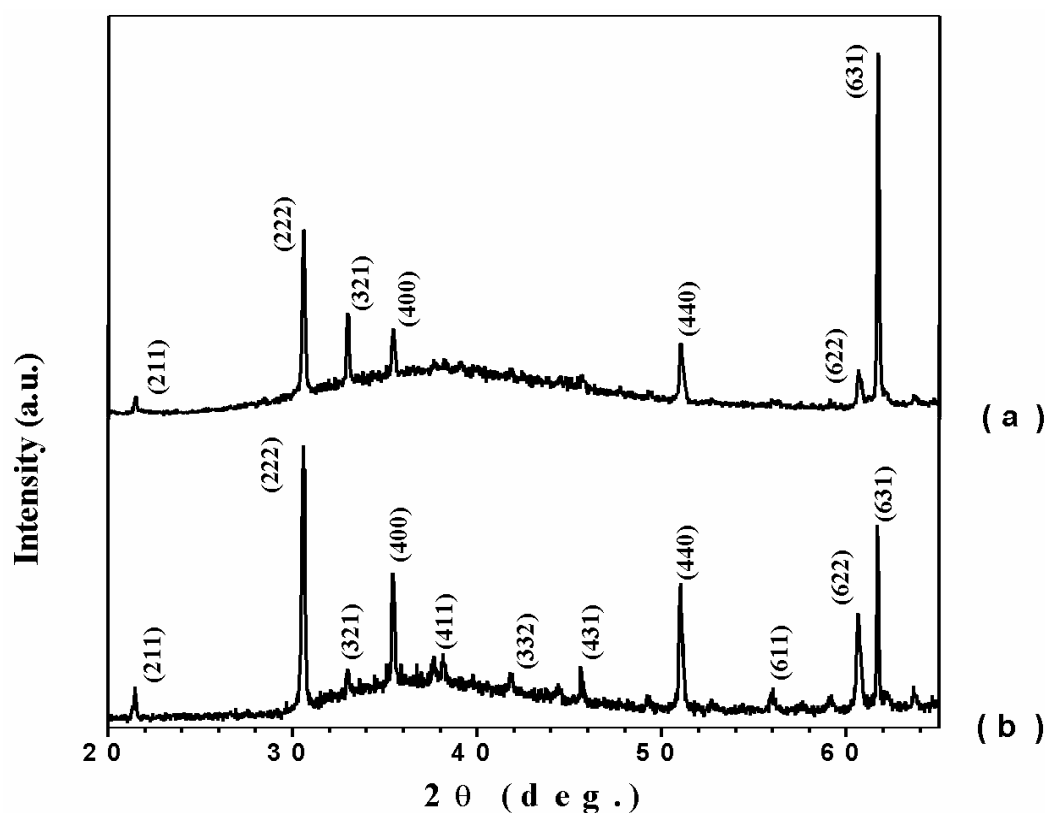


**Figure 2.22.** XRD patterns of the ITO nanowires obtained by (a) procedure 1 and (b) procedure 2 (the gel route).

The SEM image of the substrate in Figure 2.23a reveals the presence of nanowires in the regions where gold had been sputtered. The nanowires were obtained in high yields as can be inferred from the SEM image in Figure 2.23b. The nanowires have diameters of ~ 50 nm with lengths of several microns. EDAX spot analysis done on different regions of single ITO nanowires reveals the molar ratio of In to Sn to be

_____

85:15, as can be seen from Figure 2.24a. The composition was uniform in different

samples.
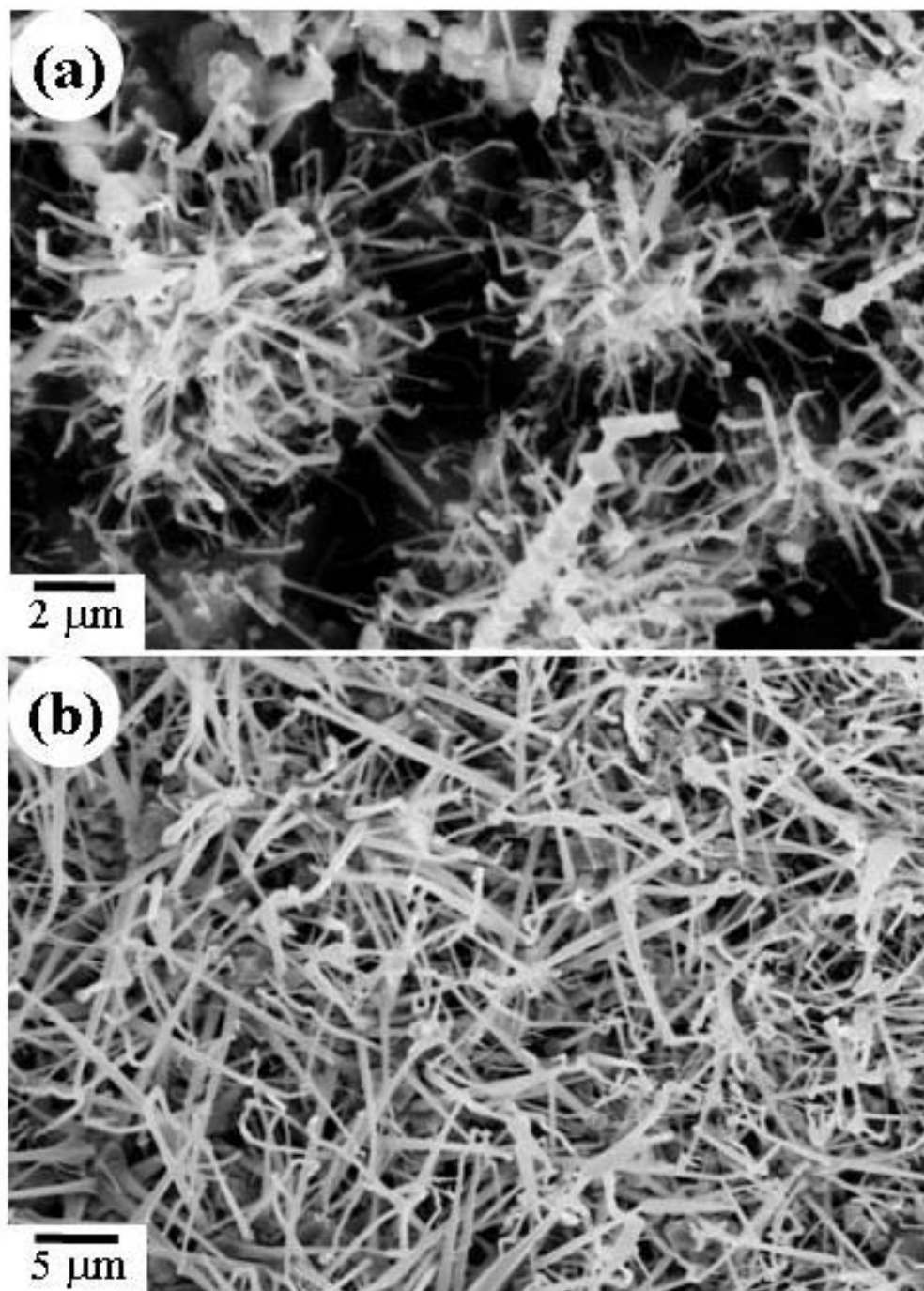


**Figure 2.23.** SEM images of ITO nanowires obtained by procedure 1.

_____
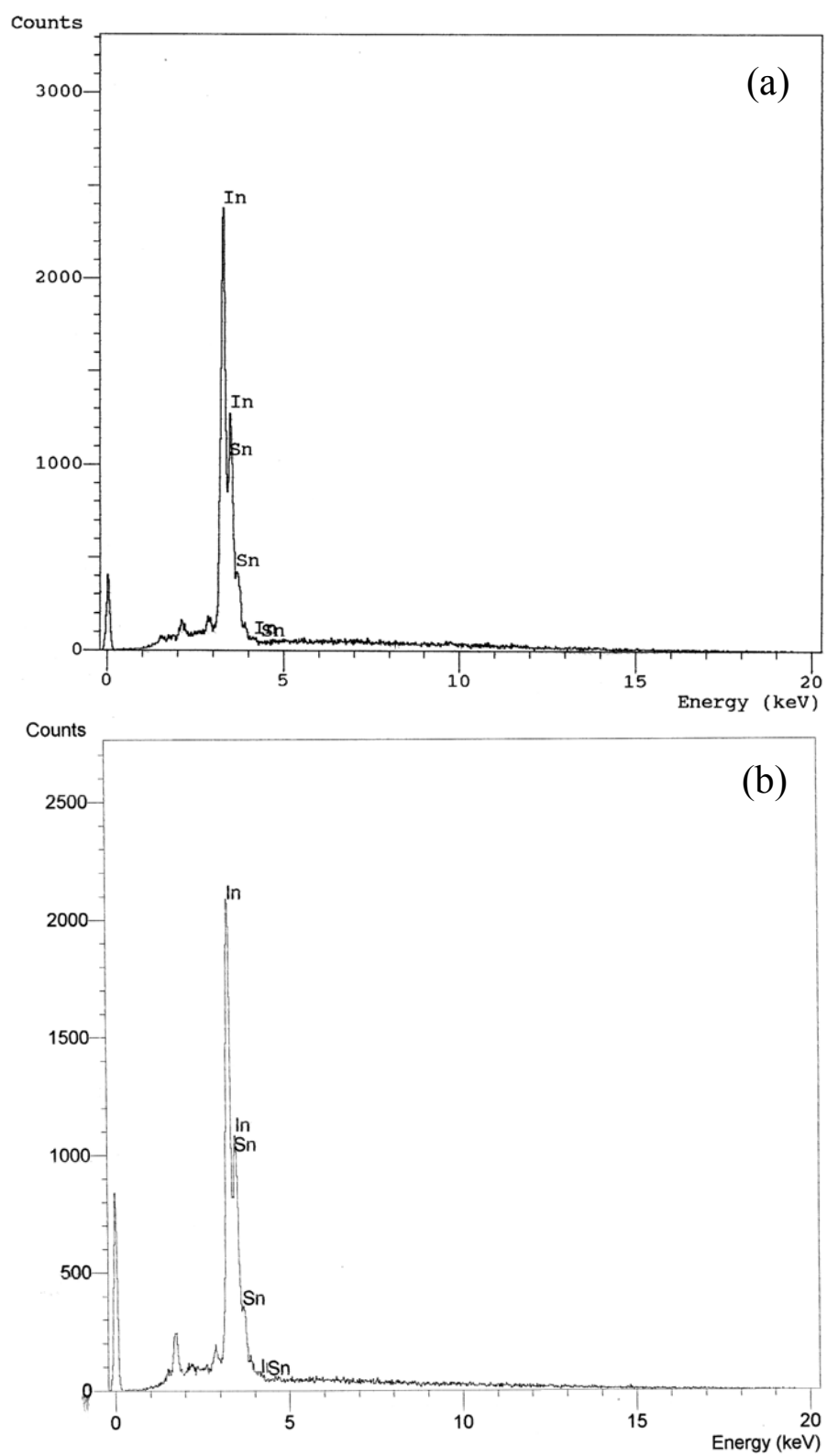


**Figure 2.24.** EDAX spectra of the ITO nanowires obtained by (a) procedure 1 and (b) procedure 2.

_____
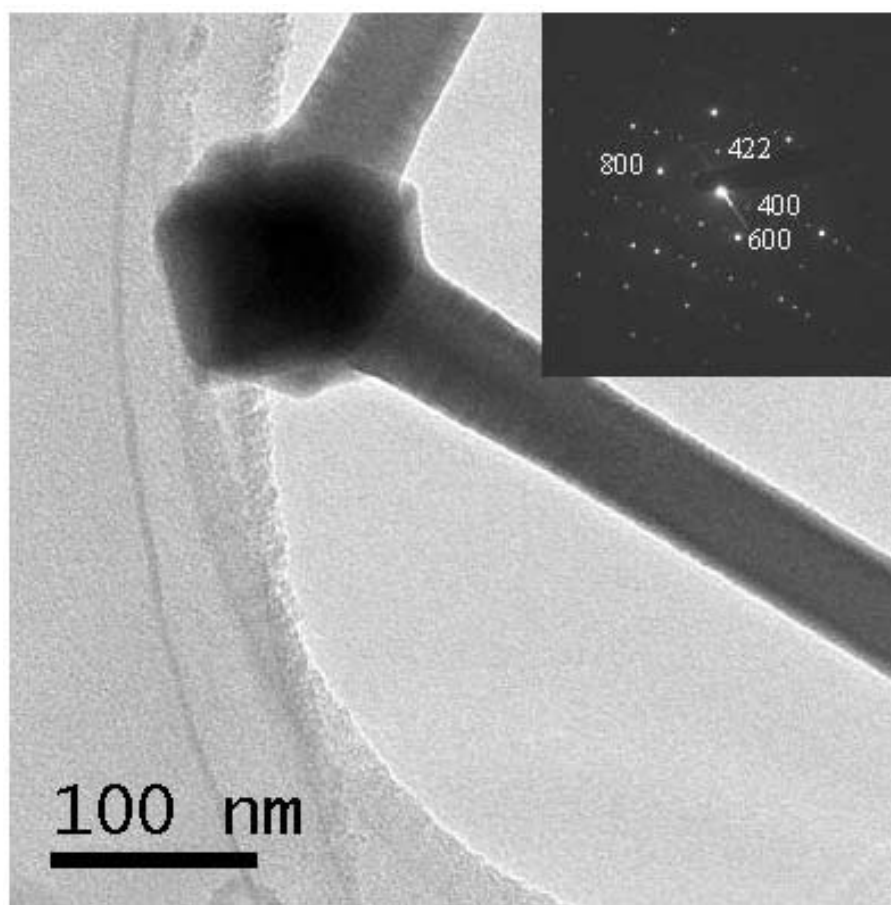


**Figure 2.25.** TEM image of an ITO nanowire obtained by procedure 1 with the catalyst particle at its tip. Inset is the SAED pattern of the nanowire.

The TEM image of a nanowire of diameter 40 nm given in Figure 2.25 shows the presence of a catalyst droplet at the end of the nanowire. The SAED pattern in the inset of Figure 2.25 exhibits diffraction spots corresponding to the (400), (600), (422) and (800) planes of cubic $In_2O_3$. In Figure 2.26 is given the HREM image of an ITO nanowire obtained by procedure 1. The image shows a spacing of 0.29 nm corresponding to the distance between the (222) planes of cubic $In_2O_3$. The growth direction of the nanowire is parallel to the (222) planes, which is indicated by an arrow. The SAED pattern and the HREM image confirm the nanowires to be single-crystalline in nature.

The XRD pattern of the nanowires obtained by procedure 2 is shown in Figure
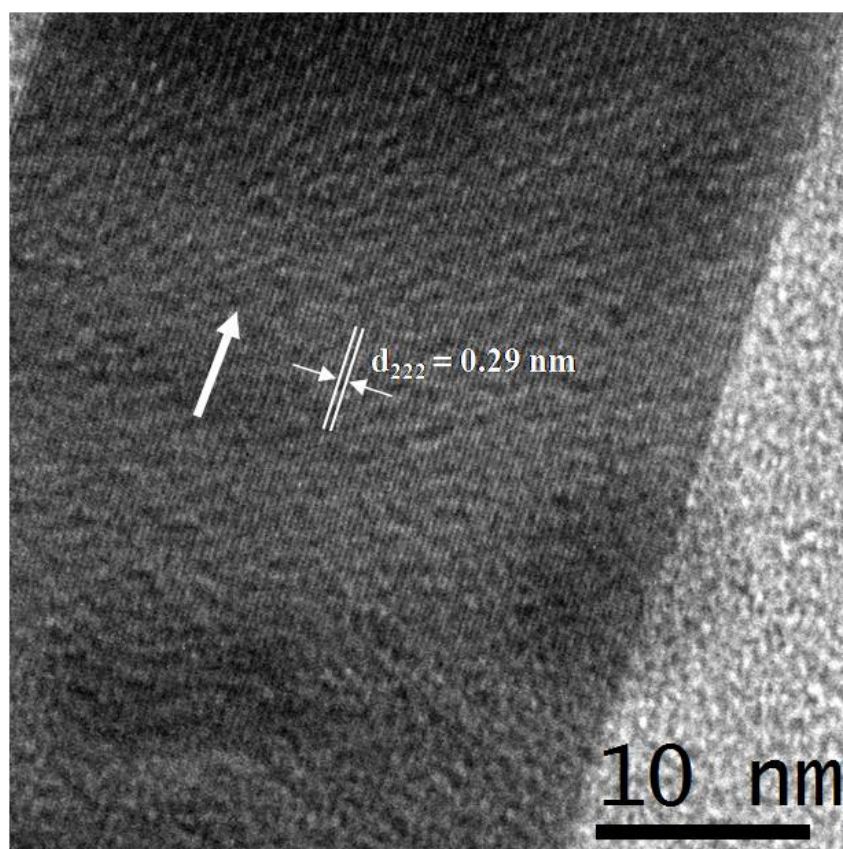
**Figure 2.26.** HREM image of an ITO nanowire, obtained by procedure 1, showing the (222) planes of cubic ITO with a d-spacing of 0.29 nm.

2.22b. In this case too, the pattern corresponds to that of cubic $In_2O_3$. The SEM image in Figure 2.27a reveals a high yield of the nanowires with diameters between 40 and 100 nm and lengths extending to tens of microns. Such a large variation in the diameter of the nanowires may be due to the different sizes of the Au catalyst nanoparticles generated during the course of the reaction. The EDAX analysis shows a uniform In:Sn ratio of 89:11 (Figure 2.24b). TEM images of the ITO sample from procedure 2 are shown in Figures 2.27b-d. The TEM image in Figure 2.27c shows the presence of an Au catalyst particle at the end of the wire. The SAED pattern in Figure 2.27c shows the diffraction spots corresponding to the (222) and (622) planes of cubic

_____

$In_2O_3$. SAED pattern of the Au catalyst particle is also given as an inset in the figure. The TEM image in Figure 2.27d corresponds to that of a nanotube, the SAED pattern in the inset showing it to be single-crystalline. The diffraction spots correspond to the (400), (440) and (622) Bragg planes of cubic $In_2O_3$.
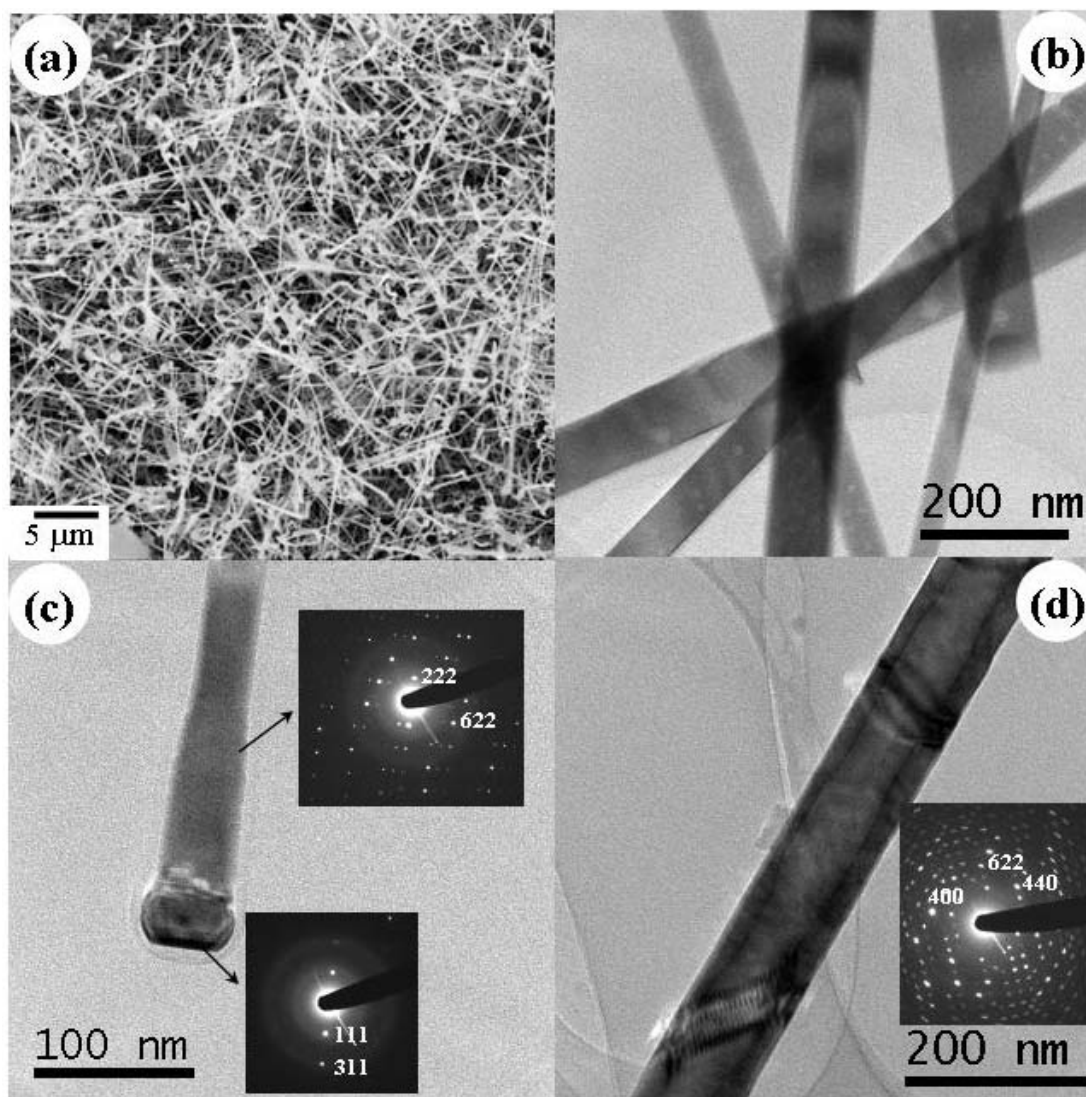


**Figure 2.27.** (a) SEM image of the ITO nanowires obtained by procedure 2; (b) and (c) TEM images of nanowires. Insets in (c) show SAED patterns of the nanowire and the Au catalyst particle. (d) TEM image of a nanotube. Inset shows the SAED pattern of the nanotube.
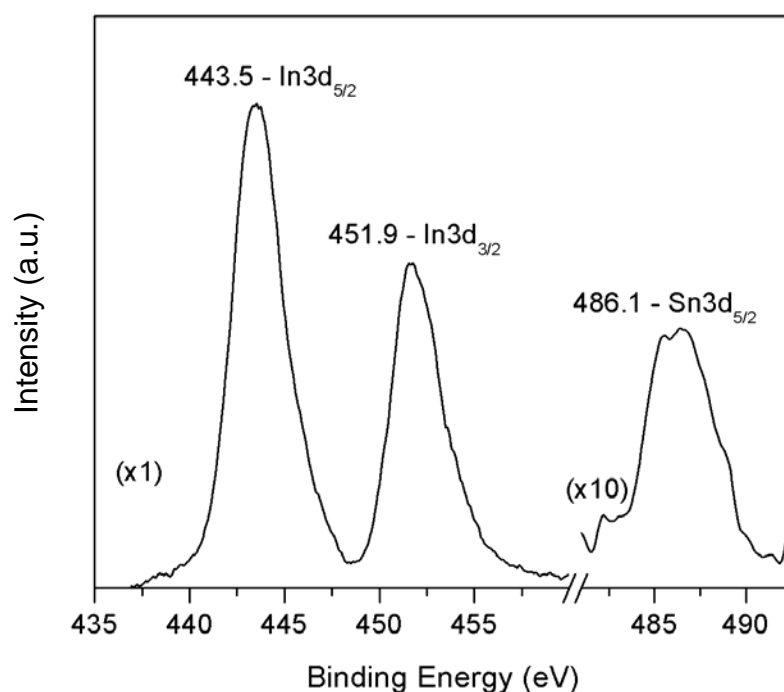
**Figure 2.28.** The core-level spectrum of the ITO nanowires, obtained by procedure 2, corresponding to In3d and Sn3d.

X-ray photoelectron spectroscopy (XPS) was carried out on the ITO nanowires prepared by procedure 2. In Figure 2.28 is given the core-level spectra corresponding to In3d and Sn3d. The characteristic peaks at 443.5 eV and 451.9 eV correspond to the binding energies of $In3d_{5/2}$ and $In3d_{3/2}$ respectively [50]. A peak found at 486.1 eV is due to $Sn3d_{5/2}$. These data show that In exists as $In^{3+}$ and Sn as $Sn^{4+}$ in the sample. The slightly lower binding energies of In3d and Sn3d from the literature values [51,52] suggest some oxygen deficiency in the ITO samples.

To check the transparency of the ITO nanowires, UV-visible absorption measurements were carried out. The UV-Vis absorption spectrum of the nanowires is given in Figure 2.29a. This shows that the ITO nanowires are transparent in the whole of the visible region, with a small absorption peak at ~ 290 nm similar to that reported in the literature [43]. The high optical transparency of the nanowires suggests

_____
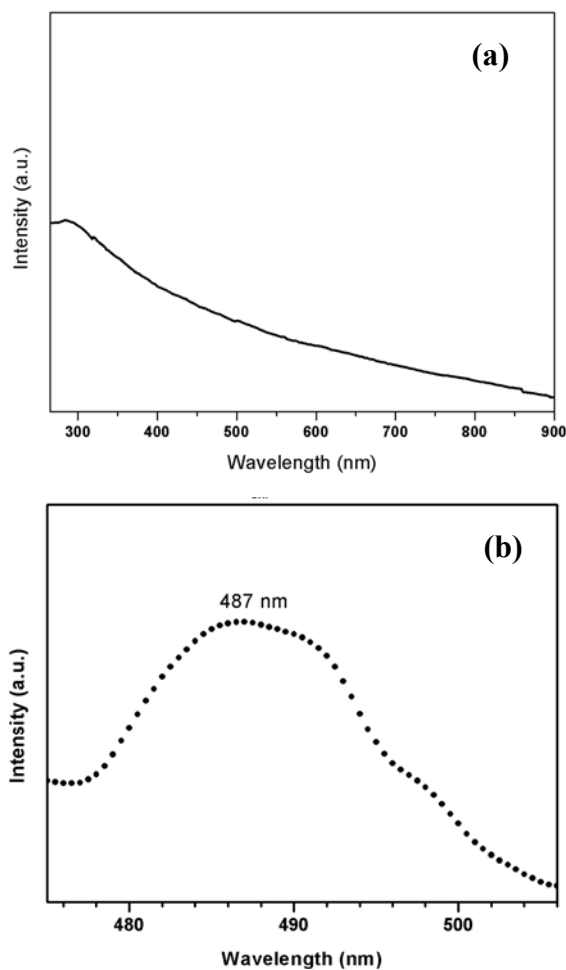


**Figure 2.29.** (a) UV-Vis absorption spectrum and (b) PL spectrum of the ITO nanowires obtained by procedure 2.

their potential applications in optoelectronic devices. PL studies on the ITO nanowires gave an emission peak at 487 nm, when excited at 280 nm. The PL spectrum of the nanowires is given in Figure 2.29b. The emission can be attributed to the surface defects and oxygen defects in the ITO nanowires. An emission peak at around 510 nm has been reported in literature [42].

By using procedures similar to 1 and 2, we were able to prepare Zn-doped ITO nanowires. An SEM image of the nanowires obtained by procedure 1 is shown in Figure 2.30a. Along with nanowires of ~ 50 nm diameter, we see the presence of

_____
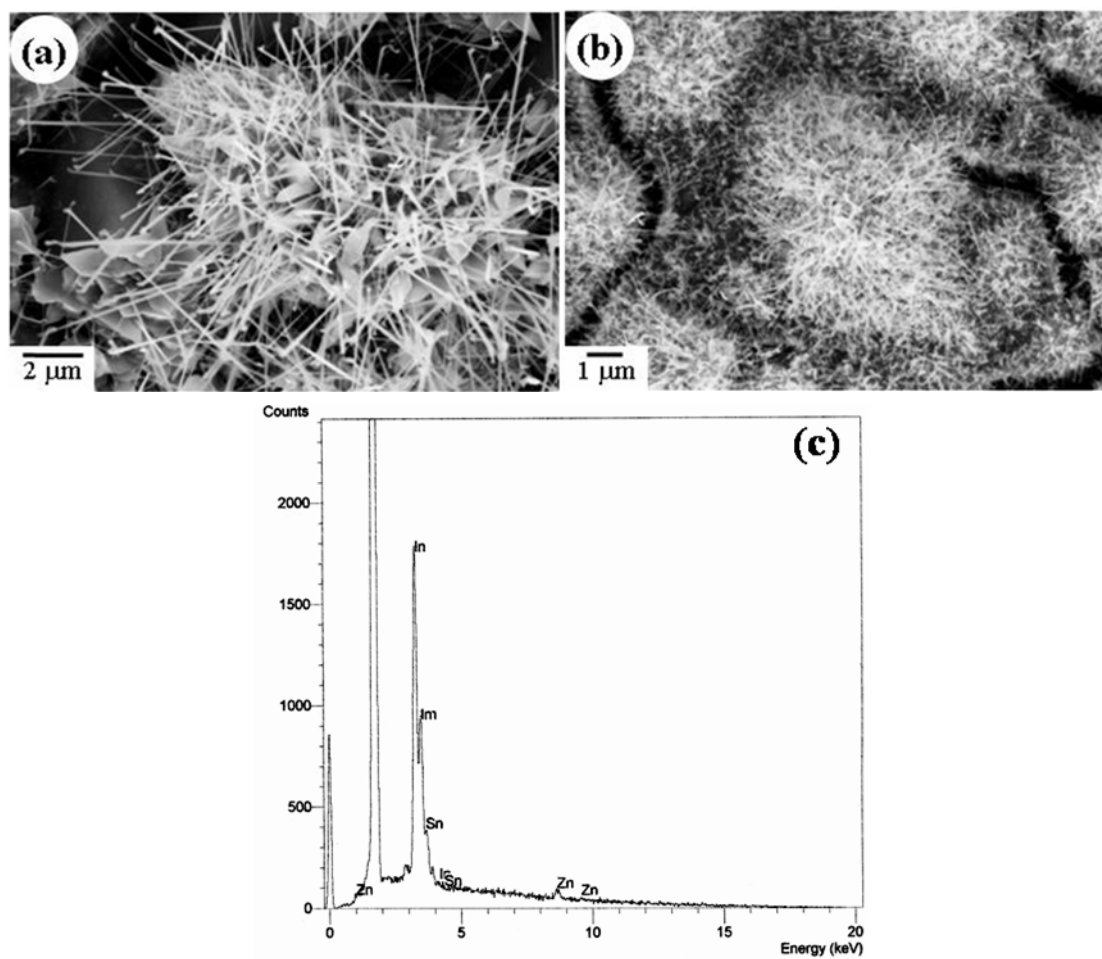


**Figure 2.30.** (a) and (b) SEM images of the Zn and Sn-doped $In_2O_3$ nanowires obtained by the carbothermal (procedure 1) and the gel route (procedure 2) respectively. (c) EDAX spectrum of the nanowires showing the presence of In, Sn and Zn.

sheet-like structures. By using the gel route (procedure 2), we were also able to obtain a good yield of nanowires of ~ 30 nm diameter as evidenced from Figure 2.30b. EDAX analysis showed that the proportion of Zn was in the range of 5-8 at.%, while that of Sn was in the range of 10-16 at.%. We show a typical EDAX spectrum in Figure 2.30c. These preliminary results show that $In_2O_3$ nanowires can be co-doped with Sn and Zn.

Based on the TEM observations we conclude that the ITO nanowires obtained by procedures 1 and 2 grow by the vapor-liquid-solid mechanism [53]. The nitrates

_____

of In and Sn decompose to give the corresponding oxides on heating. In procedure 1, the oxides of In and Sn are reduced by the carbon (graphite) to give the corresponding suboxides or metals. In procedure 2, carbon is produced *in-situ* by the organic material. The reactive oxidic species are carried by the Ar gas to the substrates where they dissolve in the Au metal to form an alloy. Supersaturation of the reactive species leads to the growth of the nanowires from the alloy particles. The TEM images in Figures 2.25 and 2.27c, showing a catalyst particle at the end of the nanowire, support the proposed mechanism.

Thus, we have successfully demonstrated the synthesis of ITO nanowires by two routes employing carbon-assisted synthesis technique. The nanowires are single-crystalline and are readily patterned on substrates. They are transparent in the visible region. Preliminary results show that it is possible to dope ITO nanowires with zinc by the methods employed.

## 2.5    Conclusions

In conclusion, it has been possible to establish the versatility of carbothermal synthesis by producing nanowires and other interesting nanostructures of MgO, as well as nanowires of $GeO_2$ and ITO. Various sources of carbon such as activated carbon, activated charcoal, graphite and MWNTs have been made use of in the various synthetic reactions. All the nanostructures obtained have been confirmed to be single-crystalline in nature. Elementary steps to co-dope Zn and Sn into $In_2O_3$ have been successfully carried out. The nanowires prepared by this method might find a variety of applications.

_____

_____

**2.6    References**

[1] See, for example, special issue on nanowires, *Adv. Mater.* 2003 **15.**

[2] P. Yang, Y. Wu, R. Fan, *Int J. Nanosci.* 2002, **1**, 1.

[3] C. N. R. Rao, F. L. Deepak, G. Gundiah, A. Govindaraj, *Prog. Solid State Chem.* 2003, **31**, 5.

[4] G. Gundiah, A. Govindaraj, C. N. R. Rao, *Chem. Phys. Lett*. 2002, **351**, 189.

[5] G. Gundiah, F. L. Deepak , A. Govindaraj, C. N. R. Rao, *Topics Cat.* 2003, **23**, 137.

[6] F. L. Deepak, G. Gundiah, M. M. Seikh, A. Govindaraj, C. N. R. Rao, *J. Mater. Res.* 2004, **19**, 2216.

[7] K C. Kam, F. L. Deepak, A. K. Cheetham, C. N. R. Rao, *Chem. Phys. Lett.* 2004, **397**, 329.

[8] G. Gundiah, G. V. Madhav, A. Govindaraj, M. Motin Seikh, C. N. R. Rao, *J. Mater. Chem*. 2002, **12**, 1606.

[9] W. Yi, S. Yu, W. Lee, I. T. Han, T. Jeon, Y.Woo, J. Lee, S. Jin, W. Cho,  J. Heo, D. Jeon, J. M. Kim, *J. Appl. Phys.* 2001, **89**, 4091.

[10] P. Yang, C. Lieber, *Science* 1996, **273**, 1836.

[11] P. Yang, C. Lieber, *J. Mater. Res.* 1997, **12**, 2981.

[12] C. O. House, *J. Am. Ceram. Soc.* 1961, **44**, 572.

[13] Z. Wei, H. Qi, P. Ma, J. Bao, *Inorg. Chem. Comm.* 2002, **5**, 147.

[14] Y. Q. Zhu, W. K. Hsu, W. Z. Zhou, M. Terrones, H. W. Kroto, D. R. M. Walton, *Chem. Phys. Lett.* 2001, **347**, 337.

[15] Z. Cui, G. W. Meng, W. D. Huang, G. Z. Wang, L. D. Wang, *Mater. Res. Bull.* 2000, **35**, 1653.

[16] J. Zhang, L. Zhang, X. Peng, X. Wang, *Appl. Phys. A* 2001, **73**, 773.

[17] Y. Li, Y. Bando, T. Sato, *Chem. Phys. Lett.* 2002, **359**, 141.

[18] H. Y. Dang, J. Wang, S. S. Fang, *Nanotechnology* 2003, **14**, 738.

[19] C. Tang, Y. Bando, T. Sato, *J. Phys. Chem. B* 2002, **106**, 7449.

[20] Y. Yin, G. Zhang, Y. Xia, *Adv. Funct. Mater.* 2002, **12**, 293.

[21] J. Zhang, L.Zhang, *Chem. Phys. Lett.* 2002, **363**, 293.

[22] R. Ma, Y. Bando, *Chem. Phys. Lett.*, 2003, **370**, 770.

[23] K. L. Klug, V. P. Dravid, *Appl. Phys. Lett.* 2002, **81**, 1687.

[24] M. Zhao, X. L. Chen, X. N. Zhang, H. Li, H. Q. Li, L. Wu, *Chem. Phys. Lett.*,
      2004, **388**, 7.

[25] Z. Zhou, S. Xie, D. Wan, D. Liu, Y. Gao, X. Yan, H. Yuan, J. Wang, L. Song,
      W. Zhou, Y. Wang, H. Chen, J. Li, *Solid State Commun.* 2004, **131**, 2462.

[26] J. Zhan, Y. Bando, J. Hu, D. Goldberg, *Inorg. Chem.* 2004, **43**, 2462.

[27] Y. B. Li, Y. Bando, D. Golberg, Z. W. Liu, *Appl. Phys. Lett.*, 2003, **83**,
      999.

[28] Y. Chen, J. Li, Y. Han, X. Yang, and J. Dai, *J. Cryst. Growth* 2002, **245**,
      163.

[29] C. N. R. Rao, G. Gundiah, F. L. Deepak, A. Govindaraj, and A. K. Cheetham, *J.
      Mater. Chem.*, 2004, **14**, 440.

[30] A. Margaryan, M. A. Piliavin, *Germanate Glasses, Structure, Spectroscopy,
      and Properties*, Artech House Inc. Press. 1993.

[31] Z. G. Bai, D. P. Yu, H. Z. Zhang, Y. Ding, Y. P. Wang, X. Z. Gai, Q. L.
      Hang, G. C. Xiong, S. Q. Feng, *Chem. Phys. Lett.* 1999, **303**, 311.

[32] Y. H. Tang, Y. F. Zhang, N. Wang, I. Bello, C. S. Lee, S. T. Lee, *Appl. Phys.
      Lett.* 1999, **74**, 3824.

[33] Y. Zhang, J. Zhu, Q. Zhang, Y. Yan, N. Wang, X. Zhang, *Chem. Phys. Lett.*

_____

2000, **317**, 504.

[34] X. C. Wu, W. H. Song, B. Zhao, Y. P. Sun, J. J. Du, *Chem. Phys.Lett.*, 2001, **349**, 210.

[35] G. Gu, M. Burghard, G. T. Kim, G. S. Düsberg, P. W. Chiu, V. Krstic, S. Roth, *J. Appl. Phys.* 2001, **90**, 5747.

[36] J. Q. Hu, Q. Li, X. M. Meng, C. S. Lee, S. T. Lee, *Adv. Mater.* 2002, **14**, 1396.

[37] I. Hambergend, C. G. Granquist, *J. Appl. Phys.* 1986, **60**, R123.

[38] B. G. Lewis, D. C. Paine, *Mater. Res. Soc. Bull.* 2000, **25**, 22.

[39] F. Zhu, K. Zhang, E. Guenther, C. S. Jin, *Thin Solid Films* 2000, **363**, 314.

[40] S. S. Sinencio, R. Williams, *J. Appl. Phys.* 1983, **54**, 2757.

[41] D. Yu, D. Wang, W. Yu, Y. Qian, *Mater. Lett.* 2000, **58**, 84.

[42] Q. Wan, Z. T. Song, S. L. Feng, T. H. Wang, *Appl. Phys. Lett.* 2004, **85**, 4759.

[43] X. S. Peng, G. W.Meng, X. F. Wang, Y. W. Wang, J. Zhang, X. Liu, L. D. Zhang, *Chem. Mater.* 2002, **14**, 4490.

[44] P. Nguyen, H. T. Ng, J. Kong, A. M. Cassell, R. Quinn, J. Li, J. Han, M. Mc Neil, M..Meyappan, *Nano Lett.* 2003, **3**, 925.

[45] G. B. Palmer, K. R. Poeppelmeier, T. O. Mason, *Chem. Mater.* 1997, 9, 3121.

[46] R. Seshadri, A. Govindaraj, H. N. Aiyer, R. Sen, G. N. Subbanna, A. R. Raju, C. N. R. Rao, *Current Sci.* 1994, **66**, 839.

[47] G. H. Rosenblatt, M. W. Rowe, G. P. W. Jr., R. T. Williams, Y.Chen, *Phys. Rev. B* 1989, **39**, 10309.

[48] M. Zacharias, P. M. Fauchet, *J. Non-Cryst. Solids* 1998, **227**, 1058.

[49] M. Zacharias, P. M. Fauchet, *Appl. Phys. Lett.*, 1997, **71**, 380.

[50] S. S. Kim, S. Y. Choi, C. G. Park, H. W. Jin, *Thin Solid Films*, 199, **347**, 155.

[51] D. Shuttleworth, *J. Phys. Chem.* 1980, **84**, 1629.

_____

[52] J. C. C. Fan, J. B. Goodenough, *J. Appl. Phys.* 1977, 4**8**, 3524.

[53] R. S. Wagner, W. C. Ellis, *Appl. Phys. Lett.* 1964, **4**, 89.

# CHAPTER 3

# Hydrogel-assisted Synthesis of Nanotubes and Nanorods of CdS, ZnS and CuS, Showing Some Evidence for Oriented Attachment

**SUMMARY**[*]

The use of a tripodal cholamide-based hydrogel as a template for the synthesis of 1D nanostructures of some metal sulfides has been discussed in this chapter of the thesis. By carrying out the reaction of appropriate metal compounds with $Na_2S$ in the presence of the hydrogel, nanotubes and nanorods of CdS, ZnS and CuS have been obtained. The nanostructures have been characterized by transmission electron microscopy and spectroscopic techniques. EDAX analysis has been used to confirm the composition of the nanostructures. The inner diameter of the metal sulfide nanotubes falls in the range 2-6 nm, while their length goes up to a few hundreds of nanometers. In the case of ZnS we could obtain nanorods as well, depending on the concentration of $Zn(OAc)_2$. The hydrogel fibers act as templates leading to the formation of the metal sulfide nanotubes comprising nanoparticles. The situation is comparable to that in oriented attachment growth and we do find evidence for oriented attachment of nanocrystals in the TEM images. Also, assembly of short nanorods to form one-dimensional chains is observed in the case of CuS.

---

_____

### 3.1      Introduction

Nanotubes and nanowires of semiconducting materials such as CdS, ZnS and CdSe have been prepared by a variety of methods [1,2]. In this context, the surfactant-assisted method is one of the novel innovations [3,4]. In this method, the surfactant molecules spontaneously organize at the critical micelle concentration (CMC) into rod-shaped micelles, thus acting as templates for the formation of nanotubes and nanowires. For example, nanotubes and nanowires of CdS and CdSe have been prepared from solutions containing surfactant such as Triton-X [3]. By using Triton-X and AOT, nanowires of Cu and Zn chalcogenides have also been synthesized [5]. CdS nanotubes and nanowires have been prepared by employing SDS rod-like micelles as the templates [6].

The surfactant-assisted method can also involve the growth of nanostructures by the oriented attachment of nanoparticles. Oriented attachment of nanoparticles is an effective means of forming anisotropic nanocrystals in solution-based routes. In this mechanism, particles undergo fusion at specific dimensionally similar crystallographic surfaces, leading to the formation of interesting nanostructures [7]. Oriented attachment of nanoparticles has been observed in several materials. Thus, Tang *et al.* [8] have reported the formation of CdTe nanoparticle chains by spontaneous organization. Formation of nanowires of PbSe by dipole-driven oriented attachment of collections of nanocrystals along identical crystal faces has been reported by Murray and co-workers [9]. By oriented attachment, Yu *et al.* [10] could obtain ZnS nanorods with cubic blend structure, in which the (111) planes of the component ZnS nanocrystals are nearly perfectly aligned. Pradhan *et al.* [11] have reported the formation of colloidal CdSe quantum wires by the oriented attachment of magic-sized clusters of CdSe. In the present study, we have employed a hydrogel for

the synthesis of nanotubes and nanowires of ZnS, CdS, and CuS, wherein they grow by oriented attachment of the nanocrystals.

## 3.2    Scope of the present study

Gels derived from low molecular weight organic compounds have been employed for the synthesis of nanotubes of mostly metal oxides. Organogelators gel solvents at low concentrations due to the formation of a three-dimensional network based on fibrous aggregates in organic fluids [12,13]. The self-assembled organogelators act as templates in the sol–gel polymerization process [14]. Shinkai and co-workers have shown that certain cholesterol derivatives can gelate tetraethyl orthosilicate (TEOS), causing silica polymerization, giving rise to hollow structures [15]. Nanotubes of some transition metal oxides have also been prepared by this templating method [16]. In all the nanotube syntheses mentioned above, organogels have been used as templates due to which metal alkoxides become the necessary inorganic precursors. In order to use simple and non-moisture sensitive metal salts as precursors, the reactions have to be carried out in an aqueous medium in which these salts are soluble. Gelation of aqueous fluids is different from that in organic solvents in that the aggregation process in aqueous environments is predominantly driven by the hydrophobic effect. A tripodal cholamide (**1**) having hydrophobic surfaces (coming from the $\beta$-face of the bile acid backbone) has been reported to spontaneously aggregate into gel fibers in predominantly aqueous media [17].

Recently, a hydrogel has been employed as templates to prepare nanotubes of metal oxides such as $SiO_2$, $TiO_2$, ZnO, $ZrO_2$, $WO_3$ and sulfates such as $BaSO_4$ and $ZnSO_4$ [18]. The nanotubes so obtained appear to be polycrystalline, and it appears that the growth of nanostructures by the hydrogel route could involve oriented

attachment of nanoparticles. Since materials with hexagonal crystal structure with a large difference in the surface energy between the (0001) plane and the other planes, are considered to favor anisotropic growth along the [0001] crystallographic direction, we sought to prepare nanotubes and nanorods of CdS, ZnS and CuS by using hydrogel template route. All the three metal sulfides have the hexagonal structure and we therefore considered it feasible to observe oriented growth of nanoparticles in the formation of one-dimensional nanostructures.

## 3.3 Experimental and related aspects

### 3.3.1 Synthesis

Tripodal cholamide hydrogelator **1** was synthesized according to the procedure reported elsewhere [17]. The average diameter of the hydrogel fibers was in the range 8-10 nm, with lengths extending up to a few hundred nanometers [18]. Nanostructures of CdS, ZnS and CuS were prepared starting with the corresponding metal acetates. Na$_2$S was used as the sulfur precursor in the synthesis. A sol of the hydrogel was obtained by dissolving 5 mg (0.0075 mmol) in 100 µL of acetic acid and 400 µL of water. In a typical reaction, for the preparation of CdS nanotubes, a gel was formed by adding 11 mg (0.04 mmol) of cadmium acetate to a solution obtained



**1**
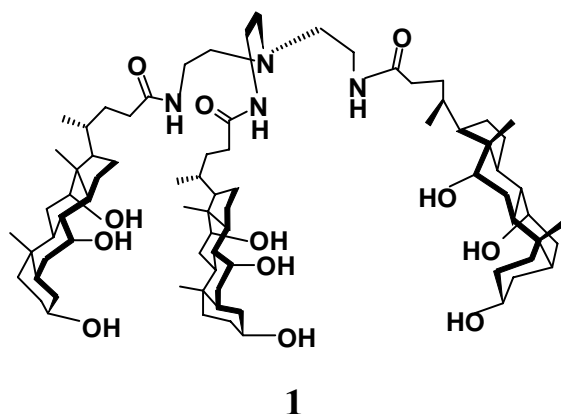
**Figure 3.1.** Schematic of the tripodal cholamide gelator

by dissolving 2.5 mg of KOH in 250 µL water and 25 µL distilled ethanol. To this gel was added the sol of the hydrogel. This was thoroughly mixed under sonication, and warmed slightly to form a sol. A white gel so obtained was allowed to stand for 24 h at 30 $^{o}$C. An aqueous solution of 3.4 mg (0.043 mmol) of $Na_2S$ dissolved in 100 µL water was added to the sol obtained by warming the white gel slightly. The sol which turned yellow instantly was shaken using a stirrer to ensure complete mixing of the reactants. The yellow gel obtained in this manner was allowed to stand for 24 h at 30 $^{o}$C.

The preparation of nanostructures of ZnS was carried out with two different concentrations of $Zn(OAc)_2$ and $Na_2S$, maintaining the gel concentration the same (0.0075 mmol), the procedure being similar to that employed in the case of CdS. In one of the reactions, 8.75 mg (0.04 mmol) of $Zn(OAc)_2$ was reacted with 3.4 mg (0.043 mmol) of $Na_2S$. This reaction led to the formation of nanorods of ZnS. When the $Zn(OAc)_2$ concentration was reduced to half [4.37 mg (0.02 mmol)], we obtained nanotubes of ZnS. CuS nanostructures were prepared starting with 5 mg (0.0075 mmol) of the gelator, 8 mg (0.04 mmol) of copper acetate and 6.25 mg (0.08 mmol) of $Na_2S$, the experimental procedure being the same as in the case of CdS. When the blue sol containing $Cu(OH)_2$ was mixed with $Na_2S$ solution, we obtained a black CuS gel. In order to remove the hydrogel template, the products containing CdS, ZnS and CuS nanostructures were washed several times with distilled ethanol.

### 3.3.2 Techniques used for characterization

*Scanning electron microscopy:* Scanning electron microscope (SEM) images were obtained on a LEICA S440i SEM. Energy dispersive analysis of X-rays (EDAX) was performed with an Oxford microanalysis group 5526 system attached to the SEM employing Links (ISIS) software and a Si(Li) detector. For SEM and EDAX the

_____

samples were spread onto a conducting carbon tape pasted on an aluminium stub, followed by sputter-coating with gold.

***Transmission electron microscopy:*** Transmission electron microscope (TEM) images were obtained with a JEOL JEM 3010, operating with an accelerating voltage of 300 kV. TEM samples were prepared by placing a drop of the sample suspensions in $C_2H_5OH$ on a Cu coated holey carbon grid, and allowed to evaporate slowly.

***UV-Vis absorption spectroscopy and Photoluminescence:*** UV-Vis absorption measurements were carried out at room temperature with a Perkin-Elmer model Lambda 900 UV/Vis/NIR spectrometer. For UV-Vis analysis the samples were dispersed thoroughly in $C_2H_5OH$. Photoluminescence (PL) measurements were carried out on $CCl_4$ suspensions of the samples, at room temperature with a Perkin-Elmer model LS50B luminescence spectrometer. The excitation wavelengths used depended on the samples studied.

## 3.4    Results and discussion

### 3.4.1   CdS nanotubes

In Figure 3.2 we show the TEM images of nanotubes of CdS, obtained after the removal of the hydrogel template. The images reveal the presence of a number of nanotubes. EDAX analysis of the CdS nanotubes confirmed their purity, giving a Cd:S ratio of 1:1. EDAX spectrum of the CdS nanotubes is given in Figure 3.3a. The TEM image in Figure 3.2a demonstrates the hollow nature of the nanotubes. The length of the nanotubes extends to a few hundred nanometers while the diameter of the inner tubule is ~ 2-3 nm, the outer diameter being in the 20-25 nm range. Electron diffraction patterns showed the nanotubes to be generally polycrystalline. A selected area electron diffraction (SAED) pattern of a single nanotube is given in the bottom
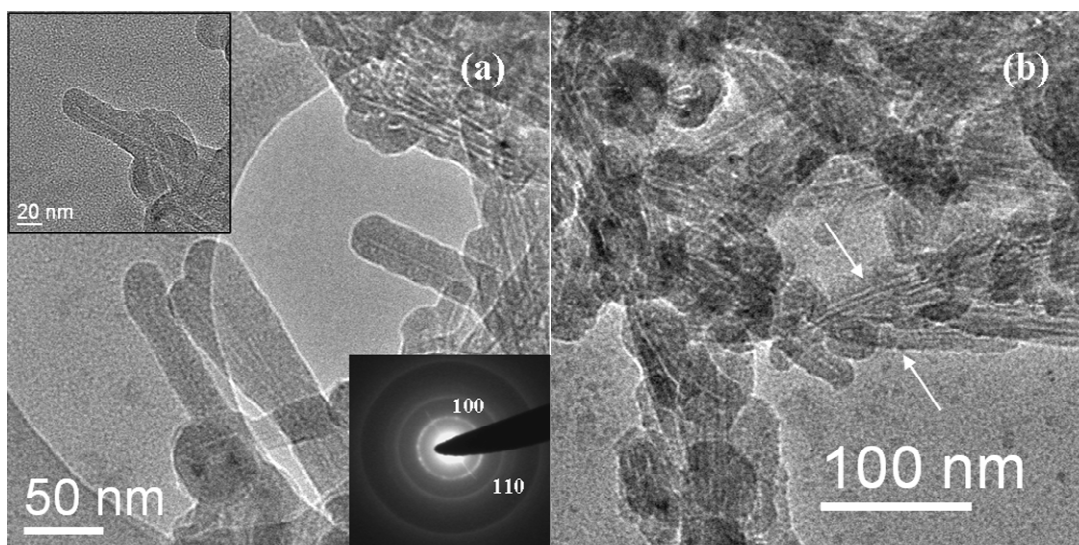
**Figure 3.2.** (a) TEM image of CdS nanotubes obtained after removal of the hydrogel template. Top inset is a high-magnification image of a single nanotube. Bottom inset is the SAED pattern of the nanotubes. (b) TEM image showing a bunch of nanotubes assembled spontaneously, indicated by the arrows.

inset of Figure 3.2a. The diffuse rings correspond to the (100) and (110) Bragg planes of hexagonal CdS. Clearly, the tripodal cholamide gel fibers act as templates, on which the CdS particles get deposited, giving rise to the nanotubes. The low magnification TEM image in Figure 3.2b suggests a possible assembly or attachment of the initially formed shorter nanotubes to form linear chains (indicated by arrows in the figure). The hydrogel might be responsible for such an attachment, the hydrogel playing a dual role of being a template to produce hollow nanotubes as well as favoring the attachment or assembly of the nanotubes.

The UV-visible absorption spectrum of the CdS nanotubes given in Figure 3.4a shows a blue-shift in the excitonic absorption band to 460 nm. The blue-shift from the bulk value of 515 nm [19] is due to quantum confinement effects in the CdS nanotubes, the inner diameter of the nanotubes being less than the Bohr-exciton diameter of CdS (6 nm). Xiong *et al.* [6] have reported an absorption band at 459 nm
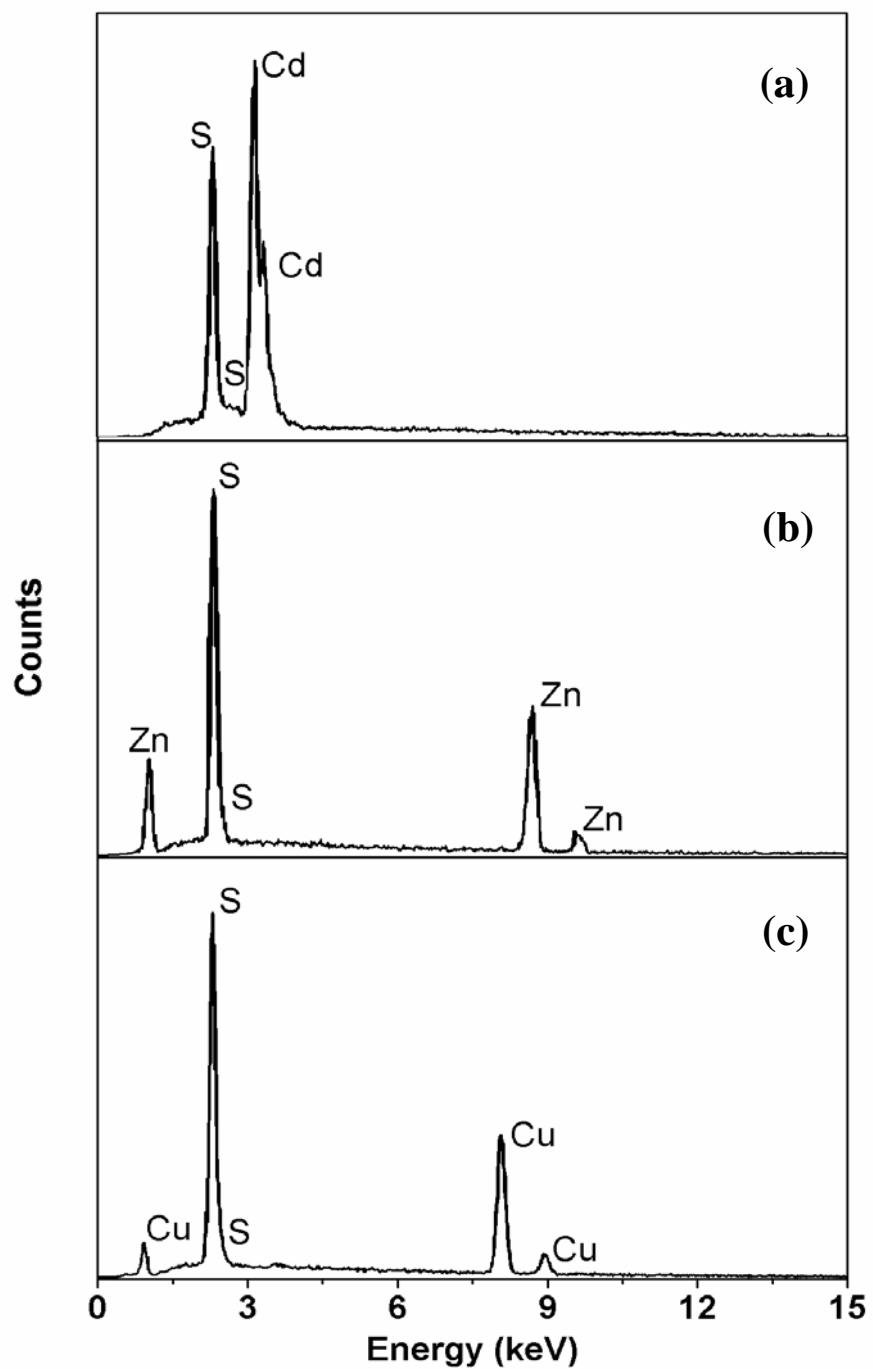
**Figure 3.3.** EDAX spectra of  (a) CdS nanotubes; (b) ZnS nanotubes and (c) CuS nanostructures obtained by using hyrdogel as a template.
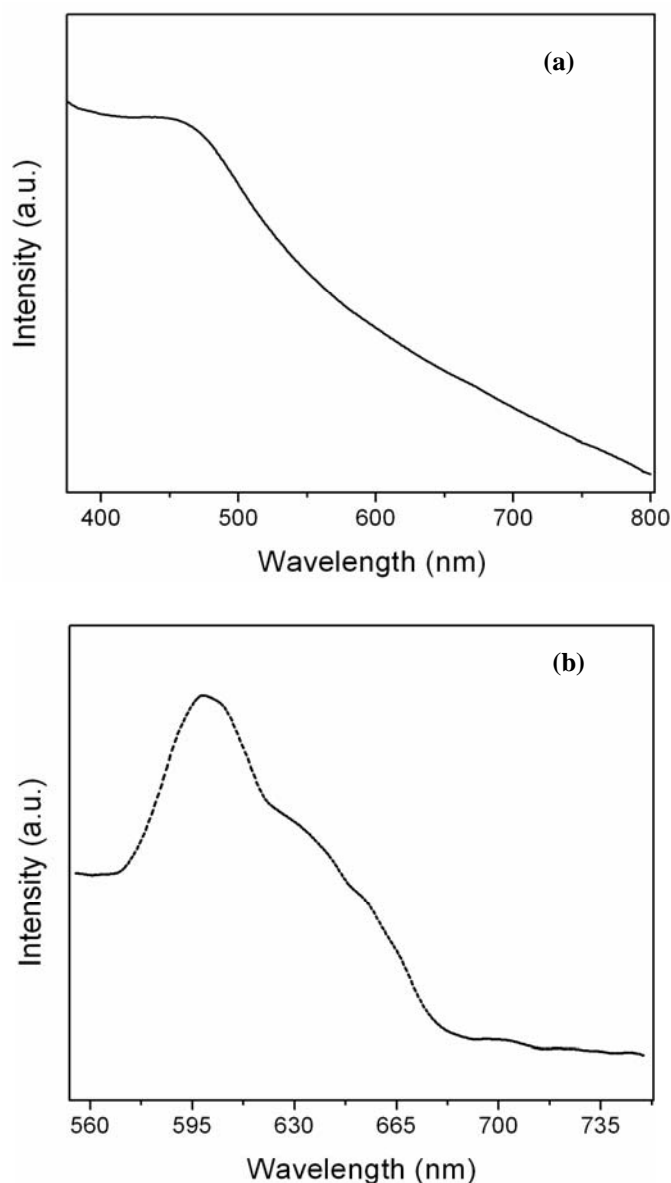
**Figure 3.4.** (a) Electronic absorption spectrum of CdS nanotubes and (b) PL spectrum of the CdS nanotubes.

for CdS nanotubes with an inner diameter of ~ 5 nm prepared by an in situ micelle-template-interface reaction. An absorption maximum ~ 450 nm has been reported in nanoparticles and hollow spheres of CdS [19,20]. In Figure 3.4b we show the photoluminescence (PL) spectrum of the CdS nanotubes prepared by us, revealing a band centered at 610 nm. This band is due to charge carriers trapped at surface defects of the nanotubes [21,22].

_____

## 3.4.2   Nanotubes and nanorods of ZnS
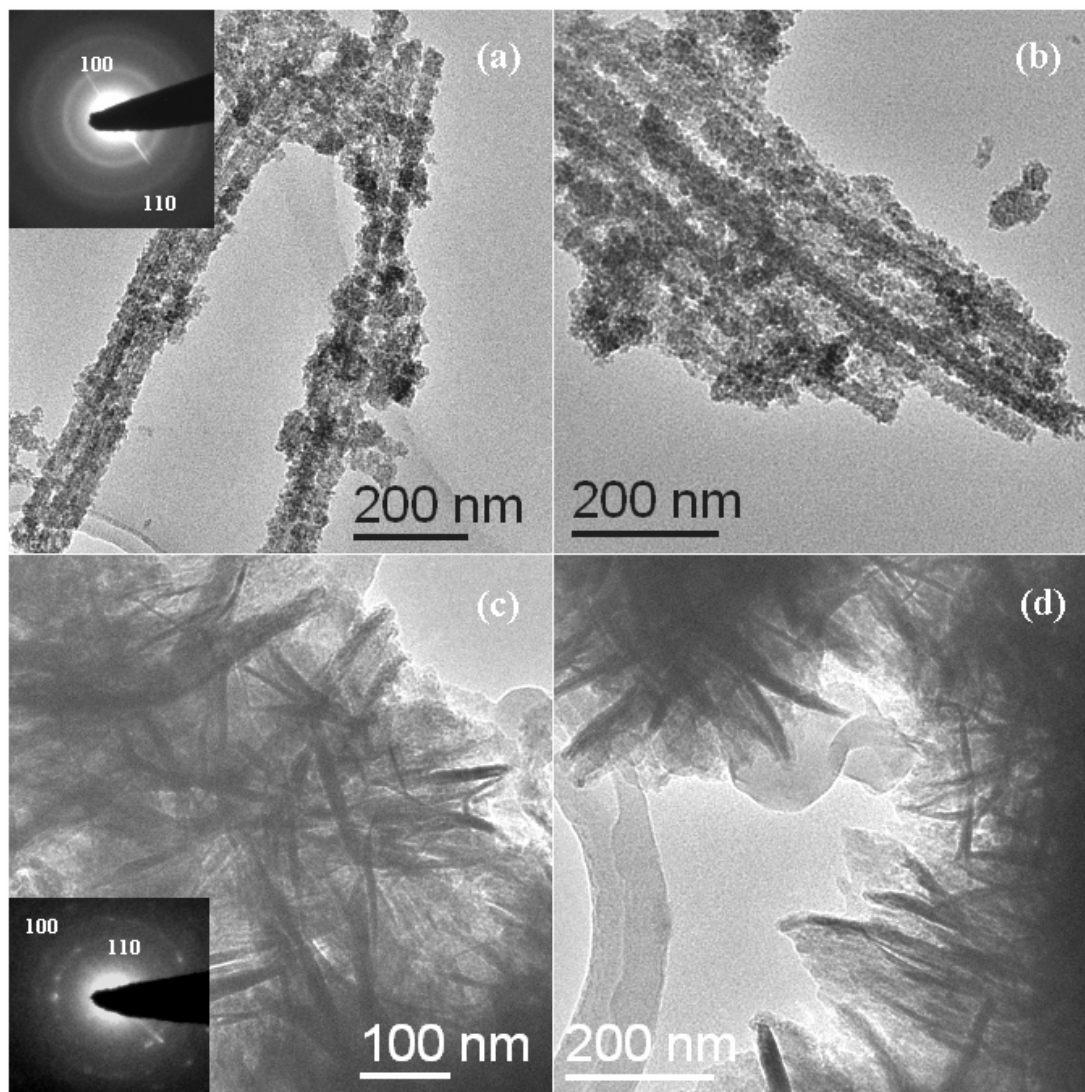


**Figure 3.5.** (a) and (b) TEM images showing nanotubes of ZnS obtained using 0.02 mmol of Zn(OAc)$_2$; (c) and (d) nanorods of ZnS obtained using a higher concentration (0.04 mmol) of Zn(OAc)$_2$. Insets are the corresponding SAED patterns.

In the case of ZnS, we could obtain nanotubes as well as nanorods depending on the concentration of $Zn(OAc)_2$. The TEM image in Figure 3.5a shows nanotubes of ZnS obtained at the lower concentration (0.02 mmol) of $Zn(OAc)_2$. The nanotubes have an inner diameter in the $\sim$ 4-6 nm range, with lengths going up to a micrometer. The TEM image shows tiny nanocrystals of ZnS making up the walls of the nanotubes. Electron diffraction patterns also reveal the nanotubes to be polycrystalline and of hexagonal structure. The SAED pattern of one of the nanotubes given in the inset of Figure 3.5a shows rings arising from the (100) and (110) planes of the hexagonal structure. A bunch of ZnS nanotubes is seen in the TEM image in Figure 3.5b. When the concentration of $Zn(OAc)_2$ was doubled (0.04 mmol), we obtained nanorods of ZnS, as shown in the TEM image in Figure 3.5c. The diameter of the nanorods is in the 10-15 nm range, with lengths extending to a few hundreds of the nanometers. The inset in Figure 3.5c shows the SAED pattern of the nanorods, with diffuse rings corresponding to the (100) and (110) planes of hexagonal ZnS. Figure 3.5d shows another TEM image of the ZnS nanorods. The images in Figures 3.5c and 3.5d suggest the formation of copious quantities of nanorods. EDAX analysis of the ZnS nanostructures gave a Zn:S ratio of 1:1. In Figure 3.3b is given the EDAX spectrum of ZnS nanotubes.

The ZnS nanotubes and nanorods were characterized by UV-visible absorption spectroscopy and PL spectroscopy. In Figure 3.6a is given the absorption spectrum of the ZnS nanotubes. The band appearing at $\sim$ 318 nm is blue-shifted relative to that of bulk ZnS (350 nm) [5]. Nanowires of ZnS of diameter $\sim$ 5 nm were reported to show an absorption maximum around 326 nm [23]. An absorption band at $\sim$ 320 nm has been reported in the case of ZnS quantum dots [24]. The PL spectrum of ZnS nanotubes given in Figure 3.6b exhibits two bands, a weak blue emission at $\sim$ 485 nm

_____
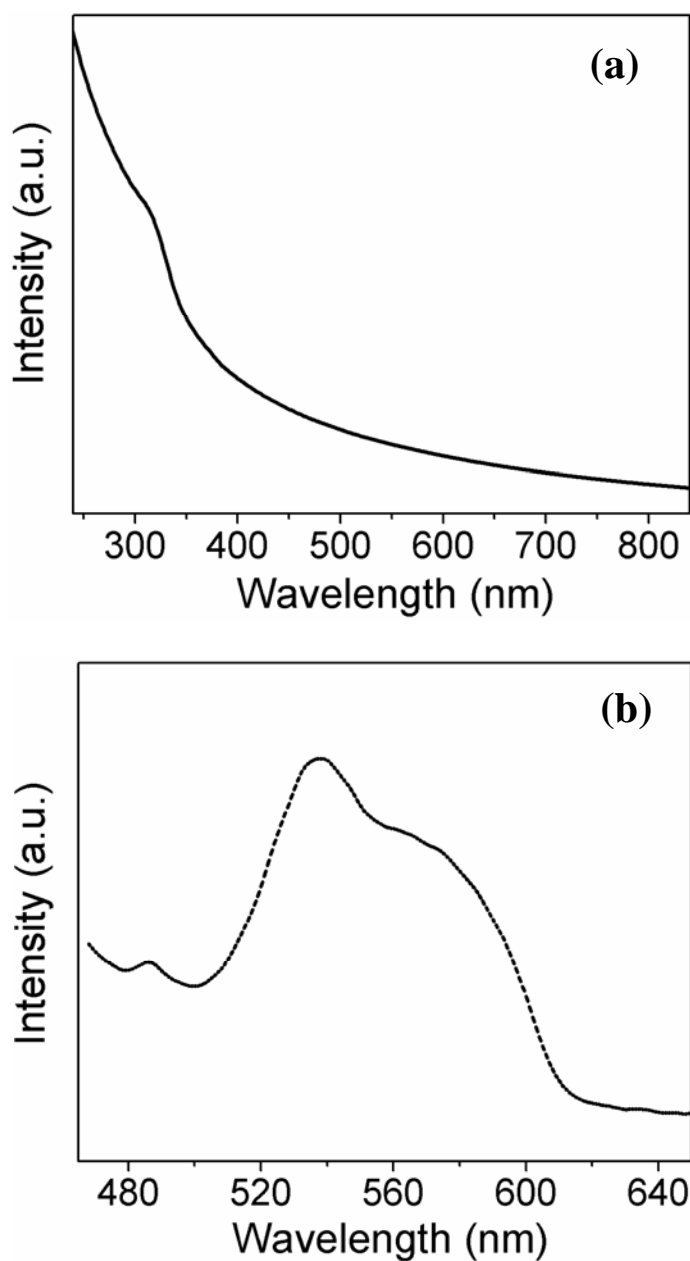


**Figure 3.6.** (a) Electronic absorption spectrum of ZnS nanotubes and (b) PL spectrum of the ZnS nanotubes.

and a strong green emission around 538 nm. The 485 nm band is attributed to zinc vacancies in the ZnS lattice. Emission bands at ~ 470 nm [25] and ~ 498 nm [26] have been reported in ZnS nanobelts. The 538 emission band is similar to that reported for ZnS nanobelts [27] and is considered to result from vacancy or interstitial states [27,28].

### 3.4.3 Nanotubes and nanowires of CuS

We obtained nanotubes and nanowires formed by oriented growth in the case of CuS, all the nanostructures having a Cu:S ratio of 1:1 as revealed by EDAX analysis. EDAX spectrum of the CuS nanostructures is given in Figure 3.3c. The TEM image in Figure 3.7a shows nanotubes of CuS with a narrow hollow region, obtained after the removal of the hydrogel template. The inner diameter of the nanotubes is ~ 5 nm with length extending to a few hundreds of nanometers. The outer diameter is in the 20-30 nm range. The nanotubes are polycrystalline as found from electron diffraction as well as the TEM images. In Figure 3.7b is given the TEM image of a single nanotube of CuS with an outer diameter of ~ 20 nm and a length of ~ 300 nm, revealing that the walls of the nanotubes are formed from nanoparticles. The SAED pattern of the nanotube given as an inset in Figure 3.7b displays diffuse polycrystalline rings corresponding to the (101) and (107) planes of hexagonal CuS. A few spots are also seen along with rings. The hydrogel fibers act as templates leading to the formation of CuS nanotubes comprising nanoparticles, just as in the case of CdS and ZnS. The situation is comparable to that in oriented attachment growth and we do find evidence for oriented attachment of nanocrystals in the TEM images. The TEM image in Figure 3.7c reveals the formation of chains of short nanorods. The chains are formed by the assembly of CuS nanorods of ~ 40 nm length, the chains themselves extending over hundreds of nanometers.

Zhang *et al.* [29] have reported the formation of self-assembled rods of $Cu_2S$. Based on the TEM images they noted the rods to be the edges of $Cu_2S$ nanodisks that are aggregated with their hexagonal planes assembled together. A similar observation has been reported with hcp-Co nanocrystals by Alivisatos *et al.* [30], wherein magnetic nanodisks are stacked face-to-face giving rise to ribbons. Lee *et al.* [31]
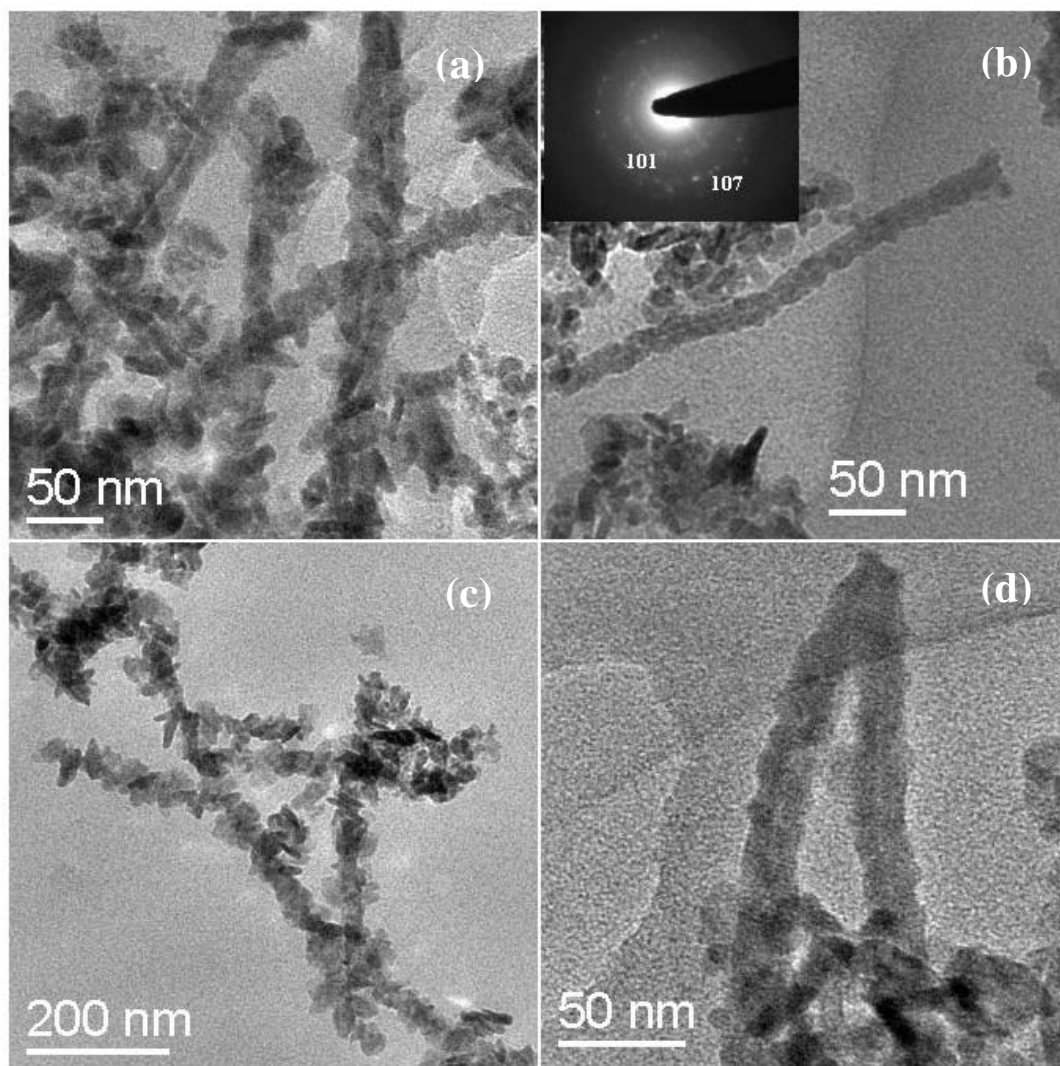
**Figure 3.7.** TEM images of (a) nanotubes of CuS obtained after the removal of the template; (b) a single nanotube; (c) chains of nanorods of CuS formed by self-assembly and (d) a V-shaped nanostructure of CuS formed by the attachment of two nanotubes. Inset in (b) is the corresponding SAED pattern.

have demonstrated that oriented attachment is an effective mechanism for the formation of chains of $SnO_2$ nanorods. They suggest that either collision of aligned nanocrystals in suspension, or rotation of misaligned nanoparticles in contact toward low-energy configurations might be responsible for the oriented attachments, and that anisotropic growth can be controlled by surfactants adsorbed preferentially on specific lattice planes of the crystal. In Figure 3.7d is given the TEM image of a V-shaped
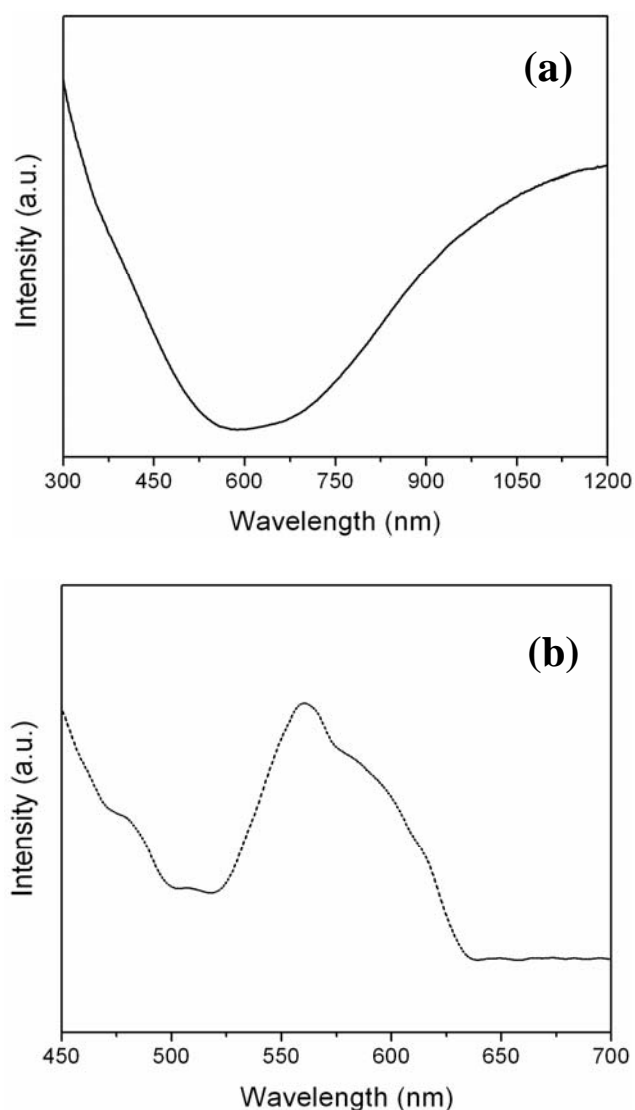
**Figure 3.8.** (a) Electronic absorption spectrum of CuS nanostructures and (b) PL spectrum of the nanostructures.

nanostructure of CuS, thought to be formed by the attachment of two nanotubes at their ends.

The electronic absorption spectrum of the CuS nanotubes given in Figure 3.8a shows the characteristic broad band of CuS in the near IR region, peaking at ~ 1200 nm. The band is attributed to an electron-acceptor state lying within the band gap [5]. A similar broad band has been reported for CuS nanocrystals [32]. The photoluminescence spectrum of CuS nanostructures given in Figure 3.8b shows a

_____

broad band peaking at 560 nm with a shoulder at 480 nm. Bulk CuS is reported to show a broad band centered at ~ 560 nm with a shoulder at ~ 587 nm [5]. The absence of any appreciable blue-shift of the emission bands of the CuS nanostructures prepared by us might be due to the formation of chains of nanorods by self-assembly.

The mechanism involved in the formation of nanotubes and nanorods of the metal sulfides in the presence of the hydrogelator is given in Figure 3.9.

### 3.5    Conclusions

By making use of a tripodal cholamide-based hydrogel, we have synthesized nanotubes and nanorods of CdS, ZnS and CuS. The nanotubes and nanorods are generally polycrystalline, suggesting the templating role of the hydrogel fibers and possible occurrence of oriented attachment. We have observed self-assembly of nanocrystals giving rise to chains of nanorods, a phenomenon similar to the growth of nanowires by oriented attachment.
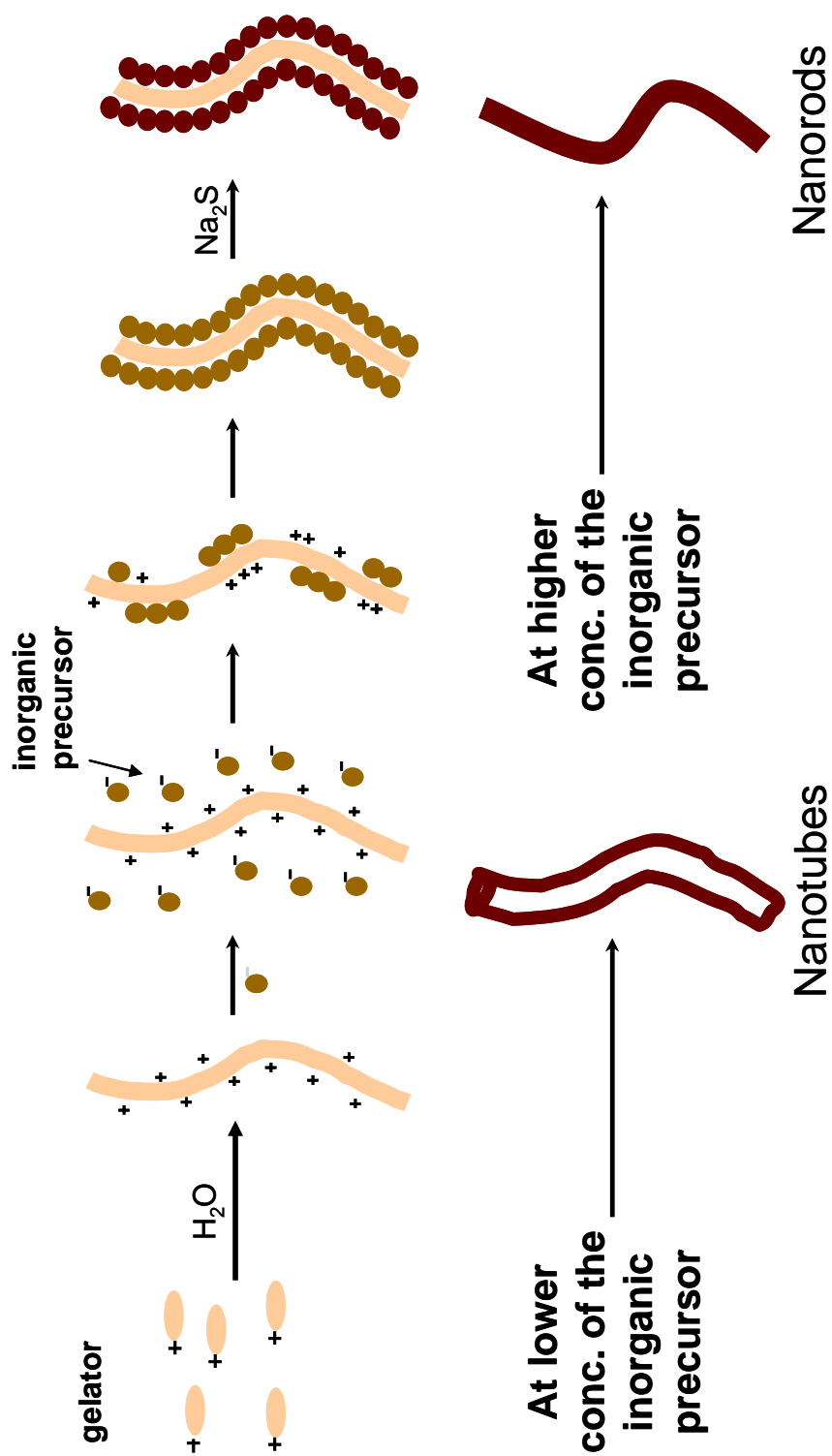
**Figure 3.9.** Schematic of the mechanism involved in the formation of nanostructures in the presence of hydrogelator.

## 3.6    References

[1] C. N. R. Rao, A. Muller, A. K. Cheetham (eds.), *The Chemistry of Nanomaterials*, Wiley-VCH, Weinheim, 2004.

[2] C. N. R. Rao, A. Govindaraj, *Nanotubes and Nanowires,* Royal Society of Chemistry, London, 2005.

[3] C. N. R. Rao, A. Govindaraj, F. L. Deepak, N. A. Gunari, M. Nath, *Appl. Phys. Lett.* 2001, **78**, 1853.

[4] Y. Xia, P. Yang, Y. Sun, Y. Wu, B. Mayers, B. Gates, Y. Yin, F. Kim, H. Yan, *Adv. Mater*. 2003, **15**, 353.

[5] F. L. Deepak, A. Govindaraj, C. N. R. Rao, *J. Nanosci. Nanotech.* 2002, **2**, 417.

[6] Y. Xiong, Y. Xie, J. Yang, R. Zhong, C. Wu, G. Du, *J. Mater. Chem.* 2002, **12**, 3712.

[7] R. L Penn, J. F. Banfield, *Science* 1998, **281**, 969.

[8] Z. Tang, N.A. Kotov, M. Giersig, *Science* 2002, **297**, 237.

[9] K.-S. Cho, D. V. Talapin, W. Gaschler, C. B. Murray, *J. Am. Chem. Soc.* 2005, **127**, 7140.

[10] J. H. Yu, J. Joo, H. M. Park, S. I. Baik, Y. W. Kim, S. C. Kim, T.J. Hyeon*, J. Am. Chem. Soc.* 2005, **127**, 5662.

[11] N. Pradhan, H. Xu, X. Peng, *Nano Lett.* 2006, **6**, 720.

[12] P. Terech and R. G. Weiss, *Chem. Rev.* 1997, **97**, 3133.

[13] K. Hanabusa, K. Hiratsuka, M. Kimura, H. Shirai, *Chem. Mater.* 1999, **11**, 649.

[14] S. Kobayashi, K. Hanabusa, M. Suzuki,M. Kimura, H. Shirai, *Chem. Lett.* 1999, 1077.

[15] J. H. Jung, Y. Ono, S. Shinkai, *Angew. Chem., Int. Ed.* 2000, **39**, 1862.

_____

[16] S. Kobayashi, N. Hamasaki, M. Suzuki, M. Kimura, H. Shirai, K. Hanabusa, *J. Am. Chem. Soc.* 2002, **124**, 6550.

[17] U. Maitra, S. Mukhopadhyay, A. Sarkar, P. Rao, S. S. Indi, *Angew. Chem., Int. Ed.* 2001, **40**, 2281.

[18] G. Gundiah, S. Mukhopadhyay, U. G Tumkurkar, A. Govindaraj, U. Maitra, C. N. R. Rao, *J. Mater. Chem.* 2003, **13**, 2118.

[19] U K. Gautam, M. Ghosh, C.N.R. Rao, *Chem. Phys. Lett.* 2003, **381**, 1.

[20] J. Huang, Y. Xie, B. Li, Y. Liu, Y. Qian, S. Zhang, *Adv. Mater.* 2000, **12**, 808.

[21] Y. Li, X. Li, C. Yang, Y. Li, *J. Mater. Chem.* 2003, **13**, 2641.

[22] B. Liu, G. Q. Xu, L. M. Gan, C. H. Chew, W. S. Li, Z. X. Shen, *J. Appl. Phys.* 2001, **89**, 1059.

[23] X. Jiang, Yi Xie, J. Lu, L. Zhu, W. He, Y. Qian, *Chem. Mater.* 2001, **13**, 1213

[24] N. Kumbhojkar, V V. Nikesh, A. Kshirgar, S. Mahamuni, *J. Appl. Phys.* 2000, **88**, 6260.

[25] P. Hu, Y. Liu, L. Fu, L. Cao, D. Zhu, *J. Phys. Chem B* 2004, **108**, 936.

[26] W-T Yao, S-H Yu, L. Pan, J. Li, Q-S Wu, L. Zhang, J. Jiang, *Small* 2005, **1**, 320.

[27] L-W Yin, Y. Bando, J-H Zhan, M-S Li, D. Golberg, *Adv. Mater.* 2005, **17**, 1972.

[28] Y. Jiang, X. M. Meng, J. Liu, Z. Y. Xie, C. S. Lee, S. T. Lee, *Adv. Mater.* 2003, **15**, 323.

[29] P. Zhang, L. Gao, *J. Mater. Chem,* 2003, **13**, 2007.

[30] V. F. Puntes, D. Zanchet, C. K. Erdonmez, A. P. Alivisatos, *J. Am. Chem. Soc.* 2002, **124**, 12874.

[31] E J. H. Lee, C. Riberio, E. Longo, E. R. Leite, *J. Phys. Chem. B* 2005, **109**, 20842.

[32] U K Gautam, B. Mukherjee, *Bull. Mater. Sci.* 2006, **29**, 1.

# CHAPTER 4

# Thin Films of Materials Formed at the

# Liquid-liquid Interface

## SUMMARY[*]

In this chapter of the thesis, the liquid-liquid interface as a medium to generate the nanocrystalline thin films of some metal chalcogenides such as ZnS, PbS, CdSe and CuSe has been discussed. The organic-aqueous interface provides a simple and elegant method of producing good crystalline films of important semiconducting materials. Ultra-thin films of ZnS have been prepared by the reaction of zinc cupferronate or zinc stearate in a toluene solution with an aqueous solution of $Na_2S$. The reaction at the interface yields excellent films which are generally single-crystalline. The effects of reaction parameters such as temperature and reactant concentration have been examined. Ultra-thin crystalline films of PbS have been obtained by the reaction of a toluene solution of lead cupferronate with the aqueous solution of $Na_2S$. Two-dimensional nanostructures in the form of ultra-thin crystalline films of CdSe and CuSe have been prepared at the organic-aqueous interface by reacting toluene solutions of metal cupferronates with an aqueous solution of N,N-dimethyl selenourea. The films have been examined using electron microscopy and optical spectroscopy. At lower concentrations of the reacting species, the CdSe films formed at the toluene-water interface at ~30 $^{\circ}$C consisted mostly of nanocrystals. With

increase in concentration as well as temperature, the interface reaction yielded thicker films which are mostly single-crystalline. We have studied the time-dependent growth of the CdSe film at the interface using UV-visible absorption spectroscopy. Ultra-thin films of CuSe formed at the toluene-water interface are generally single-crystalline. Apart from single-crystalline films of metal sulfides, we could obtain metalsulfide-bilayer such as CuS-CdS at the toluene-water interface by employing the respective metal cupferronates.

A time evolution study of the polycrystalline Au and CdS films as well as the single-crystalline CuS films carried out by employing atomic force microscopy (AFM) is presented. With the help of ultra-high vacuum AFM, the effect of mechanical vibrations on the formation of Au nanoparticulate films has been looked into. The rheological properties of thin films of CuS and CdS prepared at the toluene-water interface have also been investigated using a biconical bob interfacial rheometer.

## 4.1    Introduction

Ultra-thin films of metals as well as metal oxides and chalcogenides constitute an important class of two-dimensional nanomaterials with several useful applications [1,2]. Synthesis of thin films of semiconductor materials is of great importance because of their potential applications in optoelectronics and other areas [3]. Several methods have been developed to synthesize these thin films [4], and these include physical methods such as thermal evaporation, laser ablation, vacuum sputtering and molecular beam epitaxy (MBE). Unlike the physical methods, chemical methods such as electrodeposition generally employ milder conditions. In the recent past, the Langmuir-Blodgett technique has been widely used to prepare nanocrystalline thin films of metals and other materials at the air-water interface [5,6]. Typical examples of films of inorganic compounds prepared in this manner are those of $Fe_2O_3$ and CdS [7,8]. The air-water interface provides a constrained environment for the synthesis of nanocrystals in an organized manner which can be directly transferred as a film onto a substrate. However, there are very few reports in the literature, where the liquid-liquid interface has been employed to prepare nanocrystals and their aggregates. Recently the interface between two immiscible liquids has been exploited to prepare nanocrystalline ultra-thin films of various metals, metal oxides and other materials [9,10]. An important advantage of the study of materials formed at the liquid-liquid interface is that it provides a means to investigate the interface itself. The method primarily involves taking a metal organic compound in the organic layer and a reducing, sulfiding or an oxidizing agent in the aqueous layer. The reaction occurs at the interface giving rise to a film at the interface with several interesting features. Thus, ultra-thin films of closely packed nanocrystals of Au, Ag, alloys and CdS have been prepared at ambient temperature at the toluene-water interface [11-13]. Apart

from polycrystalline films, the interface reactions also yield substrate-free ultra-thin films of materials in single-crystalline form. For instance, ultra-thin films of CuS and CuO wherein the entire film is a two dimensional single-crystal have been reported [14]. We have been able to prepare ultra-thin films of ZnS, PbS, CdSe and CuSe at the toluene-water interface. While the ZnS, PbS and CuSe films are generally single-crystalline in nature, the CdSe films are partly single-crystalline. The metalsulfide-bilayer CdS-CuS could also be obtained at the toluene-water interface by employing the respective metal cupferronates.

### *Rheology of thin films*

The study of the structure and dynamics of two-dimensional films formed at fluid interfaces is currently an active area of research [15]. Besides being relevant to many industrial and biomedical applications, ultrathin films of nanomaterials also serve as model systems to probe the viscoelastic and flow behavior of 2D complex fluids. Many of the studies on the dynamics of 2D films extend mostly to Langmuir monolayers of insoluble surfactants, polymers and proteins [16]. Very few studies exist at present on the dynamic behavior of films of particles [17], and hardly any on nanocrystalline films [18]. This is because any rheological measurements on such films involve their deposition on soft substrates or their formation at fluid interfaces, the chemical strategies for which are not presently well developed. Moreover, the instrumentation to probe the viscoelastic interfacial properties of such 2D systems is not very well established. For a 2D film, the in-plane shear deformation at the interface arises due to a change in the shape of the surface, while keeping the area constant. For a viscoelastic surface, on applying a sinusoidal shear deformation $\gamma = \gamma_o$ exp(i$\omega$t) at an angular frequency $\omega$, and strain amplitude $\gamma_o$, an out of phase response

is obtained for the deviatoric part of the surface stress tensor defined as $\sigma = G^* \gamma$, where $G^* = G' + i\, G''$. Here $G'$ and $G''$ correspond to the interfacial storage and loss moduli which describe the elastic and viscous response of the film, respectively. In amplitude sweep experiments, an oscillatory shear of different strain amplitudes is applied at a constant angular frequency. At low strain amplitudes, $G'$ and $G''$ remain constant as expected in the linear viscoelastic regime. By applying an oscillatory shear of low strain amplitude at different angular frequencies, linear viscoelastic measurements probe the structural relaxation of the film. At large strain amplitudes, in amplitude sweep experiments, the viscoelastic response becomes nonlinear when $G'$ and $G''$ are no longer a constant, but decay monotonically.

## 4.2    Scope of the present study

Thin films of ZnS, a wide band gap (3.6 eV) material, have been used in injection lasers [19] and flat-panel displays [20]. Thin films of ZnS have been prepared by various methods such as spray pyrolysis [21], chemical bath deposition (CBD) [22], successive ion layer absorption and reaction (SILAR) [23], electrodeposition [24], MBE [25] and metal organic chemical vapor deposition [26]. Pawaskar et al. [27] have reported the preparation of a polycrystalline film of ZnS which is a mixture of cubic and hexagonal phases by reacting an aqueous solution of zinc sulfate with $H_2S$ dissolved in $CCl_4$. PbS thin films are used in IR detectors and LEDs [28,29]. Nanopyramidal particulate films of PbS have been obtained by treating an aqueous solution of lead nitrate with $CCl_4$ solution saturated with $H_2S$ [30]. Photochemically, by irradiating a solution containing lead acetate and sodium thoisulphate, PbS thin films have been obtained [31]. PbS thin films have also been prepared by techniques such as CBD [32], electrochemical atomic layer epitaxy [33]

and SILAR [34].

Thin films of CdSe have been a subject of extensive investigation due to their wide range of applications in solar cells, and transistors for photoelectronic and display devices [35-38]. Thin-films of CdSe, with a bulk band-gap of 1.74 eV, and high carrier mobility are an attractive alternative to Si thin films commonly used in solar cells and liquid-crystal display devices. Several methods have been employed for their preparation including CBD, electrodeposition, vacuum evaporation and spray pyrolysis [39-42]. Fabrication of a transparent CdSe solar cell with improved efficiency has been reported by Morel and coworkers [36], wherein a 1-2 $\mu$m thick film was deposited on a ZnO or $SnO_2$ substrate by physical vapor deposition. Hg-doped thin-films of CdSe prepared by CBD have been shown to exhibit improved conductivity [43]. Thin films containing both cubic and hexagonal phases of CdS and CdSe have been obtained by reacting an aqueous solution of cadmium carbonate with $H_2S/H_2Se$ dissolved in $CCl_4$ in a LB trough [44]. CuSe is another semiconducting material with potential applications in solar cells, superionic conductors, thermoelectric devices and microwave shield coatings [45-49]. CuSe thin-films, with *p*-type semiconducting behavior, have been prepared by Zainal *et al.* [50] using a combination of chemical precipitation and dip coating technique. Thin-films of CuSe have also been prepared by CBD [51,52]. Most of the synthesis techniques employed for the synthesis of thin-films are tedious and yield polycrystalline films. The defects and grain boundaries in polycrystalline films create trap states and act as carrier scattering centers, thus reducing the carrier mobility and transparency of the films. It is, therefore, desirable to develop suitable techniques that would yield thin films of these materials with relative ease and at the same time reduce the polycrystalline nature of the films.

In the present study, ultra-thin crystalline films of ZnS and PbS have been prepared by liquid-liquid interface method, by reacting cupferronates or stearates of Zn and Pb in toluene with an aqueous solution of $Na_2S$. We also report the preparation of ultra-thin films of CdSe and CuSe at the toluene-water interface, by the reaction of metal cupferronates dissolved in toluene with N,N-dimethylselenourea dissolved in water. Transmission electron microscope studies have revealed the films of ZnS, PbS and CuSe to be single-crystalline in nature. In contrast to other methods, the liquid-liquid interface method affords a one-step synthesis, enabling preparation of substrate-free single-crystalline thin films at room temperature. The films formed at the interface have been investigated by X-ray diffraction, electron microscopy and optical spectroscopy. The effect of varying reaction parameters such as temperature, time, organic solvent and the metal source on the morphology and growth of the films has been examined. Apart from the single-crystalline metal sulfide thin films at the organic-aqueous interface, we could also obtain bilayered thin film of metal sulfides such as CdS-CuS at the interface, one on top of the other.

So far, different characterization techniques such as X-ray diffraction, electron microscopy and optical spectroscopy were employed to study the thin films of various materials prepared at the organic-water interface. Here, we have used atomic force microscopy (AFM) to study in detail the morphology and growth of thin films of nanocrystalline Au and CdS films as well as the single-crystalline CuS films. Au, CuS and CdS thin films, each grown for contact times of 30 min, 60 min, 120 min and 180 min at the toluene-water interface were imaged in detail using the scanning probe microscope.

A recent model for the formation of films of gold nanoparticles proposed on the basis of a synchrotron x-ray scattering study assumes that 13-member magic-

clusters of 1.2 nm gold nanoparticles are first generated at the interface [53]. Although this model could explain out-of-plane and in-plane x-ray scattering data, direct evidence of the presence of 1.2 nm nanoparticle could not be obtained. Here we show that 1.2 nm gold particles are indeed formed on the basis of a high-resolution atomic force microscopy (AFM) study carried out in ultra-high vacuum (UHV), on films transferred onto silicon substrates from toluene-water interface. The reaction was carried out on an anti-vibration table which reduces macroscopic interdiffusion. On the other hand, reactions carried out on a table without anti-vibration fixtures resulted in thicker films.

### *Interfacial rheology*

Recently, there has been a considerable amount of interest in the nonlinear viscoelastic behavior of many 3D metastable complex fluids [54]. Under oscillatory shear, at large strain amplitudes, $G'$ decreases monotonically whereas $G''$ exhibits a distinct peak before it decays at larger strain amplitudes with the decay exponents of $G'$ and $G''$ in the ratio 2:1. It was also shown recently that many of the features observed for this nonlinear viscoelastic behavior in 3D also hold for an ultrathin film of metal nanoparticles [18] formed at fluid interfaces as well as Langmuir monolayers of sorbitan tristearate [55] indicating that the behavior is more general. Moreover, it was seen that the nonlinear viscoelastic measurements can be used successfully to extract the intrinsic structural relaxation time for insoluble surfactant monolayers, as in 3D systems. Hence it is relevant in this context to examine further, the generality of this behavior between 2D and 3D systems and extend our studies to nanocrystalline films. Two dimensional arrays of metal and semiconductor nanoparticles are known for their unique optical and electronic properties which find many novel applications

[56]. Potential applications of these arrays or films in electrical or optical devices would involve their transfer from fluid interfaces to a solid support. Since the quality of the transferred film depends crucially on the morphology as well as material properties, it is relevant to examine the structure and dynamics of these films formed at the interface through rheological measurements.

In the present study, the interfacial properties of ultrathin films of ~ 50 nm thickness formed by CdS nanoparticles, 3-5 nm in diameter at the toluene/water interface, as well as a single crystalline continuous film of CuS under both steady and oscillatory shear have been investigated using a biconical bob interfacial rheometer [57]. The study clearly reveals two distinct nonlinear viscoelastic behavior for the CdS and CuS films depending on the film morphology.

## 4.3    Experimental and related aspects

### 4.3.1    Synthesis

#### 4.3.1.1  Metal chalcogenide thin films

***ZnS and PbS films***

In order to prepare the ultra-thin films of ZnS, zinc cupferronate [$Zn(cup)_2$] and zinc stearate [$Zn(st)_2$] were used as the sources of zinc, and $Na_2S$ was used as the sulfur source. $Zn(cup)_2$ was prepared by stirring an aqueous solution of $Zn(CH_3COO)_2$ and cupferron taken in a molar ratio of 1:2, at 0 °C. The cupferronate so obtained was washed with water and air-dried. In a typical reaction, 5 mg of the dried $Zn(cup)_2$ (0.014 mmol) was dissolved in 50 mL of toluene by continuous ultrasonication for about 45 minutes. An aqueous solution of $Na_2S$ was prepared by dissolving 5.7 mg of the sulfide (0.07 mmol) in 30 mL of water (the ratio of Zn:S being 1:5). An excess of $Na_2S$ is necessary for the reaction to go to completion. The

_____

Na$_2$S solution was taken in a 100 mL beaker and ~ 10 mL of toluene was added to it, to make an interface. The organic part containing Zn(cup)$_2$ was then slowly added to the organic layer with the help of a dropper, along the sides of the beaker. After ~ 30 minutes of the reaction, the interface appeared white. The reaction was continued for 12 h, when a white colored film covered the entire interface. The film was gently lifted onto different substrates for characterization. The reaction was repeated by varying the reaction conditions such as temperature and time, the concentration of Zn(cup)$_2$, and the metal precursor. The other metal precursor used was zinc stearate, Zn(st)$_2$, prepared by adding an aqueous solution of Zn(CH$_3$COO)$_2$ to molten sodium stearate (the molar ratio being 1:2) at ~ 100 $^o$C. The Zn(st)$_2$ thus obtained was washed with hot water and dried.

For preparing PbS thin films, lead cupferronate [Pb(cup)$_2$] was used as the lead precursor. Pb(cup)$_2$ was prepared by mixing ice-cold aqueous solutions of Pb(CH$_3$COO)$_2$ and cupferron, just as in the case of Zn(cup)$_2$. In a typical preparation of the PbS film, 6 mg of Pb(cup)$_2$ (0.012 mmol) was dissolved in 50 mL of toluene by ultrasonication. 6 mg of Na$_2$S (0.077 mmol) was dissolved in 40 mL of water in a 250 mL crystallization dish. In this case also it is necessary to use an excess of Na$_2$S in order to obtain a good film at the interface. The Pb(cup)$_2$ solution was added to the organic layer with the help of a dropper. The interface turned black within a few seconds. The dish was left undisturbed for about 12 h for completion of the reaction.

### *CdSe and CuSe films*

Cadmium cupferronate and copper cupferronate were used as the sources of Cd and Cu respectively. The metal cupferronates were prepared by stirring together aqueous solutions of the respective metal acetates, M(CH$_3$COO)$_2$ (M=Cd or Cu) and

cupferron taken in a molar ratio of 1:2, at 0 °C. The cupferronates so obtained were washed with water and air-dried. The seleniding agent employed for the interface reactions was N,N-dimethylselenourea (DMSU). CdSe thin films were prepared as follows. In a typical reaction, 0.001 mmol of DMSU was dissolved in 30 mL of water in a beaker of diameter 5 cm. This was followed by the addition of 30 mL of toluene solution of 0.001 mmol of Cd(cup)$_2$, slowly along the sides of the beaker. For the complete dissolution of Cd(cup)$_2$ in toluene, the addition of a drop of *n*-butylamine was necessary. The interface attained a light brown color after a couple of hours. The reaction was continued for ~12 h, when a brown colored film covered the entire interface. The reaction was repeated by varying the reaction conditions such as temperature, and concentration of the reacting species. CuSe thin films were prepared by reacting the organic part, prepared by dissolving 0.001 mmol of Cu(cup)$_2$ in 30 mL of toluene, with the aqueous part prepared by the dissolution of 0.001 mmol of DMSU in 30 mL of water. pH of the medium was maintained at ~10 by the addition of a few drops of NaOH to the aqueous part initially. After ~12 h of the reaction, a dark grey colored film was formed at the interface. The metal selenide films were gently collected onto glass substrates for characterization.

### 4.3.1.2 Metal chalcogenide bilayer

Bilayer thin film of metal chalcogenides: CdS-CuS, was prepared at the toluene-water interface. Metal cupferronates were used as the metal precursors and Na$_2$S was used as the sulfur precursor. To obtain the CdS-CuS bilayer, CdS film was first prepared at the interface by reacting the toluene solution of Cd(cup)$_2$ with aqueous Na$_2$S solution. In a typical reaction, 0.004 mmol of Cd(cup)$_2$ dissolved in 10 mL toluene was reacted with 0.008 mmol of Na$_2$S dissolved in 10 mL water in a 25

mL beaker. The interface turned yellow, pointing to the formation of CdS film. A drop of *n*-octylamine was required for the complete dissolution of Cd(cup)$_2$ in toluene. After 10 h of the reaction, the toluene layer was replaced by fresh toluene. Such a process of washing the film formed at the interface was repeated several times. This was followed by the slow injection of 4 mL of 0.016 mmol aqueous Na$_2$S solution to the bottom layer, with minimal disturbance to the toluene layer and the interface. To the organic phase 10 mL of 0.003 mmol toluene solution of Cu(cup)$_2$ was added gently along the sides of the beaker. The color at the interface acquired a greenish tinge immediately, indicating the formation of CuS film. The film at the interface was left undisturbed for 10 h. The sulfide-bilayer formed at the interface was characterized by electron microscopy and optical spectroscopy techniques.

### 4.3.1.3   Atomic force microscopic study

The samples for AFM were prepared by halting the reaction at the interface after the specified times and transferring a portion of the film onto Si substrate.

*Au film*

For the preparation of ultra-thin films of Au at the interface, Au(PPh$_3$)Cl, synthesized based on a known procedure was used [58]. In a typical reaction, 5 mL of 0.76 mM Au(PPh$_3$)Cl toluene solution was allowed to stand in contact with 8 mL of 3.12 mM aqueous NaOH solution in a 25 mL beaker (3 cm diameter) at 35 $^{\circ}$C. Once the two layers stabilized, 250 μL of 16 mM THPC (tetrakishydroxymethylphosphoni-umchloride) was injected into the aqueous layer, with minimal disturbance to the toluene layer and the toluene-water interface. After 10 minutes, the reaction at the interface was stopped by carefully removing the toluene layer using a dropper. The pale yellow Au film formed at this stage of the reaction was lifted from the interface

onto a Si substrate. The above procedure was repeated for 30 min, 60 min, 120 min and 180 min of the reaction. Within 180 min we could see a brightly colored sturdy film at the interface.

### CdS film

Cadmium cupferronate $[Cd(cup)_2]$ and $Na_2S$ were used as the cadmium and sulfur precursors respectively, for the synthesis of CdS thin films at the interface. In a typical reaction, 10 mL of 0.3 mM toluene solution $Cd(cup)_2$ (containing *n*-octylamine) was slowly added to 10 mL of 0.6 mM aqueous $Na_2S$ solution in a 25 mL beaker. The interface turned yellow immediately. Reaction at the interface was arrested after 30 min by removing the upper toluene layer. The film at the interface was gently transferred onto a Si substrate for AFM studies. Likewise, CdS films formed at the interface after 60 min, 120 min and 180 min of the reaction were also collected onto Si substrates.

### CuS film

In order to prepare CuS thin film at the interface, we employed copper cupferronate $[Cu(cup)_2]$ and $Na_2S$ as the precursors of copper and sulfur respectively. In a typical reaction, 10 mL of 0.3 mM of $Cu(cup)_2$ in toluene was slowly added to 10 mL of 1.5 mM $Na_2S$ solution taken in a 25 mL beaker. The reaction between $Cu(cup)_2$ and $Na_2S$ imparted a green color to the interface within a couple of moments. After 30 min, reaction at the interface was halted by removing the toluene layer. Thin film from the interface was gently lifted onto a Si substrate for AFM. The procedure was repeated for 65 min, 120 min and 180 min of the reaction as described above.

**4.3.1.4   Effect of vibrations on the formation of gold nanoparticle aggregates**

The reaction was carried out in two identical 25 mL beakers by keeping one on a vibration isolation table and the other one on a regular laboratory table. In both the cases, 2 mL of 1.5 mM solution of triphenylphosphine gold chloride ($Au(PPh_3)Cl$) in toluene was allowed to stand in contact with 3.2 mL of 6.25 mM aqueous NaOH solution at room temperature. After the stabilization of the interface between the two liquids, 60 μl of 50 mM THPC was injected into the aqueous layer with minimal disturbance to the toluene layer. The reaction was terminated by taking out the toluene layer slowly after 15 minutes. After the termination of the reaction, the nanoparticle films formed at the interface were transferred onto silicon substrates (1 cm × 1 cm). The procedure was repeated for 1 hour and 2 hours of the reaction.

**4.3.1.5  Interfacial rheology**

*CdS film*

112 mL of 0.6 mM of $Na_2S$ in water (deionized, Millipore) was taken in a shear cell. The edge of the bicone was positioned at the air/water interface with a precision of 1 μm. 112 mL of 0.3 mM toluene solution of cadmium cupferronate containing 40 μl of *n*-octylamine was added carefully along the cone axle without disturbing the liquid-liquid interface. The temperature of the interface was maintained at 22 °C. To obtain a dense particulate film of CdS, reactions were carried out by increasing the concentration of cadmium cupferronate and $Na_2S$ to 1.2 mM and 2.4 mM respectively. The raw data was numerically analyzed after each measurement to determine the interfacial moduli and the interfacial steady shear viscosity, and takes into account the correction to the flow field from the bulk phases [8]. To estimate the particle size and the thickness of the film after the rheological measurements, the film

was transferred onto a Si or glass substrate as required.

***CuS film***

112 mL of 0.67 mM copper cupferronate, in toluene was added carefully along the cone axle to a subphase consisting of 112 mL of 2.88 mM of $Na_2S$ in water, with the bicone positioned at the interface as described above.

### 4.3.2    Techniques used for characterization

***X-ray diffraction:*** X-ray diffraction (XRD) patterns of the films were recorded using a Siemens 5005 diffractometer with Cu Kα radiation. The films were lifted onto glass slides for this purpose.

***Scanning electron microscopy:*** Scanning electron microscopy (SEM) images were obtained on LEICA S440i and FEI Nova 600 scanning electron microscopes. For this, the films were lifted onto a glass or Si substrate and sputter-coated with gold. Energy dispersive analysis of X-rays (EDAX) was performed with an Oxford microanalysis group 5526 system attached to the SEM employing a Si (Li) detector.

***Transmission electron microscopy:*** Transmission electron microscope (TEM) images were obtained with a JEOL JEM 3010, operating with an accelerating voltage of 300 kV. The film was lifted from the interface onto a glass slide, dried and subsequently redispersed in $CCl_4$ by ultrasonication. A drop of the suspension was then put on a holey carbon coated Cu grid and allowed to dry slowly. In the case of CdS-CuS bilayers, they were directed lifted onto the Cu grids from the interface.

***UV-Vis absorption spectroscopy and Photoluminescence:*** UV-Vis absorption measurements were carried out at room temperature with a Perkin-Elmer model Lambda 900 UV/Vis/NIR spectrometer using quartz cuvettes. A dispersion of the film in $CCl_4$ was used for these measurements. The growth of the CdSe films was

monitored *in situ,* using a specially designed quartz apparatus that allows the film to stand perpendicular to the probe beam. Photoluminescence (PL) measurements were carried out at room temperature with a Perkin-Elmer model LS50B luminescence spectrometer. The excitation wavelengths used depended on the samples studied. $CCl_4$ dispersions of ZnS and PbS, and toluene dispersions of CdSe and CuSe were used for the PL measurements.

***Optical profilometry:*** Thickness of the PbS film was measured using Wyko NT1100 optical profiler (Veeco, USA).

***Atomic force microscopy:*** AFM studies were carried out using an AFM set-up-Dimension 3100 SPM with NS-IV controller (Veeco, USA) in both contact as well as non-contact modes. The Au, CdS and CuS films were deposited onto Si substrates, directly from the interface after the fixed time periods, from the start of the reaction. High resolution ultra high vacuum (UHV) AFM measurements were carried out using an Omicron STM at $3 \times 10^{-10}$ mbar pressure in non-contact mode with a Si tip.

***Interfacial rheology:*** All rheological measurements were carried out using an Interfacial Rheology System (IRS) which consists of a commercial research rheometer (Physica MCR from Anton Paar) with an interfacial rheology cell based on bicone geometry [8]. The 2D films of CuS and CdS were prepared in-situ in the shear cell.

***Small angle X-ray scattering:*** Small angle x-ray scattering (SAXS) measurements were carried out for q values in the range 0.01 to 0.1 $\text{Å}^{-1}$ using Cu $K_\alpha$ radiation (0.154 nm) from a sealed tube X-ray generator (Bruker AXS, Nanostar) with cross-coupled Gobel mirrors and a three-pinhole collimation, operating at 45 kV, 35 mA. Data were collected using a 2D position sensitive detector (HI-STAR). Films formed at the toluene-water interface, were deposited on a mica sheet of thickness ~200 nm.

Typical exposure time lasted up to 10 hours. For background correction, the same mica substrate without the film was used.

## 4.4 Results and discussion

### 4.4.1 Metal chalcogenide thin films

*ZnS films*

In Figure 4.1a and 4.1b are given the photographs of ZnS and PbS thin films respectively, seen floating at the toluene-water interface.

Figure 4.2a displays the XRD pattern of a ZnS film obtained by the reaction of 5 mg of $Zn(cup)_2$ in 50 mL of toluene with 5.7 mg of $Na_2S$ in 30 mL of water at ~ 30 $^oC$ for 12 h. The diffraction peaks observed at $26.9^o$, $47.5^o$ and $56.7^o$ correspond to those of wurtzite ZnS (JCPDS no. 36-1450; a = 3.82 Å, c = 6.257 Å). The broad hump in the pattern in the $15^o$–$40^o$ range is due to the glass substrate on which the film was placed. To examine the composition of the film, we recorded the EDAX spectra at various parts of the film. Figure 4.2b shows the EDAX spectra, establishing the Zn:S ratio to be 1:1 in the entire film.

A SEM image of the ZnS film is shown in Figure 4.3a. It can be seen that the film extends over a wide area, covering several micrometers of the substrate. Some rod-like features are also seen on the surface of the film. Interestingly, we observe that the two sides of the film facing the organic and the water layer are distinctly different in appearance. Shown in Figure 4.3b is a SEM image of the side facing the water layer. This side of the film is much smoother, and also the rod-like features seen in Figure 4.3a are absent. We also see a few cracks, probably resulting from the difference in the wettability in the two solvents. A typical TEM image of the film is given in Figure 4.3c. Notably, we do not see crystals embedded in the

_____
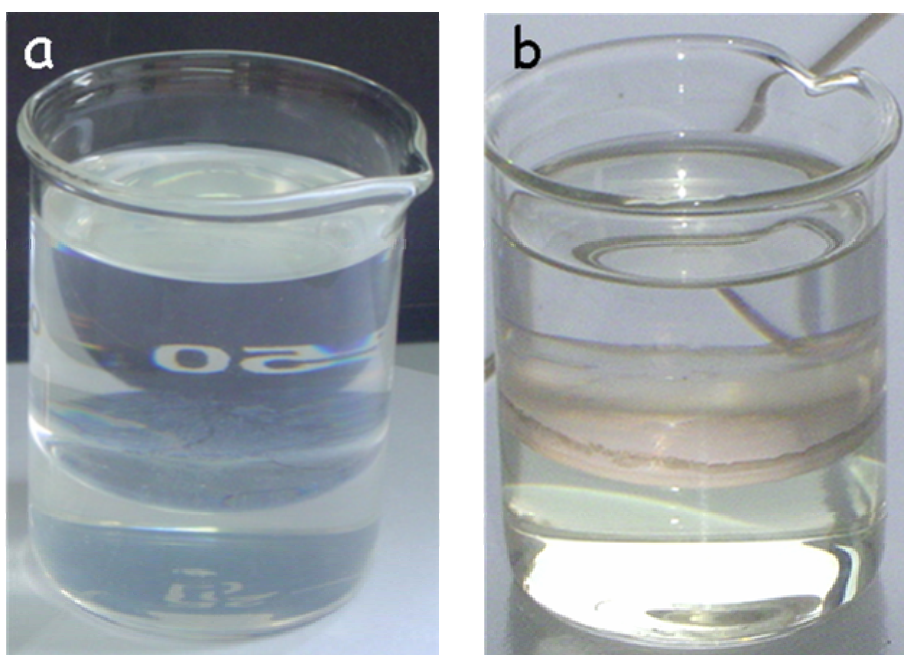


**Figure 4.1.** Thin films floating at the toluene-water interface (a) ZnS and (b) PbS the film.
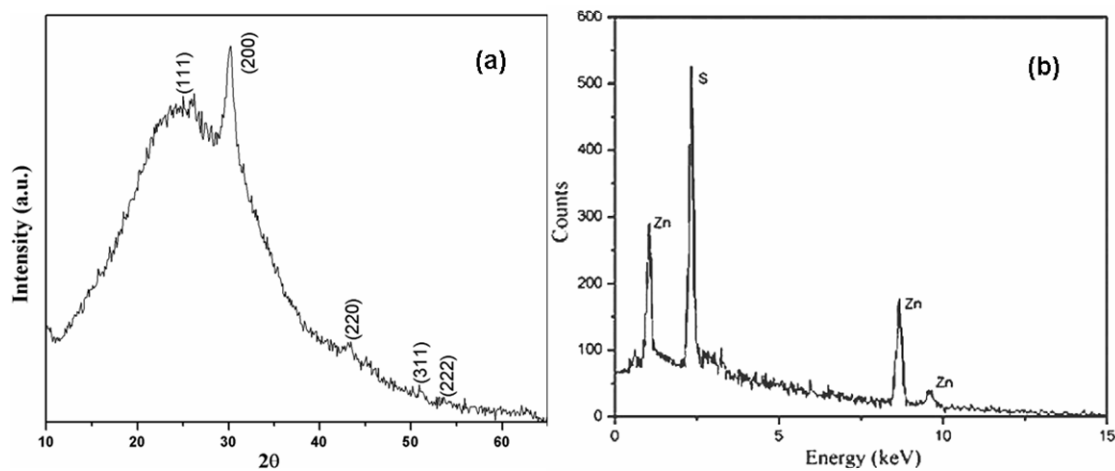


**Figure 4.2.** (a) XRD pattern of the ZnS film obtained by the reaction of 5 mg of Zn(cup)$_2$ in 50 mL of toluene at ~30 $^o$C for 12 h and (b) EDAX spectrum of the film.

film. Instead, the film appears to be part of a single crystal. The film was indeed found to be single-crystalline from the high-resolution electron microscopy (HREM) and selected area electron diffraction (SAED). Figure 4.3d shows an HREM image of the film. The lattice spacing of 0.32 nm (literature value: 0.33 nm) corresponds to the (100) planes of hexagonal ZnS. The Bragg spots in the SAED pattern (inset in Figure

4.3d) conform to the 0001 zone axis of hexagonal ZnS and confirm the single-crystalline nature of the film. It appears that the growth of the film occurs along the AB plane of the crystal. Along with the single-crystalline film, we also see rod-like structures, although few in number (see the TEM images in Figures 4.3e and 4.3f). These structures (also observed in the SEM image in Figure 4.3a) consist of nanocrystals of ZnS, as can be seen from the TEM images. The SAED pattern of the rod-like structures, shown as an inset in Figure 4.3f, confirms their identity. It is likely that the organic component of the cupferronate complex sticks to the surface of the film to form such nanostructure assemblies. Due to the absence of the organic component in the aqueous layer, the side of the film facing the aqueous layer appears clean and smooth.

Figure 4.4a shows a TEM image of the film obtained by reacting 5 mg of $Zn(cup)_2$ in 50 mL of toluene with 5.7 mg of $Na_2S$ at ~ 80 $^o$C. As seen from the image, the high temperature employed in the reaction breaks the film, possibly due to the increased turbulence and interdiffusion between the two layers. Such an effect had been observed in the case of CuS thin films as well [14]. The SAED pattern of the film is shown in the inset in Figure 4.4a. At lower concentrations of the reactant, the films obtained become porous in nature. Figure 4.4b shows a SEM image of the film obtained by reacting 1 mg of $Zn(cup)_2$ in 50 mL of toluene at ~ 30 $^o$C. ZnS films with extremely smooth surfaces were obtained by using $CCl_4$ as the organic solvent instead of toluene. Figure 4.4c shows a SEM image of a ZnS film obtained at ~30 $^o$C by taking 5 mg of $Zn(cup)_2$ in $CCl_4$. A TEM image of the film is shown in Figure 4.4d. The diffraction spots observed in the SAED pattern (inset) establish the identity and single-crystalline nature of the film. Due to the higher density of $CCl_4$, the organic layer was at the bottom, while the top layer was the aqueous $Na_2S$ solution. The rod-
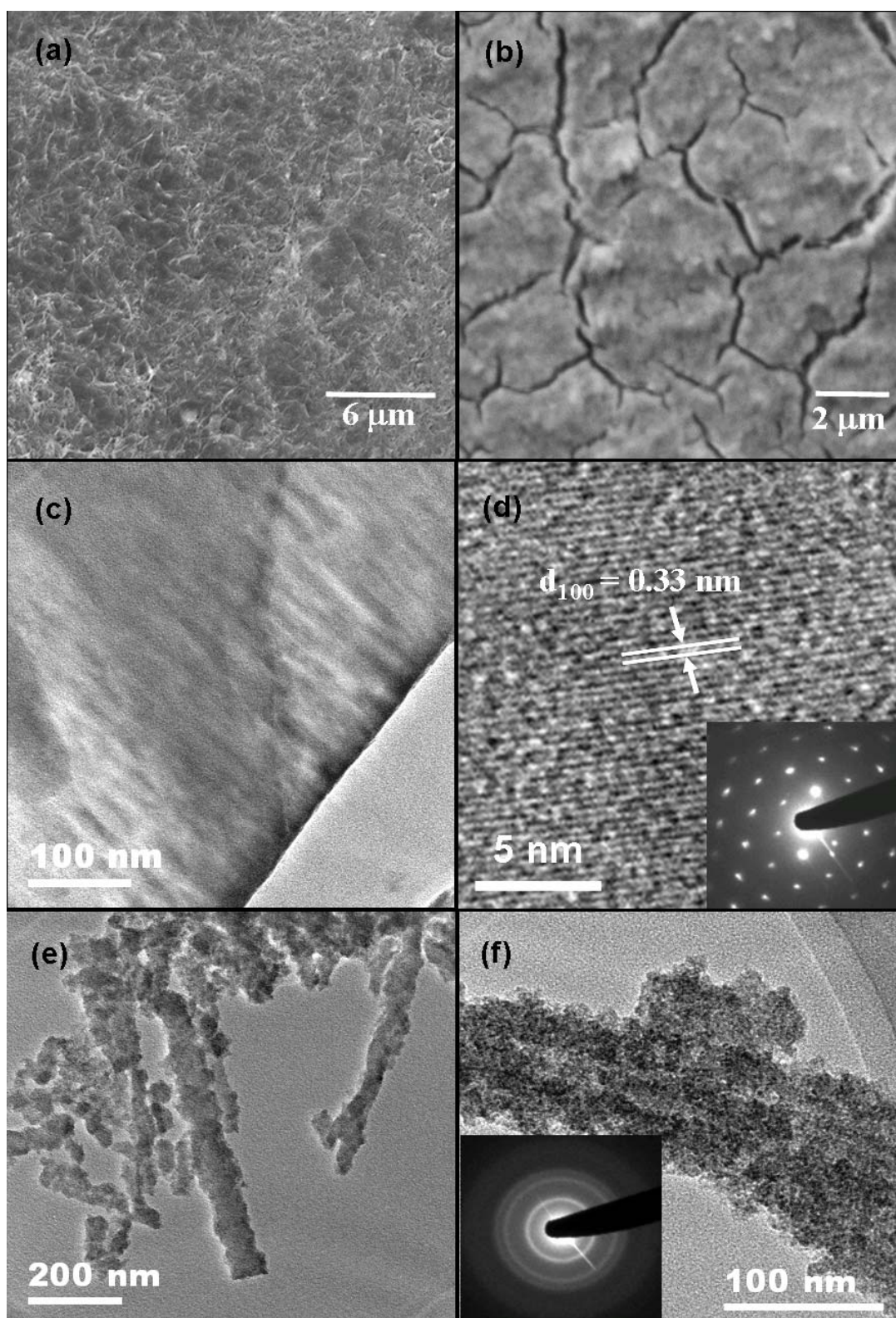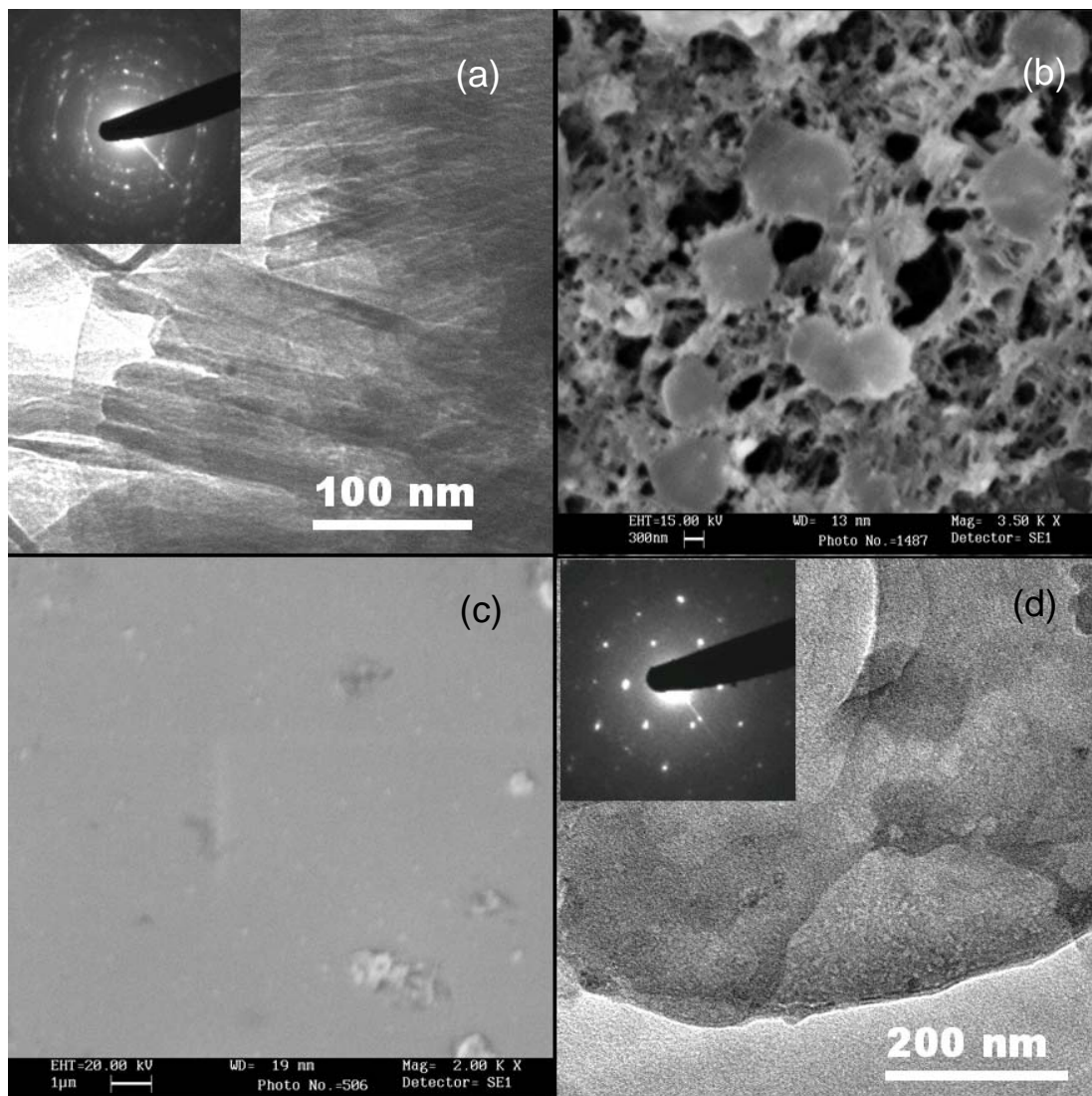
**Figure 4.3.** ZnS film obtained by the reaction of 5 mg of Zn(cup)$_2$ in 50 mL of toluene at ~30 $^o$C. SEM images showing the side facing the (a) toluene, (b) water layers; (c) TEM image of the film; (d) HREM image of the ZnS film showing the (100) planes of hexagonal ZnS. (e), (f) TEM images of rod-like assemblies of ZnS nanocrystals.

**Figure 4.4.** (a) TEM image showing a broken ZnS film, obtained by the reacting 5 mg of Zn(cup)$_2$ in 50 mL of toluene at ~80 $^o$C. Inset is the SAED pattern of the film; (b) SEM image of a ZnS film obtained by reacting 1 mg of Zn(cup)$_2$ in 50 mL of toluene at ~30 $^o$C; (c) SEM image of the ZnS film obtained at ~30 $^o$C by reacting 5 mg of Zn(cup)$_2$ in 50 mL of CCl$_4$, and (d) the corresponding TEM image of the film. Inset is the SAED pattern of the film.

like features obtained by using toluene as the solvent are absent here. This observation shows that the rod-like nanostructures may get formed at the additional nucleation sites provided by the organometallic precursor.

The ZnS films formed at the interface were further analyzed using UV-Visible and photoluminescence spectroscopy (PL) techniques. Figure 4.5a(i) shows the UV-Vis absorption spectrum of a ZnS film obtained by reacting 5 mg of $Zn(cup)_2$ in 50 mL of toluene at ~30 $^o$C for 12 h. The absorption band at ~320 nm is close to that of bulk ZnS which absorbs at ~340 nm [59]. The PL spectrum of the ZnS film in Figure 4.5a(ii) displays a broad emission band centered at ~425 nm, which can be attributed to the presence of sulfur vacancies in the ZnS lattice [60]. Figure 4.5b shows the absorption spectrum of a ZnS film obtained by reacting 5 mg of $Zn(cup)_2$ in 50 mL of toluene at ~30 $^o$C for 1 h, and 10 h. An absorption band is observed at ~285 nm after 1 h of the reaction, which is considerably blue-shifted from that of the bulk. After 10 h of the reaction, the absorption intensity increases and the peak gets red-shifted to ~320 nm, due to the increased thickness of the film.

We obtained ultra-thin films of ZnS by using $Zn(st)_2$ as the Zn source as well. Unlike the films described so far, portions of these films were polycrystalline. The two TEM images displayed in Figure 4.6 show a single-crystalline portion as well as a poly-crystalline portion of a ZnS film obtained by reacting 5.4 mg of $Zn(st)_2$ dissolved in 30 mL toluene with 6.7 mg of $Na_2S$ (the ratio of Zn:S being 1:10) dissolved in 30 mL water at ~ 80 $^o$C. The corresponding SAED patterns are shown as insets. Reactions carried out at lower temperatures were incomplete.
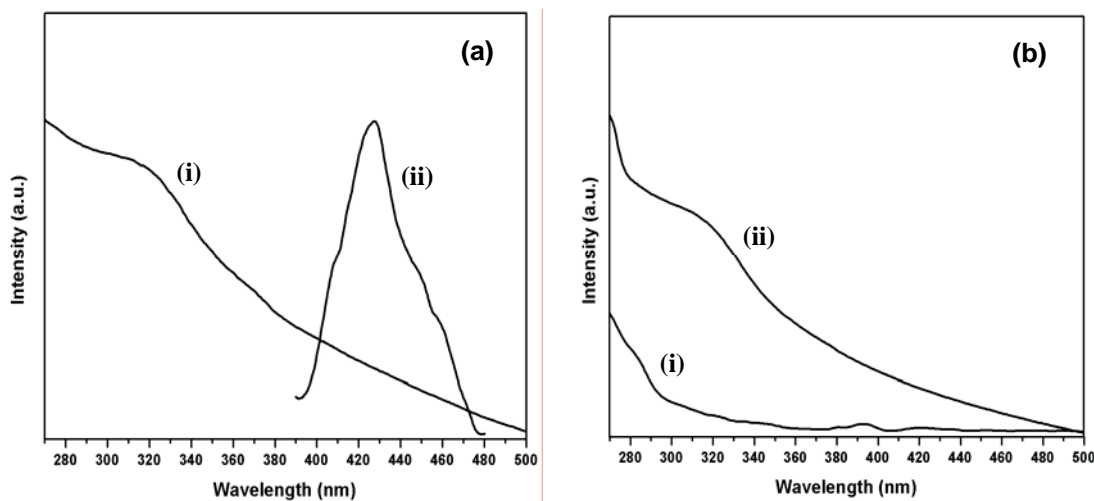
**Figure 4.5.** (a) (i) UV-Vis absorption spectrum and (ii) PL spectrum of ZnS film obtained by reacting 5 mg of Zn(cup)$_2$ in 50 mL of toluene at ~30 $^o$C for 12 h; (b) UV-Vis absorption spectra of the ZnS film obtained after (i) 1 h and (ii) 10 h of the reaction.
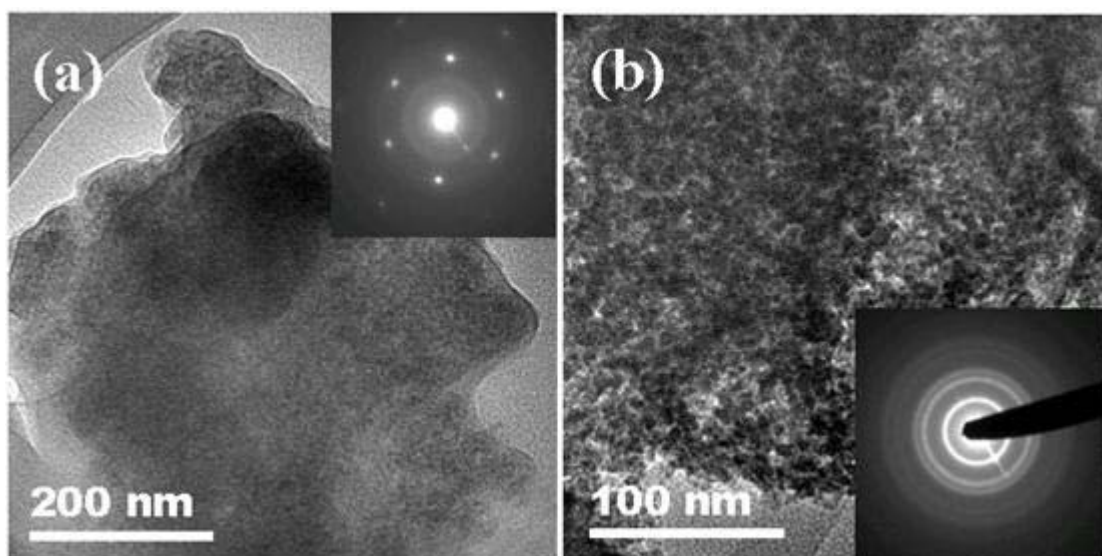


**Figure 4.6.** TEM images of ZnS films obtained by reacting 5 mg of Zn(st)$_2$ in 50 mL of toluene at ~80 $^o$C: (a) a continuous single-crystalline and (b) a polycrystalline film. Insets are the corresponding SAED patterns.

*PbS films*
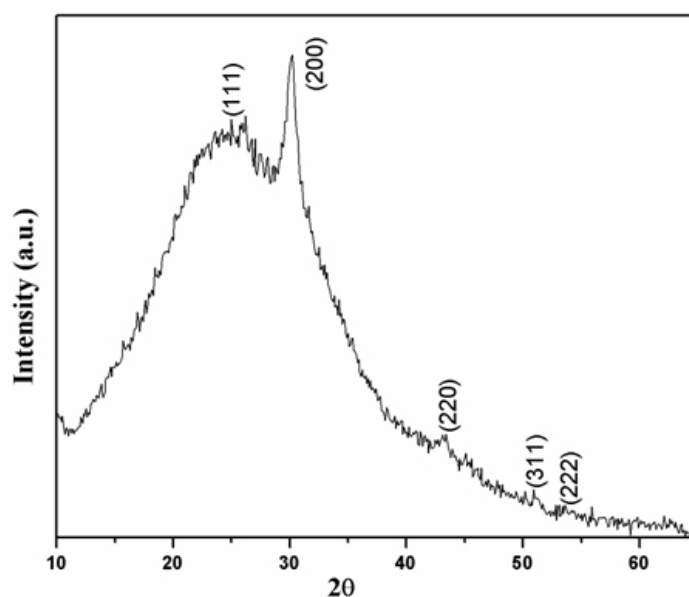


**Figure 4.7**. XRD pattern of a PbS film obtained by the reaction of Pb(cup)$_2$.

We could prepare ultra-thin films of PbS at the toluene-water interface. An XRD pattern of the film obtained by reacting 6 mg of Pb(cup)$_2$ with 6 mg of Na$_2$S at ~ 30 °C for 12 h is displayed in Figure 4.7. All the peaks in the pattern could be indexed on cubic PbS phase (JCPDS no. 05-0592; a = 5.936Å). The broad hump observed in the 10°- 40° range is due to the glass substrate.  EDAX analysis showed the Pb:S in the film to be close to 1:1.

A SEM image of the PbS film is shown in Figure 4.8a, revealing its smooth and continuous nature, extending over several square micrometers. Figure 4.8b shows a representative TEM image of the film. The SAED pattern in the inset is an indication of the single-crystalline nature of the film. An HREM image of the film is shown in Figure 4.8c. The separation between the lattice fringes is found to be 0.32 nm, corresponding to the separation between the (200) planes of cubic PbS. However, we also observed nanocrystals of PbS embedded in some parts of the film, as shown

in Figure 4.8d. Thickness of the PbS thin film was observed to be of the order of 4 nm measured using an optical profiler.
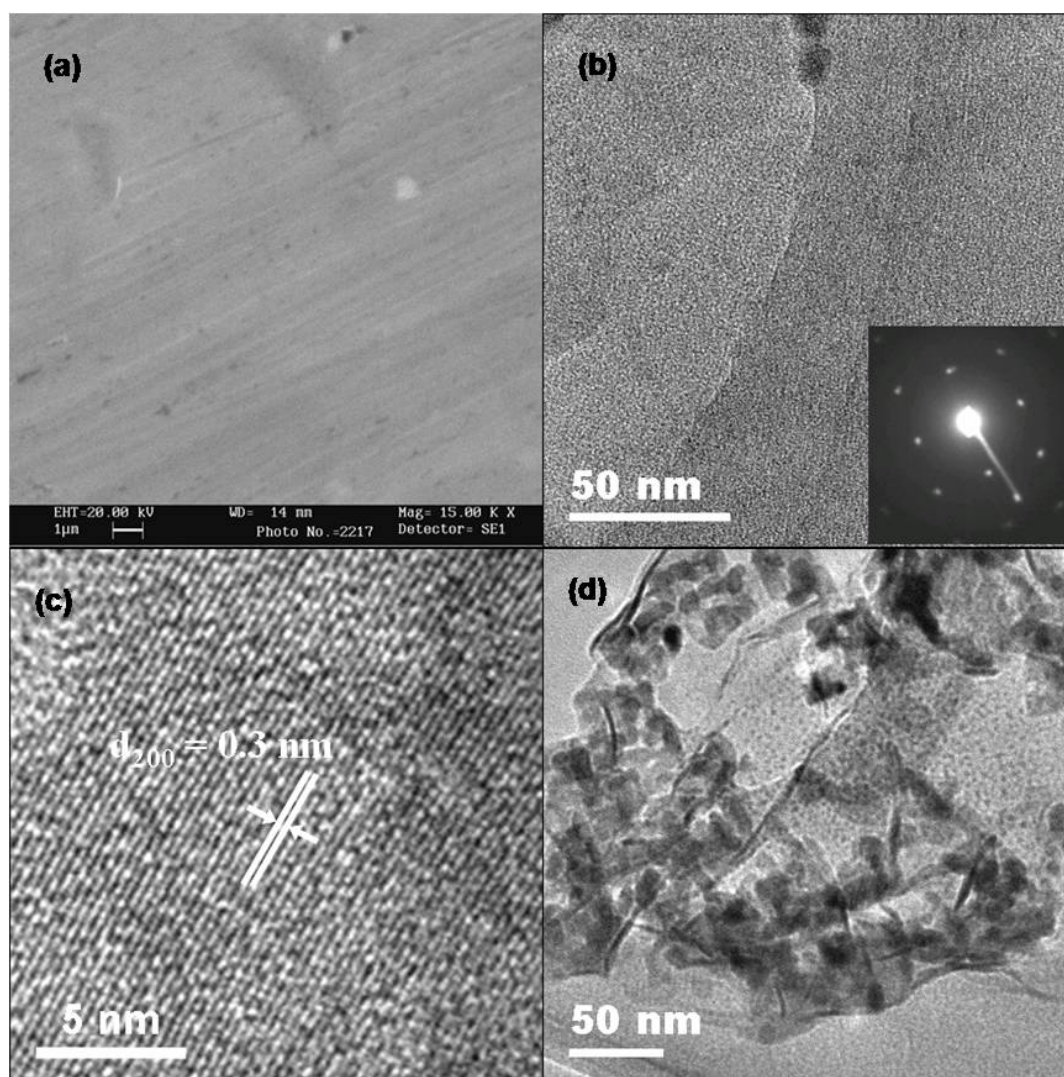


**Figure 4.8.** (a) SEM image of PbS film obtained by reacting Pb(cup)$_2$ in toluene with aqueous Na$_2$S solution at ~30 $^o$C, showing its smooth and continuous nature; (b) TEM image of the PbS film. Inset is the SAED pattern. (c) HREM image of the film; (d) TEM image of the film, showing nanocrystals of PbS.

The PbS film was further analyzed by UV-Vis absorption spectroscopy. The spectrum showed two absorption bands, one at ~ 270 nm and the other one at ~ 285 nm (Figure 4.9). The first band at the lower wavelength could be attributed to the higher order excitonic transition involving lead energy levels, and the second one to a transition between sulfur occupied energy states and lead unoccupied energy states [61]. However, these bands show blue-shifts compared to the values reported in the literature for PbS nanocrystals [62].
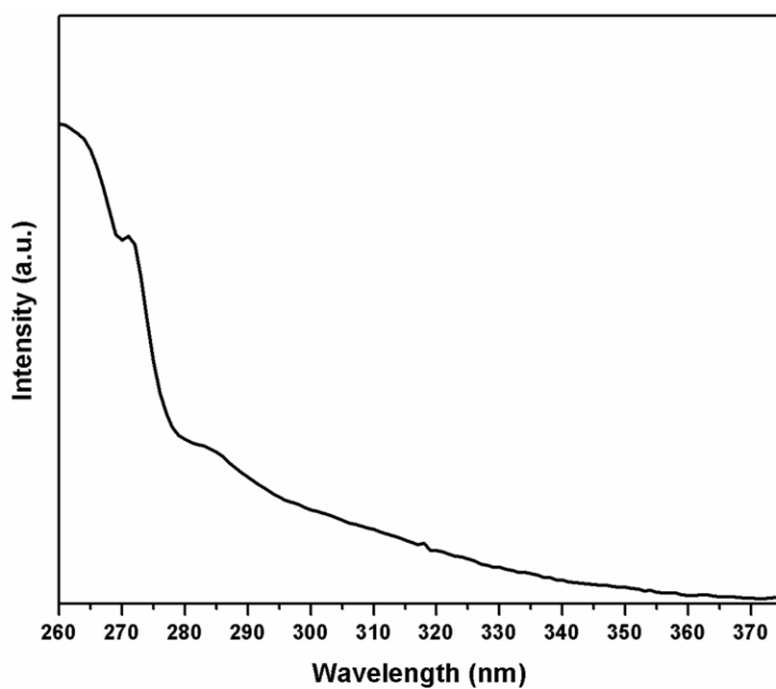


**Figure 4.9.** UV-Vis absorption spectrum of the PbS film

*CdSe and CuSe films*
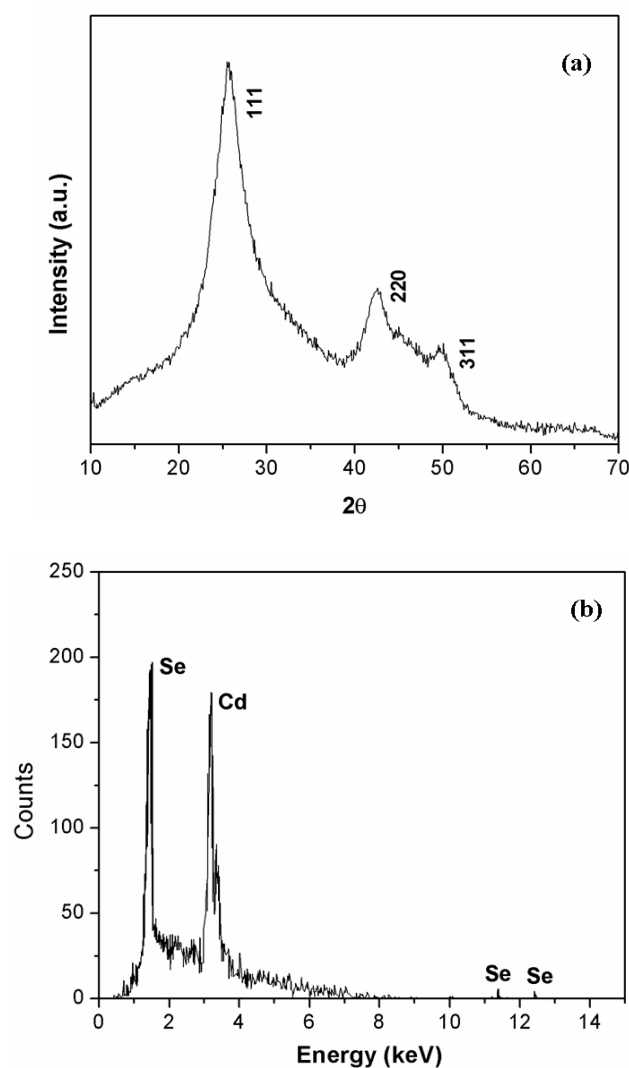


**Figure 4.10.** (a) XRD pattern of a CdSe film obtained by the reaction of 30 mL of 0.001 mmol of Cd(cup)$_2$ in toluene with 0.001mmol of DMSU dissolved in 30 mL water at ~30 $^{\circ}$C in a beaker of diameter 5 cm; (b) EDAX spectra of the film.

The reaction of 0.001 mmol of Cd(cup)$_2$ in 30 mL of toluene with 0.001 mmol of DMSU in 30 mL of water at ~ 30 $^{\circ}$C for 12 h yielded cubic CdSe at the toluene-water interface, as evidenced by the X-ray diffraction measurements. Figure 4.10a shows the XRD pattern of the CdSe film with reflections corresponding to those of cubic CdSe (JCPDS card no.19-0191, a = 6.08 Å). EDAX measurements (Figure 4.10b) on different regions of the film confirmed the composition of the film to be
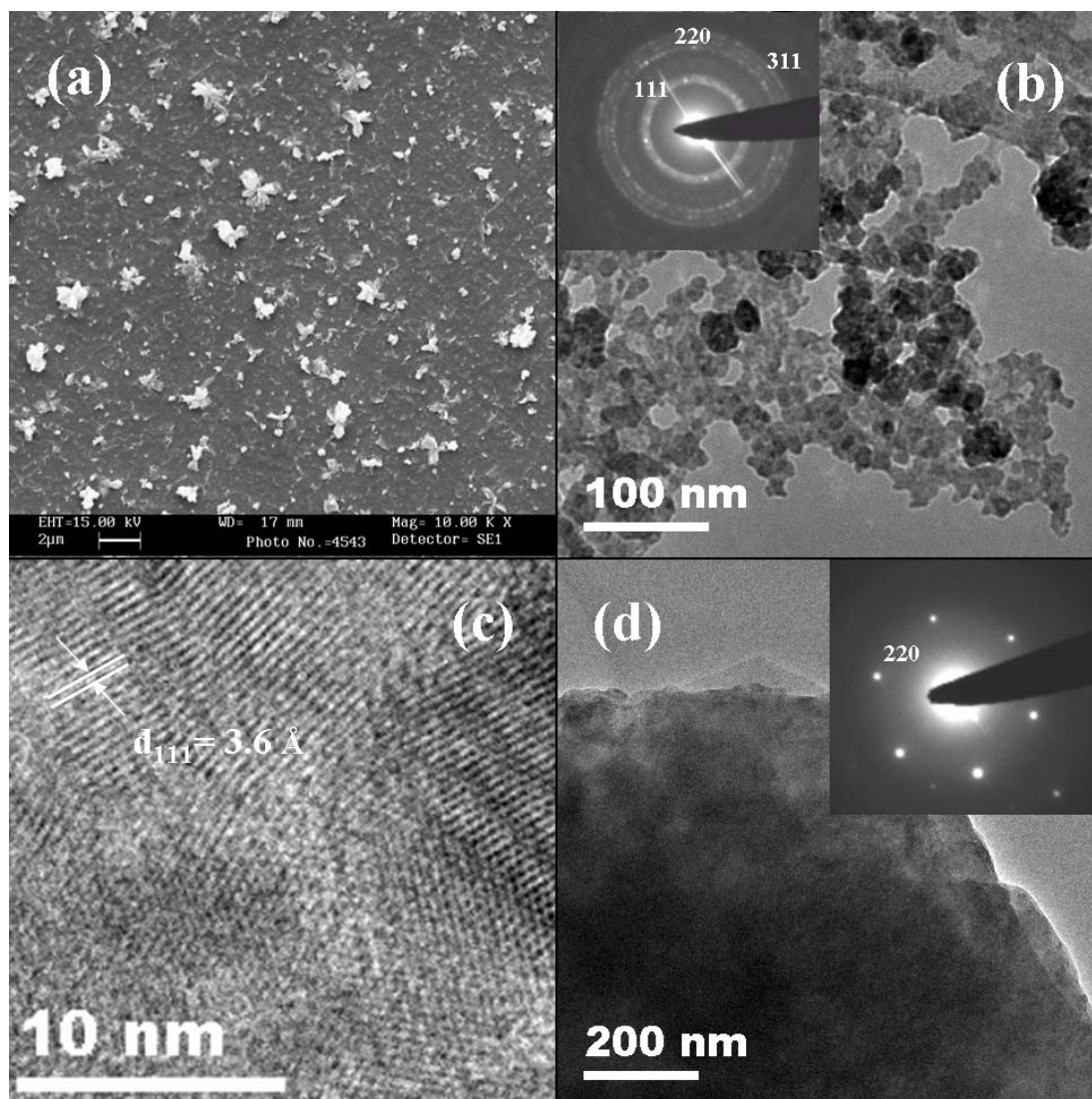
**Figure 4.11.** (a) SEM image of the CdSe film obtained by the reaction of 30 mL of 0.001 mmol toluene solution of Cd(cup)$_2$ with 0.001mmol aqueous solution of DMSU at ~30 $^{\circ}$C in a beaker of diameter 5 cm; (b) TEM image of the film showing particles of CdSe. Inset is the corresponding SAED pattern; (c) HREM image of the CdSe film showing the (111) planes of cubic CdSe and (d) TEM of a single-crystalline portion of the same film. SAED pattern of the film is given as the inset.

homogenous throughout with Cd:Se ratio of 1:1.

The interface reaction yielded a CdSe film that covers the entire interface area of ca. 20 cm$^2$. The morphology and the microstructure of this film were investigated using SEM and TEM. A SEM image of the film is shown in Figure 4.11a. As seen in the image, the CdSe film is continuous and extends over the entire surface of the substrate. Small clusters of particles are also seen on the surface of the film, identified as CdSe by EDAX measurements. TEM images revealed the film to be made up of CdSe nanocrystals with diameters ranging from 8 nm to 20 nm as shown in Figure 4.11b. If we assume the reaction to be complete and the entire interface to be covered by the film, the thickness of the film works out to be ~18 nm (amount of Cd(cup)$_2$ used for the reaction =0 .001 mmol, area of the interface = 20 cm$^2$, volume of a cubic CdSe unit cell = 224x10$^{-3}$ nm$^3$). The inset in Figure 4.11b gives the SAED pattern showing rings corresponding to the (111), (220) and (311) planes of cubic CdSe. Individual particles constituting the film are single-crystalline as was evidenced by HREM images. HREM images show the (111) lattice planes of cubic CdSe separated by a distance of 0.36 nm, as seen in Figure 4.11c. What is interesting is that along with the films comprising the nanocrystals, there are some portions of the film which are single-crystalline in nature. The presence of nanocrystals in addition to the film can be understood as follows. Since the films themselves comprise nanocrystals, it is possible that any nanocrystals formed after a film of optimal thickness is formed (by the diffusion controlled reaction) get deposited on or around the film. A TEM image of a single-crystalline portion of the film is shown in Figure 4.11d. The corresponding SAED pattern shown in the inset of Figure 4.11d also establishes the single-crystalline nature of the film.

In Figure 4.12, we show the UV-visible absorption spectrum of a CdSe film.

An absorption onset observed at ~700 nm corresponds to bulk CdSe. Two additional bands observed around 485 nm and 535 nm correspond to higher order transitions [63]. The photoluminescence spectrum of the film (inset in Figure 4.12) shows an emission peak centered at 805 nm, which is marginally red-shifted due to surface defects.
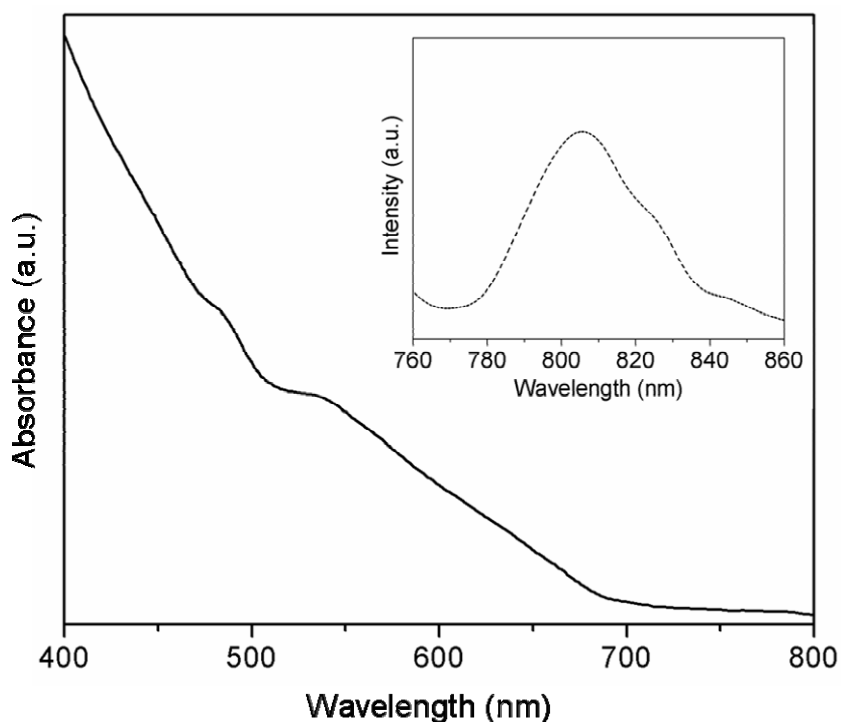


**Figure 4.12.** UV-Visible absoprtion spectrum of a CdSe film obtained by the reaction of 0.001 mmol toluene solution of Cd(cup)$_2$ with 0.001 mmol of aqueous DMSU solution at ~30 $^o$C. Inset is the PL spectrum of the film.

An increase in the concentration of the reacting species resulted in a faster growth of the films, which are likely to be thicker. When the reaction was carried out using 0.003 mmol of Cd(cup)$_2$ in 10 mL of toluene and 0.003 mmol of DMSU in 10 mL of water at ~30 $^o$C in a beaker of diameter 2.5 cm, we observed formation of the film at the interface within an hour of the addition of the reactants. The UV-visible

absorption spectrum of this film was similar to the one shown in Figure 4.12, though with higher absorbance values due to the increased thickness of the film. TEM images show that the film is composed largely of single-crystalline portions (~60%) along with the nanoparticles. A TEM image of the single-crystalline portion of the film is given in Figure 4.13. The corresponding SAED pattern of the film is shown as the inset in Figure 4.13. The Bragg spots in the SAED pattern correspond to the (111) and (311) planes of cubic CdSe. When the concentration of the reactants was reduced (to obtain films of estimated thickness 4 nm and 8 nm), we did not obtain any film at the interface.
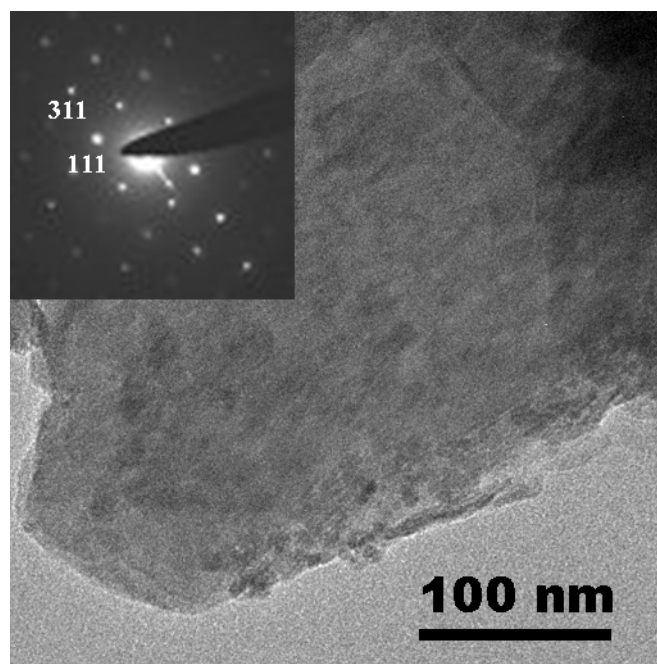


**Figure 4.13.** TEM of a single-crystalline portion of the CdSe film obtained by the reaction of 0.003 mmol of Cd(cup)$_2$ dissolved in 10 mL of toluene with 0.003 mmol of DMSU dissolved in 10 mL of water at ~30 $^{\circ}$C in a beaker of diameter 2.5 cm. Inset is the SAED pattern of the film

_____
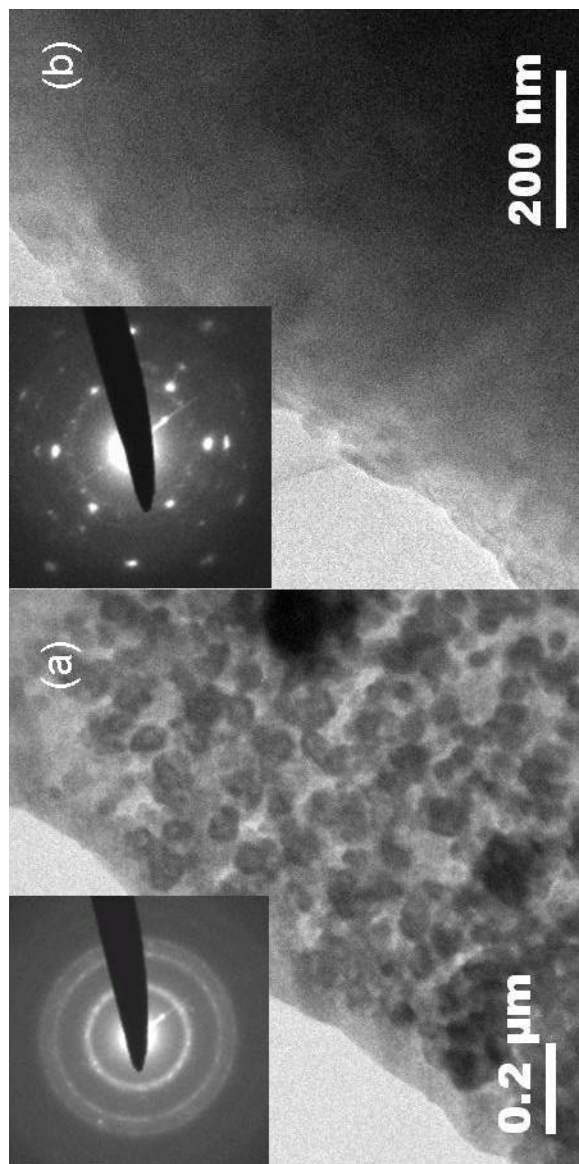


**Figure 4.14.** TEM images of (a) the CdSe film obtained by reacting 10 mL of 0.003 mmol toluene solution of Cd(cup)$_2$ with 10 mL of 0.003 mmol aqueous DMSU solution at ~70 °C, showing fused nanocrystals and (b) a single-crystalline portion of the same CdSe film. The corresponding SAED patterns are given as the insets.

We also carried out the interface reaction at a temperature of ~70 $^{\circ}$C for different concentrations of the reacting species, maintaining all the other conditions the same. At the higher temperature, for a given concentration of the reacting species, the CdSe particles had a tendency to assemble together to yield one-dimensional rod-like nanostructures, though the size of the particles remained nearly the same. Recall that the reactions carried out at lower temperatures yielded nanocrystals fused in a chaotic manner. Reactions carried out with higher concentration of the reactant species at higher temperatures resulted in the favorable formation of single-crystalline CdSe films. Figure 4.14a shows a TEM image of the CdSe film with fused nanocrystals, obtained by the reaction of 0.003 mmol toluene solution of Cd(cup)$_2$ with 0.003 mmol aqueous DMSU solution at ~70 $^{\circ}$C. The process of fusion of nanocrystals is facilitated at ~70 $^{\circ}$C and hence there is greater proportion of the single-crystalline film compared to isolated particles, as against the reactions carried out with same reactant concentrations but at lower reaction temperature. A TEM image of a single-crystalline portion of the film is given in Figure 4.14b. The SAED pattern (inset in the figure) clearly indicates its single-crystalline nature.

We have studied the time-dependent growth of the CdSe films formed at 30 $^{\circ}$C at the toluene-water interface using UV-visible absorption spectroscopy. Shown in Figure 4.15a are the UV-visible absorption spectra of the CdSe films recorded *in situ* with increasing reaction time, obtained using 30 mL of 0.214 mmol toluene solution of Cd(cup)$_2$ and 30 mL of 0.214 mmol aqueous DMSU solution. The spectra show an increase in the absorption intensity with reaction time indicating the growth of the film. All the spectra show an absorption onset at ~700 nm corresponding to the bulk band-gap of CdSe and two higher order absorption bands at 485 nm and 535 nm. These features were seen in the spectrum recorded even after three minutes of the
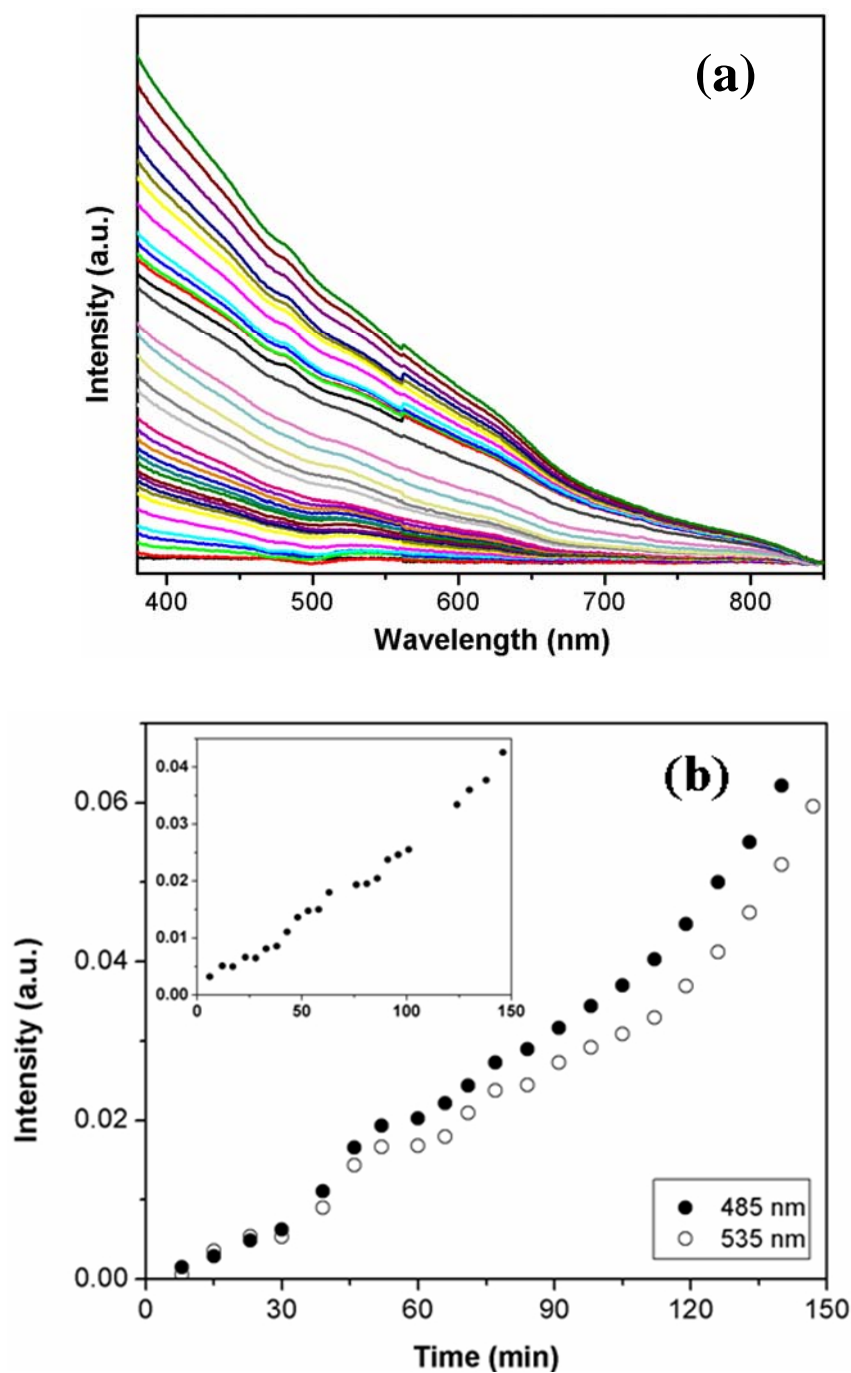
**Figure 4.15.** (a) Optical spectra of CdSe films recorded *in situ,* obtained using 30 mL of 0.214 mmol toluene solution of Cd(cup)$_2$ and 30 mL of 0.214 mmol aqueous solution of DMSU at room temperature, showing increasing absorbance as the film grows with reaction time. The steps observed at 560 nm are caused by the detector change. (b) A plot showing the time dependent growth of the absorption bands at two different wavelengths. Inset is a similar plot obtained using half the concentration of the reacting species.

addition of the reactants. With increase in reaction time, the spectra grow in intensity, but without appreciable shift in the position of these peaks. This suggests that CdSe nanoparticles are formed at the interface within the first few minutes, possessing a size beyond the quantum confinement regime. In other words, the particle size remains essentially constant with time. The thickness of the film, however, increases steadily with time as suggested by the increase in the absorption intensity. In Figure 4.15b, shown are the intensity versus time plots for the 485 nm and 535 nm bands. The plots show a monotonic increase. The inset in Figure 4.15b shows a plot obtained, starting with half the concentrations of the reactant species. The lowering of concentrations slows down the growth process, but the nature of the growth curve remains the same.

The reaction of Cu(cup)$_2$ dissolved in toluene with aqueous DMSU solution resulted in extended CuSe films at the toluene-water interface. In Figure 4.16a, we show the XRD pattern of the CuSe film obtained by the reaction of 0.001 mmol of Cu(cup)$_2$ in toluene with 0.001 mmol of aqueous DMSU solution at ~30 $^o$C. The diffraction peaks correspond to that of hexagonal CuSe (JCPDS card no. 27-0185, a = 3.984 Å, c = 17.28 Å ). The broad hump in the pattern in the 15$^o$–40$^o$ range is due to the glass substrate on which the film was placed. A SEM image of the film is given in Figure 4.17a, showing its continuous nature, extending over wide areas. The ratio of Cu:Se in the film was confirmed to be 1:1, as revealed by the EDAX spectra given in Figure 4.16b. TEM images reveal the CuSe film to be smooth, continuous and devoid of particles, unlike the CdSe films. Figure 4.17b shows a typical TEM image of a portion of the film. We have acquired SAED patterns of the film at various portions which yielded hexagonal Bragg spots corresponding to the (102) and (110) lattice
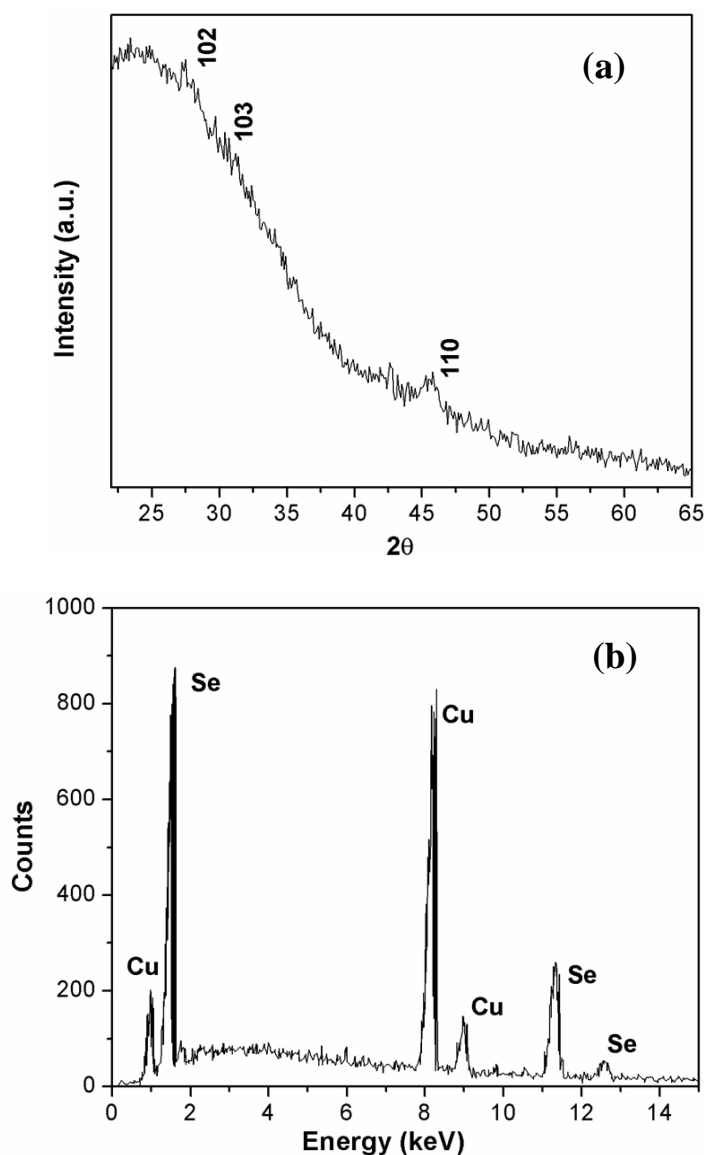
**Figure 4.16.** (a) XRD pattern of the CuSe film obtained by the reaction of 30 mL of 0.001 mmol of Cu(cup)$_2$ dissolved in toluene with 0.001mmol of DMSU dissolved in water at ~30 $^o$C; (b) EDAX spectra of the film.

planes of hexagonal CuSe, as shown in the inset of Figure 4.17b. The HREM images (Figure 4.17c) of the film showed the (100) planes with a lattice spacing of 0.35 nm corresponding to hexagonal CuSe. The SAED pattern as well as the HREM image confirm the single-crystalline nature of the CuSe films. The films, when subjected to prolonged ultrasonication broke down leading to nanorods of diameter 10-20 nm, and

nanocrystals of diameter 20-50 nm, as can be seen from the TEM image in Figure 4.17d. The SAED pattern of the nanostructures obtained after sonication is given as an inset in Figure 4.17d.
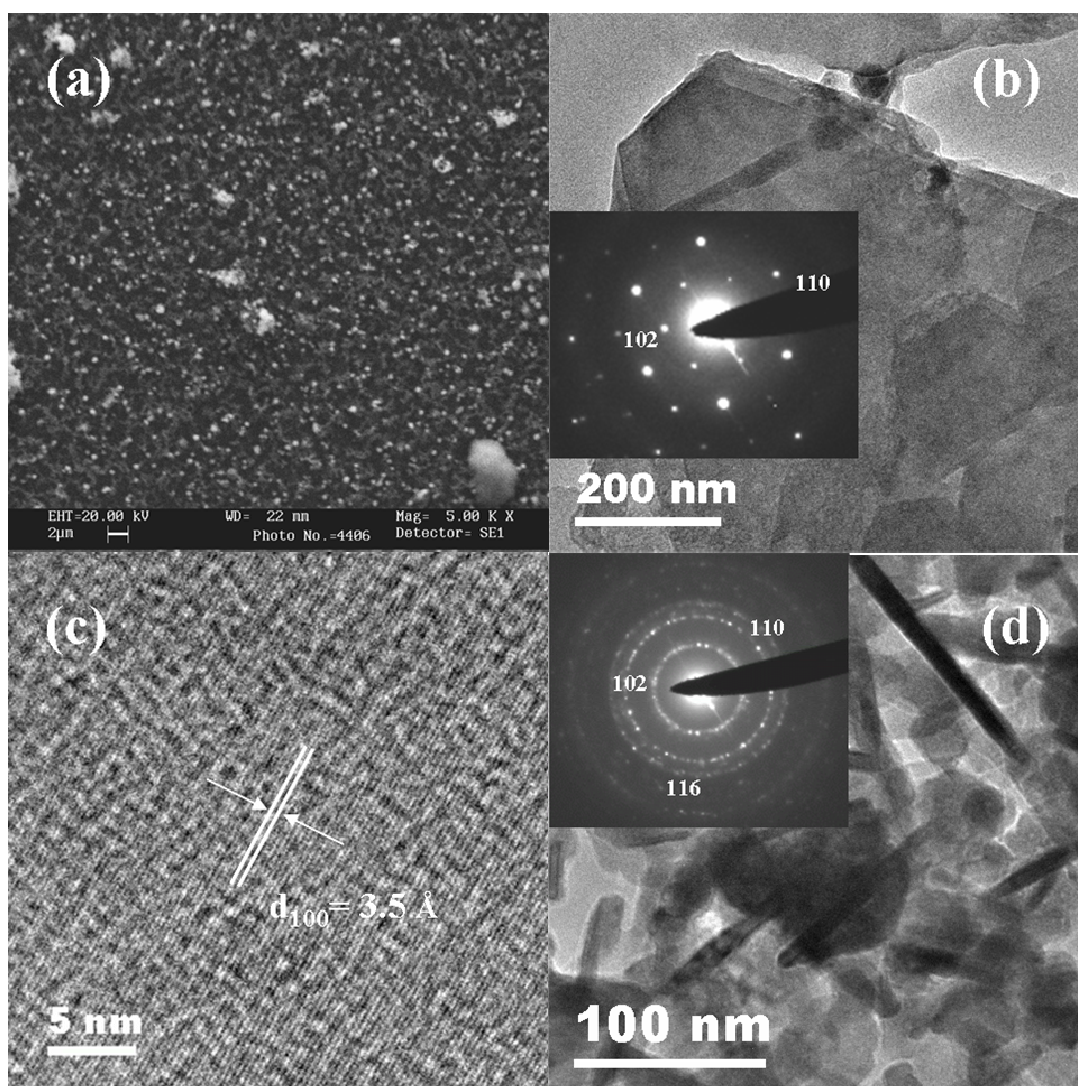


**Figure 4.17.** (a) SEM image of the CuSe film obtained by the reaction of 0.001 mmol of Cu(cup)$_2$ dissolved in 30 mL of toluene with 0.001 mmol of DMSU dissolved in 30 mL of water at ~30 $^o$C; (b) TEM image showing a single-crystalline portion of the film. Inset is the SAED pattern of the film; (c) HREM image of the film showing the (100) planes of hexagonal CuSe; (d) TEM of same film showing nanorods and nanocrystals of CuSe obtained by ultrasonication. The corresponding SAED pattern is given as the inset.

_____

Thin films of CdS and CdSe formed at the organic-water interface are polycrystalline in nature while those of other metal chalcogenides form single-crystalline films [9]. This could be due to the presence of amines in the organic layer, required to dissolve the cadmium precursor. The reaction rate increases with the increase in the reactant concentrations and reaction temperature, and the product is capped by the amine soon after formation. Such capping may also be responsible for the absence of any increase in particle size.

### 4.4.2 Metal chalcogenide bilayer

In Figure 4.18(a) is given an SEM image of the CdS-CuS bilayer obtained at the toluene-water interface, the top layer being CuS. The EDAX spectrum of the sample is given in Figure 4.18b. It shows the presence of both Cu and Cd, with Cd:Cu:S at % = 50:48:2. The amount of Cd detected is low because of CdS being the bottom layer. TEM image of the bilayer in Figure 4.19a shows the presence of both the upper CuS layer as well as the bottom CdS layer. Thin films of CuS obtained at the toluene-water interface are reported to be extended and single-crystalline [14]. On the other hand, thin films of CdS are always composed of nanocrystals due to the presence of *n*-octylamine present in the reaction system, which caps the CdS nanocrystals [13]. The formation of single-crystalline CuS thin film as well as nanocrystalline CdS film is confirmed by the HREM images, as can been seen in the Figures 4.19b and 4.19c. The HREM image in Figure 4.19b shows the (100) Bragg planes of hexagonal CuS separated by a distance of 0.33 nm. The SAED pattern taken from the region shows single-crystalline spots as well as polycrystalline rings which could be assigned on the basis of the hexagonal phase of CuS and the cubic phase of CdS respectively. Figure 4.19c shows HREM image obtained from the region away
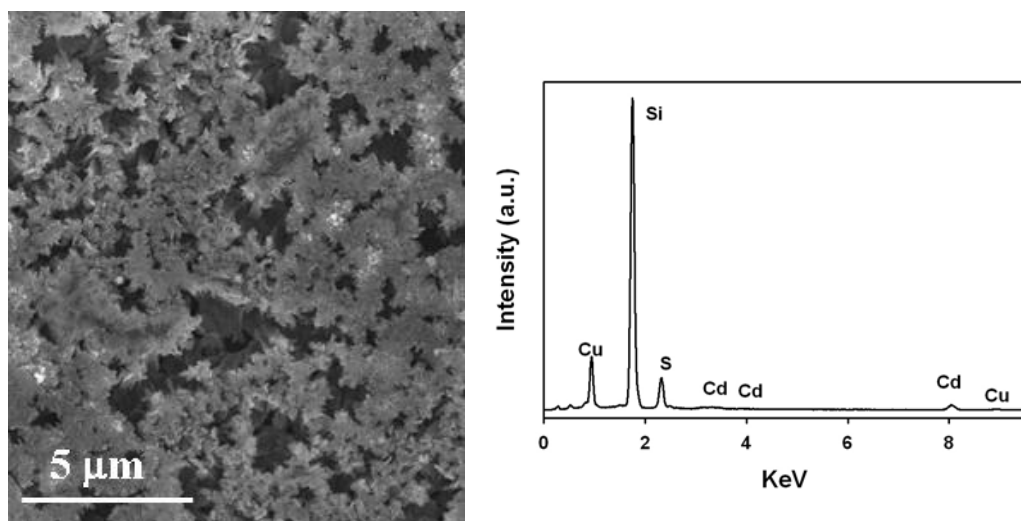
**Figure 4.18.** (a) SEM image and (b) EDAX spectrum of of CdS-CuS bilayer formed at the toluene-water interface.
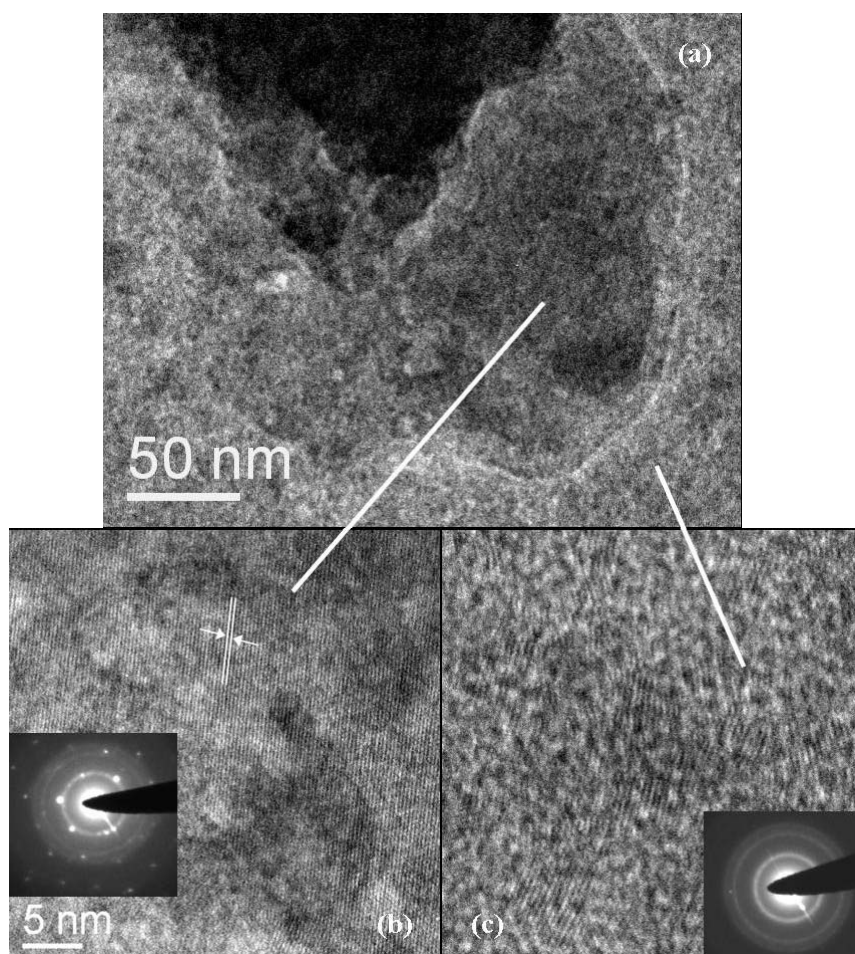


**Figure 4.19.** (a) TEM image of the CdS-CuS bilayer; HREM images of the (b) upper CuS layer and (c) bottom CdS layer. Insets are the corresponding SAED patterns.

_____

from the upper film (marked by the line), confirming the single-crystalline nature of the nanoparticles of diameter ~ 5nm, which comprise the bottom film. The image shows the (111) lattice planes of cubic CdS, separated by a distance of 0.34 nm. Thus, TEM studies show that the two layers formed at the interface are separate, without any coalescence.
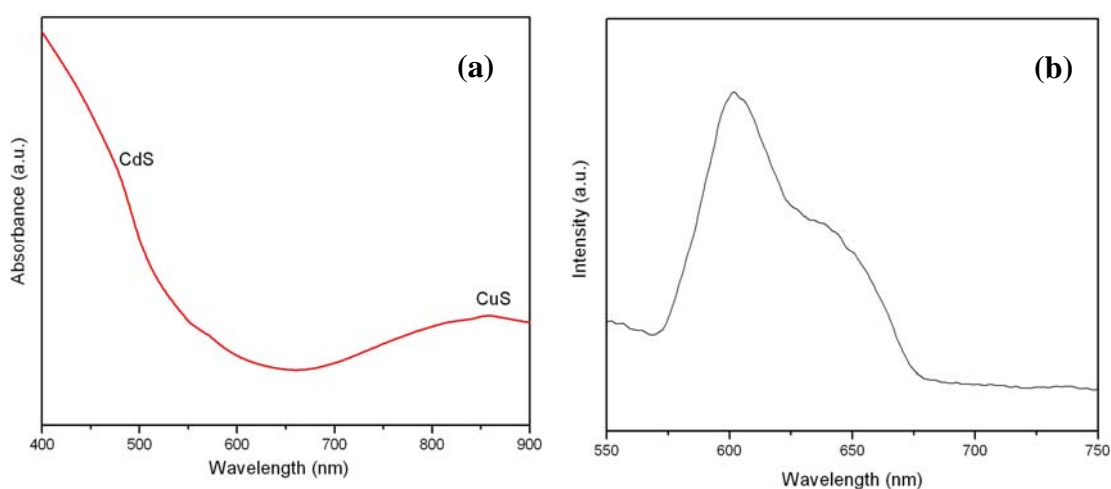


**Figure 4.20.** (a) UV-Vis absorption spectrum of the CdS-CuS bilayer formed at the toluene-water interface and (b) the corresponding PL spectrum.

The bilayer-film at the interface was further investigated using optical spectroscopy. UV-Vis absorption spectrum of the sample in Figure 4.20a shows a broad absorption band in the near IR region, corresponding to covellite CuS [64]. The spectrum also shows an excitonic absorption band centered at ~ 470 nm corresponding to CdS, which is blue-shifted from the bulk value due to quantum confinement in the CdS nanoparticles [13]. PL spectrum of the film is given in Figure 4.20b. It shows a band centered at ~ 600 nm, arising due to the charge carriers trapped at the surface defects of the CdS layer. Thus, the bilayered thin films, obtained in such

146

a manner, with the properties of both the semiconducting films are envisaged to have potential applications in optoelectronics.

### 4.4.3    Atomic force microscopic study

AFM image, obtained from the amplitude channel, of the as-prepared Au film collected after 10 min of reaction at the toluene-water interface is given in Figure 4.21a. It shows a film made up of nanoparticles of diameter in the range 5-7 nm, separated by a distance of ~ 1 nm. The nanocrystals are found to aggregate to give rise to structures of diameter ~ 70-100 nm. These small nanocrystals (marked by arrow) can be however seen in the magnified image of one of the aggregates, given on the left hand side in Figure 4.21 a. The amplitude image in Figure 4.21a also shows bigger aggregates or hump-like structures of diameter ~ 150 nm. These are denoted by arrows in the amplitude image. 3D surface plot of the film given in Figure 4.21b shows the general morphology of the sample. Nanoparticle aggregates can be seen in the plot. On scanning the film after repeated washing with toluene, we observed aggregates with an average diameter of ~ 70 nm, made up of the 5-7 nm nanoparticles. FESEM images of the washed sample (see Figure 4.22) show spherical particles in the 5-7 nm size range and a few nanoparticle aggregates in the size range 20-30 nm. EDAX analysis carried out on the different regions of the film showed the presence of carbon and phosphorous, from the metal precursor as well as the reducing agent (THPC). XPS studies have indeed shown that the Au nanoparticles have coatings of the organic precursor and the reducing agent [65]. Continuous exposure of the film to high energy electron beam resulted in the formation of rings, arising from the decomposition of the organic moiety. One such ring is marked by an arrow in Figure 4.22b.
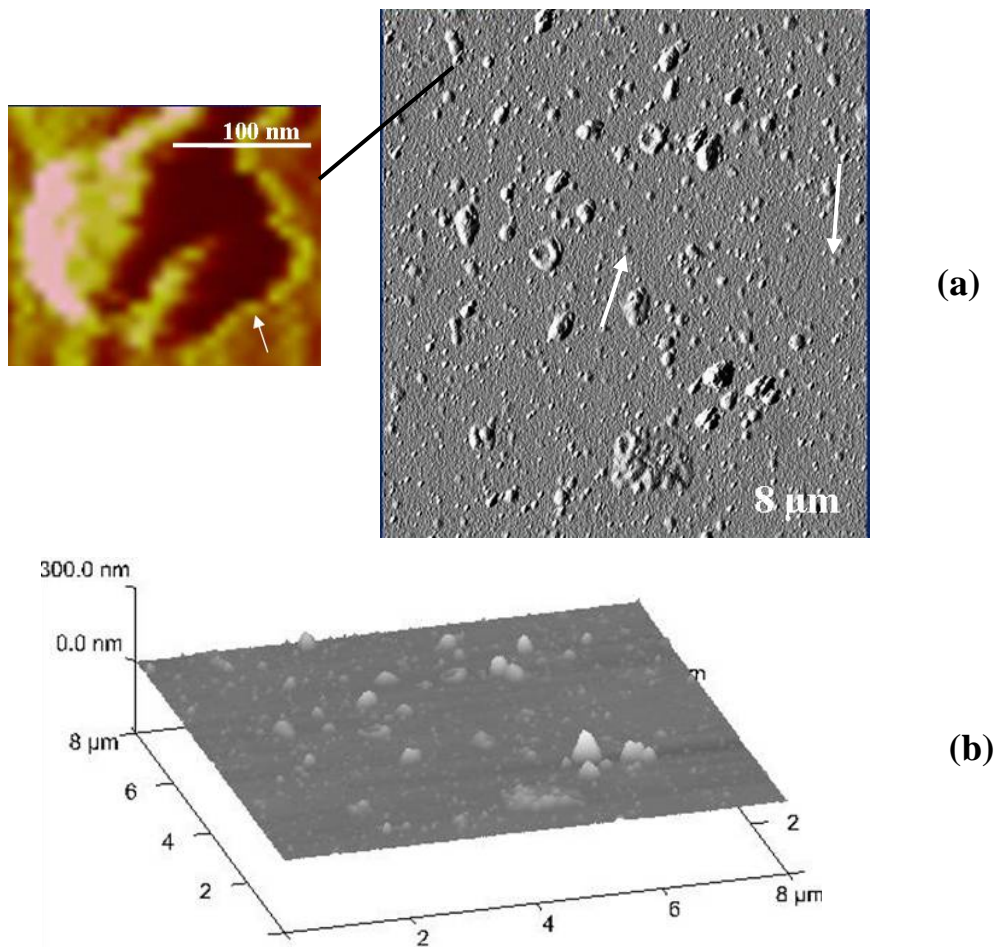
**Figure 4.21.** (a) Tapping mode AFM image (amplitude channel) of Au film grown at the toluene-water interface for 10 min; along with the magnified portion showing the individual nanocrystals, and (b) the corresponding 3D surface plot.
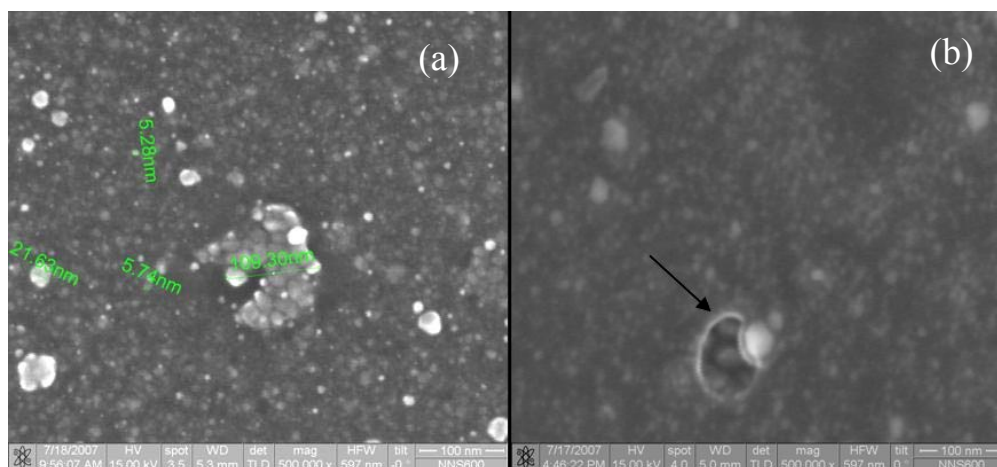


**Figure 4.22.** (a) and (b) FESEM images of toluene-washed Au film grown for 10 min at the toluene-water interface.

Thus, the unreacted organic molecules, remaining even after the washing, might be covering the entire nanocrystalline Au film surface. Therefore, the nanoparticle aggregates observed in the amplitude image in Figure 4.21a are supposed to be assemblies of gold nanoparticles along with the organic molecules, belonging to the unreacted metal precursor and the reducing agent. Recent studies on the formation and growth of Au films at the toluene-water interface by X-ray scattering and diffuse reflectivity using synchrotron radiations have shown that organic moieties do cap tiny Au nanocrystals of diameter 12 Å [53]. These organic-capped nanoparticles then form clusters, which arrange in a hexagonal fashion at the organic-aqueous interface. The studies also show that the presence of organic molecules lead to a decrease in the interfacial tension. The thickness of the as-prepared Au 10 min sample is measured to be ~ 40 nm, corresponding to several monolayers of nanoparticles. Calculated root mean square (rms) roughness values of the 10 min samples fall in the range 7-10 nm.

Enhanced reduction of Au salt at the interface with time leads to the addition of new layers at the liquid-liquid interface. Amplitude image of Au film obtained after 30 min of the reaction (Figure 4.23a) shows a new layer of particle aggregates constituted by nanocrystals of size in the range 5-7 nm. The average size of aggregates seen on the surface is ~ 70-100 nm. The amplitude image in Figure 4.23a shows humps (denoted by arrows) of size in the range 400-600 nm. The humps as well as the nanoparticle aggregates can be seen in the 3D surface plot of the 30 min film given in Figure 4.23b. Such hump-like structures of diameter ~ 150 nm were found in the 10 min sample as well. That, the large humps seen in the images arise due to coverage by organic ligands is evidenced by the fact that on washing the film with toluene we see only nanoparticle aggregates of size ~ 100 nm. An amplitude image of the washed 30 min film is given in Figure 4.23c. Thus, the humps observed

**(a)**



**(b)**



**(c)**



**Figure 4.23.** (a) Tapping mode AFM image (amplitude channel) of Au film grown at the toluene-water interface for 30 min; (b) the corresponding 3D surface plot and (c) AFM image of the film obtained after washing with toluene.

in Figure 4.23a should be nanoparticle aggregates with a thick coating of the unreacted organic molecules. An increase in the size of the humps is an indication that the reduction of the Au ions might be taking place at the interface region just above

the water surface, as well, by the diffusion of Au ions from the toluene layer through the already formed nanoparticles layers. The formation of new layers might be occurring simultaneously in the top region of the interface, which is closer to the toluene layer, as well as, in the bottom region that is closer to the water layer. Thickness of the as-prepared sample is measured to be ~ 60 nm. This film having an rms roughness value of ~ 14 nm, as expected is rougher than the 10 min one, due to the presence of big humps.

The amplitude image of the Au film obtained after 60 min of the reaction is given in Figure 4.24a. With time, the coverage of the film on the substrate increases, though the size of the nanoparticles making up the aggregates remains the same. The image shows the presence of nanoparticle aggregates of size in the range 80-100 nm. In this sample also we could find humps of size in the range 400-600 nm, which disappeared on washing with toluene. On the right-hand side in Figure 4.24a is given the corresponding 3D surface plot, showing a denser film in comparison to that obtained after 30 min. Thickness of the 60 min sample is measured to be ~ 80 nm. An increase in the measured thickness confirms the formation of new layers, resulting in a multilayered film at the interface. Roughness calculations gave an rms value of ~ 15 nm.

As the reaction proceeds further, the number density of the nanoparticle aggregates on the surface of the film decreases, as evidenced by the amplitude image of the sample obtained after 120 min of the reaction (Figure 4.24b). Nanoparticle aggregates of size ~ 80-100 nm, which were abundant in the topmost layer in the 30 min and the 60 min samples, reduced a lot in number in the 120 min sample. At the same time, we could observe more number of the hump-like structures in the 120 min film. As in the case with the 30 min and 60 min films, after washing the 120 min film
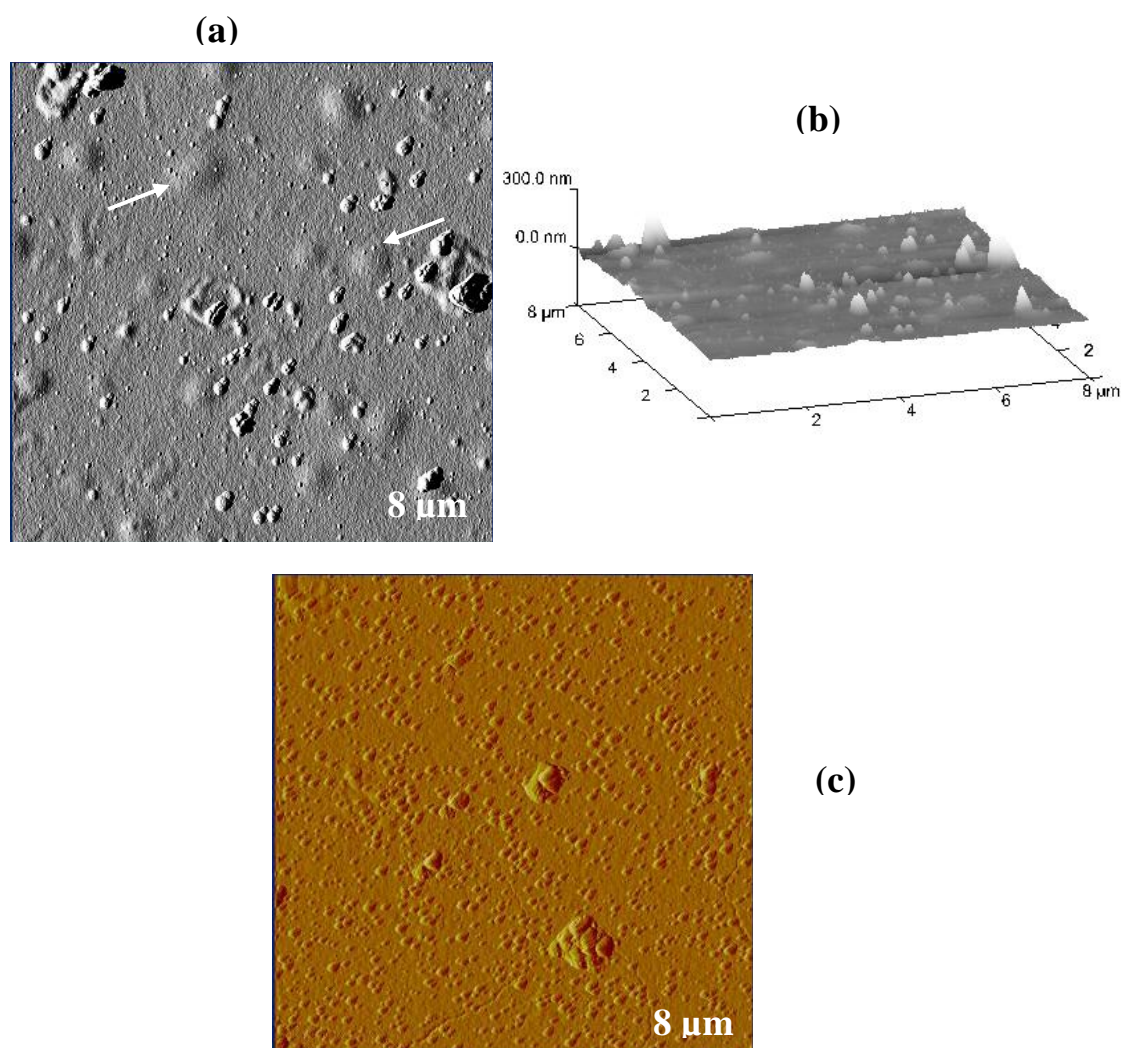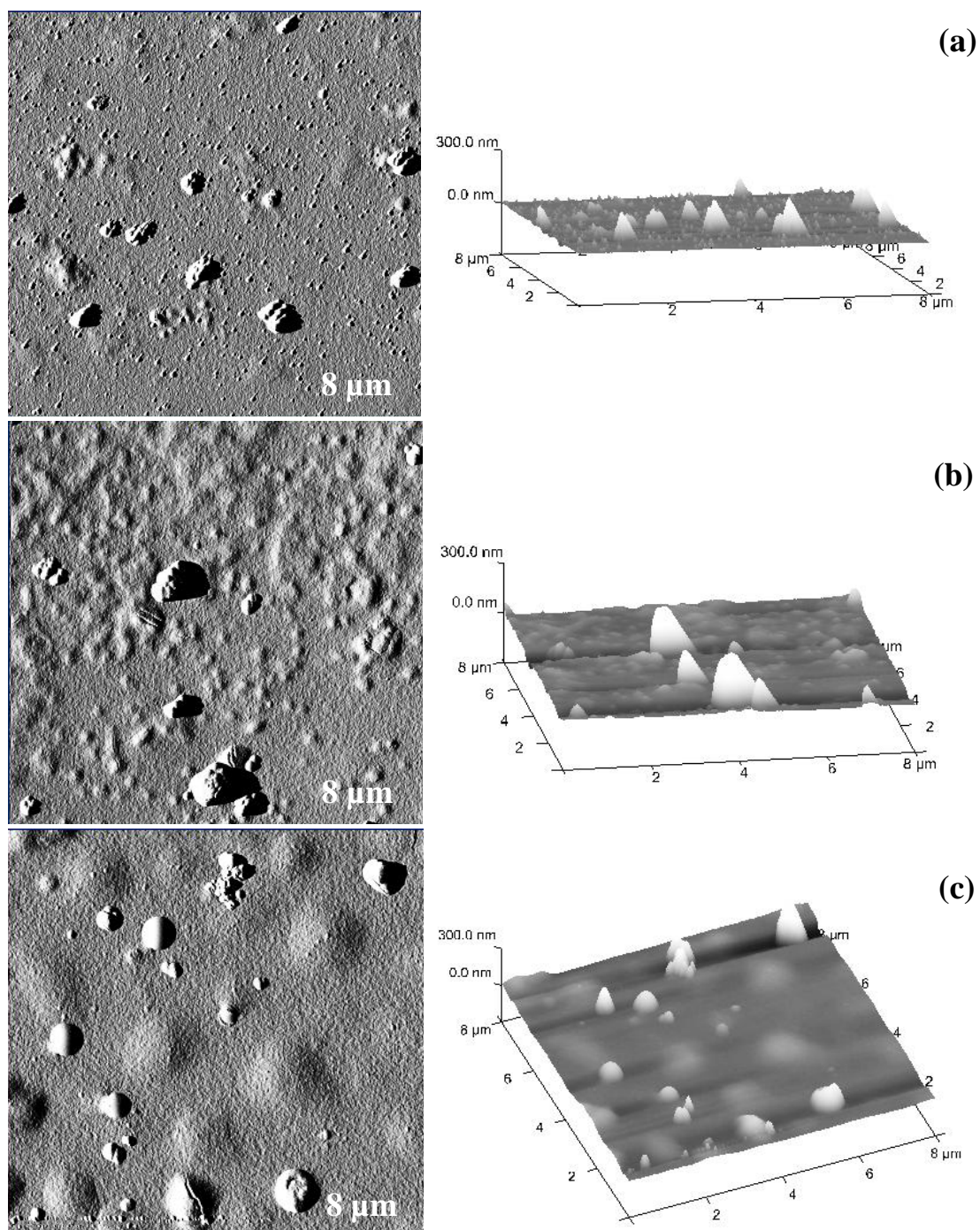
_____



**Figure 4.24.** Tapping mode AFM images (amplitude channel) of Au film grown at the toluene-water interface for (a) 60 min; (b) 120 min and (c) 180 min, along with the corresponding 3D surface plots.

with toluene, the humps disappeared. The thickness of 120 min sample is measured to be ~ 140 nm. The observed decrease in the number of particle aggregates on the surface and an increase in the number of humps, along with an increase in measured thickness is an indication that the reaction might be taking place at a faster rate in the interface region closer to the aqueous phase, compared to the upper region which is closer to the toluene phase. Rms roughness of the film is calculated to be ~ 30 nm, much higher than that of the 30 min and the 60 min samples, probably due to an increase in the number of humps.

The amplitude image of the 180 min sample given in Figure 4.24c shows some nanoparticle aggregates of size in the range 200-300 nm, on the surface of the nanoparticulate film. But similar to the 120 min sample, particle aggregates of size ~ 80-100 nm were few in number in the topmost layer, in the 180 min sample. The humps, also seen in the 10 min, 30 min, 60 min, and the 120 min samples, are observed to have grown in size in the 180 min sample. The humps in the 180 min sample are measured to be in the size range 800 nm -1 μm. The humps can be clearly seen in the 3D surface plot given in Figure 4.24c. After washing the film with toluene, the humps did disappear, showing that the unreacted organic moieties can indeed form such large humps. The 180 min sample has almost the same thickness as the 120 min one, ~ 140 nm. Thus, the topmost layer probed in the 120 min sample as well as the 180 min samples should be the same. A large increase in the hump size, but without any change in the measured thickness compared to the 120 min sample, indicates that between 120 min and 180 min reaction has mainly occurred in the interface region just above the water surface. The rms roughness value is calculated to be same as that of the 120 min sample, ~ 30 nm.
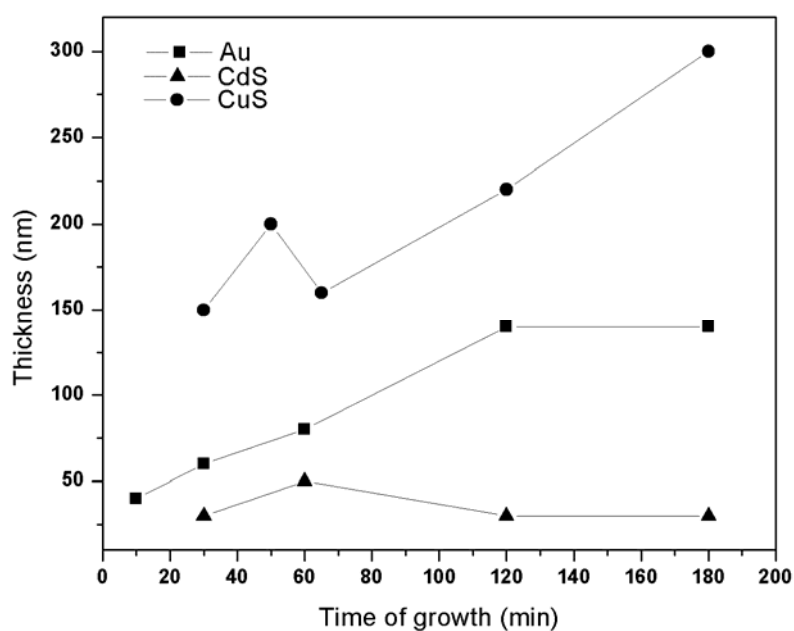
**Figure 4.25.** Thickness vs time of growth plots for Au, CdS and CuS films prepared at the toluene-water interface.

Figure 4.25 shows the variation in thickness of the Au films (closed squares) collected at different stages of growth. During the reaction period from 10-120 min, new layers of nanocrystals get added up. As a result, up to 120 min of the reaction the thickness of the Au film shows a linear increase. Rate of reaction leading to the formation of nanoparticles in the uppermost layer seems to slow down before 120 min of the reaction. This might be the reason for a pronounced decrease in the number, and an increase in the average size of nanoparticle aggreagates observed in the uppermost layer, in the 120 min and 180 min samples. After 120 min, rate of reaction in the interface region closer to the aqueous phase might be accelerating, compared to that in upper region which is closer to the toluene phase, leading to an increase in the size of the hump-like structures.

Contact mode AFM deflection image of the CdS film obtained after 30 min of the reaction is given in Figure 4.26a. It shows a film composed of nanoparticles. The
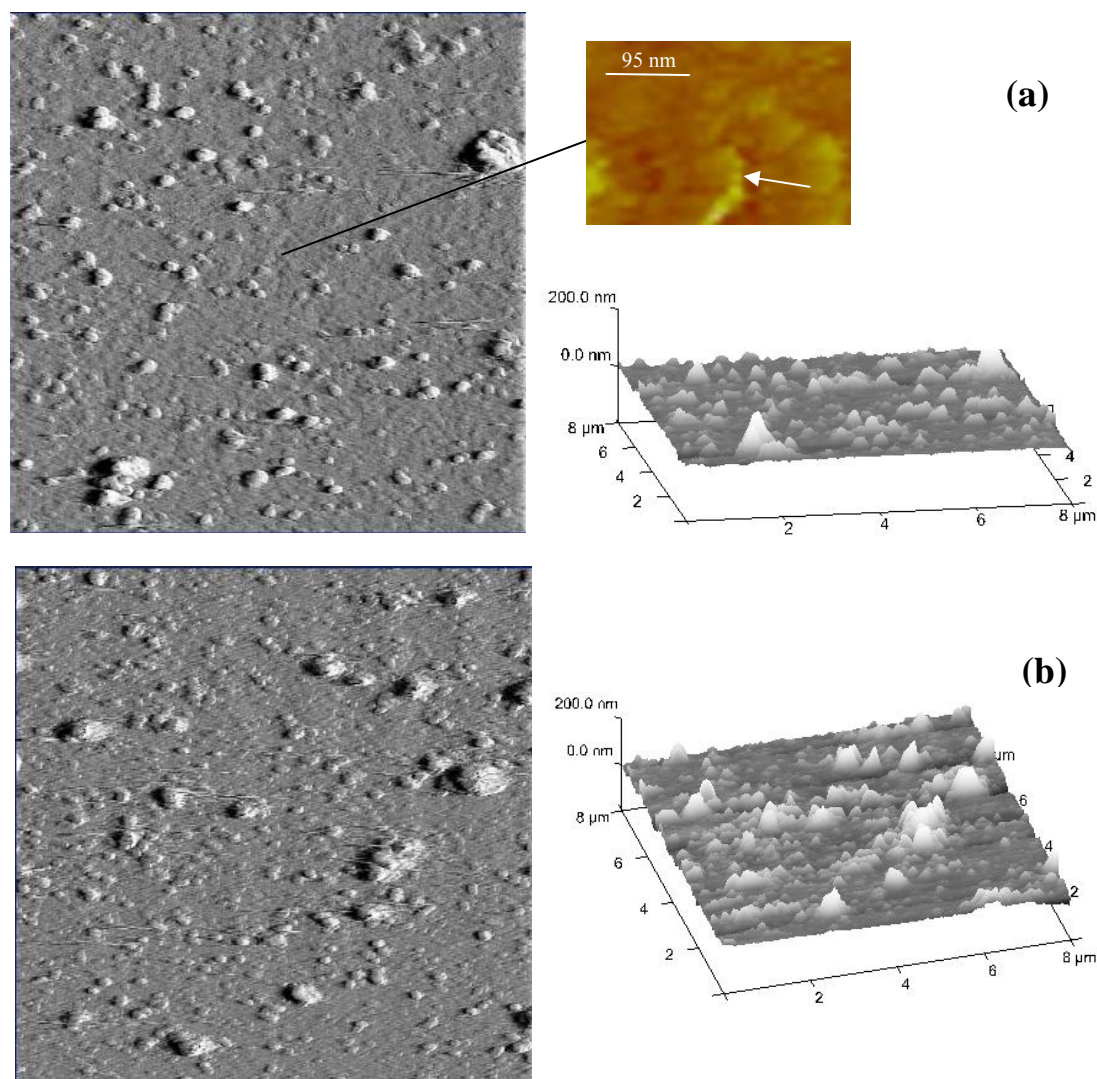
**Figure 4.26:** Contact mode AFM images (deflection channel) of CdS films grown at the toluene-water interface for (a) 30 min and (b) 60 min, along with the corresponding 3D surface plots.

nanoparticles were found to be of diameter in the range 5-7 nm. A magnified image given on the top right hand side in Figure 4.26a shows the individual nanoparticles forming the aggregates (denoted by an arrow). The deflection image in Figure 4.26a also shows nanoparticle aggregates of size in the range 80-200 nm, on the surface of the film. Measured thickness of the sample is ~ 30 nm. Rms roughness of the film is calculated to be in the range 7-10 nm. 3D surface plot of the sample given in Figure

4.26a shows the topmost layer, containing nanoparticle aggregates, which is still in its growing stage. The formation of CdS nanocrystals of size 5.5 nm at the toluene-water interface at 30 $^{o}$C has been reported [13].

Deflection image of the CdS film obtained after 60 min of the reaction is given in Figure 4.26b. The number density of the nanoparticle aggregates in the uppermost layer increases with time but size of the aggregates remains almost the same in both the samples (compare the deflection images in Figures 4.26a and 4.26b). Also, the nanoparticle aggregates grow taller. This can be seen clearly in the 3D surface plot of the 60 min film in Figure 4.26b. Thickness of the 60 min sample is measured to be ~ 50 nm. An increase in the height of the particle aggregates might be the reason for the increase in the measured thickness of the 60 min film compared to the 30 min one. Rms roughness of the film is calculated to be in the range 10-14 nm, higher in comparison with that obtained after 30 min. The increase in the value of roughness might be due to an increase in the height of the particle aggregates.

As the reaction proceeds, the number density of nanoparticle aggregates increases further and they come closer to each other. Also, the size distribution of the aggregates narrows down (80-100 nm). Deflection image of the film obtained after 120 min of reaction is given in Figure 4.27a. With reaction time, as the number of nanocrystals being formed increases, growth of aggregates along the vertical direction in the uppermost layer gets suppressed. The nanoparticles constituting the aggregates spread out laterally. This reduces the height of the aggregates and they get closer to each other. The measured thickness of the 120 min sample is ~ 30 nm, which is lower than the 60 min sample. A decrease in the thickness might be resulting from the reduction in the height of the nanoparticle aggregates. So probably, the same uppermost layer which showed a sporadic distribution of nanoparticle aggregates in
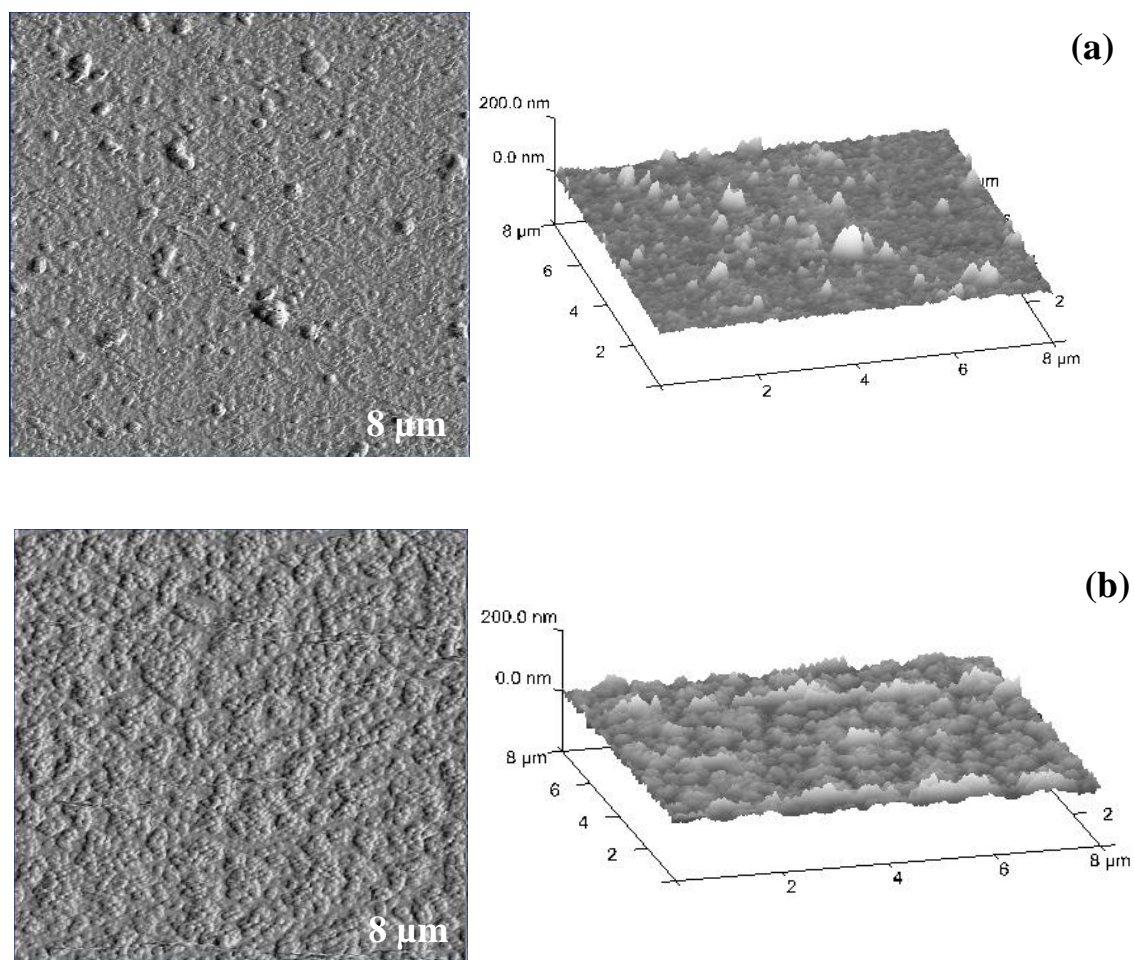
**Figure 4.27.** Contact mode AFM images (deflection channel) of CdS films grown at the toluene-water interface for (a) 120 min and (b) 180 min, along with the corresponding 3D surface plots.

the 30 min as well as in the 60 min samples grows into a more dense layer within 120 min of the reactrion. The 3D surface plot of the 120 min sample is given in Figure 4.27a. Roughness measurements gave rms values in the range 7-10 nm

In Figure 4.27b is given the deflection image of the CdS film obtained after 180 min of the reaction. It shows groups constituted by closely packed aggregates of nanoparticles (5-7 nm diameter) of average size ~ 80 nm and almost the same height, separated from each other by a distance of ~ 50 nm. The individual aggregates forming the groups are calculated to be ~ 10 nm apart. This tendency, to attain more or less a uniform height might be the reason for the observed gap in between the groups, which in turn finally results in a close-packed layer. Thickness of the 180 min film (~30 nm) is measured to be the same as the 120 min one, a result of the growth of the film mainly in a lateral fashion. 3D surface plot of the sample, given in Figure 4.27b, also shows a film containing nanoparticle aggregates of almost uniform height. Rms roughness values of the film fall in the same range as that of the 120 min one.

The plot given in Figure 4.25, denoted by closed triangles, shows the behavior of thickness with time of growth for CdS films. The nanoparticle aggregates in the uppermost layer first grow in the vertical direction, followed by the spreading out of the individual nanoparticles laterally to form a close-packed layer, joined in by more and more of the newly forming nanocrystals. Growth of the nanoparticle aggregates in the vertical direction might be the reason for an increase in the measured thickness of the 60 min CdS sample. Spreading out of the individual nanocrystals laterally, and the subsequent formation of a close-packed layer after 60 min results in a decrease in thickness of the film from 50 nm to 30 nm for the 120 min as well as the 180 min samples. After 180 min, the above process of initial vertical growth and subsequent lateral growth might repeat to form new layers of nanocrystals at the interface. But

158

there is a limit to the number of layers formed since the film formation at liquid interfaces is a diffusion-controlled process. SAXS measurements carried out on the CdS film grown at the toluene-water interface have shown the film to be a 2D percolating network of pores, with the pores forming a surface fractal of dimension 2.5 (described in detail in section 4.4.5 of this chapter).

In Figure 4.28a is given a tapping mode amplitude AFM image of CuS film grown at the interface for 30 minutes. It shows the presence of nanoparticle aggregates of size in the range 50-100 nm as well as much bigger ones. The size of the nanoparticles forming the assemblies is found to be in the range 7-8 nm, separated by a distance of less than 1 nm. 3D surface plot of the film is also given in Figure 4.28a. As can be seen from the surface plot as well as the deflection image, the distribution of nanoparticle aggregates within a specified area is thin in the sample. The distance between the aggregates goes even up to a couple of microns. The thickness of the film is measured to be ~ 150 nm. The rms roughness of film is found to be ~ 40 nm.

As the reaction proceeds, the initially formed nanoparticle aggregates come closer to each other and pack themselves at the interface to give flakes or uneven pieces of CuS, which coalesce with time, finally to give a homogeneous film at the interface. Amplitude image of the CuS film obtained after 50 min of the reaction, given in Figure 4.28b, shows flakes (marked by arrows) which are formed by nanoparticle aggregates of average size ~ 130 nm. The aggregates are found to be ~ 40-50 nm apart in the flakes. The formation of flakes has been observed in rheological measurements carried out on CuS films formed at the toluene-water interface, where the films break at certain fixed boundaries on the application of shear (see section 4.4.5 of this chapter). Thickness of the film was measured to be ~ 200 nm. The 50 min

_____
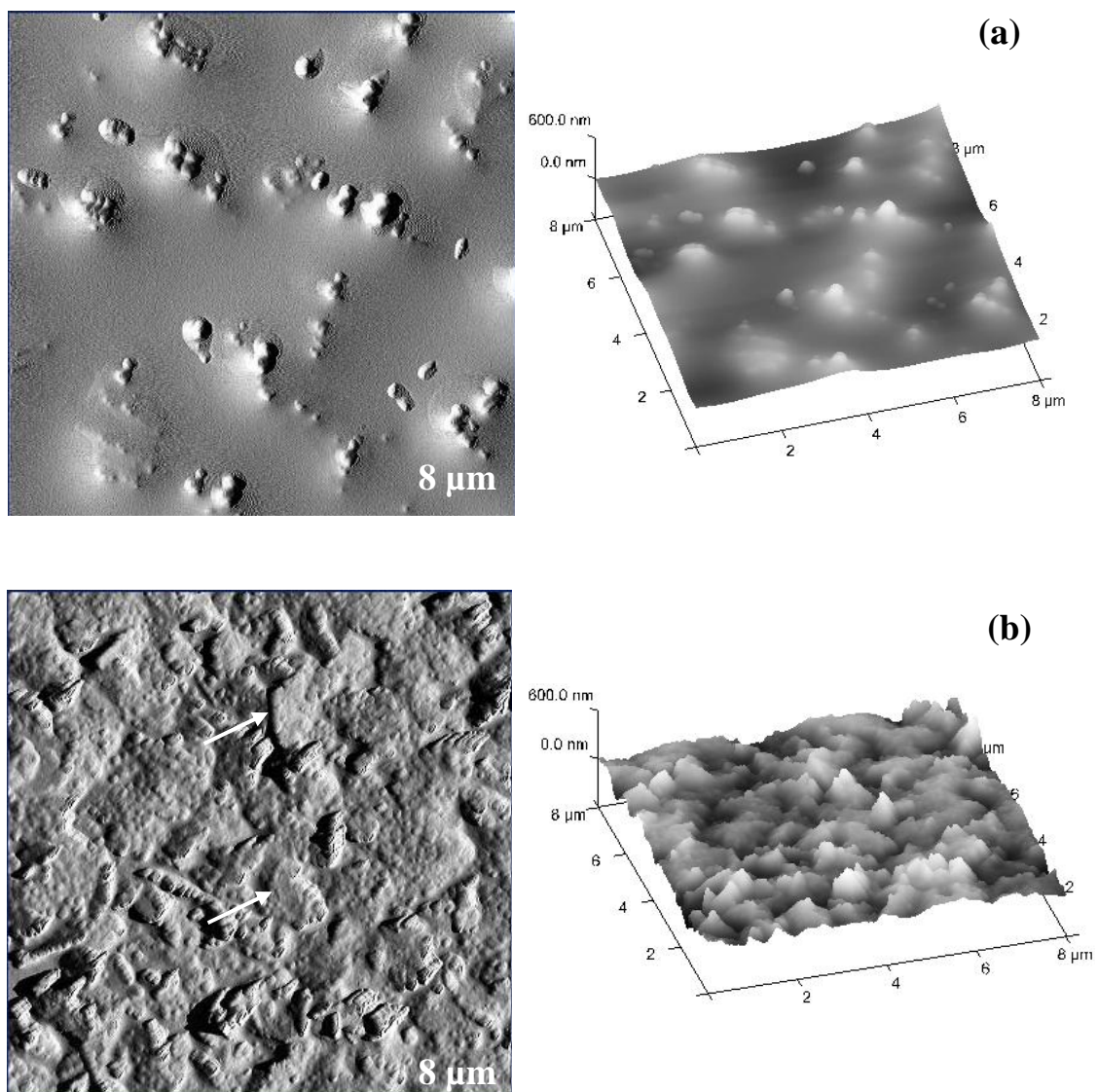


**Figure 4.28.** Tapping mode AFM images (amplitude channel) of CuS films grown at the toluene-water interface for (a) 30 min and (b) 50 min, along with the corresponding 3D surface plots.

film with an rms roughness value of ~ 55 nm is found to be much rougher compared to the one obtained after 30 min. The increase in roughness is attributed to the formation of flakes of uneven heights. 3D surface plot of the 50 min CuS film showing the flakes is given in Figure 4.28b.

The flakes of CuS observed in the 50 min sample coalesce at the interface within the next 15 min of reaction, as is evidenced by the amplitude image of the CuS film grown at the interface for 65 min in Figure 4.29a. Hardly any gap is observed in between the individual flakes. The distance between the nanoparticle aggregates in the flakes decreases to 10-20 nm. Thus, during coalescence of flakes, the nanoparticle aggregates constituting the flakes also come closer to each other. Thickness of the sample obtained after 65 min is measured to be ~ 160 nm. With time, the number of flakes increases and they coalesce to give a close-packed film at the interface. Thus, the height of the flakes decreases and correspondingly, the thickness of the film. The amplitude image as well as the 3D plot given in Figure 4.29a show a smoother and a more uniform film at the interface compared to the one obtained after 50 min. Rms roughness of the film is calculated to be ~ 30 nm. The decrease in roughness compared to the 50 min film can be attributed to the formation of dense, close-packed film by coalescence of the flakes.

In Figure 4.29b is given the amplitude image of the CuS film obtained after 120 min of the reaction. The image shows the presence of nanoparticle aggregates of average size of ~ 130 nm. With time many more nanocrystals of diameter in the range 7-8 nm form by the diffusion of reactants across the interface from the two immiscible layers, whose self-assembly gives rise to aggregates of size ~ 130 nm. The magnified image given on the right hand side in Figure 4.29b shows the individual nanoparticles
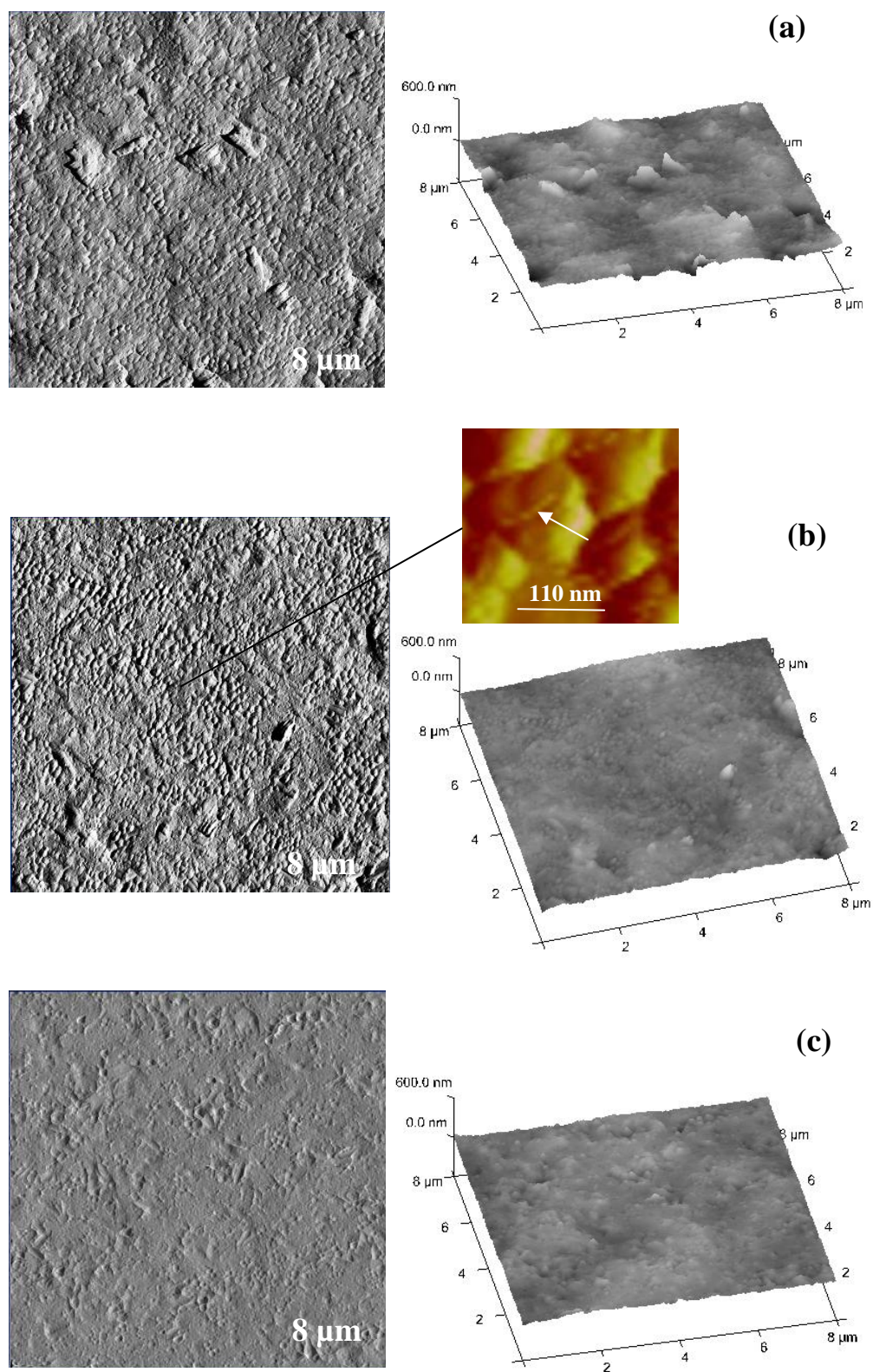
**Figure 4.29.** Tapping mode AFM images (amplitude channel) of CuS films grown for of CuS films grown at the toluene-water interface for (a) 65 min and (b) 120 min, and (c) contact mode AFM image (deflection channel) of the film grown for 180 min. The corresponding 3D surface plots are given along side.

162

(denoted by an arrow) constituting the aggregates. The aggregates pack themselves to form flakes. Coalescence of the flakes, which ensues, gives rise to a dense, continuous film. Individual flakes are hardly seen in the case of the 120 min film, similar to that of the 65 min sample. The thickness of the sample is measured to be ~ 220 nm. The increase in thickness indicates the formation of multiple layers at the interface, with time. Thus, the aggregates seen in the amplitude image in Figure 4.29b are supposed to be of a new layer. 3D surface plot of the sample given in Figure 4.29b shows a smooth and continuous film. Roughness calculations yielded a lower rms value of ~ 20 nm, compared to the previous sample. Better coalescence of the flakes might be the reason for the further decrease in the calculated roughness of the film.

The CuS film obtained after 180 min of the reaction is a very uniform and continuous one. Thickness of the sample is measured to be ~ 300 nm. A contact mode deflection image of the sample is given in Figure 4.29c, showing the nanoparticle-aggregates and the coalescing flakes, of the uppermost layer. It is to be noted that the individual nanocrystals could hardly be observed. Thus, indicating proper coalescence of nanocrystals. This is in contrast to that of Au and CdS, where the individual nanoparticles ever remain at a distance of ~ 1 nm from each other. This is due to the presence of capping agents THPC and *n*-octylamine respectively, present in the reaction systems. Rms roughness value of the sample is similar to that of the 120 min one, calculated to be ~ 20 nm. A point to be noted is that since more layers are getting added up continuously after 65 min of the reaction, the images obtained are of newer layers at different stages of their growth. 3D surface plot of the 180 min film (Figure 4.29c) shows the formation of a very uniform film.

In Figure 4.25, the plot represented by closed circles illustrates the variation of thickness of CuS films formed at the interface with reaction time. Growth is observed

to be linear in between 30-50 min of the reaction. During this period, nanoparticle aggregates pack themselves to form big uneven pieces or flakes which grow to attain a constant height. In the next 15 min of the reaction, the flakes coalesce resulting in their height reduction. This in turn results in a relative decrease in the thickness of the whole film. Thus, from 50-65 min of the reaction, we actually observe the growth of the same layer. After 65 min till 180 min of the reaction, again we see a linear increase in the thickness of the film. This is an indication of the formation of new layers at the interface.

Formation of single-crystalline, homogeneous and extended thin films of CuS at the toluene-water interface at room temperature has been reported [14]. Transmission electron microscopy was used as a tool by them to study the structure of the thin films. In the current study, AFM images confirm the formation of continuous, extended films.

### 4.4.4 Effect of vibrations on the formation of Au nanoparticle aggregates

The fluctuations in the voltage of the photodiode due the fluctuation of the reflected beam are shown in Figure 4.30b. It is evident from Figure 4.30b that the amplitude of voltage fluctuations obtained from simple table is larger than that from the anti-vibration table. The width of the distribution of the voltage fluctuations for simple table is obtained as $w_1 = 7.4$ mV while in case of anti-vibration table $w_2$ is 2.3 mV. This and the corresponding reduction of amplitude in the specular direction, is the direct evidence of larger interfacial fluctuations at toluene-water interface on simple table compared to anti-vibration one. The power spectra obtained through Fourier transform of the voltage fluctuations for the simple table as well as for the anti-vibration table are shown in Figure 4.30c. The fluctuation in air-cushioned anti-

164
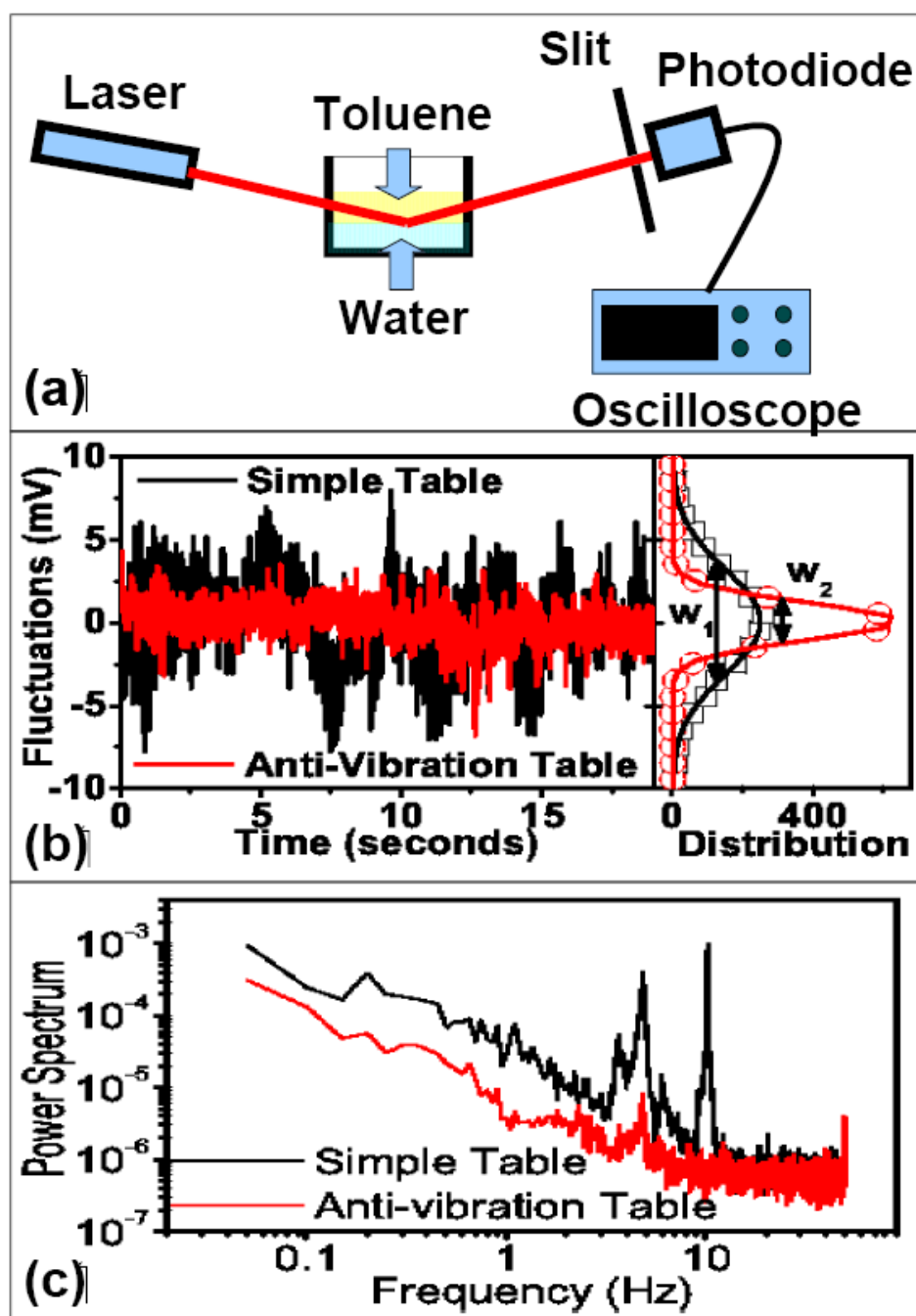
**Figure 4.30.** (a) Schematic of the optical set-up used to measure the interfacial vibrations of toluene-water interface. (b) The voltage fluctuations as a function of time detected in the photodiode due to the fluctuation of reflected laser beam from toluene-water interface. The black solid line corresponds to the fluctuations when the beaker containing toluene-water interface was placed on a simple table and red solid line when placed on anti-vibration table. The distribution of the fluctuations (symbols, red (simple table), black (anti-vibration table)) is shown just right to it along with Gaussian fits (Solid lines) with the corresponding FWHMs $w_1$ & $w_2$. (c) The power spectrum of the voltage fluctuations averaged over 15 measurements obtained from toluene-water interface on simple and anti-vibration tables.

vibration table is reduced substantially especially around 10 Hz frequencies. It should be mentioned here that coupling of vibration of the table with liquid-liquid interface is non-trivial and depends on liquid thicknesses and surface area. It will be interesting to study the interfacial reaction by driving the table with various frequencies.

The topography of Au films grown at the toluene-water interface for 15, 60 and 120 minutes of the reaction on regular laboratory table is shown in Figures 4.31a, 4.31c and 4.31e respectively. The corresponding images for the films obtained by reaction on vibration isolation table are shown in Figures 4.31 b, 4.31d and 4.31f. Thickness of the films is obtained from the height distributions extracted from the regions (insets in Figure 4.31) across the edges of the films. Thickness of the gold nanoparticulate film obtained after 15 minutes of the reaction on the vibration-isolation table is measured to be ~ 2.3 nm (Figure 4.31b), which is ~10 nm thinner than the one obtained by the reaction on simple table (Figure 4.31a). As the reaction proceeds, the films grow in thickness, on both simple as well as anti-vibration tables with a thickness difference of ~ 10 nm. After 1 hour of the reaction, thickness of the films obtained using normal and anti-vibration tables is measured to be ~ 28 nm (Figure 4.31c) and ~ 20 nm (Figure 4.31d) respectively. In the next 1 h of the reaction, the thickness values reach ~ 39 nm (Figure 4.31e) and ~ 30 nm (Figure 4.31f), for the simple and the anti-vibration table respectively.

High-resolution UHV AFM (tapping mode) images of the Au films obtained after 15 minutes of the reaction on normal and anti-vibration tables are shown in Figure 4.32. It is apparent that the height fluctuations are small in both the images due to the presence of organic capping. In the image of the sample prepared on the normal table the average in-plane size of the aggregates is much higher, with a broad size distribution. But the film grown on anti-vibration table clearly showed presence of
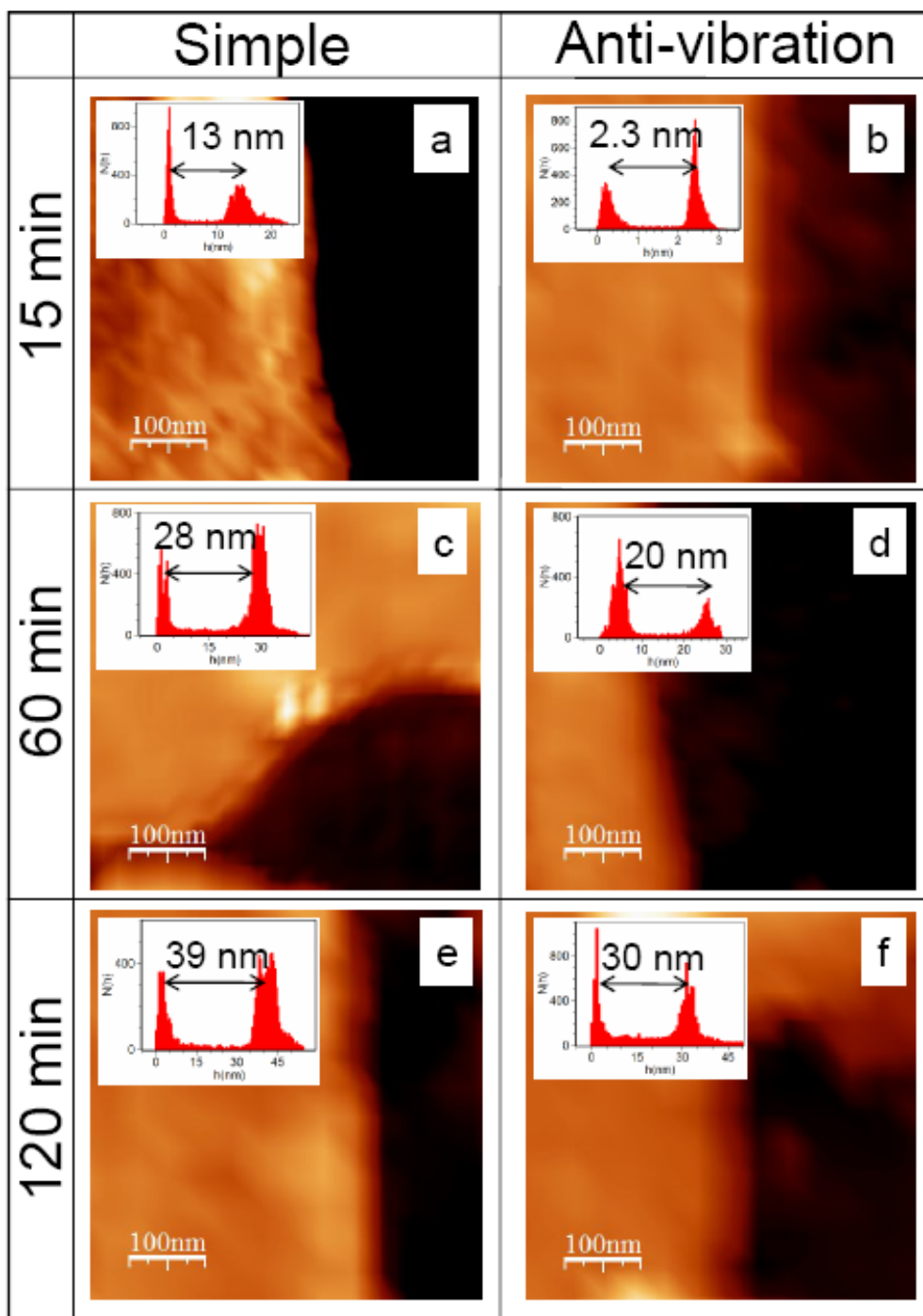
**Figure 4.31.** Tapping mode AFM images of Au films obtained by reactions on simple and anti-vibration tables respectively after 15 minutes (a) and (b); 60 minutes (c) and (d) and 120 min (e) and (f). The dark & bright regions in the images correspond to substrate and nanoparticle film. The height distributions are shown in each of the insets showing two peaks corresponding to the substrate surface and the film surface. The distances between the peaks determine the average thickness of the films.
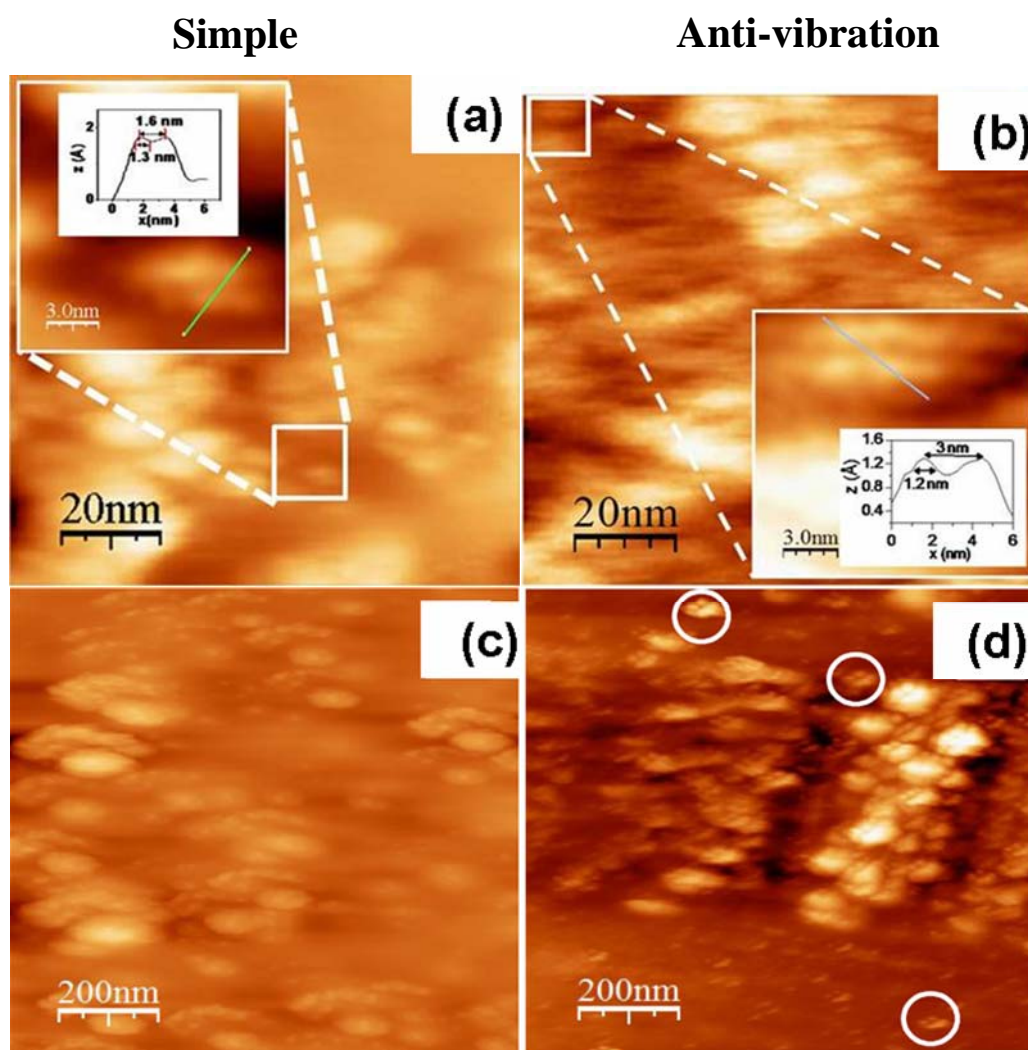
**Figure 4.32.** (a) High-resolution UHV AFM (tapping mode) images of nanoparticles obtained after 15 minutes of reaction on (a) & (c) a normal table, and (b) & (d) anti-vibration table. The regions marked under white squares in (a) & (b) are magnified to show the individual nanoparticles. The insets inside the magnified images are the height profiles to show the particle sizes and separation. 8 nm clusters have been marked by the circles in (d).

primarily 8 nm particles (refer Figure 4.32d). The clusters of this size having 13 member 1.2 nm gold nanoparticles with 1.1 nm organic shell were predicted from X-ray analysis [53]. The images shown in the corresponding insets are magnified

versions of the regions marked by white squares. Both the insets show the presence of individual nanoparticles of sizes ~ 1.2 nm.

The EDS data of the films prepared on the anti-vibration and normal tables given in Figures 4.33a and 4.33b respectively show the presence of Au Mα and P Kα, expected from the organic coating of gold nanoparticles. Under both the reaction conditions the strength of the Au Mα peak increases with reaction time but relative strength of the P peak remains almost constant. This indicates the formation of nanoparticle aggregates having constant gold-to-organic ratio in both types of films.
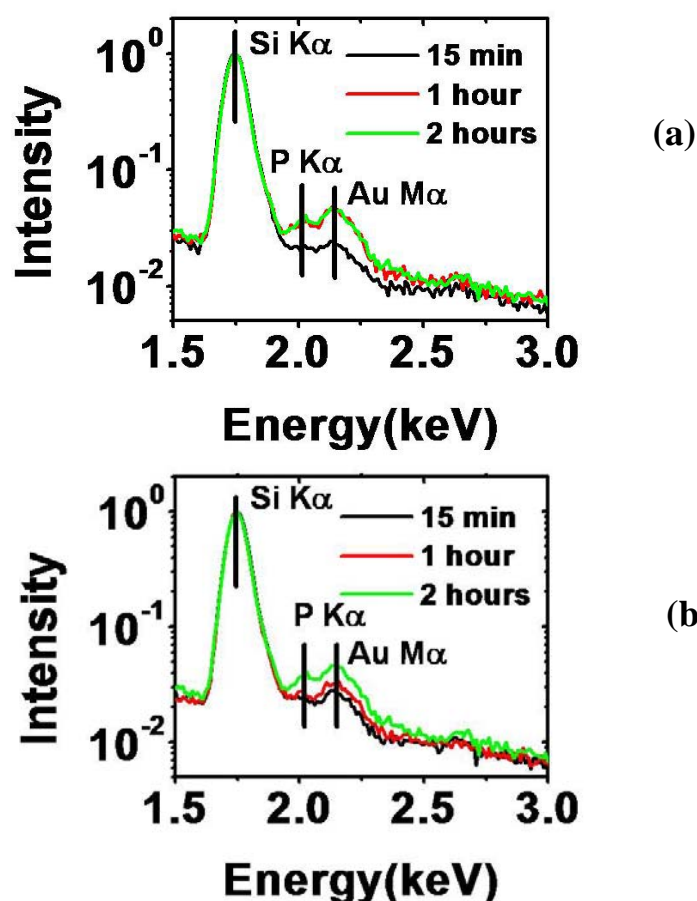


**Figure 4.33.** EDS data as a function of energy normalized with respect to the Si Kα peak are shown for films formed on (a) normal table and on (b) anti-vibration table with different reaction times.

_____

### 4.4.5   Interfacial rheology of CdS and CuS thin films

To follow the CdS and CuS thin film buildup at the interface, an oscillatory

shear of strain amplitude 0.01 % at an angular frequency of 10 rad/s was applied. All

measurements were made on the films only after G′ and G″ reached the saturation.

This ensures that the buildup of the films is complete. Different measurements for a

given reactant concentration were made on a freshly formed film and the preshear

ensures that at a given reactant concentration the initial conditions are identical.

On increasing the concentration of the reagents in the two liquids, the

saturation of G′ and G″ occurs earlier. This is evident from Fig 1, where for the CdS

film obtained at low reactant concentration the saturation of the viscoelastic moduli

occur after 30 minutes (Figure 4.34, curves $a_1$, $b_1$). With increase in the reactant

concentration, the storage and the loss moduli saturate at higher values and the

saturation is achieved at much shorter timescales (Figure 4.34, curves $a_2$, $b_2$).

Interestingly for the CuS film, after the initial transition from the viscous to elastic be-

havior on film formation, periodic breaks are observed up to 20 min (Figure 4.34,

curves $a_3$, $b_3$). This is followed by an increase in the storage and loss moduli after

which they saturate.

SEM measurements on the CdS films indicate a porous morphology for the

film formed at low reactant concentrations (Figure 4.35a). With increase in the

concentration of the reactants, the particle density in the film increases and its

porosity decreases (Figure 4.35b). TEM measurements indicated them to be

composed of single-crystalline nanoparticles of diameter ~ 5 nm and ~ 8 nm, for films

obtained at low and high concentrations respectively [13]. TEM image of the CuS

film (Figure 4.36) reveal the single-crystalline, continuous nature of the film [14]. A

steady shear of 1 s$^{-1}$ on the continuous CuS film resulted in disks of diameter in the
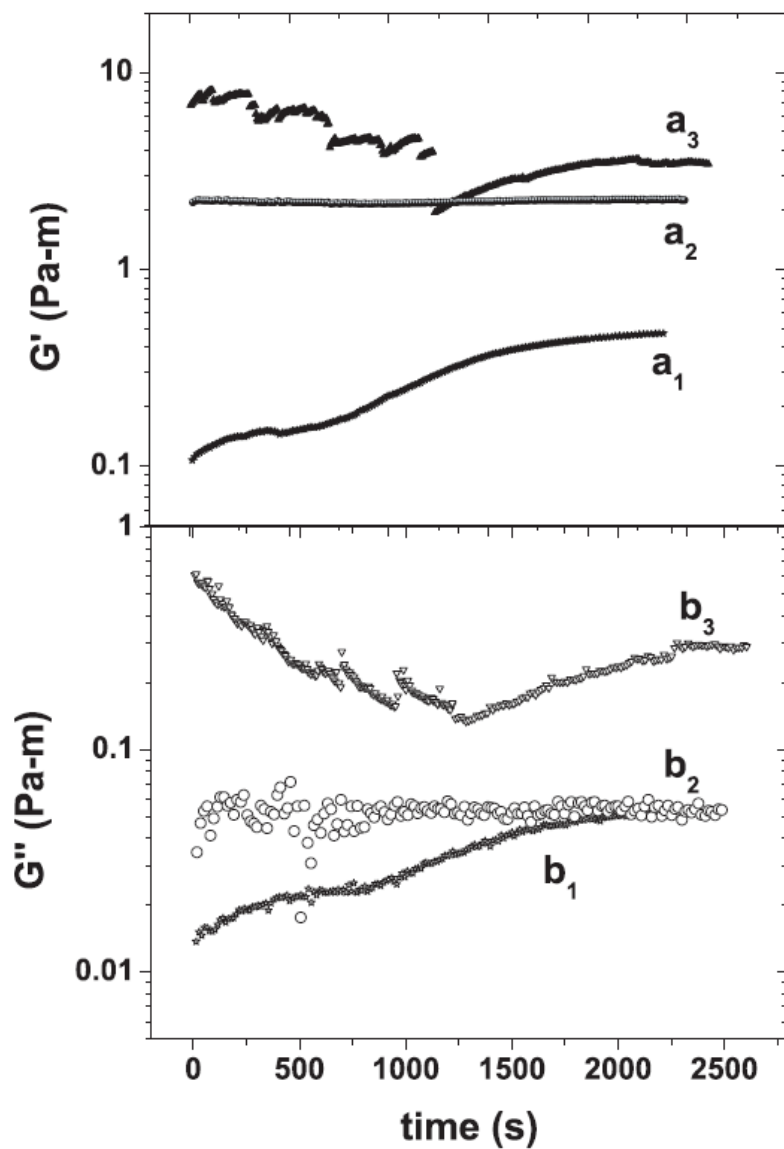
**Figure 4.34.** The evolution of the storage and loss moduli for the CdS film formed at low reactant concentration (curves $a_1$ and $b_1$), CdS film formed at high reactant concentration (curves $a_2$ and $b_2$) and the CuS film (curves $a_3$ and $b_3$) are shown.

_____
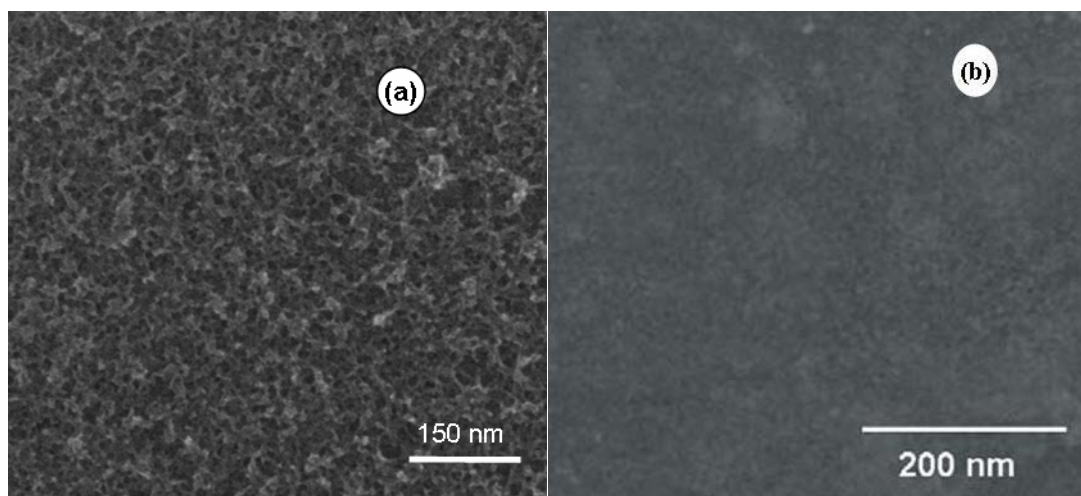


**Figure 4.35.** SEM images of CdS film formed at the toluene-water interface at 22 $^{\circ}$C. (a) The porous film formed using 0.3 mM Cd(cup)$_2$ solution, and (b) densely packed film obtained using 1.2 mM Cd(cup)$_2$ solution.
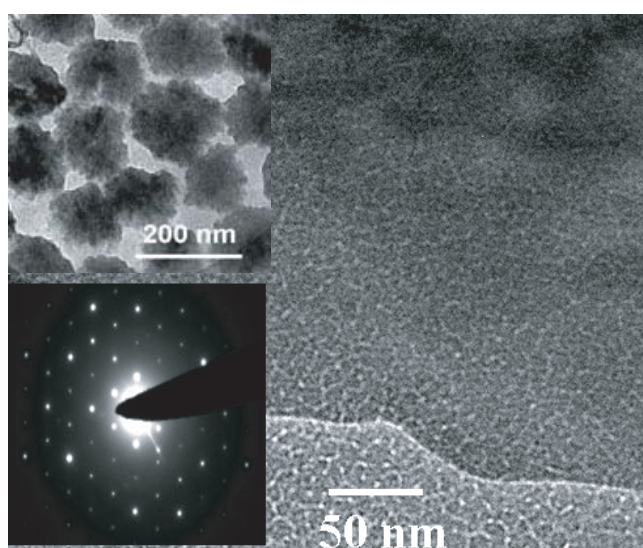


**Figure 4.36.** TEM image of CuS film formed at the toluene-water interface at 22 $^{\circ}$C. SAED pattern of the film is given as the bottom inset. Top inset is the TEM image of the CuS film, after a steady shear of 1 s$^{-1}$, showing the presence of disks.

172

range 100-200 nm (Figure 4.36).

Small angle x-ray scattering studies were carried out to investigate the pore structure of the porous CdS film formed at low reactant concentrations. The power law dependence of the scattering intensity I(q) on the scattering vector $q$ can be used to characterize the pore morphology [66]. The intensity I(q) of the small angle scattering from a pore fractal with fractal dimension D is given by I(q) $\sim$ q$^{-D}$. The pore fractal is obtained from a mass fractal by interchanging the pore space with mass. In general, the small-angle scattering characteristic of a pore fractal is observed at q values corresponding to which the pores may be treated as point scatterers. The scattering at higher q values characterizes the size of the structure producing the scattering, I(q) $\sim$ q$^{-(6-D)}$. The scattering curve obtained for the CdS film at low reactant concentrations exhibits two distinct slopes (Figure 4.37). At length scales > 20 nm, the intensity is proportional to $q^{-3.5}$ which indicates that the film consists of pores bounded by surfaces with a fractal dimension of 2.5. This was found to be valid up to the largest length scales that could be probed by the experimental set up which is 63 nm. The decrease in the power law exponent to 2.2 for length scales < 20 nm, suggests a change in the morphology of the film from a surface fractal to a pore fractal. The scatterers at these length scales are pores which possibly arise due to the presence of interconnected microcracks on the film surface. A similar behavior with two distinct fractal regimes above and below a characteristic length scale has been reported earlier for lignite coal and hydrocarbon source rocks [67,68].

AFM was carried out to measure the thickness of the films. Thicknes of the CdS films varied in the 45-60 nm range depending on the concentrations of the reactants. CuS film was measured to be ~ 50 nm thick.
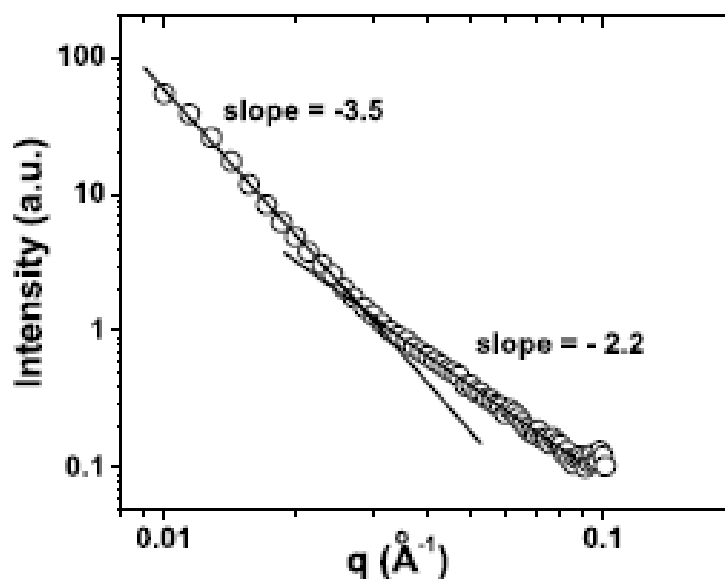
**Figure 4.37.** Small angle X-ray scattering data (after background subtraction) of the porous CdS film formed at low reactant concentrations.

### 4.4.5.1  Interfacial oscillatory shear on the nanofilms

**Amplitude sweep**

To characterize the strength of the films, amplitude sweep measurements (Figure 4.38) were carried out by varying the strain amplitude $\gamma$ from 0.01 to 100 % and by keeping the angular frequency fixed at 10 rad/s. At low strain amplitudes, both $G'$ and $G''$ are independent of $\gamma$ for all the films which corresponds to linear viscoelastic regime. The extent of this linear region is found to vary for the CuS and CdS films.

For CdS films, it is seen that in films formed at low reactant concentrations, the storage and loss moduli decay monotonically above a critical strain amplitude (Figure 4.38a). Though subsequent amplitude sweeps on the same film leads to a decrease in the storage modulus, the film does not rupture completely, indicating a recovery of the structure of the film when the external oscillatory shear stress imposed is removed. An increase in the storage and loss moduli is seen for the films formed at

higher reactant concentrations (Figure 4.38b). Moreover, a peak in $G''$ is observed above a critical strain amplitude. A power law decay is observed for the storage and loss moduli with $G' \sim \gamma^{-2}$ and $G'' \sim \gamma^{-1}$. The decay exponents of the storage and loss moduli for the CdS films obtained at higher concentrations are always found to be in the ratio 2:1. Repeated measurements on the same film yield nearly identical curves.

The decrease in the storage and loss moduli at strain amplitudes higher than the linear viscoelastic regime indicates a disruption in the structure of the film. When $G'$ and $G''$ are not in the linear region, these can be regarded only as apparent values. However, the strain sweep illustrates the general trends in the variation of moduli or structure with strain amplitude. The reproducibility of the amplitude sweep curves also indicates the structural recovery of the films. For the particulate films of CdS, the behavior may be understood as follows. Applying large strain amplitudes lead to the breakdown of the particulate network to form isolated clusters of nanoparticles. Since these clusters remain trapped at the interface, on cessation of dynamic shear, the clusters aggregate to restore the network. Since the amplitude sweeps were carried out immediately in succession upon cessation of the previous shear, it implies that the network structure is recovered instantaneously.

The nonlinear viscoelastic behavior of the CuS film is found to be independent of the reactant concentration. At large strain amplitudes, $G'$ decreases monotonically whereas $G''$ exhibits a peak above a critical strain amplitude (Figure 4.38c) before decreasing at higher values of $\gamma$. At large strain amplitudes, a power law decay is observed for $G'$ and $G''$ with the decay exponents in the ratio 2:1. Subsequent amplitude sweeps carried out on the same film yielded nearly identical curves suggesting a recovery of the structure in the absence of external stress. However, the apparent structural recovery indicated by successive amplitude sweeps on the single

crystalline and continuous CuS film is intriguing. This is because imposing large strain amplitudes can lead to a breakdown in the continuous structure of the film. TEM images of the film recovered after a large amplitude oscillatory shear do indicate that the continuous film transforms to a layer composed of hard disks of 100-200 nm diameter (see Figure 4.36, top inset). Hence the apparent structural recovery of the film might be due to the presence of these disks.
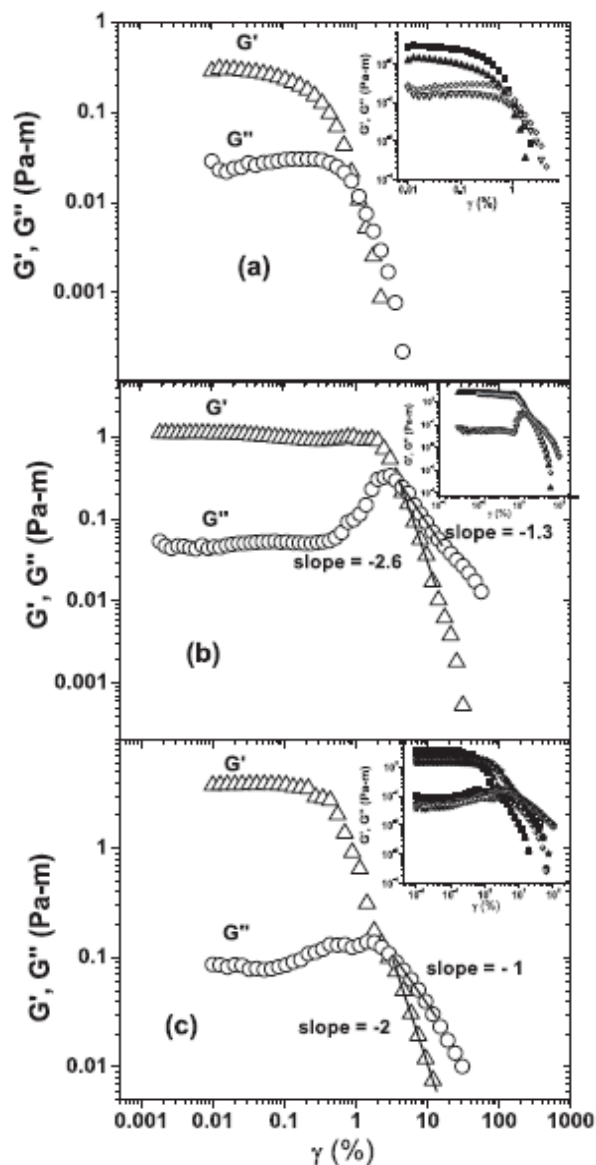


**Figure 4.38.** Strain amplitude sweep measurements on thin films of a) CdS (low reactant concentrations) b) CdS (high reactant concentrations) c) CuS, formed at the toluene-water interface at 22 ∘C. The insets show the curves obtained for subsequent amplitude sweep measurements on the same film. The angular frequency was fixed at 10 rad/s.

The interesting result from the above studies is the large strain-amplitude behavior observed for the films. The peak in $G''$ observed at large strain amplitudes, is a universal feature of many 3D systems ranging from highly cross-linked associative polymers [69], dense colloidal suspensions [70], electrorheological fluids [71], colloidal glasses [72], emulsions [73] and gels [74]. It was also seen recently in some 2D systems such as Langmuir monolayers of insoluble surfactants [55]. Though such a picture emerges from the soft glassy rheology model where a peak in $G''$ is present at the glass transition and absent above [75], it was shown recently that this nonlinear viscoelastic behavior of the storage and loss moduli is more general. The peak in $G''$ at large strain amplitudes is proposed to arise from the dependence of the structural relaxation time $\tau$, on the strain-rate amplitude [54,76] given by:

$$1/\tau = 1/\tau_o + A \mid \dot{\gamma} \mid^\upsilon \qquad (1)$$

where A is a constant and $\tau_o$ is the intrinsic relaxation time. Here the strain-rate amplitude, $\mid \dot{\gamma} \mid = \mid \gamma \mid \omega$ where $\mid \gamma \mid$ is the strain amplitude and $\omega$ the angular frequency. For a simple Maxwell model for $G^*(\omega)$, this would lead to a power law decay of $G'$ and $G''$ at high strain amplitudes, with $G' \sim \mid \gamma \mid^{-2\upsilon}$ and $G'' \sim \mid \gamma \mid^{-\upsilon}$. This behavior is known to be prominent in systems which exhibit slow dynamics including glassy systems. The value of the exponent $\upsilon$ is 1 for CuS film and 1.28 for the CdS film. In many 3D metastable complex fluids as well as in some 2D systems, where the peak in $G''$ is observed, the value of the exponent $\upsilon \leq 1$. Hence the large strain amplitude behavior observed presently for the CdS film where $\upsilon > 1$ is noteworthy.

**Frequency sweep**

Frequency sweep measurements were carried out on the films (Figure 4.39), to probe the structural relaxation of the film by keeping the strain amplitude $\gamma$ fixed at very low values corresponding to the linear viscoelastic regime.

For the CdS films, γ was fixed at 0.01% and the angular frequency was varied from 0.01 to 50 rad/s. For the film formed at low reactant concentrations (Figure 4.39a), G′ is nearly independent of ω over the range of angular frequencies probed. At low angular frequencies (< 0.1 rad/s), G″ is nearly a constant. However at higher frequencies, a power law dependence is observed with $G'' \sim \omega^{-0.16}$. For the CdS film obtained at high reactant concentration (Figure 4.39b), the storage modulus remains constant whereas the loss modulus exhibits a weak power law dependence on the frequency with $G'' \sim \omega^{-0.1}$ over the range of frequencies probed.

The strain amplitude for the CuS film was fixed at 0.01 % and the angular frequencies were varied over the range 0.01 to 100 rad/s (Figure 4.39c). The film is elastic at the angular frequencies probed (G′ > G″). At low frequencies, the storage modulus G′ remains nearly independent of the angular frequency whereas the loss modulus G″ exhibits a minima at 10 rad/s beyond which $G'' \sim \omega^{-0.7}$. Moreover a power law dependence of G″ on $\omega$ is also observed at low angular frequencies, with $G'' \sim \omega^{-0.29}$.

The above study on the CuS and CdS nanofilms clearly indicates that the films exhibit a solid-like behavior over the range of angular frequencies studied with G′ > G″. Surprisingly the frequency response of the single-crystalline, continuous CuS film and that of the CdS film obtained at high reactant concentration is very similar to the nanofilm of Ag nanoparticles, reported earlier, and is a characteristic feature of soft glassy systems [75]. Soft glassy rheology model does predicts such a low frequency behavior just below the glass transition with G′ nearly a constant and $G'' \sim \omega^{x-1}$ where x = 1 corresponds to the glass transition. Accordingly, the effective noise temperature, x is 0.77 for CuS film and 0.9 for CdS film. The frequency sweep measurements discussed above indicate that linear viscoelastic measurements carried
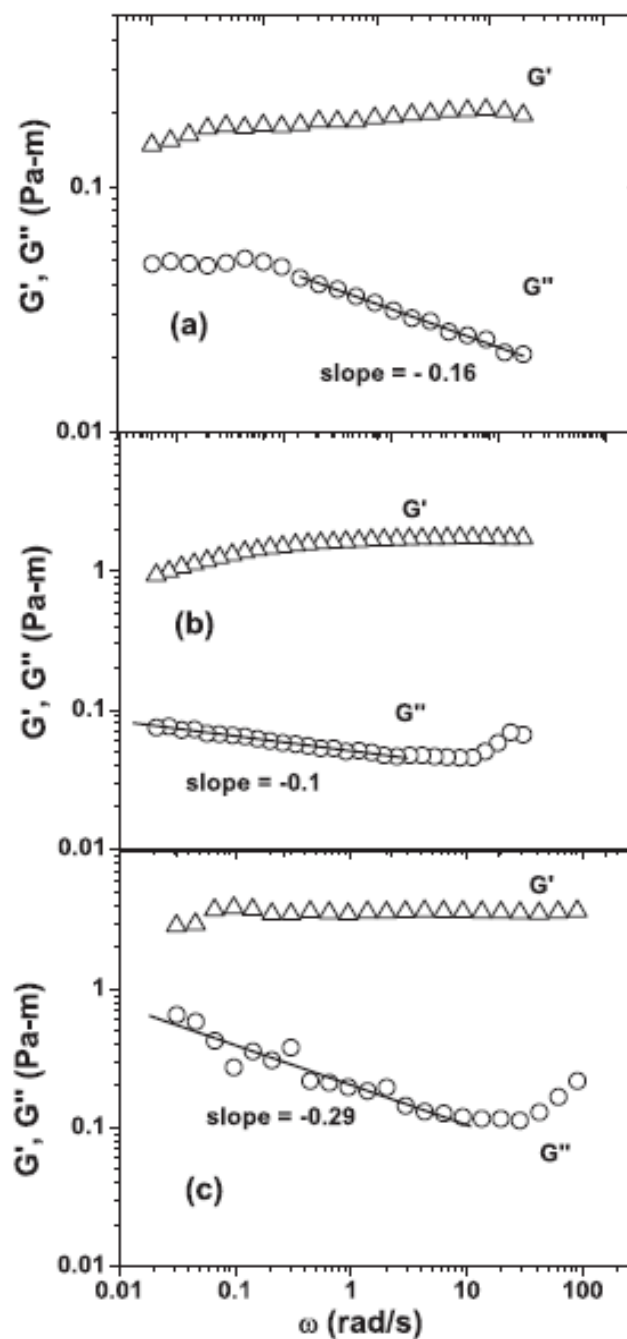
**Figure 4.39.** Frequency sweep measurements on a) CdS (low reactant concentration), b) CdS (high reactant concentration) and c) CuS nanofilms formed at the toluene-water interface at 22 ∘C . The strain amplitude was fixed at 0.01 %. The storage modulus (open triangles) is higher than the loss modulus (open circles) for the films at the angular frequencies probed.

out over the experimentally accessible range of frequencies cannot probe the structural relaxation in these nanofilms.

**Strain-rate frequency sweep**

It was shown recently by Weitz and co-workers that the nonlinear viscoelastic behavior where the peak in G″ appears could be used successfully to extract the structural relaxation times in many 3D metastable systems when the crossover frequencies are not experimentally accessible [54]. They proposed that the distinct shear thickening peak in G″ at high strain amplitudes can arise in metastable systems with long structural relaxation time when the relaxation time is strain-rate dependent. It is relevant in this context to examine whether the nanofilms under study exhibit a strain-rate dependence of the structural relaxation time.

In a regular frequency sweep experiment, the strain amplitude is kept constant whereas the angular frequency is varied over a given range. Hence the strain rate amplitude $|\dot{\gamma}| = |\gamma|\omega$ varies for each data point. The strain-rate dependence of the structural relaxation time can be obtained by varying both the strain amplitude as well as the angular frequency such that the product is constant during the frequency sweep measurements. The frequency sweep measurements carried out on the CuS nanofilm at the toluene-water interface at 22 $^{o}$C, for different values of strain-rate amplitudes ranging from 0.001 s$^{-1}$ to 0.5 s$^{-1}$ are shown in Figure 4.40. The low frequency region, where a liquid-like behavior is observed (G′ < G″), shifts to higher frequencies on increasing the strain-rate amplitudes. A power law dependence of the storage and loss moduli is observed at low angular frequencies with G′ ~ $\omega^{1.4}$ and G″ ~ $\omega$. The crossover frequency shifts to higher frequencies with increase in strain-rate amplitude, confirming the strain-rate dependence of $\tau$ (see inset in Figure 4.40f). The power law
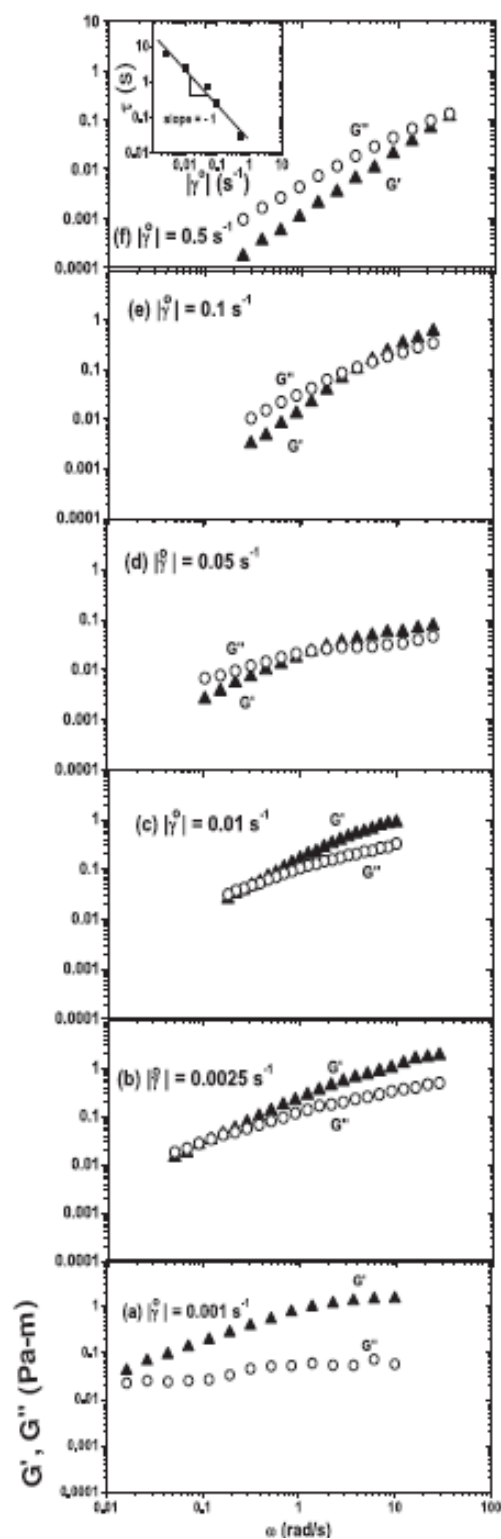
**Figure 4.40.** Frequency sweep measurements carried out on CuS nanofilm at the toluene-water interface 22 °C at constant strain-rate amplitudes $|\dot{\gamma}| = |\gamma|\omega$. G′ (filled triangles) and G″ (open circles) at different strain rate amplitudes a) 0.001 s$^{-1}$; (b) 0.0025 s$^{-1}$; (c) 0.01 s$^{-1}$; (d) 0.05 s$^{-1}$; (e) 0.1 s$^{-1}$ and f) 0.5 s$^{-1}$ are shown. Plot of structural relaxation time vs strain -rate is given as an inset in (f).

exponent $v$ is equal to -1, which is nearly the same as the decay exponent of G″ obtained from amplitude sweep measurements. Recall that for $\tau \sim |\dot{\gamma}|^{-v}$, a simple Maxwell model for G*($\omega$) would lead to G′ $\sim \gamma^{-2v}$ and G″ $\sim \gamma^{-v}$.

The low frequency behavior of the film below the glass transition (Figure 4.39c) where G″ increases as $\omega$ decreases, appear to indicate that the system will achieve structural relaxation, by exhibiting a peak in the loss modulus at lower frequencies. However, for a system undergoing ageing, the characteristic relaxation time is typically of the order of the age of the system itself. Moreover, the amplitude of the loss modulus decreases and that of the storage modulus increases with the age of the system.

### 4.4.5.2  Interfacial steady shear

Under steady shear, a finite yield stress is observed for the nanofilms, as seen from the flow curves given in Figure 4.41. For the CuS nanofilm, the interfacial shear stress remains constant for the shear rates varying from 0.01 s$^{-1}$ to 10 s$^{-1}$. The finite yield stress $\sigma_y = \sigma(\dot{\gamma} \rightarrow 0)$ is 0.003 Pa-m. For the CdS film, the finite yield stress is 0.00024 Pa-m and the film begins to rupture steadily at shear rates $> 0.05$ s$^{-1}$. We have also examined whether the empirical Cox-Merz rule holds for the films under study. Cox-Merz rule suggests that for a shear thinning fluid, the steady shear viscosity $\eta$ ($\dot{\gamma}$) can be related to the dynamic viscosity $\eta^*(\omega)$ such that $\eta(\dot{\gamma}) = |\eta^*(\omega)|$ with $\dot{\gamma} = \omega$. Recall that $|\eta^*(\omega)| = [(G')^2 + (G'')^2]^{1/2} / \omega$.

Figure 4.41 shows the plot of $\eta(\dot{\gamma})$ vs $\dot{\gamma}$ and $|\eta^*(\omega)|$ vs $\omega$ for the different nanofilms at 22 °C. It can be seen that a significant deviation from the Cox-Merz rule is observed for all the films at the shear rates studied.

For systems which exhibit a finite yield stress under steady shear, an extended Cox-Merz rule is found to be valid at high strain amplitudes [77,78], where a correlation exists between steady shear viscosity and the complex dynamic viscosity $\eta(\gamma^{\cdot}) = \eta^{*}(|\gamma|\omega)$ with $\gamma^{\cdot} = |\gamma|\omega$, where $|\gamma|\omega$ is the shear rate amplitude. We examined the validity of this rule for the different nanofilms. In the present system, at high shear rates, the superposition between steady and large amplitude oscillatory shear is valid for both CuS and CdS nanofilms (Figure 4.41). This is not surprising since both steady as well as an oscillatory shear of large strain amplitude involve a large scale deformation that can lead to the rupture of the film.
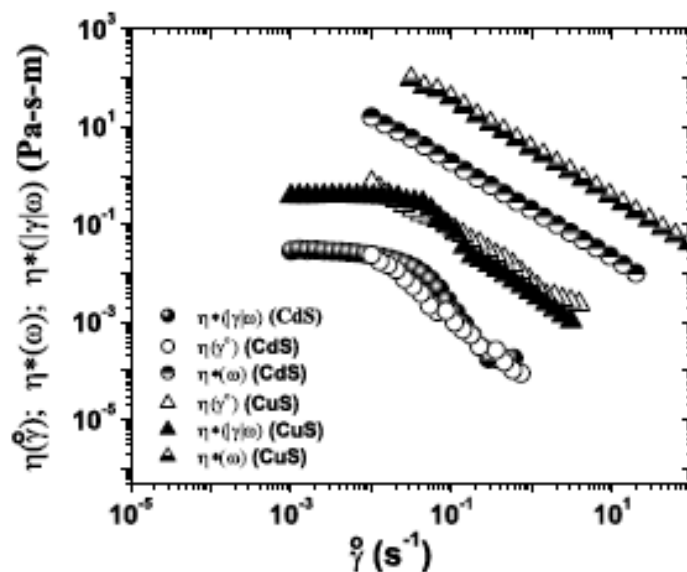


**Figure 4.41.** Dynamic and steady shear viscosities as a function of strain-rate amplitude $|\gamma^{\cdot}| = |\gamma|\omega$, angular frequency ($\omega$) and shear rate ($\gamma^{\cdot}$) measured on CuS (triangles) and CdS (circles) nanofilms are shown. A significant deviation from the empirical Cox-Merz rule (described in the text) is observed for dynamic (half filled symbols) and steady shear viscosities (open symbols). However the extended Cox-Merz rule is reasonably obeyed as seen from the superposition of $\eta^{*}(|\gamma|\omega)$ (filled symbols) at an angular frequency of 10 rad/s with the steady shear viscosity (open symbols).

The superposition between steady and dynamic shear viscosity observed for the different nanofilms (Figure 4.41) provides a clue to the physical origin of the peak

in G″ in the nonlinear viscoelastic measurements. It confirms that the peak in G″ arises not due to an intrinsic shear thickening behavior [79] but from the viscous shear thinning. A large deformation under steady shear or an oscillatory shear of large strain amplitudes leads to a structural rearrangement within the film that drives its structural relaxation to higher frequencies.

## 4.5    Conclusions

Thus, via a simple liquid-liquid interface method it has been possible to prepare thin films of the sulfides ZnS, PbS, as well as the selenides CdSe and CuSe under ambient conditions employing the respective metal cupferronates. Electron microscopy has revealed the single-crystalline nature of ZnS, PbS and CuSe thin films. It is noteworthy that unlike the LB technique where films of nanocrystals are obtained, or other thin-film deposition techniques such as CVD where stringent conditions are required, the liquid-liquid interface method is remarkably simple, yielding even substrate-free single-crystalline films under ambient conditions. The effect of various reaction parameters such as temperature, time, reaction concentrations, and solvent on the nature and properties of the films formed at the interface has been studied. Apart from single-crystalline films of metal sulfides, we could obtain metalsulfide-bilayer such as CdS-CuS at the toluene-water interface by employing the respective metal cupferronates. A time evolution study of the polycrystalline Au and CdS films as well as the single-crystalline CuS films has been carried out by employing atomic force microscopy. Effects of vibrations on the growth of Au nanoparticulate films have been looked into with the help of UHV AFM. In the case of films produced on the anti-vibration table, we get smoother and thinner films and even a monolayer film of the 1.2 nm gold-core with a 1.1 nm organic-coating. The films obtained by reactions on the normal table are much thicker

and composed of aggregates of core-shell nanoparticles. Besides describing features of such nanocrystalline films and their mode of formation, their rheological properties have been examined. The rheological studies show that the single-crystalline CuS film as well as the multilayered CdS film exhibits a viscoelastic behavior strongly reminiscent of soft-glassy systems. The single-crystalline CuS film as well as the multilayered CdS film exhibits a viscoelastic behavior strongly reminiscent of soft-glassy systems, suggesting the formation of a two-dimensional glass at the toluene-water interface. Though both CuS as well as the CdS films exhibit a finite yield stress under steady shear, the CdS films are found to rupture at high shear rates.

## 4.6     References

[1] P. Hoyer, R. Konenkamp, *Appl. Phys. Lett*. 1995, **66**, 349.

[2] K. K. Schuegraf, *Handbook of Thin-film Deposition Processes and Techniques*:

   *Principles, Methods, Equipment and Applications*; Noyes Pub.: Park Ridge (1988).

[3] M. Krishnan, J. R. White, M. A. Fox, *J. Am. Chem. Soc.* 1983, **105**, 7002.

[4] J. D. Dow, I. K. Schuller, *Interfaces, Superlattices, and Thin films; Materials Research Society Symposia Proceeding* **77**, 1987.

[5] M. C. Petty, *Langmuir-Blodgett films: An Introduction*; Cambridge Univ. Press: Cambridge, 1996.

[6] S. Erokhina, V. Erokhin, C. Nicolini, *Langmuir* 2003, **19**, 766.

[7] L. F. Chi, S. Rakers, M. Hartig, H. Fuchs and G. Schmid, *Thin Solid Films* 1998, **327**, 520.

[8] E. S. Smotkin, C. Lee, A. J. Bard, et al. *Chem. Phys. Lett.* 1988, **152**, 265.

[9] C.N.R. Rao, G.U. Kulkarni, V. V. Agrawal, U. K. Gautam, M. Ghosh, U. Tumkurkar, *J. Colloid Interface Sci.* 2005, **289**, 305.

[10] C. N. R. Rao, S. R. C. Vivekchand, K. Biswas, A. Govindaraj, *Dalton Trans.* 2007, 3728.

[11] C. N. R. Rao, G. U. Kulkarni, P. J. Thomas, V. V. Agarwal, P. Saravanan, *J. Phys. Chem. B*. 2003, **107**, 7391.

[12] V. V. Agrawal, P. Mahalakshmi, G. U. Kulkarni, C. N. R. Rao, *Langmuir* 2006, **22**,1846.

[13] U. K. Gautam, M. Ghosh, C. N. R. Rao, *Chem. Phys. Lett.* 2003, **381**, 1.

[14] U. K. Gautam, M. Ghosh, C. N. R. Rao, *Langmuir* 2004, **20**, 10775.

[15] D.A.Edwards, H.Brenner, D. T. Wasan, *Interfacial Transport Processes and Rheology*, Butterworth-Heinemann, 1991.

[16] M. A. Bos, T. V. Vliet, *Adv. Colloid and Interface Sci.* 2001, **91**, 437.

[17] P. Cicuta, E. J. Stancik, G. G. Fuller, *Phys. Rev. Lett.* 2003, **90**, 236101.

[18] R. Krishnaswamy, S. Majumdar, R. Ganapathy, V. V. Agrawal, A. K. Sood, C. N. R. Rao, *Langmuir* 2007, **23**, 3084.

[19] T. Yamamoto, S. Kishimoto, S. Ida, *Phys. B* 2001, **308**, 916.

[20] M. Bredol, J. Merikhi, *J. Mater. Sci.* 1998, **33**, 471.

[21] M.C. López, J.P. Espinos, F. Martín, D. Leinen, J.R. Ramos-Barrado *J. Crys. Growth* 2005, **285**, 66.

[22] S.D. Sartale, B.R. Sankapal, M. Lux-Steiner, A. Ennaoui, *Thin Solid Films* 2005, **480,** 168.

[23] S. Lindroos, Y. Charreire, D. Bonnin and M. Leskelä, *Mater. Res. Bull.* 1998, **33**, 453.

[24] B. W. Sanders, A. H. Kitai, *J. Crys. Growth* 1990, **100**, 405.

[25] M. Yokoyama, K. Kashiro, S. Ohta, *Appl. Phys. Lett.* 1986, **49**, 411.

[26] O. Osasona, A. Djebah, I. A. O. Ojo, et al., *Optical Materials* 1997, **7**, 109.

[27] N. R. Pawaskar, S.D. Sathaye, M. M. Bhadhbhade, K.R. Patil, *Mater. Res. Bull.* 2002, **37**, 1539.

[28] R. S. Kane, R. E. Cohen, R. Silbey, *J. Phys. Chem.* 1996, **100**, 7928.

[29] P. Gadenne, Y. Yagil, G. Deutscher, *J. Appl. Phys.* 1989, **66**, 3019.

[30] R. Hawaldar, U. Mulik, K. Patil et al., *Mater. Res. Bull.*, 2005, **40**, 1353.

[31] M. Ichimura, T. Narita, K. Masui, *Mater. Sci. Eng. B*, 2002, **96**, 296.

[32] P. K. Nair, M. T. S. Nair, V. M. García et al., *Sol. Energy Mater. Sol. Cells* 1998, **52**, 313.

[33] T. Torimoto, S. Takabayashi, H. Mori, S. Kuwabata, *J. Electroanal. Chem.* 2002, **522**, 33.

[34] J. Puiso, S. Lindroos, S. Tamulevisius, M. Leskelä, V. Snitka, *Thin Solid Films*, 2003, 428, 223.

[35] R. K. Pandey, S. Mishra, S. Tiwari, P. Sahu, B. P. Chandra, *Sol. Energy Mater. Sol. Cells* 2000, **60**, 59.

[36] P. Mahawela, S. Jeedigunta, S. Vakkalanka, C.S. Ferekides, D.L. Morel, *Thin Solid Films* 2005, **480**, 486.

[37] M. J. Deen, S. L. Rumyantsev, D. Landheer, D. X. Xu, *Appl. Phys. Lett.* 2000, **77**, 2234.

[38] S. C. Lee, M. J. Lee, *J. Appl. Phys.* 2000, **88**, 1999.

[39] R. L.Morales, M. R. Falfán, O. P. Moreno et al., *J. Electrochem. Soc.* 1999, **146**, 2546.

[40] K.R. Murali, V. Subramanian, N. Rangarajan, et al. *J. Electroanal Chem.* 1994, **368**, 95.

[41] K. R. Murali, K. Srinivasan, D. C. Trivedi, *Mater. Sci. Eng., B* 2004, **111**,1.

[42] T. Elango, V. Subramanian, K.R. Murali, *Surf. Coat. Technol.* 2000, **123**, 8.

[43] V.M. Bhuse, *Mater. Chem. Phys.* 2005, **91**, 60.

[44] K.R. Patil, D.V. Paranjape, S.D. Sathaye et al. *Mater. Lett.* 2000, **46**, 81.

[45] S. T. Lakshmikumar, *Mater. Solar Cells* 1994, **32**, 7.

[46] R.S. Mane, S.P. Kajve, C.D. Lokhande, S.-H. Han, *Vacuum* 2006, **80**, 631.

[47] C. L. Clement, M. N. Spallart, S.S.K. Haram, S.V. Santhanam, *Thin Solid Films* 1997, **302**, 12.

[48] V.M. Bhuse, P.P. Hankare, K.M. Garadkar, A.S. Khomane, *Mater. Chem. Phys.* 2003, **80**, 82.

[49] I. Grozdanov, *Synthetic Met.* 1994, **63**, 213.

[50] Z. Zainal, S. Nagalingam, T. C. Loo, *Mater. Lett.* 2005, **59**, 1391.

[51] M. Dhanam, P.K. Manoj, R.R. Prabhu, *J. Cryst. Growth* 2005, **280**, 425.

[52] R. R. Pai, T. T. John, M. Lakshmi, K.P. Vijayakumar, C. S. Kartha, *Thin Solid Films* 2005, **473**, 208.

[53] M. K. Sanyal, V. V. Agrawal, M. K. Bera, K. P. Kalyanikutty, J. Daillant, C. Blot, S. Kubowicz, O. Konovalov, C. N. R. Rao, *J. Phys. Chem. C* 2008, 112, 1739 .

[54] H. M. Wyss, K. Miyazaki, J. Mattson, Z. Hu, D. R. Reichman, D. A. Weitz, *Phys. Rev. Lett.* 2007, **93**, 238303.

[55] R. Krishnaswamy, S. Majumdar, A. K. Sood, *Langmuir*, 2007, **23**, 12951.

[56] G. Schmid (Ed:), *Nanoparticles: From Theory to Applications*, Wiley-VCH, 2004.

[57] P. Erni, P. Fischer, E. J. Windhab, *Rev. Sci. Instrum.* 2003, **74**, 4916.

[58] Khan, M.; Oldham, C.; Tuck, D. G. *Can. J. Chem.* 1981, **59**, 2714.

[59] J. Nanda, S. Sapra, D. D. Sarma, N. Chandrasekharan, G. Hodes, *Chem. Mater.* 2002, **12**, 1018.

[60] N. I. Kovtyukhova, E. V. Buzaneva, C. C. Waraksa, T. E. Mallouk, *Mater. Sci. Eng.B* 2000, **69**, 411.

[61] M. T. Nenadovic, M. I. Comor, V. Vasic, O.I. Micic, *J. Phys. Chem.* 1990, **94**, 6390.

[62] J. H. Warner, A. R. Watt, M. J. Fernee, N. R. Heckenberg, H. R. Dunlop, *Nanotech.* 2005, **16**, 479.

[63] V. I. Klimov, *J. Phys. Chem. B* 2000, **104**, 6112.

[64] U.K. Gautam, B. Mukherjee, *Bull. Mater. Sci.* 2006, **29**, 1.

[65] V. V. Agrawal, G. U. Kulkarni, C. N. R. Rao, J. Phys Chem B 2005, **109**, 7300.

[66] P. W. Schmidt, *J. Appl. Cryst.*1991, **24**, 414.

[67] A. P. Radlinski, C. J. Boreham, *Phys. Rev. B* 1996, **53**, 14152.

[68] P. U. Sastry, D. Sen, S. Mazumdar, K. S. Chandrasekaran, *Solid State Commun.* 219, **114**, 219.

[69] V. Tirtaatmadja, K. C. Tam, D. R. Jenkins, *Macromol.* 1997, **30**, 1426.

[70] F. Yziquel, P. J. Carreau, P. A. Tanguy, *Rheol. Acta.* 1999, **38**, 14.

[71] M. Parthasarathy, D. J. Klingenberg, *J. Non-Newtonian Fluid Mech* 1999, **81**, 83.

[72] T. G. Mason, D. A. Weitz, *Phys. Rev. Lett.* 1995, **75**, 2770.

[73] T. G. Mason, M. Lacasse, G. S.Grest, et al. *Phys. Rev. E* 1997, **56**, 3150.

[74] P. Panizza, D. Roux, V. Vuillaume, C. Y. D. Lu, M. E. Cates, *Langmuir* 1998, **58**, 738.

[75] P. Sollich, F. Lequex, P. Hebraud, M. E. Cates, *Phys. Rev. Lett* 1997, **78**, 2020.

[76] K. Miyazaki, H. M. Wyss, D. A. Weitz, D. A. Reichman, *Europhys.Lett.* 2006, **75**, 915.

[77] D. Doraiswamy, A. N. Mujumdar, I. Tsao, A. N. Beris, S. C. Danforth, A. B. Metzner, *J. Rheol.* 1991, **35**, 647.

[78] A. Mujumdar, A. N. Beris, A. B. Metzner, *J. Non-Newtonian Fluid Mech.* 2002, **102**, 157.

[79] R. L. Hoffmann, *Trans. Soc. Rheol.* 1972, **16**, 155.

# CHAPTER 5

# High-temperature Synthesis of Large Pore Mesoporous Fm3m Aluminosilicates

**SUMMARY**

Preparation of cubic cage type mesoporous aluminosilicates (AlKIT-5) at temperatures higher than 100 $^o$C has been presented in this chapter. Al has been incorporated into KIT-5 framework at different temperatures. The materials have been characterized by various techniques such as XRD, HR-SEM, EDS, HR-TEM and $N_2$ adsorption. It has been found that the synthesis temperature plays a significant role in controlling the textural parameters of the materials. Al content, pore diameter and pore volume of these aluminosilicates have been found to be drastically higher compared to those prepared at 100 $^o$C. It has been also demonstrated that the distribution of mesopores can be controlled by varying the synthesis temperature, which otherwise cannot be achieved for the materials prepared at low temperatures by employing a single type of template. Interestingly, these materials, prepared at higher temperatures have been found to show superior catalytic activity in the acetylation of veratrole by acetic anhydride even at the room temperature, in comparison to those prepared at 100 $^o$C, AlMCM-41, and other zeolite materials.

### 5.1     Introduction

Mesoporous materials based on silica with ordered structure for long have been an area of active research due to their significant applications in diverse fields such as catalysis, drug delivery, fuel cells, sensors, adsorption, and nanoscience due to their high surface area and pore volume, and tunable nanopores [1-5]. Ordered mesoporous silicas such as MCM-41 [6], MCM-48 [7], SBA-3 [8], SBA-15 [9], and KIT-1 [10], which were initially discovered, comprise 2-D hexagonal arrays of non-intersecting pores. Later on discovered silicas with ordered cage-like mesoporous structures (OSCMs) have received much attraction owing to the high pore connectivity and superior textural parameter tailoring opportunities offered by them [1]. Their discovery was a major milestone in the field of mesoporous materials, which helped to extend the cage dimensions attainable for zeolites from micropore to the mesopore range (2-50 nm). For instance, cubic I*m3m* SBA-16 [11], P*m3n* characteristic of both SBA-1 and SBA-6 [11], F*m3m* KIT-5 [12], and F*m3m* with hexagonal intergrowth FDU-1 [13], have been reported. OSCMs are thought to be more advantageous than traditional mesoporous materials especially in catalysis, adsorption, and immobilization and separation of bulky biomolecules, because of the presence of numerous adsorption sites which are easily accessible via 3D pore channels and their improved resistance to pore blocking. OSCMs, with easily accessible pores from the surface compared to those of unidimensional systems, synthesized in the form of thin films have been reported to exhibit significant sensing properties [14]. OSCMs have also been used as templates in the preparation of nanocrystals [15] and mesoporous carbon [16].

In order to increase the ion exchange capability, acidity and catalytic reactivity of pure mesoporous silica, incorporation of heteroatoms such as V [17], Mo [18], and

Al, Sn, Zn and Mn [19] into the siliceous framework has been carried out. More recently Al substituted 3D cubic KIT-5 material at 100 $^o$C has been reported [20]. Herein, we report the hydrothermal synthesis of Al incorporated KIT-5 (AlKIT-5) materials at temperatures higher than 100 $^o$C, with improved textural parameters. Also, these AlKIT-5 materials, prepared at higher temperatures are found to be better catalysts in the acylation of veratrole using acetic anhydride.

## 5.2    Scope of the present study

The use of block copolymers as templates in the synthesis of large-pore OSCMs has recently attracted much interest owing to their ability to direct the formation of the pores of varying sizes depending on the synthesis temperature [12,13,21]. The triblock copolymer Pluronic F127 has been used as a template by Kleitz and co-workers recently for preparing cubic F*m3m* mesoporous silica (KIT-5) with large pores and high specific volume [12]. The KIT-5 materials with tunable pores and interesting structure find many applications as templates, catalysts etc. In spite of their advantages, applications of the OSCMs in fields such as catalysis, adsorption and separation are limited due to their neutral framework, weak acidity and low ion-exchange capacity, which can be overcome by the incorporation of heteroatoms into the silica framework. Nonetheless, it is extremely difficult to incorporate metal ions into the mesoporous silicas with three-dimensional cage-like porous structures prepared in a highly acidic medium. This is mainly due to the high solubility of the metal source under such a condition. Recently, Vinu *et al.* demonstrated the incorporation of Al into the cage type mesoporous silica (KIT-5) [20] in a highly acidic medium by controlling the water to HCl molar ratio, at 100 °C. Unfortunately, the materials exhibited a low Al content and a small pore diameter.

_____

Commercial preparation of important ketones is usually carried out in batch reactors over conventional homogenous catalysts catalysts such as $AlCl_3$, $FeCl_3$ and HF [22]. These catalysts which are used in more than the stoichiometric amounts cause environmental pollution. Also, their separation from the product mixture is rather difficult. Heterogeneous catalysts, on the other hand are environmentally benign, reusable and can be easily recovered. Zeolites such as Hβ and HY have been used as catalysts, in the synthesis of the industrially important ketone, acetoveratrone (obtained by the acetylation of verarole) which is the precursor of papaverine, an antispasmodic. However, the catalysts have been found to deactivate easily [23]. Hence, there is still a good demand for catalysts with better textural parameters and acidity for the acetylation of veratrole.

Here we describe the successful preparation of ultra-large pore AlKIT-5 materials with a high Al content using Pluronic F127 as the template, at synthesis temperatures higher than 100 $^o$C. It has been found that the synthesis temperature plays a significant role in controlling the Al content, pore volume, pore diameter, and acidity of the materials. We find that the synthesis carried out at high temperatures results in formation of a more open than cage-like pore structure. These materials, prepared at higher temperatures show very high catalytic activity in the acetylation of veratrole by acetic anhydride even at temperatures as low as 35 $^o$C, in comparison to those prepared at 100 $^o$C and other zeolite materials.

## 5.3    Experimental and related aspects

### 5.3.1   Synthesis

The mesoporous aluminosilicates (AlKIT-5) samples were prepared hydrothermally using Pluronic F127 as the template, and TEOS and aluminium isopropoxide (AiPr) as the sources of Si and Al respectively. In a typical synthesis, 5.0 g of F127

was dissolved in the required amount of HCl (35 wt %) and 240 g of distilled water by stirring for 4 h at 45 $^{o}$C. To this mixture, 24.0 g of TEOS and 1.986 g of AiPr was added ($n_{Si}/n_{Al}$ = 12). The resulting mixture was stirred for 24 h at 45 °C. The reaction mixture was then treated hydrothermally for 24 h at 130 °C under static condition in a Teflon-lined autoclave. The solid product was filtered without washing and dried at 100 °C. The dried sample was calcined at 540 °C for 10 h. The procedure was repeated by carrying out the hydrothermal reaction at temperatures of 150 °C and 180 °C.

## 5.3.2 Techniques used for characterization

X-ray diffraction patterns of the calcined products were recorded using a Rigaku diffractometer with Cu K$_{\alpha}$ radiation, operating at 40 kV and 40 mA. Energy dispersive X-ray spectroscopy (EDS) analysis and elemental mapping of the samples were carried out using Hitachi S400 HR-FESEM at an accelerating voltage of 30kV. High-resolution transmission electron microscopy (HRTEM) images were obtained on JEOL JEM- 2100 F, operating at an accelerating voltage of 200 kV. N$_2$ adsorption-desorption isotherms were measured at -196 $^{o}$C on a Quantachrome Autosorb 1 volumetric adsorption analyzer. Prior to the measurements the samples were outgassed at 250 °C for 3h. Pore-size distribution of the samples was calculated using Barrett-Joyner-Halenda (BJH) method.

The average wall thickness of the materials (h) was calculated using the following equation, as proposed by Ravikovitch et al. [27].

$$h = [D_{me}/3] [1-\varepsilon_{me}] / \varepsilon_{me}$$

Where, $D_{me}$ is the diameter of the cavity of a cubic unit cell of length *a*, $\varepsilon_{me}$ is the volume fraction of regular cavities and $\nu$ is the number of cavities present in the

unit cell (for Fm3m space group, $\nu = 4$).

***Catalytic reactions:*** Acetylation of veratrole with acetic anhydride ($Ac_2O$) was carried out in liquid phase. In a typical reaction, 2.61 g (18.89 mmol) of veratrole was treated with 0.39 g (3.82 mmol) of acetic anhydride in the presence of 0.15 g catalyst (5 wt% of total reaction mixture) at 35 $^o$C in a two-necked round bottom flask fitted with a condenser. The sample collected after 1 hr of the reaction was analyzed using the gas chromatograph GC-2010 (Shimadzu Corp.).

## 5.4 Results and discussion:

To examine the composition of the aluminosilicate materials synthesized at different temperatures, HRSEM-EDS and inductively coupled plasma analysis (ICP) were carried out. The EDS spectra of the calcined materials prepared at (i) 130 $^o$C, (ii) 150 $^o$C and (iii) 180 $^o$C are given in Figure 5.1 a. The spectra showing peaks only for O, Al and Si indicate the purity of the samples, thus confirming the complete removal of the surfactant used as the template. The $n_{Si}/n_{Al}$ ratios of the aluminosilicates obtained from the EDS analysis are consistent with those obtained from ICP analysis. The $n_{Si}/n_{Al}$ values are found to increase with increase in the synthesis temperature of the AlKIT-5 samples. As listed in Table 5.1, the $n_{Si}/n_{Al}$ ratio decreases from 36 for calcined AlKIT-5 synthesized at 130 $^o$C to 31 for that prepared at 150 $^o$C, and reaches a value of 25 for the material prepared at 180 $^o$C. The large difference in the $n_{Si}/n_{Al}$ ratio of the synthesis gel which is 12, and the calcined materials indicates an appreciable loss of Al during the synthesis. The loss of Al can be accounted to the low pH of the synthesis medium (~2) leading to a very high solubility of the Al source. However, it is to be noted that these AlKIT-5 materials prepared at high temperatures show a drastic increase in the amount of incorporated Al, compared to that prepared at
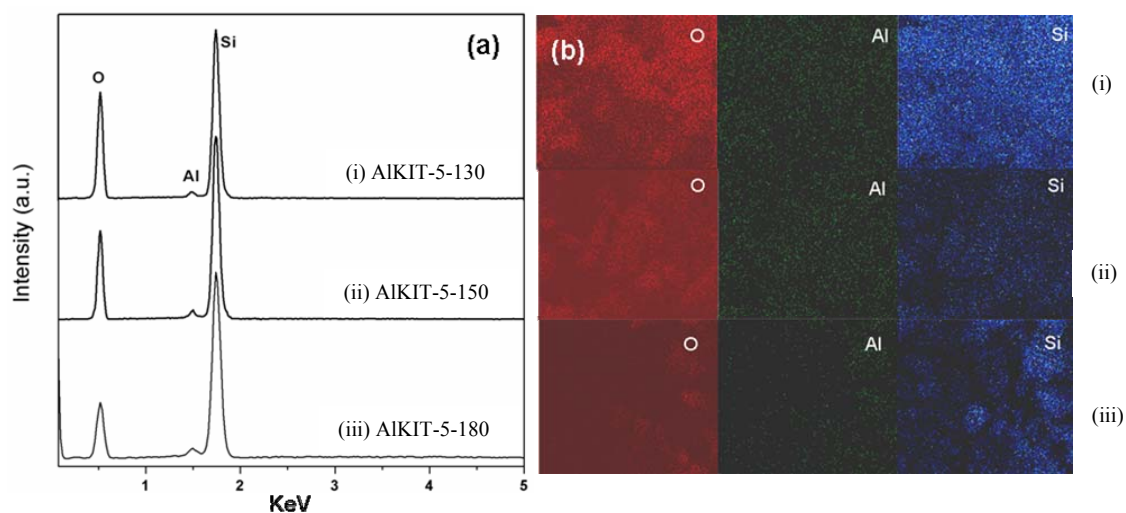
**Figure 5.1.** (a) HRSEM-EDS spectra of AlKIT-5 materials prepared at (i) 130 $^o$C, (ii) 150 $^o$C and (iii) 180 $^o$C, and (b) the corresponding elemental mappings.

| Catalyst | $a_0$ (nm) | $n_{Si}/n_{Al}$ (product) | $A_{BET}$ ($m^2g^{-1}$) | $V_P$ ($cm^3g^{-1}$) | $dp_{ads}$ BJH (nm) | Wall thickness (nm) |
|---|---|---|---|---|---|---|
| AKT-130 | 19.1 | 36 | 796 | 1.08 | 7.3 | 2.0 |
| AKT-150 | 19.8 | 31 | 596 | 1.18 | 9.2 | 1.9 |
| AKT-180 | 21.8 | 25 | 392 | 1.12 | 13.5 | 2.2 |

**Table 5.1.** Textural parameters of the the AlKIT-5 materials synthesis at different temperatures.

100 $^{o}$C ($n_{Si}/n_{Al}$ = 44) [1]. The higher Al content in the samples prepared at higher temperatures can be attributed to the increased rate of condensation of silanol groups during the formation of the silica framework, which leads to an increased incorporation of Al metal into the framework. Elemental mappings of the AlKIT-5 materials prepared at 130 $^{o}$C (i), 150 $^{o}$C (ii) and 180 $^{o}$C (iii) are given in Figure 5.1 b, showing the uniform distribution of Al and Si atoms.
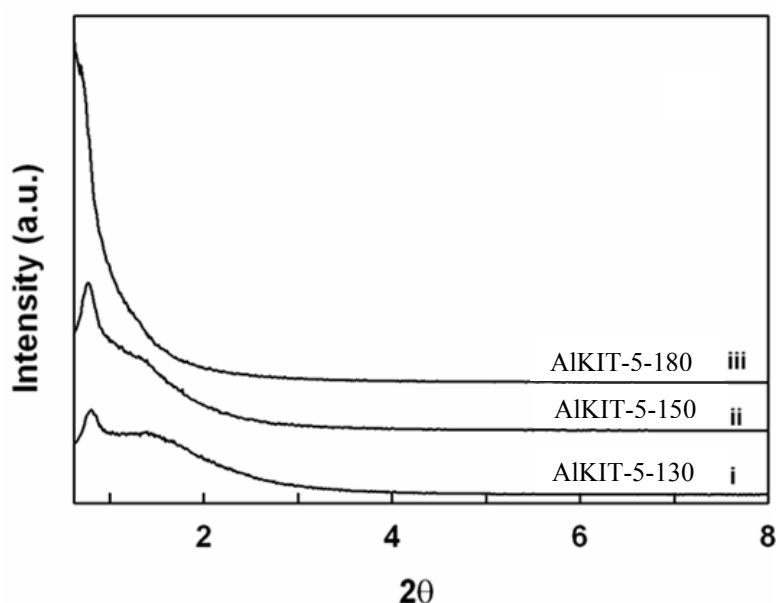


**Figure 5.2.** XRD patterns of AlKIT-5 materials prepared at (i) 130 $^{o}$C, (ii) 150 $^{o}$C and (iii) 180 $^{o}$C.

XRD patterns of the aluminosilicates synthesized at the different temperatures given in Figure 5.2 are typical of materials with long range ordered domains. The reflections correspond to the (111), (200) and (220) Bragg planes of cubic silica (Fm3m space group) [20]. As can be observed from Figure 5.2, the diffraction peaks shift towards lower 2θ values with increase in the synthesis temperature of the aluminosilicates, corresponding to an increase in the unit cell length from 19.1 nm to 21.8 nm (see Table 5.1). The unit cell length ($a_o$) of the

_____

AlKIT-5 samples is given in Table 5.1. Increase in Al content as obtained from ICP and EDS analyses and the increase in unit cell constant with increasing temperature of synthesis indicates increased amount of Al incorporation into the silica network. This suggests that with increase in synthesis temperature, the interaction between the Al oxo species and the silica species enhances. Also, as can be seen from Figure 5.2, increasing the synthesis temperature leads to dampening of the diffraction peaks probably due to a structural transformation of the AlKIT-5 materials from 3D cage type system to a more planar system. For AlKIT-5, prepared by the same method at 100 $^{o}$C, the unit cell constant was found to be 16.9 nm [20]. The higher value of lattice constant for the AlKIT-5 materials prepared at higher temperatures also indicates increased incorporation of Al into the silica network.
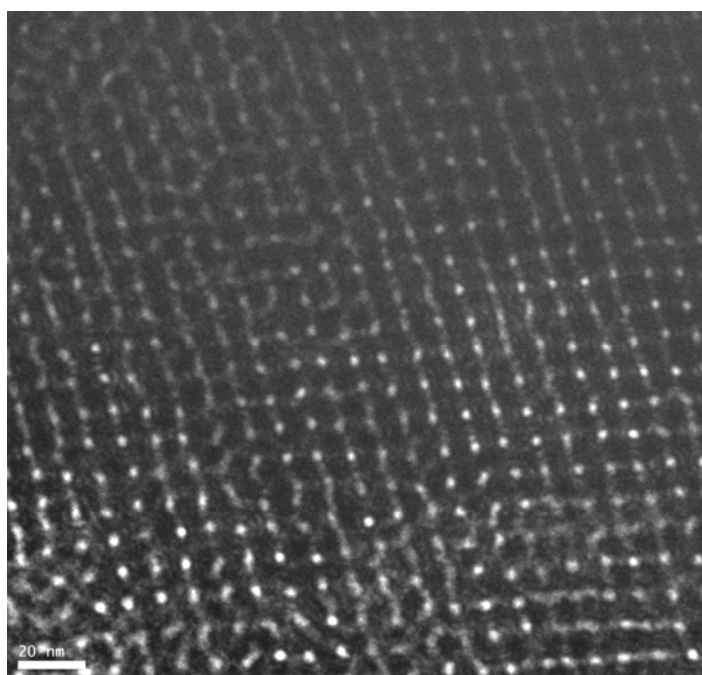


**Figure 5.3.** HRTEM image of AlKIT-5 prepared at 130 $^{o}$C.

The HRTEM image of AlKIT-5 synthesized at 130 $^{o}$C in Figure 5.3 confirms the presence of 3D mesoscopic ordering in the material. The image shows a highly

ordered network composed of linear arrays of mesoporous channels, a characteristic of well-ordered mesoporous silica.

In Figure 5.4 are given the $N_2$ adsorption isotherms of AlKIT-5 materials prepared at the three different hydrothermal temperatures. All the plots exhibit type IV curve with a hysteresis loop, a characteristic of mesoporous materials. AlKIT-5 prepared at 130 $^{o}$C (Figure 5.4a) shows a broad hysteresis loop, typical of a 3-D cage-type mesoporous material. As can be seen from Figure 5.4, with increase in synthesis temperature, the hysteresis loop narrows down, indicating a transformation from a 3-D cage-type pore structure to a more open pore structure. Thus AlKIT-5-180, showing a very narrow loop, seems to be structurally more close to a planar material. Such a structural transformation with increasing synthesis temperature was evident from the XRD patterns (Figure 5.2) of the materials as well. The capillary condensation step shifts to higher relative pressures as the synthesis temperature increases, resulting from the corresponding increase in pore diameter. Pore diameters obtained from the adsorption branch of the isotherm is given in Table 5.1, showing an increase from 7.3 nm for AlKIT-5-130 to 13.5 nm for AlKIT-5-180. It is to be noted that the AlKIT-5 materials prepared at 100 $^{o}$C, had very small pores (5.2 nm). Thus, by carrying out the synthesis at temperatures higher than 100 $^{o}$C, pore diameter of the AlKIT-5 materials could drastically be increased. Pore size distribution (PSD) curves of the materials are also given in Figure 5.4, along with the isotherms. As can be seen from the PSDs, AlKIT-5-130 exhibits a bimodal distribution of mesopores, whereas for AlKIT-5-150 and AlKIT-5-180 the PSD is unimodal. Also, the PSD widens with increase in the synthesis temperature. As can be seen from Figure 5.4, AlKIT-5-180 shows a very wide distribution of pores in comparison to AlKIT-5-130 and AlKIT-5-150. This increase in broadness of the pore size distribution with synthesis temperature, again

_____
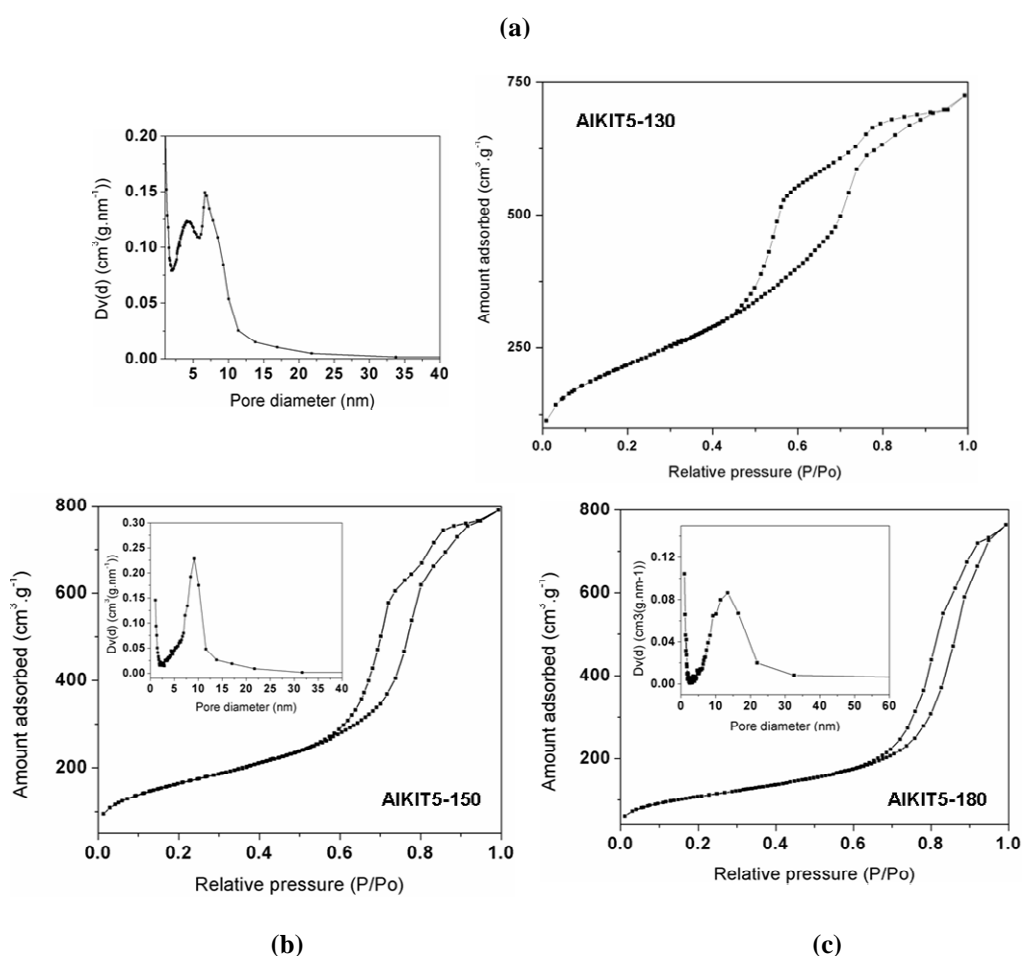
Figure 5.4. Nitrogen adsorption isotherms along with the PSDs of AlKIT-5 materials prepared at (a) 130 °C, (b) 150 °C and (c) 180 °C.

indicates a structural transformation in the materials at very high temperature, from a 3-D cage structure to a more open pore structure.

On increasing the synthesis temperature from 130 °C to 180 °C, the specific surface area of the materials is found to decrease by a considerable amount. AlKIT-5-130 shows a very high specific surface area of 796 m$^2$/g, which decreases to 392 m$^2$/g for AlKIT-5-180. The pore volume of the AlKIT-5 materials increases as a function of synthesis temperature from 1.08 cm$^3$/g for AlKIT-5-130 to 1.18 cm$^3$/g for AlKIT-5-150. But for the aluminosilicate prepared at 180 °C, the pore volume is measured to be 1.12 cm$^3$/g. The decrease in the specific pore volume for AlKIT-5-180 might be

_____

due to the almost complete loss of the cage-type structure for the material at the very high temperature. The calculated wall thickness of the materials, which depends on the total pore volume, shows a trend similar to that of total pore volume with rise in the synthesis temperature. It should be stressed here that the AlKIT-5 material prepared at 100 $^{\circ}$C had a very low pore volume of 0.45 cm$^3$/g. Thus, the synthesis carried out at high temperatures helps to drastically increase the pore volume of the aluminosicliates, in addition to their pore diameter. On the other hand, the wall thickness of these AlKIT-5 materials, prepared at high temperatures, is calculated to be lower than that of AlKIT-5-100 (4 nm).

Increase in pore diameter of the aluminosilicates with increase in the synthesis temperature can be attributed to the changes in the nature of the micelles, formed by the temperature sensitive triblock copolymer Pluronic F127 [(EO)$_{97}$(PO)$_{69}$(EO)$_{97}$]. The polyethylene oxide (PEO) chains of the surfactant are hydrophilic and polypropylene oxide (PPO) chains are hydrophobic at low temperatures. With increase in temperature the hydrophilicity of the PEO chains decreases. The decrease in hydrophilicity or a corresponding increase in the hydrophobicity leads to an enhanced interaction of the PEO chains with the PPO chains of the micelle, resulting in a longer hydrophobic part in the micelles. This results in an increase in the overall size of the micelles. Such an increase in the micelle size might be the reason for a drastic increase in the pore diameter of the AlKIT-5 materials with increase in synthesis temperature. The observed bimodal PSD for AlKIT-5-130 might be arising from the formation of mainly two types of micelles with different size of hydrophilic head region. With increase in synthesis temperature, since the hydrophilic region slowly starts diminishing, PSD changes from bimodal to unimodal. The variations in the micelle size as a function of temperature is reflected on the broadening of the PSD

_____

of the AlKIT-5 materials as well. The enhanced interaction of the PEO chains with the PPO chains at higher temperatures can also result in the withdrawal of the chains to the hydrophobic micelle core, giving rise to holes or voids in the silica walls. This might be the reason for the formation of an open pore structure at very high temperatures. Such a transformation from a cage-like to a more open structure has been reported with increase in synthesis temperature in the case of cubic FDU-1 and KIT-5 [12,21].

We have studied the catalytic activity of the AlKIT-5 materials synthesized at different temperatures on the acetylation of veratrole (1,2-dimethoxy benzene) at 35 $^{o}$C using acetic anhydride (see Table 5.2). AlKIT5-130 gives a very high conversion of acetic anhydride at 43% after 1 h of the reaction. Though all the catalysts show 100 % selectivity, the conversion decreases with increasing synthesis temperature of the AlKIT-5 materials. AlKIT-5-150 shows a decreased rate of 33%, and AlKIT-3-180 a further decrease in conversion at 29%. Since the acetylation reaction proceeds through acylium intermediate RCO$^{+}$ produced from the adsorption of acetic anhydride onto the Bronsted acidic sites of AlKIT-5 catalysts, conversion should be favored by enhanced Bronsted acidity of the catalysts. Bronsted acidity of Al-doped mesoporous silica materials is attributed to tetrahedral Al sites in the framework [20]. A very low conversion brought about by AlKIT-5-180 indicates less number of tetrahedral Al sites in the material. With increase in synthesis temperature even though Al content in the AlKIT-5 materials increases, the structural transformation from a cage- type mesoporous structure to a more open structure seems to decrease the number of active sites in the materials which in turn leads to a decrease in the acetic anhydride conversion. AlKIT-5-130 showed higher conversion rates of 60% and 75% after 1h when the acetyltion of veratrole was carried out at 50 $^{o}$C and 60 $^{o}$C respectively. It is

| Catalyst | Acetic anhydride conversion (%) |
|----------|----------------------------------|
| AKT-130  | 43 |
| AKT-150  | 33 |
| AKT-180  | 29 |

**Table 5.2.** Catalytic activity of the AlKIT-5 materials prepared at different temperatures, on the acetylation of veratrole using acetic anhydride at 35 $^{o}$C. Time of the reaction = 1h.

to be noted that the AKIT-5 synthesized at 100 $^{o}$C did not show any conversion at 35 $^{o}$C. It was found to be active only at higher temperatures, showing a conversion of 50% after 2 h at 60 $^{o}$C [20]. Lower Al content, thus lesser number of active sites, in the AlKIT-5 might be the major reason for its poor catalytic activity. Thicker walls (4 nm) which bury the active catalytic sites in the case of AlKIT-5-100 might also be a factor in reducing its catalytic activity, in comparison to the materials prepared at higher temperatures. Also, the acetic anhydride conversion of 75% given by AlKIT-5-130 at 60 $^{o}$C is much higher than that reported for various zeolitic materials such as Hβ, HY, H-modernite and H-ZSM-5 at the same temperature [20].

## 5.5 Conclusions

In conclusion, it has been possible to incorporate Al into mesoporous silica (KIT-5) framework at high temperatures by employing a temperature-sensitive

_____

triblock copolymer surfactant as the template. The effect of synthesis temperature in modifying the textural parameters of the mesoporous materials has been studied. With increase in synthesis temperature, the materials are found to structurally transform from a 3-D cage type mesoporous structure to a more open pore structure. Al content, pore diameter and pore volume of these AlKIT-5 materials are found to be drastically higher than those of AlKIT-5 prepared at 100 $^o$C. Also, the AlKIT-5 materials prepared at high temperatures are found to be catalytically active in the acylation of veratrole, even at temperatures as low as 35 $^o$C.

_____

## 5.6    References

[1] R. Xu, W. Pang, J. Yu, Q. Huo, J. Chen, *Chemistry of Zeloites and Related Porous Material- Synthesis and Structure*; John Wiley and Sons, (Asia) (2007).

[2] Q. Huo, D. I. Margolese, G. D. Stucky, *Chem. Mater.* 1996, **8**, 1147.

[3] P. T. Tanev, T. J. Pinnavaia, *Science* 1995, **267**, 865.

[4] J. S. Beck, J. C. Vartuli, W. J. Roth, M. E. Leonowicz, C. T. Kresge, K. D. Schmitt, C. T-W. Chu, D. H. Olson, E. W. Sheppard, S. B. McCullen, J. B.    Higgins, J. L. Schlenker, *J. Am. Chem. Soc.* 1992, **114**, 10834.

[5] C. T. Kresge, M. E. Leonowicz, W. J. Roth, J. C. Vartuli, J. S. Beck, *Nature* 1992, **359**, 710.

[6] C.-Y. Chen, H.-X. Li, M. E. Davis, *Micropor. Mater.* 1993, **2**, 17.

[7] A. Monnier, F. Schuth, Q. Huo, D. Kumar, D. Margolese, R.S Maxwell, G. D. Stucky, M. Krishnamurty, P. Petroff, A. Firouzi, M. Janicke, B. F. Chmelka, *Science* 1993, **261**, 1299.

[8] Q. Huo, D. I. Margolese, U. Ciesla, P. Feng, T. E. Gier, P. Sieger, R. Leon, P. M. Petroff, F. Schuth, G. D. Stucky, *Nature* 1994, **368**, 317.

[9] D. Zhao, Q. Huo, J. Feng, B. F. Chmelka, G. D. Stucky, *J. Am. Chem.Soc.* 1998, **120**, 6024.

[10] R. Ryoo, J. M. Kim, C. H. Ko, C. H. Shin, *J. Phys. Chem. B* 1996, **100**, 17 718.

[11] Y. Sakamoto, M. Kaneda, O. Terasaki, D. Zhao, J. M. Kim, G. D. Stucky, H. J. Shin, R. Ryoo, *Nature* 2000, **408**, 449.

[12] F. Kleitz, D. Liu, G. M. Anilkumar, I-S. Park, L. A. Solovyov, A. N. Shmakov, R. Ryoo *J. Phys. Chem. B* 2003**, 107***, 14296.

[13] J. R. Matos, M. Kruk, L. P. Mercuri, M. Jaroniec, L. Zhao, T. Kamiyama, O. Terasaki, T. J. Pinnavaia, Y. Liu, *J. Am. Chem. Soc.* 2003, **125**, 821.

_____

[14] T. Yamada, H. S. Zhou, H. Uchida, M. Tomita, Y. Ueno, T. Ichino, I. Honma, K. Asai, T. Katsube, *Adv. Mater.* 2002, **14**, 812.

[15] S. Besson, T. Gacoin, C. Ricolleau, C. Jacquiod, J. P Boilot, *Nano Lett.* 2002, **2**, 409.

[16] R. Ryoo, S. H. Joo, M. Kruk, M. Jaroniec, *Adv. Mater.* 2001, **13**, 677.

[17] L. X. Dai, K. Tabata, E. Suzuki, T. Tatsumi, *Chem. Mater.* 2001**, 13**, 208.

[18] L. X. Dai, Y. H. Teng, K. Tabata, E. Suzuki, T. Tatsumi, *Microporous Mesoporous Mater.* 2001, **44-45**, 573.

[19] R. Ryoo, S. Jun, J. M. Kim, M.J. Kim, *Chem. Commun.* 1997, 2225.

[20] P. Srinivasu, S. Alam, V. V. Balasubramanian, S. Velmathi, D. P. Sawant, W. Bohlmann, S. P. Mirajkar, K. Ariga, S. B. Halligudi, A. Vinu, *Adv. Funct. Mater.* 2008, **18**, 640.

[21] M. Kruk, M. Jaroniec, *Chem. Mater.* 2003**, 15**, 2942.

[22] G.A. Olah, *Friedel-Crafts and Related Reactions*; Wiley, New York (1973).

[23] P. Moreau, A. Finiels, P. Meric, J. Mol. Catal. 2000, **154**, 185.